ABSTRACT

Title of dissertation: EXPERIMENTAL STUDIES OF FLUCTUATIONS AND TRANSPORT AT SOLID SURFACES.

Daniel Barker Dougherty, Doctor of Philosophy, 2004

Dissertation diredcted by: Professor Ellen D. Williams
Department of Physics

Fluctuations are used in a variety of surface systems as an experimental tool to gain insight into surface transport properties. The fluctuations of monatomic steps are studied with variable temperature STM to determine understand the kinetics of mass transport on Al-chemisorbed Si(111) surfaces. The same technique is employed to understand the kinetics of edge diffusion on Pb(111) spiral steps both in equilibrium and out of equilibrium. It also used to investigate the fluctuations of domain boundaries between structural phases of Pb on Si(111). Deterministic mass transport involved in the decay of metastable structures on Pb(111) microfacets is also investigated with variable temperature STM and the validity of the detachment-limited model of transport kinetics addressed for that system. Finally, the fluctuations in macroscopic sample resistance are used to elucidate the nature of the conduction onset in submonolayer films of Ag grown on Si(111) at low temperature. Such measurements indicate that the system is best modeled by an off-lattice percolation system and therefore the role of the substrate in the conduction onset must be minimal.

EXPERIMENTAL STUDIES OF FLUCTUATIONS AND TRANSPORT AT SOLID SURFACES

by

Daniel Barker Dougherty

Thesis submitted to the Faculty of the Graduate School of the
University of Maryland, College Park in partial fulfillment
of the requirements for the degree of
Doctor of Philosophy
2004

Advisory Committee:

Professor Ellen D. Williams, Chair
Professor Theodore L. Einstein
Professor Janice E. Reutt-Robey
Professor John D. Weeks
Professor Michael S. Fuhrer

Dedication

To my parents: David and Diane Dougherty

Acknowledgements

I had remarkable luck as a graduate student, first in being taken on as a research assistant with no experience by Prof. Ellen Williams, and next in having the opportunity to work in her lab continuously for my entire graduate career. Ellen has been the ideal research director, providing a balance between freedom and focus that made work in her group exciting and rewarding. Apart from her sometimes spooky physical insight, she has always managed to make me feel confident in our work, and therefore immeasurably benefited my ability to present it in public.

Prof. Ted Einstein deserves the credit for directing me to Ellen's office when I was a first-year graduate student looking for research experience. My subsequent interactions with him have been no less productive. He has been a valuable teacher and collaborator from the very beginning. His group's close relationship with Ellen's group is, in my opinion, the most unique advantage to working in surface science at the University of Maryland.

In addition to Ellen and Ted, I owe thanks to the other members of my thesis committee, Prof. Janice Reutt-Robey, Prof. John D. Weeks, and Prof. Michael S. Fuhrer. They came together and combed through this work on somewhat short notice and provided substantial insight and improvements. Prof. Janice Reutt-Robey, the Dean's representative on the committee, has been a long-time collaborator and experimental advisor. In my earliest experimental work, I often wore out my welcome in her labs by monopolizing her spot-welding equipment. In my most recent experimental work, I physically removed many thousands of dollars worth of UHV hardware from her lab

(with her permission of course). She has tolerated all of this with good-natured enthusiasm.

Ellen's first real project for me was to help research scientist, Igor Lyubinetsky, on STM studies of Al/Si(111). Igor was thus given the unenviable task of introducing me to the day-to-day details of working on UHV-STM. This also meant he had to fix many of my inevitable mistakes. His supreme patience in this duty was fairly astounding. I rarely saw him agitated, even in the middle of the night as our last sample hung precariously from its perch in the STM stage due to my inexperienced manipulations.

Other senior scientists in the group over the years have also been a valuable resource. Konrad Thurmer taught me how to do his wonderful Pb/Ru experiments, and was an interesting person and exciting scientist. Oleksandr Bondarchuk passed on a wealth of surface science experience, particularly in electron spectroscopy, and was a stimulating collaborator as well as a fun roommate at conferences. Bill Cullen continues to be an important collaborator and has provided a model of patience and care in experimental work.

Many graduate students that I have interacted with over my years at Maryland have been very helpful. Chief among them was Ruchi Yogsunthon, a former student of Ellen's. While our particular research projects never overlapped, we shared an office for several years and in that time Ruchi became a true scientific "elder sister", advising me on topics raging from novel adhesive methods to what T.V. shows were worth watching. She remains a close friend and trusted scientific mentor.

Also in Ellen's group, Tosh Degawa has been a valuable friend and co-worker. His calm and rational demeanor provides a useful counter-balance to my tendency toward

excitability. Apart from the many discussions we have had over the years about esoteric topics in statistical physics (in which Tosh is a master) he can be counted on to help with the dirtiest grunt work in the lab. In fact, the single picture of life as a graduate student that I would paint if I could is that of Ruchi, Tosh, and myself lying on the dirty floor, struggling to support an ancient monstrosity of a diffusion pump that we had decided to repair.

Magda Constantin, a graduate student in S. Das Sarma's group, has been a theoretical collaborator almost from the very first project I worked on. She always leaves her door open and is willing to listen to my problems understanding theoretical work or even my own data. Luckily, she has also always been willing to disagree with me when necessary, to the great benefit of science in general and this dissertation in particular.

Ted Einstein's group has been full of friends and co-workers. Post doc's Howard Richards and Ferenc Szalma and graduate students Hailu Bantu and Tim Stasevich subscribe wholeheartedly to their advisor's belief in the importance of close contact between experimentalists and theorists. Prof. John Weeks and his student Tong Zhao and recent post-doc Madhav Ranganathan have also gone beyond the call of duty in this regard.

Technical assistance and advice from many areas has been important to the completion of the work described in this thesis. Prof. Dennis Drew's group, especially Dr. Don Schmadel, has always been a useful neighbor across the hall. Prof. Michael Fuhrer and his group provided a similar resource, particularly in the last two years of my work at Maryland. Tom Loughran in the Electrical Engineering clean room made time in

his busy schedule to help me make Moly contact pads in his e-beam evaporator on short notice.

On the non-technical side, the MRSEC staff deserves recognition. Shirley Winter, Donna Hammer, Jennifer Stott, Julie Callis, and Carolyn Garvey are always patient and willing to help the sometimes distracted and self-centered graduate students. Al Godinez and Jesse Anderson in physics receiving and purchasing made me feel like I have at least some allies in the administrative details lab work.

I doubt any graduate student would ever succeed without the kind and expert assistance of Jane Hessing. For the entire time I was at Maryland, even in my first year, she always seemed to be expecting me when I poked my head in her door. Not only that, but she seemed to know exactly what I was going to need help with and have the appropriate file or form within easy reach.

From an entirely personal perspective, I want to thank the University of Maryland Cycling team for being a fun and much-needed diversion from graduate school. Finally, Sarah Giffitts' unique outlook and unwavering encouragement during the writing of this thesis helped keep my life balanced by reminding me that there are some things that transcend professional pursuits.

TABLE OF CONTENTS

LIST OF FIGURES

Chapter 1

Introduction: Surface Steps and Mass Transport

The continuum step model for describing nanoscale mass transport on solid surfaces is introduced. Langevin equations describing the fluctuations of isolated monatomic steps are derived from a coarse-grained Hamiltonian and the major statistical characterizations of fluctuating steps are introduced. The value of kinetic parameters determined from the study of step fluctuations for a predictive understanding of deterministic transport is illustrated. Universality classes of interface fluctuation models are also described, as are the first-passage statistics for stochastic processes.

1.1 Motivation

Excitement about the potential technological advances that may result from the study of nanometer-scale physics provides a significant driving force for modern condensed matter physics. Of course, much of nanoscience is simply the current incarnation of what has been traditionally called surface science. Solid surfaces are the natural stage for the fabrication of small-scale structures and surface science techniques (e.g. Scanned Probe Microscopies) are natural for nanometer-scale characterization. In fact, surface reconstructions are self-assembled nanostructures and may ultimately provide templates for more exotic fabrication.

An important fundamental question that arises naturally in the investigation of the nanoworld is how to approach physical systems that contain too many constituent particles to allow a practical atomic-scale description, but whose physical size is small enough that ordinary continuum descriptions will not properly capture their behavior[1]. The perspective that will be taken in the following work is that of an intermediate continuum-type picture of processes on solid surfaces. It is possible to coarse-grain over the outrageously complicated atomic degrees of freedom without eliminating the discrete features fundamental to nanoscale behavior. The discrete features that seem to be most relevant for small-scale surface processes are monatomic steps. These are simply linear defects that result whenever there is an incomplete crystal plane on the surface. The picture of solid surfaces that we will find extraordinarily useful for understanding nanoscale mass transport is one where the surface is made up of continuous monatomic steps separated by continuous terraces. The motion of such steps will often be found to govern surface evolution and furthermore the fluctuations of such steps can be used to

access the potentially dominant stochastic behavior at the nanoscale as well the essential mesoscopic kinetic and thermodynamic parameters required to make quantitative predictions.

In the next section, we will introduce in more detail the thermodynamics and kinetics of steps on solid surfaces with particular attention to the continuum step model. Next we will develop the Langevin treatment of step fluctuation dynamics and show how to extract important continuum parameters from the experimental observation of step fluctuations. The use of such parameters in understanding and predicting deterministic surface evolution will be illustrated. We will also describe a theoretical treatment of interface fluctuations, developed in the spirit of thermal critical phenomena, in which scaling exponents are used to define dynamic universality classes for interface models. Finally we will introduce first-passage statistics for fluctuating interfaces as a potentially valuable new method of characterization.

1.2 Steps on Surfaces

Presently, it is possible to observe in great detail the real-space structure of solid surfaces from the atomic to the micrometer scale using Scanning Tunneling Microscopy (see chapter 2). As has been known for more than half a century[2], monatomic steps are a common and extremely important feature of any surface. Such steps often form regular arrays as a result of a slight miscut of the surface from a high symmetry direction. An example of one of these so-called vicinal surfaces is shown in figure 1.1. This is a 3000 nm image of a Si(111)-(7x7) surface prepared on a wafer miscut from the (111) plane by about 0.4º toward the $[2\bar{1}\bar{1}]$ direction. The steps are geometrically constrained

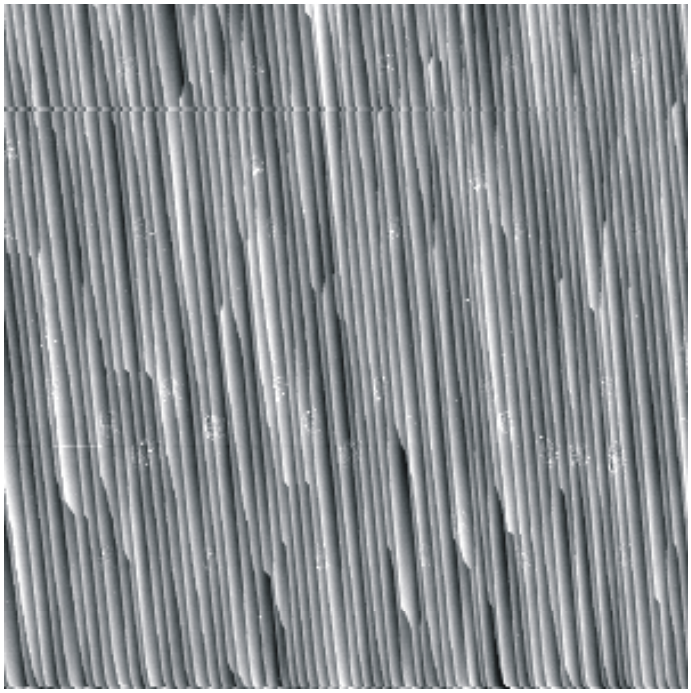

Figure 1.1 3 μm x 3 μm STM image of a vicinal Si(111)-(7x7) surface.

by this miscut to be 45 nm apart on average (since a Si step height is 3.14 Å, the step separation is L = 3.14/(tan0.4)= 450 Å). Steps can also exist on surfaces due to sputter damage that is not annealed away, growth processes forming large but finite islands, or even bulk dislocations that terminate by intersecting a perfect surface. In truth, steps are the most common nanoscale defect on nearly any surface.

As an extended defect, there is an energy cost to forming a step that can be treated thermodynamically. Before discussing the thermodynamics of steps, let us explicitly describe the continuum step model that will provide the needed mesoscale perspective for dealing with surface mass transport. Figure 1.2 shows schematically the two views of steps on surfaces. The picture on the top is a ball model that depicts the reality of steps on surfaces: they are composed of atoms that can meander around the surface in fairly complicated spatial patterns. The lower figure depicts the continuum step model of this situation. Here the step is described as a *continuous stochastic function x(y,t)* (the coordinate system follows the so-called "Maryland notation" with y running parallel to the average step direction and x running perpendicular to it). It will be shown in what follows that we can describe the thermodynamics and kinetics of such a continuous object using only a few parameters as opposed to the enormous number of parameters that would be required to make a complete atomic-scale description of nanoscale mass transport. These few parameters have been referred to as "key measurables" in a recent review by Jeong and Williams[1] and extracting them from experimental data will occupy a significant part of this thesis.

The free energy per unit length of a step β includes naturally the energy cost of forming a step as well as the increase in entropy created by the step ($\beta=\beta_0-TS_0$ with S_0

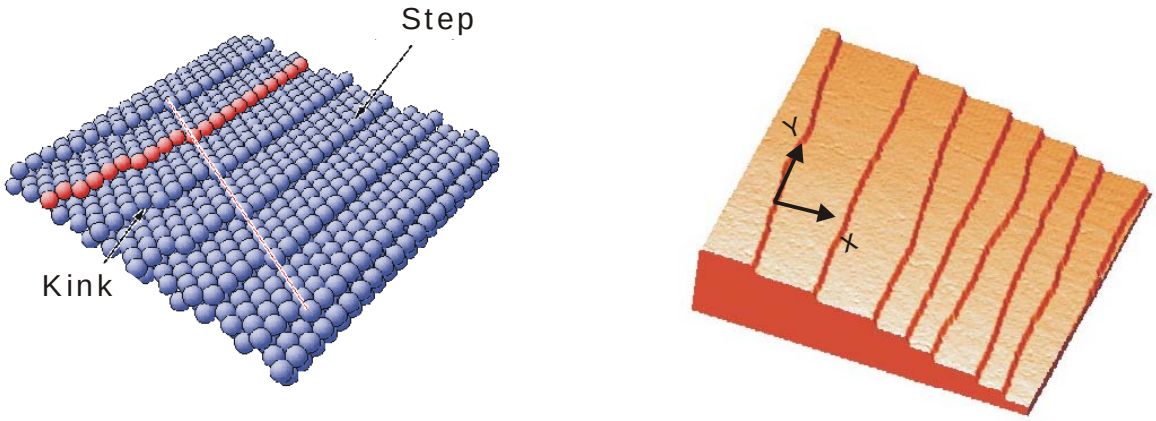

Figure 1.2 Left: atomic view of a stepped surface. Right: continuum step picture where steps are continuous line boundaries. Note the coordinate system on the left hand picture.

being the configurational entropy of a step due to its spatial meandering along the surface[1]). We can then write a free energy functional for an isolated step as[1, 3-6]

$$F[x(y)] = \int \beta(\theta) ds \qquad (1.1)$$

where *ds* represents an arc length along the continuous step and the possible dependence of β on average step direction is made explicit. The angle θ is conventionally defined as the complement of the local slope of the step in the surface plane so that $\frac{dy}{dx} = \tan\left(\frac{\pi}{2} - \theta\right)$. Changing over to the coordinate system in figure 1.2 we can re-write Eq. 1.1 as a functional of *x(y)* (ignoring for now the time dependence in the step position):

$$F[x(y)] = \int \beta(\theta) \sqrt{1 + (\partial_y x)^2}\, dy \qquad (1.2).$$

Before saying more, we should note that in the above equations step interactions are not included. For the work to be presented later, step interactions have not been found to be important. Nevertheless, steps always have some sort of interaction, even if it is only a steric (or entropic) repulsion that prevents them from crossing each other to create overhangs on the surface. Discussions of step interactions and references to situations where they are important can be found in both the review by Jeong and Williams[1] and the review by Giesen[3].

Equation 1.2 should in principle allow any thermodynamic quantity to be determined by taking the appropriate functional derivative. There are several approximations that will make it easier to use, however. The essential one is simply that *dx/dy* is small, or that the step does not wander very far from its high-symmmetry

direction. We can then expand both β and the radical in Eq. 1.2 to second order in *dx/dy* to get the following integral:

$$F = \int \frac{\tilde{\beta}}{2} \left(\partial_y x\right)^2 dy \qquad (1.3).$$

Here the quantity $\tilde{\beta}$ is a new parameter called the *step stiffness* and is defined by:

$$\tilde{\beta} = \beta\left(\frac{\pi}{2}\right) + \frac{\partial^2 \beta}{\partial \theta^2} \qquad (1.4).$$

Very often (especially at elevated temperatures) the second derivative in Eq. 1.4 is approximately zero and then the stiffness is simply the free energy per unit length of the step. Step stiffness will be seen throughout this work to be the single fundamental thermodynamic parameter of the continuum step model. It is in fact one of our "key measurables" and we can use equation 1.3 to immediately obtain an experimentally relevant result. Following Jeong and Williams[1], we can use the Fourier transform of the step profile *x(y)* to diagonalize Eq. 1.3 and compute the spatial correlation function defined by:

$$G(y) = \left\langle (x(y) - x(y_0))^2 \right\rangle \qquad (1.5).$$

The average can be computed in Fourier space by:

$$G(y) = \frac{k_B T}{2\pi} \int dq \frac{2(1 - \cos(qy))}{\tilde{\beta} q^2} \qquad (1.6)$$

and has the small y limit

$$G(y) = \frac{k_B T}{\tilde{\beta}} y \qquad (1.7).$$

This simple result is of great value in allowing the experimental determination of the step stiffness. If we take an STM snapshot of a step or an array of steps, it is possible to

digitally extract step profiles *x(y)* and then compute the spatial correlation function directly using Eq. 1.5. The initial slope of the measured *G(y)* then immediately gives the step stiffness at the temperature of the experiment. An example of this procedure can be found in chapter 3 of this work.

Step stiffness is a phenomenological continuum step parameter that quantifies how difficult it is to produce a bend in the continuum step function *x(y)*. Significantly, nothing in our above discussion refers to atomic details. Of course, that was the whole point of introducing the continuum step model, but it is nevertheless instructive to see what kind of connection we can make between the step stiffness and microscopic models of step structure. The simplest model of a step is a simple one-dimensional solid-on-solid model[1] where ε is the energy cost of creating a single kink in an otherwise straight step. In this model, the spatial wandering of the step can be analyzed by analogy to a 1D random walk[1, 4]. The motion in the *y* direction can be considered as the motion in time of a simple random walker. This leads by simple analogy to the linear increase of *G(y)* found in Eq. 1.7. The slope of *G(y)* in the 1D SOS model is (again by analogy) called the *step diffusivity* and is simply the mean squared size of a kink, b^2. With this parameter, the spatial correlation function is

$$G(y) = \left\langle (a_n n)^2 \right\rangle \frac{y}{a_p} = \frac{b^2}{a_p} y \quad (1.8),$$

where n is the (integer) size (or depth) of the kink, a_n is the lattice constant projected perpendicular to the step edge, and a_p is the projection parallel to it.

In the SOS model the average in Eq. 1.8 can be computed since the energy of a kink of size n is $E(n)=n\varepsilon$ and this expression can be used to compute the complete

partition function for the model. The step diffusivity for relatively small kink energies on a square lattice is then given in terms of the microscopic kink energy as:

$$b^2 = 2a_p^2 \exp\left(\frac{-\varepsilon}{k_B T}\right) \qquad (1.9).$$

(Note that the factor of 2 is replaced by 3/2 if the lattice is triangular instead of square[7]). This result thus provides us with a connection between the continuum step stiffness and an atomic scale energetic parameter. This is very interesting: kink energies can in fact be calculated using first-principles techniques[7]. On simple elemental metal surface it is very likely that the SOS model is adequate to understand step thermodynamics, but for more complicated surfaces with reconstructions and significant relaxations this may not be the case.

In this section, using a coarse-grained continuum step free energy, we have arrived at a simple thermodynamic characterization of surface steps that can be measured experimentally and even understood to a certain extent using microscopic models. The next section will show how the same continuum step model can also be used to understand the dynamics of step fluctuations with only a few simple kinetic parameters.

1.3 Langevin Theory of Step Dynamics

One of the most famous examples of phenomenological modeling (that was instrumental in the development of the atomic picture of matter) is that of Brownian motion of colloidal particles. In 1828, Robert Brown observed the apparently random motion of suspended pollen grains and attributed it to something intrinsic to the particles and not a macroscopic process like fluid flow or evaporation[8]. Of course, the actual cause of the random motion was collisions of thermally moving fluid molecules with the

colloidal particles as recognized independently by Einstein[9] and Smoluchowski[10]. A very simple way to model this process was suggested by Langevin[11] and provides the spirit with which most investigations of step fluctuations are currently conducted[1, 3, 12]. The Langevin formalism for Brownian motion incorporates all of the microscopic complexity of the molecular motion of the fluid into a phenomenolgical "noise" term in the equations of motion for a Brownian particle. This can reproduce the apparently random velocity of the particle and also allows the calculation of observable quantities such as the mean-squared displacement of the particle[8].

We will model step dynamics with a Langevin formalism that similarly incorporates the complicated atomic scale transport processes on the surface into phenomenolgical noise. In general, we can express the step velocity by the functional relation[6]:

$$\partial_t x(y,t) = f[x(y,t)] + \eta(y,t) \qquad (1.10).$$

The functional f is used to describe the deterministic relaxation processes involved in the step motion. It depends on exactly what process is being modeled and can be nonlinear or nonlocal. In some cases it is possible to provide microscopic justification for the form of $f[x(y,t)]$[13] but often it is obtained from considerations of the symmetry of the process it is used to describe[14]. The noise term η has an amplitude and correlations that are also determined by the process under consideration.

For isolated surface steps (of primary concern in this work), there are three important surface transport processes that can govern the relaxation of fluctuations[1, 3, 5, 6, 15-17]. Figure 1.3 shows a schematic representation of the processes. The simplest, called attachment/detachment (AD) or 2D-evaporation/condensation (2D-EC), involves the

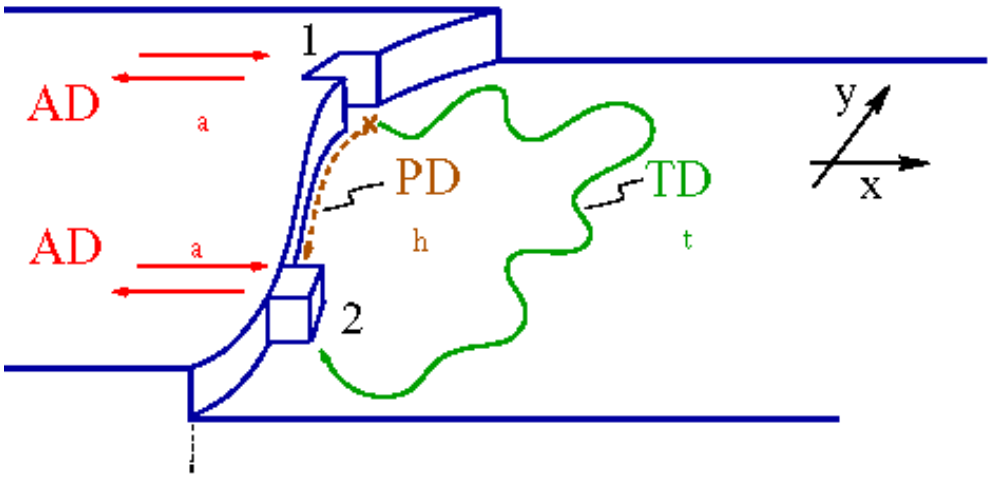

Figure 1.3 Schematic of the three surface mass transport processes important for the fluctuations of isolated steps. AD=Attachment/Detachment, PD=Periphery Diffusion (or step-edge diffusion), TD=Terrace Diffusion.

random exchange of mass between the step and its adjacent terrace. Microscopically, rate-limiting AD means that there is some barrier to exchange that makes it slower than other processes. In terms of the functional in Eq. 1.10, the deterministic relaxation for such a process is governed by the free energy change associated with step displacement. This can be written using Eq. 1.3 as the following functional equation[4]:

$$\partial_t x(y,t) = -\frac{\Gamma_a}{k_B T}\left(\frac{\delta F}{\delta x}\right) + \eta \,. \qquad (1.11)$$

In this equation we have introduced the analog of a (Stokes-type) friction coefficient, Γ_a, that will be called the step attachment/detachment mobility. It is simply the linear kinetic parameter governing the AD process and is another example of a key measurable within the continuum step picture[1]. If we perform the functional derivative in Eq. 1.11, the following linear stochastic partial differential equation results:

$$\partial_t x(y,t) = \frac{\Gamma_a \tilde{\beta}}{k_B T}\left(\frac{\partial^2 x}{\partial y^2}\right) + \eta \,. \qquad (1.12)$$

Equation 1.12 provides a simple (and exactly solvable[14]) model for the AD process that can be used to calculate experimentally measurable quantities. In addition, we can apply the basic theorem of fluctuation physics to better understand the noise term and its relation to surface kinetics. For AD processes, the statistical properties of the noise are as simple as possible: the noise is uncorrelated or "white" in both space and time and has zero mean[4, 12]. This can be written explicitly as:

$$\langle \eta(y,t)\eta(y',t') \rangle = D\delta(y-y')\delta(t-t') \,. \qquad (1.13)$$

The noise magnitude has been expressed as some constant, *D*, but this number is in fact not independent of the phenomenological parameters already introduced. Fundamental to statistical physics (and perhaps forming the basis for this entire thesis) is the *Fluctuation-*

Dissipation Theorem that relates dissipative transport coefficients to the autocorrelation function of a noise term[8, 18]. For example, in the case of a randomly forced Brownian particle, the strength of the random force (i.e. the noise magnitude) is proportional to the friction coefficient of the fluid in which the particle is suspended[19]. In the case of AD fluctuation kinetics of a step edge, the noise magnitude D is related to the step mobility simply by $D=2\Gamma_a$[4]. Thus, for this simple surface transport process we have only two parameters to model the near-equilibrium structure and dynamics of steps. The step stiffness determines the equilibrium step structure and the step mobility determines the kinetics of fluctuations of the step about its equilibrium structure. It is remarkable that we are able to describe completely the behavior of a complicated, extended defect like a step with such a small set of parameters. This is the great power of the continuum step model, as will be demonstrated throughout the present work.

From equation 1.12, we can proceed to obtain experimentally measurable quantities by Fourier transformation. The step position can be decomposed into modes of wavelength q, and its derivatives computed[6]:

$$x(y,t) = \sum_q \exp(iqy) x_q(t) \qquad (1.14a)$$

$$\partial_t x_q = -\frac{x_q}{\tau(q)} + \eta_q . \qquad (1.14b)$$

Here we have introduced the time constant $\tau(q)$ for relaxation of a mode of wavelength q. We will see shortly that this function is perhaps the most useful in understanding step fluctuations. The Fourier transform of the noise has correlations and an amplitude given by essentially the same reasoning as in real-space (equipartition and fluctuation-dissipation theorems). The form Eq. 1.14 can be substituted into Eq. 1.12 and we can

solve for almost any quantity of interest. In particular the correlation function of a Fourier mode is very useful. This is defined by:

$$G_q(t-t') = \left\langle \left| x_q(t) - x_q(t') \right|^2 \right\rangle . \qquad (1.15)$$

Solving Eq. 1.12 for this quantity yields:

$$G_q(t-t') = \frac{2k_BT}{\tilde{\beta}q^2}\left(1 - \exp\left(\frac{|t-t'|}{\tau(q)}\right)\right). \qquad (1.16)$$

where the prefactor in front of the parentheses is simply determined by comparison with the static correlation function of the previous section and application of the equipartition of energy among the step modes. Equation 1.16 is completely general; it does not depend on the specific transport process governing the fluctuations. The details of the specific process will enter only in the specific form of the function $\tau(q)$. For AD processes at the step edges, the time constant has the very simple form:

$$\tau(q) = \frac{k_BT}{\tilde{\beta}q^2\Gamma_a} . \qquad (1.17)$$

This relation is experimentally measurable. Using a real-space technique (e.g. STM, or an electron microscopy) it is possible to obtain a time-lapsed sequence of step configurations. These configurations can be numerically decomposed into their constituent Fourier modes and the time constant for decay of each mode extracted. If $\tau(q)$ decays with the inverse square of q then (assuming steps are approximately isolated, see chapter 3) it can be concluded that the rate-limiting surface transport process is attachment-detachment. In addition, from fits of experimental correlation functions to Eq. 1.16 it is possible to extract *both* key measurables, the step stiffness and mobility, from the data. An example of this procedure applied to Si(111) steps observed at high

temperature with REM can be found in Bartelt et al.,[12] and more recent examples can be found in the LEEM experiments performed at the University of Illinois at Urbana-Champaign[20].

Often the Fourier space description of step fluctuations is not experimentally feasible. Particularly for STM experiments, in which step fluctuations can be significantly faster than the imaging rate, it is necessary to monitor the time dependence of a single point on a step edge rather than the time dependence of the entire step configuration[1, 3, 21]. In this case, the experimental quantity of most interest is the real-space temporal correlation function defined by:

$$G(t) = \left\langle \left(x(t) - x(t_0) \right)^2 \right\rangle, \qquad (1.18)$$

where the angular brackets signify an average over all initial times t_0. Naturally, exact results for *G(t)* can be obtained by Fourier transforming $G_q(t)$. For the specific case of AD processes the temporal correlation function is:

$$G(t) = \sqrt{\frac{4k_B T \Gamma_a t}{\pi \tilde{\beta}}}. \qquad (1.19).$$

This equation provides an alternative way of judging whether fluctuations are limited by AD kinetics. Instead of looking for a q^{-2} dependence of $\tau(q)$, we look for a $t^{1/2}$ dependence of *G(t)*. Then, from fits of experimental *G(t)* curves to a power law, the combination of stiffness and mobility appearing under the radical can be obtained. This method of data analysis has the disadvantage of requiring an independent determination of the step stiffness from the spatial correlation function *G(y)* (as described in the previous section), but is nevertheless capable of providing all the important continuum step properties.

A second important surface transport process that often governs step fluctuations (especially on metal surfaces near and below room temperature[3]) is the diffusion of mass parallel to the step edge. This so-called periphery diffusion (PD) or step-edge diffusion (SED) can be modeled using the same procedure as the AD process described above but with a different relaxation functional in the Langevin equation and different correlations of the noise term. The basic distinguishing microscopic feature of SED is that, since mass is running along the step edge, the number of atoms on the step must be conserved. This is put in the continuum step model by requiring the average step position to be constant. The Langevin equation is modified following the procedure developed for the study of the dynamics of critical phenomena[22]. In the case where an order parameter for a continuous phase transition is conserved, the dynamics are modified by making the functional in Eq. 1.10 expressable as a conserved current (this is Model B of Hohenberg and Halperin while nonconserved AD kinetics is Model A[22]). For SED this results in the Langevin equation:

$$\partial_t x(y,t) = \frac{\Gamma_h}{k_B T}\nabla^2\left(\frac{\delta F}{\delta x}\right) + \eta_c \ . \qquad (1.20)$$

The Laplacian operator in front of the functional derivative ensures that the relaxation term is conservative and the noise term has the subscript *c* to indicate that its correlations must also enforce conservation. The new "friction coefficient", Γ_h, is the edge-hopping mobility and describes the rate of mass transport along the step edge. After evaluating the derivative, the equation is:

$$\partial_t x(y,t) = -\frac{\Gamma_h \tilde{\beta}}{k_B T}\nabla^4 x(y,t) + \eta_c \, . \qquad (1.21)$$

The conserved noise still has zero mean but the correlations are modified from the simple white noise used to model AD kinetics:

$$\langle \eta_c(y,t)\eta_c(y',t')\rangle = 2\Gamma_h \nabla^2 \delta(y-y')\delta(t-t'), \qquad (1.22)$$

where we have employed the fluctuation-dissipation theorem to express the noise strength in term of the SED mobility. The Laplacian in front of the spatial delta function means that the noise is the result of a *white current* (this is useful in performing numerical integrations). Since both terms in Eq. 1.21 can be written as some sort of current, we are ensured a continuity equation that establishes the conservative nature of the SED process.

Of course, the q dependence of $\tau(q)$ is different for the case of SED kinetics. It reads:

$$\tau(q) = \frac{k_B T}{\Gamma_h \tilde{\beta} q^4} \qquad (1.23)$$

and allows the experimental time constants to be used to distinguish fluctuations governed by this process from the AD process. The form of the real-space temporal correlation function is also distinct for SED and is given by[1, 3, 4, 23]

$$G(t) = \Gamma\left(\frac{3}{4}\right)\left(\frac{(k_B T)^3 \Gamma_h t}{\tilde{\beta}^3}\right)^{1/4}. \qquad (1.24)$$

$G(t)$ grows much more slowly in time for SED-limited kinetics than AD-limited kinetics. The function again conatins only the two key measurables, stiffness and mobility, in the continuum step model ($\Gamma(3/4)$ is just the gamma function of 0.75 and is numerically equal to 1.2254…). The SED process can clearly also be modeled in the continuum step

picture using the thermodynamic stiffness (which is independent of dynamics) and the single kinetic parameter, Γ_h.

A third isolated step transport process is simple terrace diffusion (TD). The transport of mass along the flat terraces between steps can also lead to fluctuations in step position. This process is the most complicated to model in the Langevin formalism because it requires a non-local functional in Eq.1.10 as well as a complicated noise correlation. The Langevin equation for isolated step terrace diffusion is[15]:

$$\partial_t x(y,t) = -\frac{4D_s c_s \tilde{\beta}\Omega^2}{k_B T} \int_{-\infty}^{\infty} \frac{\partial^2 x}{\partial y^2}\bigg|_{y'} \frac{b^2 - (y-y')^2}{\left[b^2 - (y-y')^2\right]^2} dy' + \eta_d(y,t), \qquad (1.25)$$

and the noise is spatially correlated with the form[15]:

$$\left\langle \eta_d(y,t)\eta_d(y',t')\right\rangle = 8D_S c_s \Omega^2 \frac{b^2 - (y-y')^2}{\left[b^2 - (y-y')^2\right]^2} \delta(t-t'). \qquad (1.26)$$

In these equations, b is a constant of order one lattice spacing. As described by Bartelt et al.[15], this noise correlation is strongly peaked near $y = 0$, becomes negative, and then very small as y (i.e. the distance along the step) increases. The kinetic parameter appearing in this model is the product of the surface diffusion coefficient D_s and the equilibrium adatom concentration c_s, and Ω is the area of the surface unit cell. The non-local nature of the Langevin equation, as well as the spatial correlation of the noise, simply arises because the motion of the step via terrace diffusion processes depends on the diffusion field on the terraces far away from the step position being considered. Remarkably given the apparent complexity in equations 1.25 and 1.26, the form of $\tau(q)$ is still a simple power of q:

$$\tau(q) = \frac{k_B T}{2D_s c_c \Omega^2 \tilde{\beta} q^3} \qquad (1.27).$$

Similarly, the temporal correlation function remains a simple fractional power of time:

$$G(t) = 0.86\left(\frac{2D_s c_c (k_B T)^2 \Omega^2 t}{\tilde{\beta}^2}\right)^{1/3} \qquad (1.28)$$

Thus, the characteristic power laws for terrace diffusion are intermediate between the power laws for AD and SED.

Having discussed the three isolated step surface transport processes that can result in fluctuating surface steps, we are forced to question whether the results obtained for these cases are of practical value. On a real surface one can easily imagine all three processes taking place in parallel resulting in fluctuations whose behavior is not understandable using any one of the three Langevin models just described. It is almost certainly the case that most surfaces have a number of transport processes happening in parallel. Mass transport processes are thermally activated however, and this means that it is almost always the case that one single process will be *rate-limiting* for the step fluctuations. It is this process (which was anticipated to a certain extent above by the frequent reference to *AD-limited kinetics* for example) which is dominant in the measured fluctuation data. In almost all cases studied experimentally, there seems to be a well-defined rate-limiting fluctuation process[1, 3, 6]. This is simply the result of the fact that even small differences in effective energy scales associated with a process translate into large differences in rates.

As in the case of step stiffness, it is possible to relate the linear kinetic parameters in the continuum step model to some microscopic energy. The detailed interpretation is not always as straightforward as the kink formation energy that determines the step stiffness. Step mobilities and diffusion coefficients are still usually observed to be

activated with some effective energy scale that may or may not be easily related to a single atomic hopping process. For example, even on a clean elemental metal surface[24], it is not difficult to imagine fairly complicated multi-step processes by which mass diffuses (collectively) along the step edge. Thus, the activation energy associated with the SED mobility Γ_h most likely will not refer to a single atom making a single hop along the step edge. In this work, we will refer to activation energies governing step mobilities (either SED mobility or AD mobility) as *effective energy scales* to emphasize the fact that the underlying microscopic processes may be collective and are not clearly attributable to a single microscopic event.

Before going on it should be noted that significant theoretical work has been done in recent years to treat step fluctuation kinetics in a more unified and complete manner than we have done in this section. Rather than writing Langevin equations for the three separate processes, several groups[5, 6, 16] have treated surface mass transport in general and derived the results obtained above as limiting cases. This has the advantage of allowing an understanding of crossover effects where the rate-limiting process on a surface can change as a function of an external parameter like temperature[25]. In addition, these treatments have relaxed the isolated step assumption and discussed the possibility that surface steps are close enough together to exchange mass. We will discuss many of these issues in more detail (especially in chapters 3 and 4) for specific experimental systems. In practice, however, most experiments can be understood from the isolated step perspective developed in this section.

1.4 Continuum Step Parameters and Surface Evolution

For illustrative purposes we will briefly describe two examples from the literature of how continuum step parameters, specifically step mobilities, can be used to quantitatively understand the deterministic evolution of surface features. As mentioned in the previous section, Bartelt et al. analyzed step fluctuations on Si(111) at 1170 K[12] and determined that the rate-limiting process at that temperature was attachment and detachment at the step edges. They determined an AD mobility of 5×10^7 Å^3/s. At 1220 K, Yang et al. observed that electromigration-induced step bunches on Si(111) coarsened with time following a $t^{1/2}$ power law[26]. Liu and Weeks[27] were then able to show that the mass transport involved in the coarsening process can be understood using the kinetic parameters determined from the step fluctuation measurements. Briefly, their approach was to write the mass current due to attachment/detachment at the step edges as being linear in the chemical potential gradient between the step and the terrace:

$$j = \frac{c_s \kappa}{k_B T}\left(\mu_{sn} - \mu_{tn}\right). \qquad (1.29)$$

In this expression, κ is the rate constant for AD, c_s is the adatom concentration, μ_{sn} is the step chemical potential of the nth step and μ_{tn} is the terrace chemical potential for that step. The AD mobility, Γ_a, determined from step fluctuation measurements[12] can be related to the kinetic parameters appearing in this expression through $\Gamma_a = 2a^4 \kappa c_s$, where a is the lattice constant on the surface[27]. With Eq. 1.29 as a boundary condition, Liu and Weeks numerically solved a complicated differential equation for the electromigration process and found that using the step mobilities of Bartelt et al. resulted in good agreement with experimental coarsening kinetics observed by Yang et al.

Another example can be found in the work of Giesen and Schulze Icking-Konert on Cu(111)[28]. They found SED limited fluctuation kinetics at room temperature and slightly above and determined the SED mobility from the temporal correlation function *G(t)* between 300 K and 500 K. They also studied the decay of a large protrusion (several tens of nanometers wide) on a Cu(111) step. By decomposing this bump into its Fourier modes and extracting the time constant for decay of the modes, the authors were able to show that its decay was also limited by SED and that the mobilities determined from the two types of measurements were in agreement.

These two examples serve to illustrate that the kinetic information obtained from the analysis of step fluctuations is widely applicable. In fact the continuum step parameters like mobility and stiffness seem to determine the kinetics of a remarkable diversity of mesoscale surface processes. It is expected that the importance of such parameters will increase as the dimensions of surface features of interest approach those of the monatomic steps themselves. Obviously, this means that the continuum step picture will be extremely valuable in the quantitative description of nano-objects.

1.5 **Dynamic Universality Classes**

Understanding fluctuating interfaces in general has been a topic of significant recent interest for statistical physicists[14]. As extended stochastic objects, interfaces represent a difficult problem in understanding the statistical mechanics of complex systems. In addition, many of the models investigated heavily were designed to understand interface *growth*[14]. Growth processes are of profound technological importance and several interface growth models are capable of capturing at least some of the essential feature of

the Molecular Beam Epitaxy process that is so important in the electronics industry. The continuum step model introduced in this chapter suggests that steps on surfaces can be thought of as one-dimensional interfaces and treated using some of the same ideas developed in the more general study of these objects.

The starting point for interface physics is the scaling ansatsz for the interface width. If the rms width of an interface of length L is given by:

$$w(L,t) = \sqrt{\frac{1}{L}\sum_{i=1}^{L}\left[x(i,t) - \bar{x}(t)\right]^2} \qquad (1.30)$$

then it is supposed that the width has a universal scaling form:

$$w(L,t) \sim L^{\alpha} f(at) \qquad (1.31)$$

The universal scaling function f has the asymptotic form:

$$f(u) \sim u^{\beta}, (u << 1) \qquad (1.32)$$

$$f(u) \sim const, (u >> 1) \qquad (1.33)$$

The two scaling exponents, α and β, called the roughening and the growth exponents respectively, serve to define a *dynamic universality class* for the interface model[14]. The width grows as a power law up to some crossover time t_x after which it saturates at the value proportional to L^{α}. The crossover time scales with the interface length as $t_x \sim L^z$. Here z is called the dynamic exponent and is equal to α/β. Thus the scaling ansatz is

$$w(L,t) \sim L^{\alpha} f\left(\frac{t}{L^z}\right). \qquad (1.34)$$

The notion of a universality class for interface growth models is of course inspired by the success of such classes in the description of static critical phenomena. Testing universality for these models in real physical systems is much harder than in the case of

critical phenomena. Obtaining enough data to judge scaling exponents can be a problem and so dynamic phenomena tend to suffer from poor reproducibility when compared with equilibrium phase transitions. Nevertheless, there is enough experimental justification for the existence of dynamic universality classes to warrant discussion (see the book by Barabasi and Stanley for extensive references[14]).

Beyond the practical value of studying step fluctuations for the insight they provide into surface mass transport, these fluctuating objects are excellent test beds for the well-developed theoretical machinery associated with growth models. In fact, many growth models are developed starting from a Langevin equation like Eq. 1.10, with the functional and the noise chosen to give the model the desired properties. The Langevin equations that we developed in the previous section each define a universality class.

The AD Langevin equation is perhaps the simplest imaginable interface model. It is often referred to as the Edwards-Wilkinson (EW) equation and was first used in the study of sedimentation processes[29]. As shown above, the model is linear and can therefore be solved exactly. The dynamic exponents have in fact already been obtained in this chapter. The interface width is simply the temporal correlation function up to a small numerical factor (the numerical difference is discussed in detail by Khare and Einstein[6]). Thus, the growth exponent β is equal to ¼ and can be read off from the form of *G(t)* for AD kinetics. The roughness exponent α describes the saturation width of the interface and can thus be read off just as easily from the spatial correlation function *G(y)* which is linear in distance y along the step edge. This gives us $\alpha = ½$ for AD kinetics. Furthermore, since we saw before that the form of *G(y)* is independent of dynamics, all three transport processes result in $\alpha = ½$ since they describe near-equilibrium dynamics.

As pointed out by Barabasi and Stanley, this value is essentially the result of the fluctuation dissipation theorem[14].

SED-limited fluctuation kinetics clearly defines a different class since it has a *G(t)* that grows more slowly in time than AD kinetics. In this model, $\beta = 1/8$ while for isolated step terrace diffusion $\beta = 1/6$. By measuring the two numbers, α and β, we can qualitatively classify the model that should best describe the interface fluctuations. For linear models like the ones used for step fluctuation such a classification is not much more than nomenclature. For more complicated models, such as might be relevant in highly nonequilibrium situations (see for example the experiments on rotating spiral steps in chapter 5 of this work), it may provide much needed insight into processes involved in the interface fluctuations.

While the notion of universal interface models may not be of serious practical value for near equilibrium step fluctuations, these fluctuation are of deep practical value in testing the experimental validity of universal interface models. This has been made evident very recently in the study of first-passage statistics for fluctuating interfaces. First-passage problems ask statistical questions like: what is the first time that a random variable attains a certain value?[30]. Such questions are physically very appealing, as they seem natural ways to address issues of stability and reliability. Mathematically, first-passsage problems are quite difficult to deal with and exact analytical results are rare[31]. In the context of interface physics, the difficulties are compounded by the complicated spatially extended nature of the systems[32]. For interfaces, a common quantity of interest is the *persistence probability* (see chapter 7 for more details). This is defines as the probability that a fluctuating interface *does not return to its initial value over a given*

time. It displays asymptotic power-law decay $p(t) \sim t^{-\theta}$, with an exponent θ (the persistence exponent) that has been found to be universal in many important interface models[31]. Since analytical studies of this property are so difficult, experimental tests of the proposed universality of persistence are of fundamental importance. For simple linear interface models (like AD or SED) there is some justification for the following simple relationship between the growth exponent and the persistence exponent[32]:

$$\theta = 1 - \beta \qquad (1.35).$$

This relationship is simple but not trivial[32]. It cannot be obtained, for example, by simple dimensional arguments, and understanding how it arises is an important basic question in the statistical physics of fluctuating spatially extended systems. As will be described in chapter 7, steps on surfaces have served as the best experimental testing ground for first-passage statistics for interfaces.

1.6 Outlook

In the chapters that follow, several recent experiments on fluctuations and mass transport will be described. We will describe step fluctuation studies on several complicated surfaces with chemical and structural inhomogeneites, step fluctuations on steps that are in a non-equilibrium situation, and the application of the Langevin formalism to the fluctuation of domain boundaries between surface phases. The important experimental studies of first passage statistics for interface will also be presented as will interesting studies of deterministic mass transport on small supported crystallites. Finally, the deep relationship between fluctuations and transport will be emphasized by presenting a study of *electrical transport* in disordered ultra-thin metal

films where the study of *electrical fluctuations* is essential to understanding the nature of the conduction.

As already mentioned, the relationship between fluctuations and transport is codified in the venerated fluctuation-dissipation theorem of statistical mechanics. It is by no means suggested as a novel concept here. Instead, this work attempts to illustrate how this relationship can be exploited to understand problems that are currently relevant to both basic and applied condensed matter physics. Furthermore, implicit in this work is the suggestion that the potential utility of the fluctuation-transport relationship will increase with the increasing practical realization of nanofabricated surface objects and associated nanotechnology.

Chapter 2

Scanning Tunneling Microscopy

The well-established technique of scanning tunneling microscopy is reviewed from a historical, theoretical, and instrumental perspective. Special attention is paid to experimental details of Variable Temperature STM (VTSTM) and time-lapsed STM of dynamic surface processes. A specific commercial VTSTM (Omicron) is described in some detail as are the experimental procedures used for the step fluctuation and mass transport studies that were performed using it.

2.1 Historical and Theoretical Background

It is not an exaggeration to say that the invention of STM and related scanned probe techniques spawned a revolution in surface science and condensed matter physics. In the recent AVS 50th anniversary issue of the Journal of Vacuum Science and Technology A, a chapter was devoted to describing the amazing new world that was revealed with this ultra-high resolution probe of real-space structure[33]. In this article, Lagally contends that STM has reached the point of being a "commodity" essential to almost any surface science lab, much like a LEED/Auger system[33]. The real-space information obtainable from STM has brought about a more microscopic and intuitive understanding of surfaces. The value of this advance cannot be underestimated; it has lead to the real possibility of *atomic-scale* control of surface structures.

Binnig and Rohrer invented the STM in 1982 at IBM's labs in Zurich[34] and only 4 years later were awarded the Nobel prize in physics for their work. Using the first STM this group was able to obtain atomically-resolved images of the Si(111)-(7x7) reconstruction that ultimately led to the complete understanding of the much-debated structure of this complicated surface[35, 36]. Before long other groups had mastered the technique and expanded it. Notably, Demuth, Tromp, and Hamers, working at IBM, and independently Feenstra and co-workers[37] developed the field of spatially resolved tunneling spectroscopy. Imaging modes like Current Image Tunneling Spectroscopy (CITS) could be used to study in detail the surface-state distribution on a surface. Again early success was obtained mapping the surface states on Si(111)-(7x7)[38].

Before a decade had passed, home-built STMs were common in many modern surface science labs. The design of these instruments was simple enough that a new

graduate student might be expected to build and implement an STM in a reasonable time frame. In the Williams group at the University of Maryland, several STMs were constructed in the early 1990's and two of them are still in occasional use at present (2004). The second decade of existence of the STM, however, saw the gradual phasing-out of this sort of home-built instrument in favor of extraordinarily high-quality commercial instruments. Currently, only the most exotic applications require the investment of time and manpower required for in-house STM design and construction. Commercial microscopes can operate under a variety of conditions (2K-1000K in temperature range, ambient pressure to UHV) so that the notion of STM as a true "tool of the trade" in surface science rings true.

A scanning tunneling microscope operates by bringing a sharp metal tip very close to a conducting or semiconducting surface and uses the sensitivity of the quantum mechanical tunneling current between the two as a probe of the surface. The essential feature that has made STM so powerful can be understood from a textbook approach to tunneling through a 1D barrier[39]. For a rectangular barrier, the current transmitted is simply exponentially dependent on the barrier width $I \propto (V/d)\exp\left(-A\sqrt{\phi}d\right)$. In this expression d is the barrier width, V is the bias across the barrier, and ϕ is the average barrier height[39]. The extreme sensitivity to barrier height in the exponential relation means that there is about a factor of ten change in tunneling current for every Angstrom change in barrier width. Thus, an STM is extraordinarily sensitive to atomic scale surface profiles. Years of study have suggested the process illustrated in figure 2.1 as the imaging mechanism of the STM. This figure shows schematically a very small cluster of atoms at the end of a

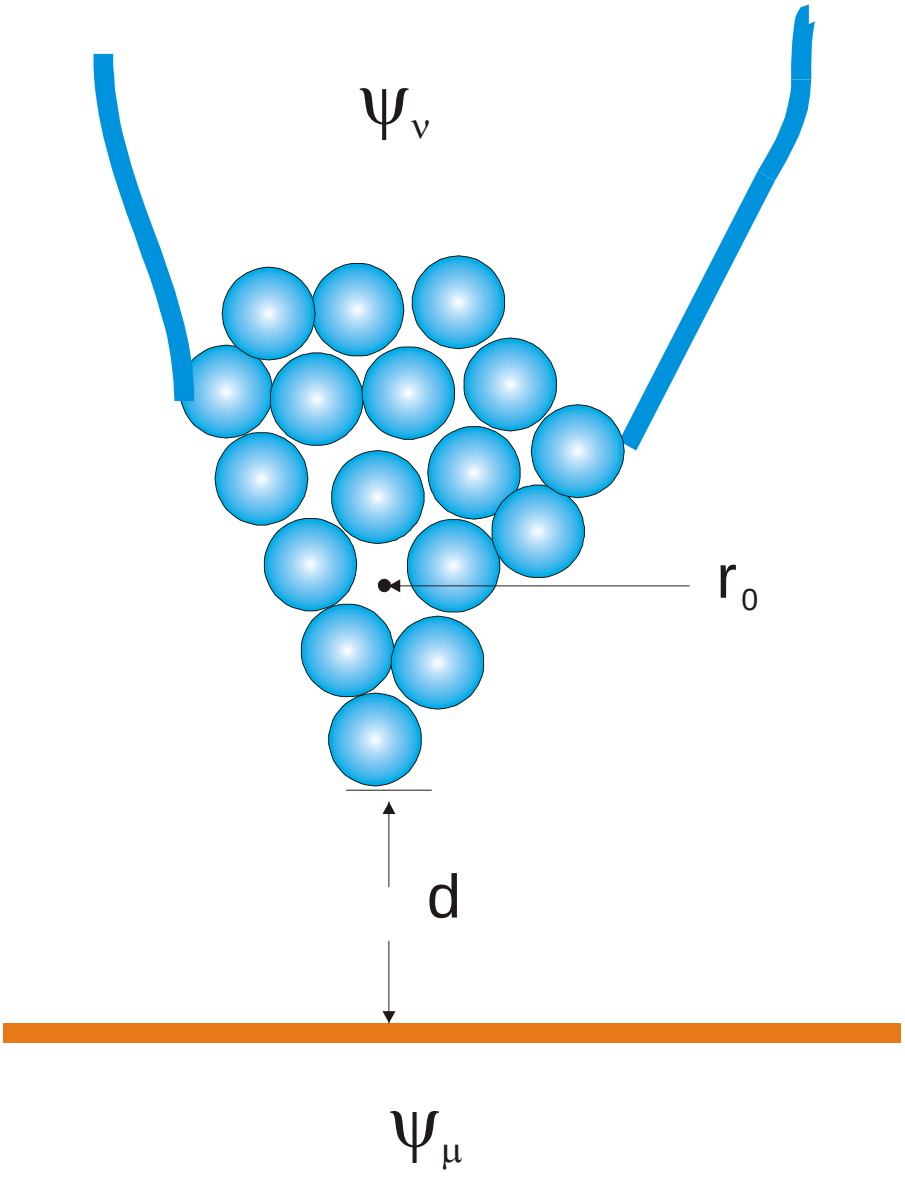

Figure 2.1 Schematic of mechanism of STM operation. Electrons tunnel across a narrow vacuum gap (width d) between a “nanotip” and the sample.

macroscopically sharpened tip acting as one electrode in a tunnel junction, where the other junction is the sample. This "nanotip" picture also indicates that the lateral resolution of the STM should be very good and that the quality of imaging is often dependent on the uncontrollable nanostructure of the probe tip.

Of course, a 1D tunneling problem is not particularly realistic, and significantly more sophisticated models have been developed to describe the operation of real microscopes. An early success and often-quoted model is that of Tersoff and Hamann[40, 41] who used the transfer Hamiltonian technique introduced by Bardeen[42] to compute tunneling current across a 3D barrier in first order time-dependent perturbation theory. We can imagine the tunneling electron starting off in the tip and ending up in the sample and computing the current from tip to sample using Fermi's golden rule. This will involve matrix elements between tips and sample wave functions like:

$$I = \frac{(2\pi)^2 e}{h} \sum_{\mu\nu} f(E_\mu)\left[1 - f(E_\nu + eV)\right] \left| M_{\mu\nu} \right|^2 \delta(E_\mu - E_\nu) \qquad (2.1)$$

where f(E) is the Fermi distribution, V is the junction bias and $M_{\mu\nu}$ is the matrix element:

$$M_{\mu\nu} = \frac{h^2}{8\pi^2 m} \int dS \left(\psi_\mu^* \nabla \psi_\nu - \psi_\nu \nabla \psi_\mu^* \right) \qquad (2.2)$$

involving both tip (μ) and sample (ν) wave functions (Fig 2.1), where the integral is taken over some surface in the vacuum gap region. The sample wave function is generally what we want to learn about using microscopy, but the tip wave function is also unknown and mostly not controllable or reproducible. The way to go about making decent theoretical descriptions of STM is to choose the best wave functions for use in equations 2.1 and 2.2.

The Tersoff-Hamann model treats the tip wave function as spherically symmetric and is sometimes called the s-wave tip model[40, 41]. The sample wave function can then be expanded in plane waves in the plane of the surface and relatively simple expressions for the tunneling current can be obtained. Such expressions can be used to estimate the vertical and lateral resolution of the STM. The important point about the tunneling current (regardless of model) is that it is always some sort of convolution of tip and sample wave functions. The Tersoff-Hamann model[40, 41] is mostly applicable to metal surfaces where the junction bias is small. With certain approximations, like small bias, this model concludes that the STM measures a contour of constant density of states at the Fermi level. The expression obtained is:

$$I \propto V\rho_s(r_0, E_F)\rho_t(E_F) \qquad (2.3),$$

where ρ_s is the density of states of the sample, r_0 is the center of the radius of curvature at the tip apex, and ρ_t is the density of states of the tip. The low-bias limit is not often obtained. In particular it is never obtained on semiconductors and instead a WKB expression for tunneling through a planar junction with finite biases can be used[43]:

$$I = \int_0^{eV} \rho_s(r_0, E)\rho_t(r_0, E - eV)T(E, V, r_0)dE \qquad (2.4).$$

In this convolution, $T(E,V,r_0)$ is the transmission probability given by:

$$T(E, eV) = \exp\left(-\frac{4\pi Z\sqrt{2m}}{h}\sqrt{\frac{\phi_s + \phi_t}{2} + \frac{eV}{2} - E}\right) \qquad (2.5).$$

The important quantities in this equation are the sample and tip work functions, ϕ_s and ϕ_t (difference between respective Fermi levels and the vacuum level), and the applied bias V. Hamers[43] describes the qualitative features of the transmission probability as follows. When eV<0, meaning the sample is at negative bias, T(E,V) is largest for E=0, i.e.

tunneling is from the Fermi level. For eV>0, positive sample bias, T(E,V) is largest at E = eV, i.e. tunneling is from the Fermi level of the tip. Intuitively, one can imagine electrons repelled from whichever of the two "electrodes" has a negative bias[43]. Negative tip bias lets tunneling electrons from the tip probe empty states on the sample, while positive tip bias allows electrons to tunnel from filled states on the sample. Clearly, STM images are strongly bias dependent. Tunneling spectroscopy with extraordinary spatial resolution can be performed by sweeping the sample bias over a range of interest and measuring the resulting current (as well as it first and second derivatives in some cases). Tunneling spectroscopy has been one of the most important applications of the technology associated with STM. No real use of it will be made in this work and since several extensive books and reviews exist[44], it will therefore not be discussed further.

In this work, STM will be used exclusively in constant-current topographic imaging mode. In this mode, where feedback adjusts the tip height to keep the tunnel current constant, the subtleties involving convolution of tip and sample density of states are not very important. Our studies are of nanometer-scale surface features (see for example figure 1.1) and so the dominant effect will almost always be the simple exponential dependence of tunnel current on gap size. The atomically resolved STM images to be presented in this work are straightforward to interpret.

In the next section, we will describe the basic design features required for any STM. The focus will be on STM's for use in Ultra-High Vacuum environments, but most of what will be said is independent of this feature. Then a section will be devoted to the specific design of the commercial STM that was used in most of the experiments described in later chapters (chapters 3-8) of this work. Particular attention will be paid to

its remarkable optimization for use at elevated temperatures. It will also be compared briefly with another commercial STM that was used in the experiments described in chapters 9 and 10.

2.2 STM Instrumentation

2.2.1 Vibration Isolation

To have a useful tunneling microscope, the first requirement is to obtain a stable tunnel junction on a subatomic scale. Given the sensitivity to gap width described in the previous section, the junction must be stable to height changes smaller than the features of interest on a surface. For metals, atomic corrugations are of order 0.1 Å, so a good STM junction should be stable to ~0.01 Å. There is no hope to attain this goal if the sample and tip are subjected to typical vibrations and shocks transmitted through the floor and air of a laboratory environment. Some vibration isolation is absolutely essential.

Environmental vibrations in most labs fall in the range of 1-100 Hz and can result from people walking, machines running, building bending modes, and other unaviodable sources. The first step in avoiding junction instabilities due to these sources is to design the STM assembly to be rigid enough that its overall resonant frequency is well above 100 Hz[39]. Good, compact designs generally have resonant frequencies in the range of several kilohertz.

Vibration isolation is achieved by constructing the STM with various damping mechanisms that quell any vibrations before they can make the tunnel junction unstable. The damping system itself must be designed with a very low resonant frequency because

it can have the effect of enhancing disturbances on resonance. A common technique is to hang the entire microscope and sample assembly from springs. Figure 2.2 shows a photograph of one of the home-built STM's in Williams' group at the University of Maryland. The microscope and sample are mounted on a large copper block that can be suspended from springs during operation. In addition to these springs, which have very low resonant frequencies but not very effective damping, strong rare-earth magnets are attached to the stationary frame near the copper block. If the copper block moves for any reason, the magnets induce eddy currents in the block that provide excellent damping. Sometimes damping and isolation are provided by mounting the microscope on a stack of viton rubber spacers or putting the entire experiment on an air table or on a giant sand pit. In UHV applications, however, the most common isolation system is the combination of metal springs and eddy current damping shown in the photograph[39]. If these two components are implemented properly, they are normally sufficient by themselves.

2.2.2 Tip Positioning and Scanning

To make a useful tunnel junction, it is necessary to have the ability to controllably position the STM tip very close to the sample. Here "close" means within several Angstroms, and "controllably" means without crashing the tip into the sample hard enough to seriously damage either one. It is also convenient to have the ability to move the tip to different lateral areas of the sample.

Most positioning mechanisms involve the use of piezoelectric ceramics. These are materials that expand or contract in response to an applied voltage. Most STM's now

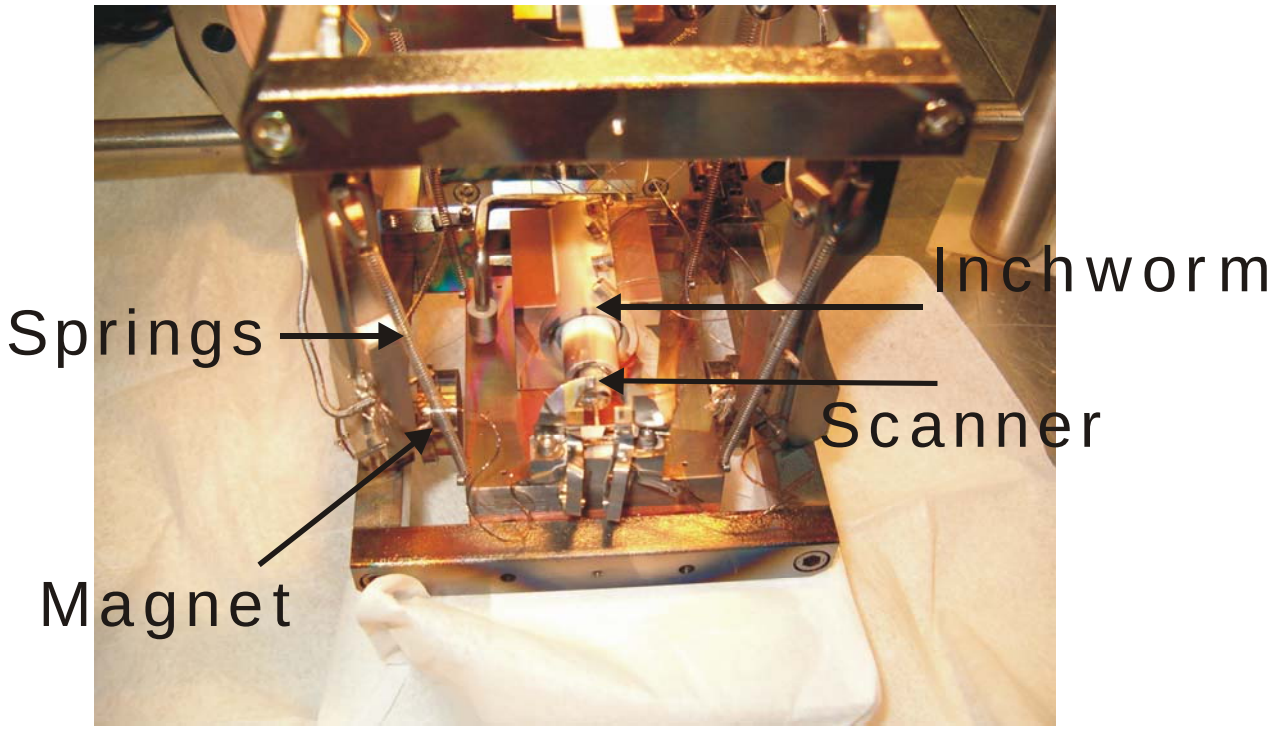

Figure 2.2 A home-built STM, with key elements described in the text labeled.

employ some version of what is known as PZT (e.g. PZT-5H[45], etc.) which is some composite of lead zirconate and lead titanate. In the photograph in figure 2.2, the positioning device is the large white cylinder. It is a commercial "Inchworm" (Burleigh) that moves the tip assembly close to the sample by a series of clampings, expansions, and unclampings. This remarkable device can control tip positioning from macroscopic lengths down to 1 Å[46]. It consists of an alumina shaft inside a housing made up of three different piezoelectric tubes. Two tubes clamp the ends of the shaft and the third central tube expands due to applied voltage and drives the motion of the shaft. Typical sensitivities for the drive are around 25 Å/V and therefore the motion can be controlled to less than an Angstrom[46]. Another way to use piezoelectrics for tip positioning is via slip-stick type inertial motion of a slider. This type of positioner will be described in more detail in the next section.

Using an inchworm, it is possible to bring the tip within tunneling range of the sample. When this is done, control of the tip is switched over to a different set of piezoelectric actuators known as the scanner. The scanner allows the relative motion of tip and sample in three orthogonal directions: *x* and *y* in the plane of the sample and *z* perpendicular to the sample. The first STM used three orthogonal piezoelectric beams as a scanner[34]. Before long a more compact and rigid tube scanner became more prevelant[45]. This geometry is shown schematically in figure 2.3. It has a piezolelectric tube sectioned into four electrodes on its outside to actuate motion in the x and y directions and an inner electrode to actuate motion in the z direction. The tip is mounted on the end of the tube and the whole tube can easily be mounted on the shaft of an inchworm. Applying a voltage across opposing outer quadrants of the tube produces a

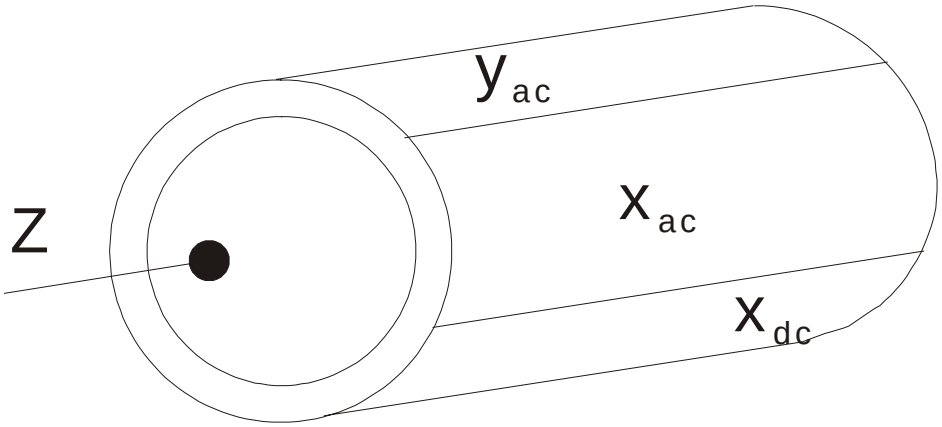

Figure 2.3 Single tube scanner. AC quadrants drive scanning and DC quadrants produce offsets.

bending of the tube that allows x (or y) motion. Applying a voltage between the inner and outer tubes produces an expansion or contraction of the tube along its axis. At present, it is rare to find an STM that does not take advantage of the single tube scanner. The compact design not only keeps the mechanical resonance frequency high enough, it also reduces cross talk and pick-up between different piezo-actuators and the tunnel current.

2.2.3 Control Electronics and Feedback

Figure 2.4 shows a schematic of typical electronics used to control an STM. The important analog pieces are a current amplifier for the small tunnel current, a feedback loop that compares this current with a reference and adjusts the z-position of the tip accordingly, and high voltage amplifiers for driving the scan and z piezo's (only one is shown in the schematic). A digital to analog converter from the control computer often provides the tip-sample bias, but it could be provided simply from a battery. The current to the tip (often at virtual ground) is amplified by a low-noise current-to-voltage converter and the signal is linearized by a logarithmic amplifier. The linear signal is compared with a "demand" current determined by the setpoint and the error signal is sent to proportional and integral (P and I in the schematic) amplifiers where it is subsequently used to adjust the z-position of the tip through a high-voltage signal to the z-electrode of the tube scanner. The schematic shown in Fig. 2.4 is the simplest possible to describe constant current topographic imaging. It could be modified by inserting sample-and-hold circuitry between the error amp and the PI circuit to break the feedback loop in tunneling spectroscopy experiments.

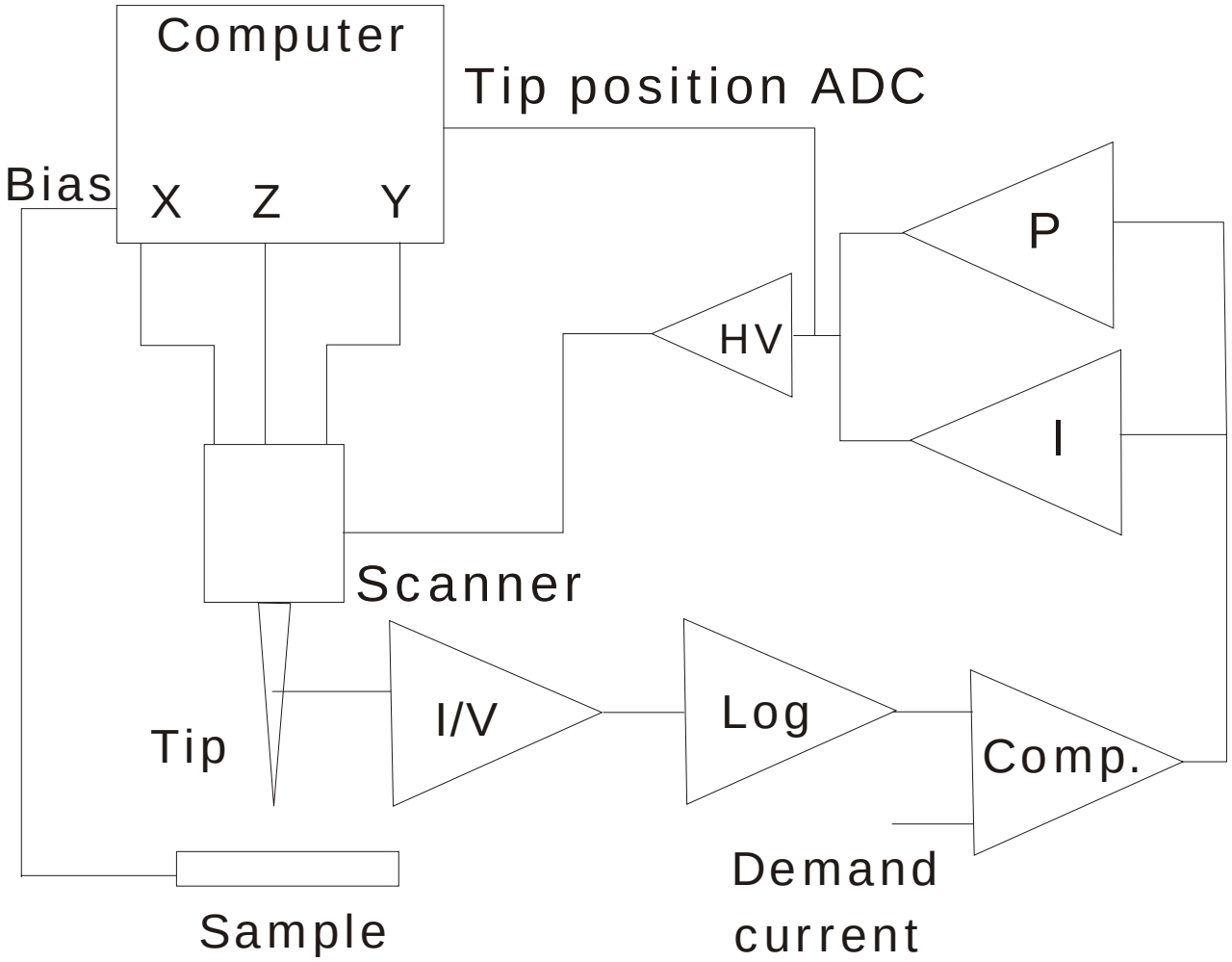

Figure 2.4 Schematic of electronics for a typical STM.

The feedback circuit is probably the most important electronic element. In contrast to many feedback systems (like for example what you might find used in a temperature controller), Scanned Probe Microscopes generally employ only proportional and integral gain. Differential gain tends to lead to instabilities that can cause tip crashes or junction instability. Proportional control adjusts the z-position in proportion to the difference between the measured current and the setpoint current. Integral control adjusts the z-position according to the cumulative average error between the measured current and the setpoint.

2.2.4 Tip Preparation

The tip is the least controllable aspect of an STM experiment. On one hand, this means that spending long hours agonizing over tip preparation details is not particularly productive (see R. Hamers' anecdote in Ref. 1). On the other hand, it also means that some experiments will likely end up being abandoned due to tip problems. Nevertheless, sufficient tip preparation technology has been developed that the lack of complete control over tip quality should not be a severe limiting factor[47]. In fact, with bravura born of many long hours of scanning, the general feeling among STM practitioners is that it is possible to obtain atomically resolved images with a sharpened nail[33].

The most common material for tips used in UHV STM experiments is tungsten. This hard, refractory metal is not easily damaged and can be electrochemically etched with a simple procedure. In our lab, following instructions from A. Melmed, we typically roughly etch a point onto a straight piece of tungsten wire using about 2 M KOH solution and about 5 VAC from a variac with a carbon counter electrode (even Cu wire could be

used for a counter electrode though). Next we finely etch the tip using a similar (3-5 VAC) voltage but with a 0.5 N solution of KOH. The solution is suspended in a fine loop of Pt wire, and the loop is moved forward over the very end of the tip under the control of an optical microscope. The etching voltage is *only* applied during the forward motion (with a simple on-off switch in series with the variac). After fine etching the tip is rinsed in very clean (HPLC grade) water for about 20 seconds. We have found this procedure produces tips capable of atomic resolution on Si(111)-(7x7) with only a slight heating (using internal bakeout heaters) in vacuum. An SEM image of a tip prepared using this procedure is shown in figure 2.5.

Ultimately, tip preparation is a little bit of black magic. The exact procedure used in any lab depends on the details of the etching equipment available. For example, if a high-quality optical microscope is not available then the procedure described above is not likely to be as successful as just described. In addition, specific applications may require the use of more exotic tip materials like gold or platinum.

Atomic resolution on metal surfaces or detailed tunneling spectroscopy experiments may require extensive *in-situ* tip treatments. Applying high tunnel currents or high bias voltages is a common method of altering the nanostructure of a tip that is judged to be unacceptable[44]. In addition, with some care a tip can be field-emitted, electron-bombarded, or ion-milled for cleaning.

2.3 Variable Temperature STM

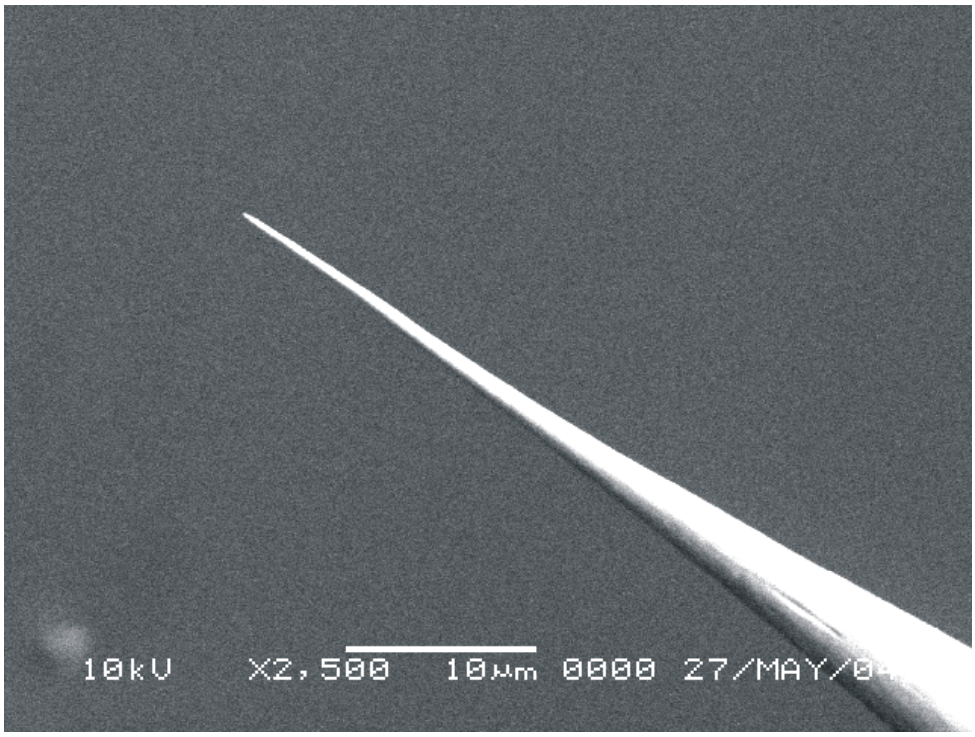

Figure 2.5 SEM image of a home-etched STM tip.

As already mentioned, most of the experiments that will be described in subsequent chapters of this work were performed on a commercial STM produced by the German company *Omicron*. Since the experiments focus on surface mass transport issues, and mass transport is usually thermally activated, the important design features of the microscope relate to its optimization for use at elevated temperatures.

The instrument is in fact a Variable Temperature STM (VTSTM) and can be used with samples held at temperatures from about 25 K to about 1400 K (at least according to manufacturer specifications). Whether this entire temperature range is accessible depends on what sample is being used and what kind of resolution is required. A photograph of the microscope stage unbolted from its steel bell jar is shown in figure 2.6a. Figure 2.6b shows the microscope through a viewport attached to the vacuum system where it is used in the Surface Physics Group at the University of Maryland. From figure 2.6a, we see the essential mechanical design features described in the last section. The four steel tubes extending perpendicular to the lower Conflat flange house steel springs from which the microscope stage is suspended during scanning. The copper fins surrounding the rim of the stage have rare-earth magnets between them to provide additional eddy current damping. The smaller cylindrical tube extending at an angle through the base of the stage provides a connection of the sample to a continuous flow cryostat (this was not used and so will not be discussed further). The sample sits on the assembly on the center of the stage and can be transferred via a wobble stick visible in figure 2.6b. Not clearly visible in the photograph is the scanner and coarse-approach assembly (it is obscured by the stage). This is

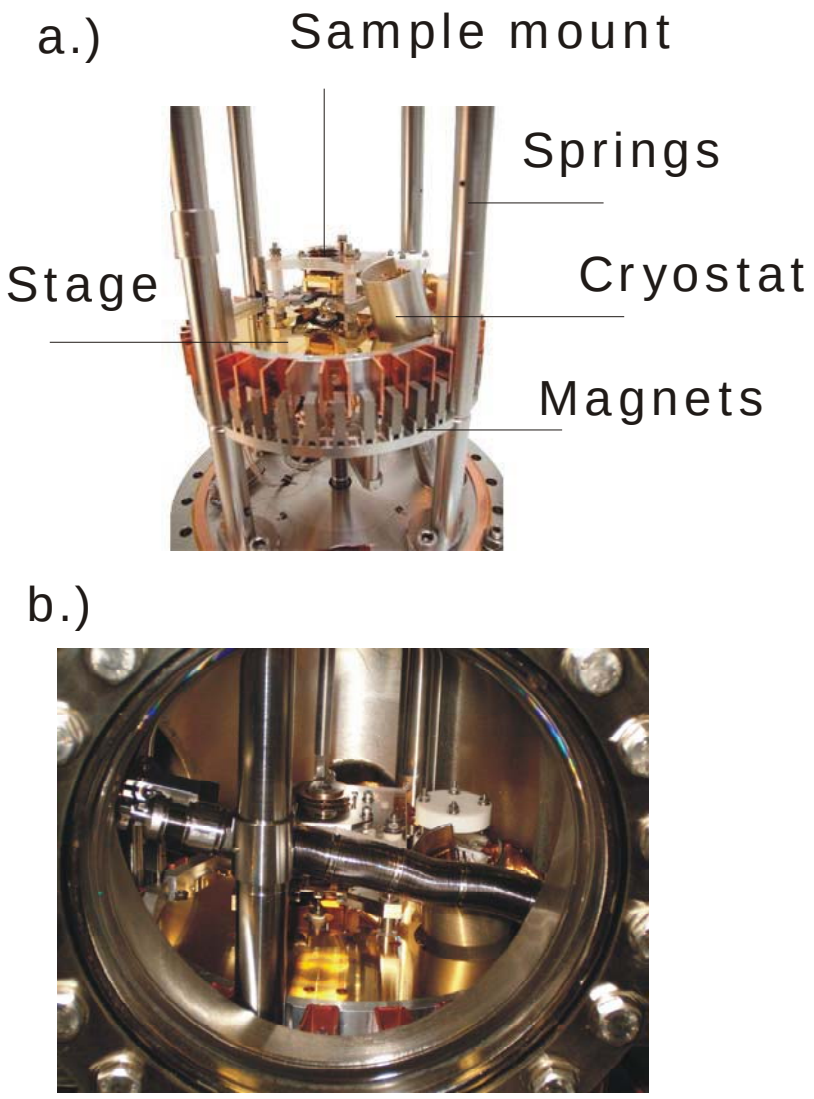

Figure 2.6 a.) Omicron VTSTM stage outside of vacuum showing main components (http://www.omicron.de/products/spm/variable_temperature_instruments/vt_stm/). b.) VTSTM in vacuum chamber at University of Maryland College Park.

probably the most important aspect of the design from the perspective of high-temperature operation.

As in most STM's, a single tube scanner is employed in the Omicron VTSTM. On its end is a magnetic receptacle where tips can be mounted and exchanged in-situ using a special tip transfer holder and the wobble stick. The scanner has a radiation shield that prevents radiative heating from a hot sample. This minimizes thermal drift as well as the risk of depoling the piezoelectric scanner.

Figure 2.7 shows a schematic of the whole scanner-sample setup. The design is cylindrically symmetric and also ensures that the sample plane is the reference for any thermal expansion during sample heating. This allows a very stable junction width and means that it is possible to scan while the temperature of the sample is changed without risk of crashing the tip or losing the tunneling signal. There is still an issue of lateral drift during heating. It is quite difficult to maintain a set lateral position during even a very small (say 20 K) temperature change. By picking a fixed surface feature, it is possible to compensate for some drift using the control software to keep the position of that feature fixed. This is actually only really useful for small drifts and in fact was not employed in any of the experiments described in this work. If it is required to regain a specific surface region after a temperature change, a better procedure is to remember the appearance of that area, move some several hundred nanometers away, and then move back after 20-30 minutes of thermal stabilization. We succesfully operated the VTSTM, with resolution sufficient for the observation of monatomic surface steps, at temperatures up to 1020 K. Much above this temperature, we observed frequent lateral jumps in step position that were presumably due to sudden thermal expansions. We attempted to minimize this

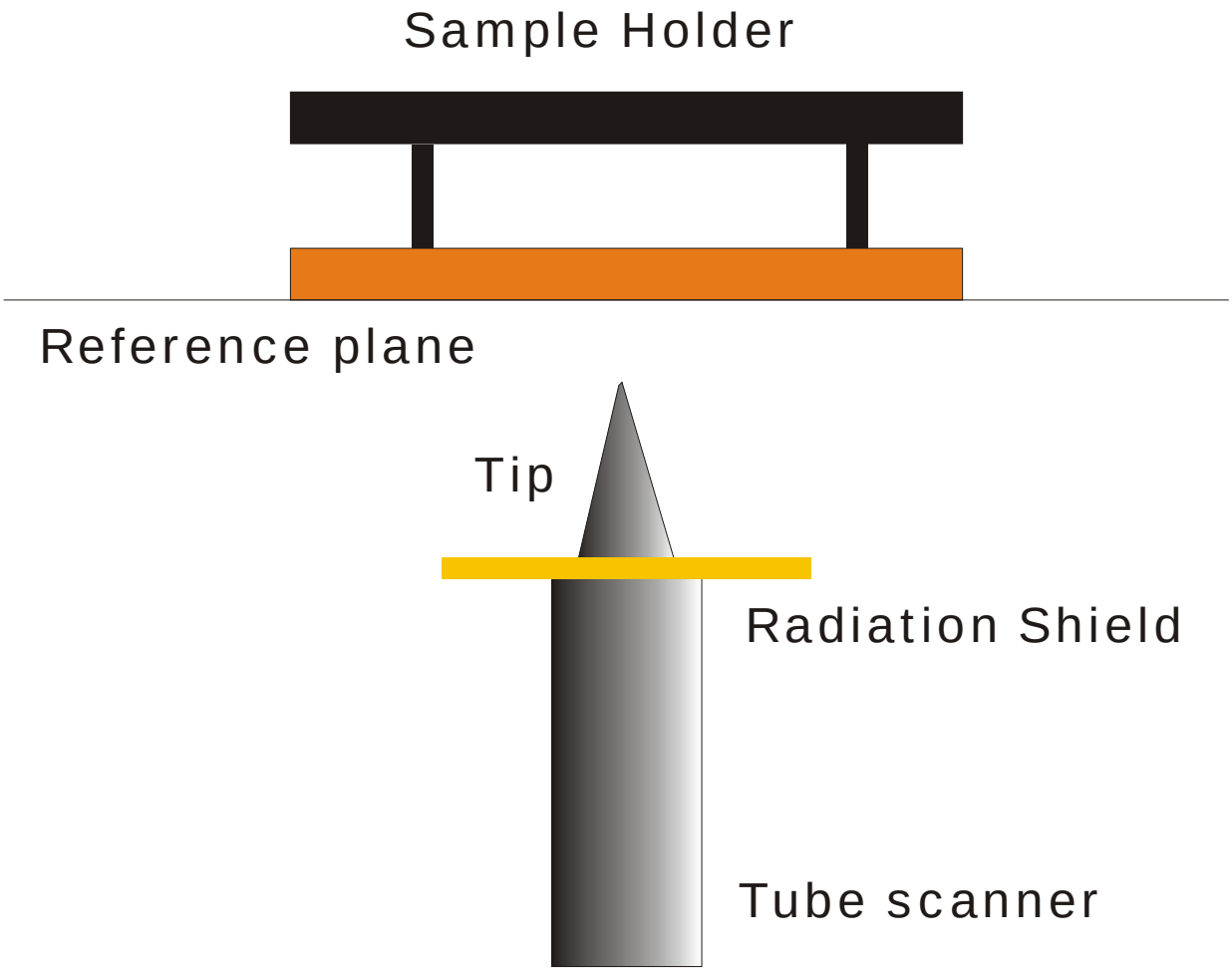

Figure 2.7 Schematic of Omicron VTSTM scanner arrangement.

effect by using samples cut as small as possible, but it never completely disappeared. Thus, it is clear that the upper temperature limit of this microscope is strongly dependent on what kind of experiment is being done.

The design features of the Omicron VTSTM are fairly standard for any STM that will be used for experiments at elevated temperatures. Kuipers, for example, designed an STM that could track a specific sample area while scanning at temperatures up to 850 K[48]. It also employed a cylindrical scanner design that maintained the sample plane as the thermal expansion reference. In addition, extensive measures were taken with the sample holder to limit lateral drift[48]. Of course, this points out the one disadvantage of using even the highest quality commercial instrument: it is much more difficult to modify when shortcomings are uncovered.

In chapter 10 experiments are described that were performed on a different commercial VTSTM. These experiments were done at low temperatures using the JEOL 4500 SPM. It is quite different in design than the STM's so far mentioned in this chapter. For the most part, this is due to the fact that the instrument was designed for optimal performance as a Force microscope. Its vibration isolation consists of a large air table on which the vacuum chamber is mounted and in-vacuum viton stacks to support the tip and sample. In addition, the sample itself is mounted on the end of the tube scanner while the tip remains stationary to allow for optical detection of the deflection of an AFM cantilever. The sample and scanner are cooled by a silver braid attached to the bottom of a bath cryostat that can be filled with liquid helium or liquid nitrogen. The performance of the microscope is noticeably different than the Omicron VTSTM for many reasons. One example is that mechanical resonances are much more pronounced with the viton

stack isolation system. This system clearly provides less efficient damping than the eddy current method used in the two STM's described earlier in this chapter. Nevertheless, the JEOL works acceptably in STM mode and illustrates the wide range of designs that can be effectively employed.

2.4 Step Fluctuation Experiments on the VTSTM

In this section we will describe the typical experiment performed with the VTSTM in which we monitor the thermal fluctuations of a surface step in real time at elevated temperature. In the experiments described in this thesis, the step motion was always fast enough that monitoring STM snapshots (i.e. pictures corresponding to a static step configuration) was not possible. Instead we employed the "line-scan"method of STM imaging to monitor the time dependence of the position of a *single point* on the step edge.

Ordinarily scanning the tip is done by applying a fast sawtooth voltage to the x-ac quadrant of the tube scanner and a slow voltage ramp to the y-ac quadrant. In this way, the x direction is scanned many times while the tip is slowly moved in the y direction. By disabling the slow scan direction, we are able to scan at high speed one x position along a step edge and obtain a time series, $x(t)$. As will be described in the chapters that follow, this time series can be used to obtain important surface mass transport information.

To obtain the time series from a line-scan image (or Pseudo-image since it isn't really a snapshot), we first perform several image-processing steps. Using the software provided by Omicron, we subtract the slope line-by-line from every line on the image.

After this, a surface step has the profile of a sawtooth. Next, we choose an area on one of the terraces between steps and perform a plane subtraction of the slope in that area. This makes the profile of a single step look like a true step function. The step position is then determined for each line in the image (usually images are 512 lines in size) by fitting the step function profile to the form $y(x) = A\tanh(x-x_0/b)+c$. This functional form has approximately the appearance of a typical step profile and enough free parameters (A, b, c, *and* x_0) to make it fit to almost any data, regardless of noise. The parameter x_0 from the least squares fit is then taken as the step position for the line under consideration. When repeated for all lines, the set of x_0's generates the needed series $x(t)$. In figure 2.8 we show an example of a line-scan pseudo image and one of the time series extracted from it. By eye, there is no way to distinguish the time series from the true evolution of the step, and we have no reason to believe that the procedure described above does not accurately determine the step position from such an image (Details of image processing and analysis can be found in Appendix B).

2.5 Summary and Conclusion

There have certainly been a huge number of chapters of this kind written by many practitioners of STM over the two decades since its inception[34]. At this point, the hope is to emphasize the use of the microscope as a valuable tool for surface science. No longer is it such an instrumental oddity that long discussions of design and construction are warranted. In the present chapter, we have outlined the very basic design principles and the few issues of design and implementation peculiar to the study of monatomic surface step fluctuations at elevated temperatures. This is of course the ultimate result of any

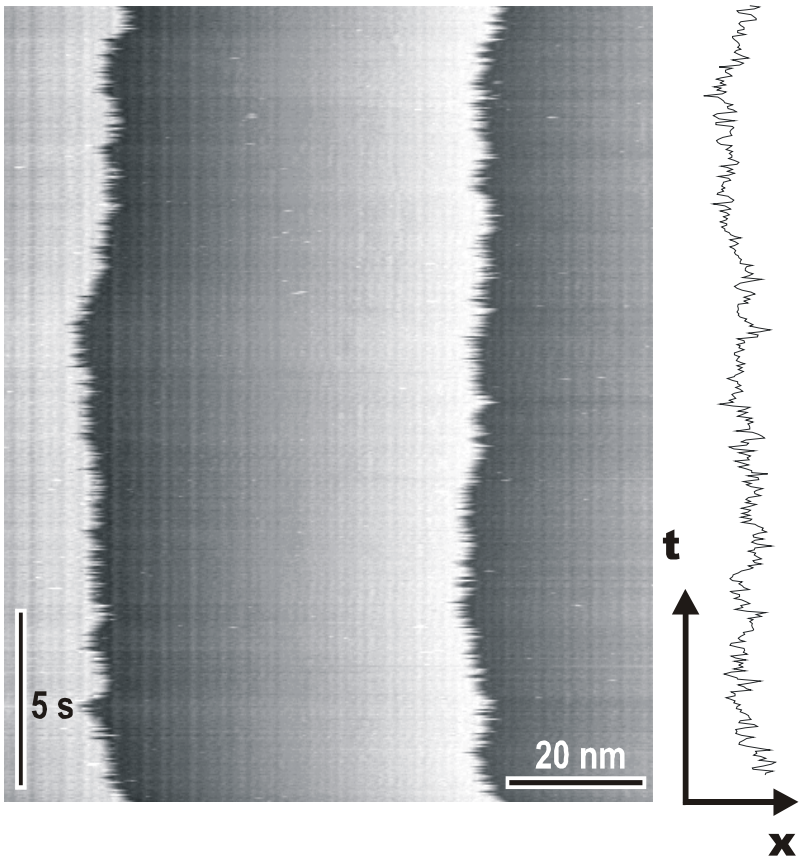

Figure 2.8 Example of pseudo-image obtained by disabling the slow scan ramp to the tube scanner. The time series to the right is obtained following the procedure described in the text and corresponds to the right-most step position from the pseudo-image. It is slightly magnified in vertical scale relative to the image.

revolution: it creates a new *status quo*. The revolutionary development of the STM (and related SPM techniques) has established a new age of intuitive, real-space understanding of surface and nanoscience. It is now almost expected that experiments in these fields will have real-space data in at least a supporting role.

Chapter 3

Step Fluctuations on Uniform Si(111)- $\sqrt{3}\times\sqrt{3}$ R30°-Al

Variable temperature STM is used to determine continuum step parameters for steps on Si(111)- $\sqrt{3}\times\sqrt{3}$ R30-Al between 770 K and 1020 K. The spatial correlation function allows the extraction of thermodynamic step diffusivities that govern the spatial meandering of the steps and the temporal correlation function allows the determination of the rate-limiting mass transport mechanism involved in step fluctuations and its associated linear kinetic parameter. With the aid of the temporal cross correlation function between near neighbor steps, we unambiguously show that the rate-limiting process by which near –equilibrium step fluctuations relax is attachment and detachment of mass at the step edge. The attachment/detachment mobility is determined from the magnitude of the temporal correlation function and its relationship to atomic processes on the surface is discussed.

Results published as:

1.) I. Lyubinetsky, D.B. Dougherty, H.L. Richards, T.L. Einstein, E.D. Williams, Surf. Sci 492 (2001) L671

2.) I. Lyubinetsky, D.B. Dougherty, T.L. Einstein, E.D. Williams, Phys. Rev. B 66 (2002) 085327.

3.) D.B. Dougherty, I. Lyubinetsky, T.L. Einstein, E.D. Williams, Phys. Rev. B in press, 2004.

3.1 Introduction

Fluctuations of monatomic steps on surfaces are commonly observed as a frizziness in the step position due to fast atomic motions at the edge[1, 3]. This is a fact of life for many metal surfaces even at room temperature. Naturally, the majority of studies of these fluctuations have focused on elemental metal surface steps[3]. In addition both Si(111) and Si(001)[12, 49, 50] step fluctuations have been analyzed statistically. In this chapter, we present the natural extension of fluctuation studies to a *chemically heterogeneous* surface[21]. The surface is the well-known $\sqrt{3}\times\sqrt{3}$ R30° reconstruction induced by the chemisorption of Al on Si(111)[51-53]. An atomically resolved STM image is shown in Fig. 3.1. This reconstruction represents a substantial increase in complexity from the elemental surfaces already mentioned but, as will be described below, its step fluctuations can be modeled using the standard Langevin formalism of chapter 1. While this is not necessarily surprising, it is nevertheless important. The considerable microscopic complexity of the $\sqrt{3}\times\sqrt{3}$ surface can be subsumed in a few continuum step parameters which themselves can be understood as arising from the existence of well-defined *effective energy scales* governing mass transport processes.

After describing experimental details, we will go on to show the results for the step thermodynamics and kinetics on the $\sqrt{3}\times\sqrt{3}$ surface. Next we will discuss an ambiguity in the interpretation of the fluctuation kinetics in terms of underlying mechanism and show how it can be resolved using a new statistical analysis of the

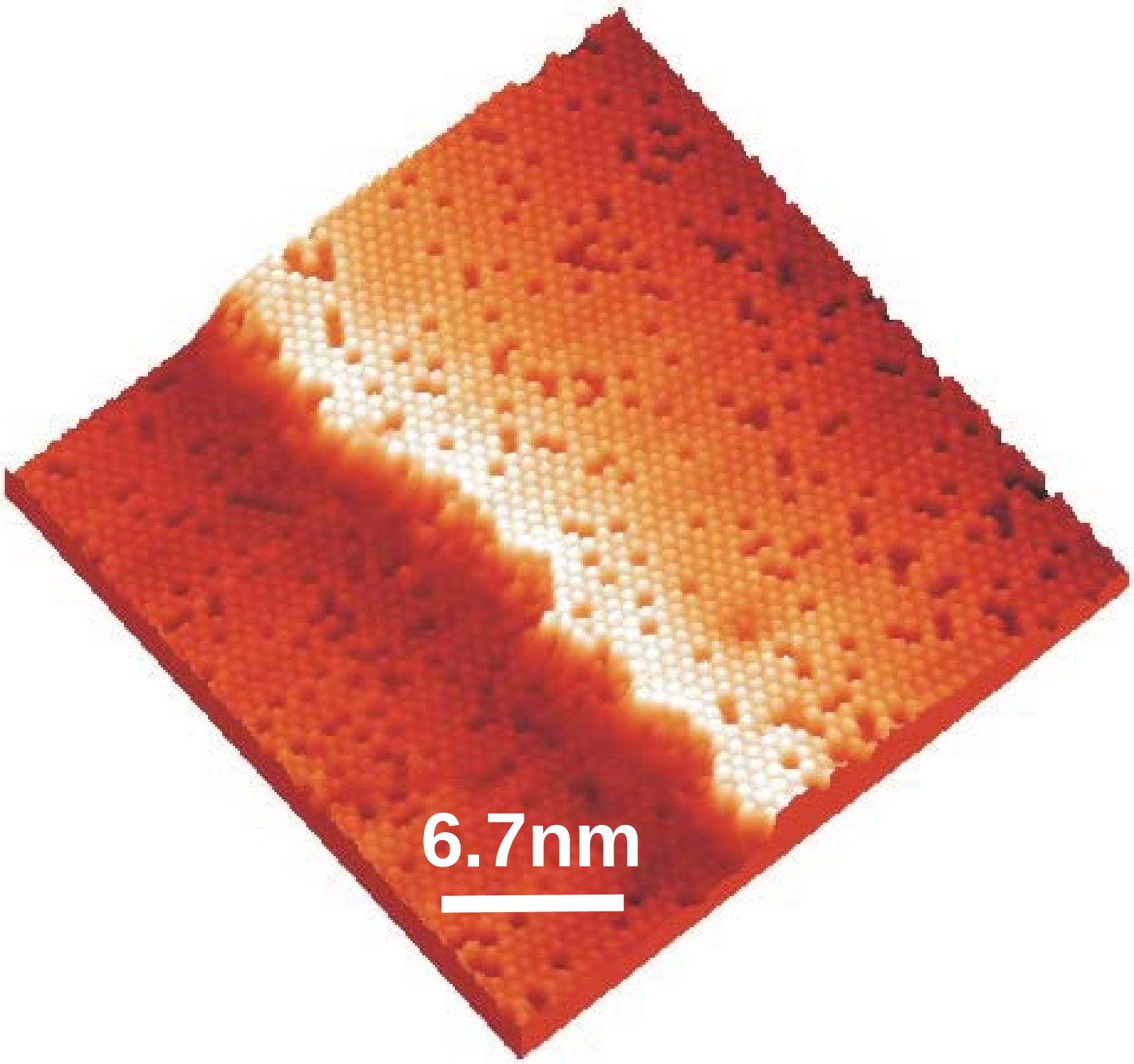

Figure 3.1. Atomically resolved STM image taken at room temperature of the Si(111)-$\sqrt{3}\times\sqrt{3}$ R30°-Al surface. For the tunneling conditions employed (+2.5V, 0.5nA), the bright spots are Al atoms and the dark balls are Si substitutional defects in the overlayer.

fluctuation data. Finally we discuss the details of the transport kinetics and the underlying effective energy scales and microscopic processes.

3.2 Experiment

To prepare the Si(111)- $\sqrt{3}\times\sqrt{3}$ R30°-Al reconstructed surface, we begin with a commercially cut and polished Si(111) wafer (As doped, 10 mΩ cm, 0.5° miscut towards [2-1-1]) and prepare the (7x7) reconstruction by direct current heating as described in appendix A. Aluminum metal was then deposited on the Si(111)-(7x7) from a hot tungsten coil at a substrate temperature of 1020 K. Deposition was performed in small steps and in between each step the surface symmetry was checked by LEED (Physical Electronics Industries). When a clear $\sqrt{3}\times\sqrt{3}$ pattern was observed over most of the sample, it was transferred to the VTSTM stage described in chapter 2. The surface was checked at room temperature by STM and if large, clean areas of the reconstruction were visible the sample was heated in the STM stage to 1020 K. After waiting about 30 minutes for the STM to thermally stabilize, the steps could be imaged at elevated temperature. For temperature-dependent measurements, the temperature of the sample in the stage was decreased in steps (of 50-100 K) with ~30-minute stabilization times between each step.

In addition to the standard STM imaging mode by which it is possible to observe the equilibrium step structure, another mode was employed to observe the step dynamics. Since the motion of the steps on this surface at high temperatures is quite fast relative to the rate at which a single STM snapshot can be obtained it was necessary to study the temporal evolution of only a single point on the step by disabling the slow-scan direction

of the piezo. To attempt to study the dynamics on this surface by taking a time sequence of snapshots would be useless since, for any snapshot, the step will have moved significantly during the imaging time. A schematic of the alternative "line-scan" or time imaging is shown in Fig. 3.2. The STM "image" in this figure is really a pseudo-image in which the vertical direction represents measurement time (23 s) obtained by scanning the tip repeatedly over the *same point* on a step edge. From such an image, the step position can be digitally extracted and used to statistically analyze the fluctuation kinetics.

Of course, the need for this line-scan imaging to study step dynamics points out a difficulty in measuring the equilibrium step structure of this surface at elevated temperature. If the steps move during the imaging time, then a snapshot cannot accurately reflect the equilibrium structure (which should correspond strictly to only one instant of time). Thus, for step structure measurements at elevated temperatures it was necessary to quench the sample back to room temperature. That this quenching experiment preserves high temperature step structure will be justified in the following section.

3.3 Results

Figure 3.3a shows a large scale STM image of a $\sqrt{3}\times\sqrt{3}$ surface taken at 970 K. The steps show the characteristic frizziness due to undersampling of fast fluctuations that has been described in the previous sections. Figure 3.3b shows an image of the same sample (different area) taken after quenching to room temperature (298 K) by quickly turning the heater current off. The cooling rate was estimated by infrared pyrometry to be greater than 200 K/s. Since the frizziness is gone in the quenched image, we will

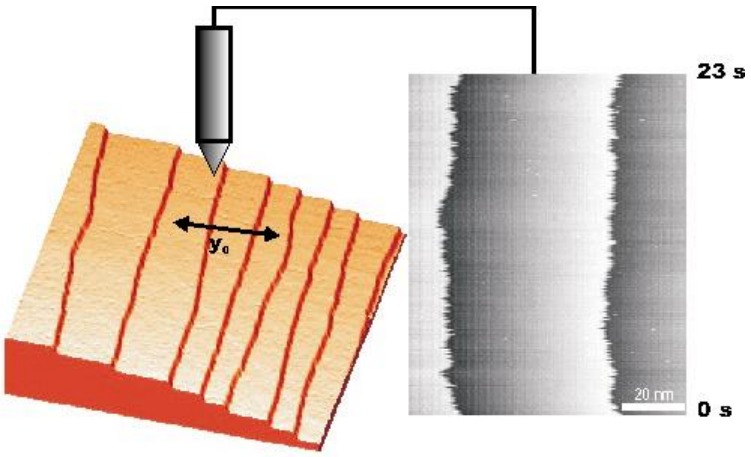

Figure 3.2. Schematic of time imaging procedure in which the STM tip scans repeatedly over the point y_0 for 23 seconds and generates the pseudo-image on the right. Note that the 3D rendering on the left is of the surface at room temperature but the line-scan image is from the true data set taken at 970 K.

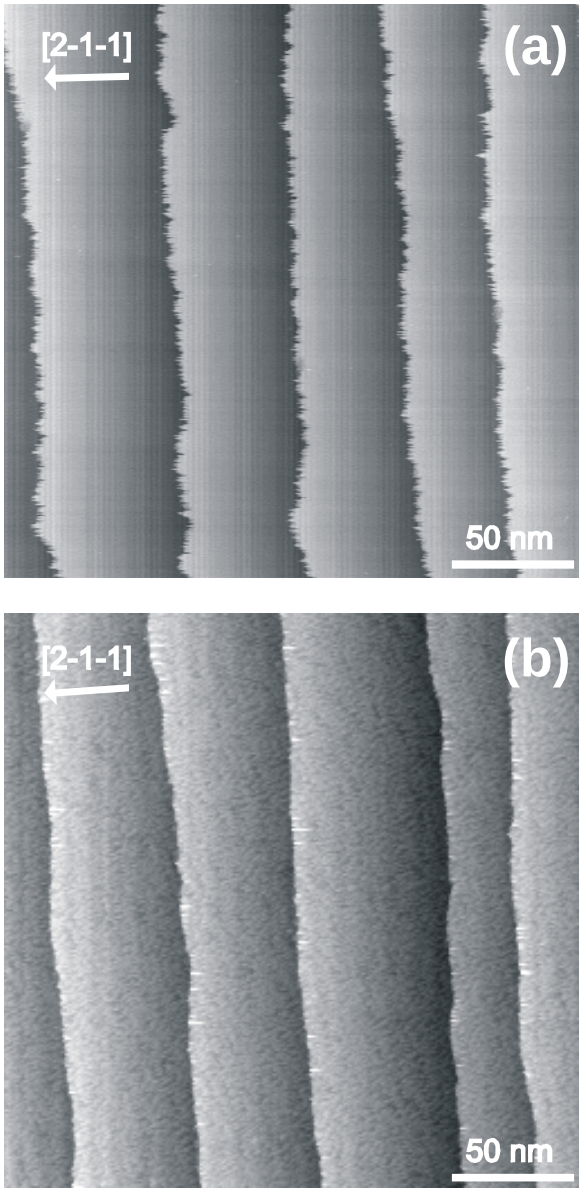

Figure 3.3 a.) STM image (250nm x 250nm, -3.5V, 0.05nA) of steps taken at 970 K. b.) quenched from 970K.

tentatively assume that it provides a close representation of the 970 K equilibrium step configuration.

We analyze the equilibrium step structure using the spatial correlation function along the step edge that was described in detail in chapter 1. It is defined by:

$$G(y) = \left\langle (x(y) - x(y_0))^2 \right\rangle \qquad (3.1),$$

where the angular brackets represent an average over all initial points, y_0 on a given step whose configuration is defined by the continuous function $x(y)$. In the small y limit, we recall from chapter 1 that this function can be used to extract the thermodynamic step stiffness parameter via[1, 3]

$$G(y) = \frac{k_B T a_p}{\tilde{\beta}} y \qquad (3.2).$$

In this relation a_p is the lattice constant parallel to the step edge, and T is temperature. Thus, experimentally measured $G(y)$ curves yield the step stiffness from their small-y slopes.

Alternatively we can express the stiffness in terms of the step diffusivity using[1, 3]

$$\frac{k_B T a_p}{\tilde{\beta}} = \frac{b^2}{a_p} \qquad (3.3).$$

The diffusivity is so-called because, when scaled by a_p, it is represents the analog of the "diffusivity" that would be associated with a random walker moving in the time-like direction y along the step. This pleasing correspondence will be used in the presentation of the $\sqrt{3} \times \sqrt{3}$ data.

Figure 4 shows the experimental justification of the use of quenching experiments to obtain data at the highest temperatures. It shows first that the frizzy step in Fig. 3a

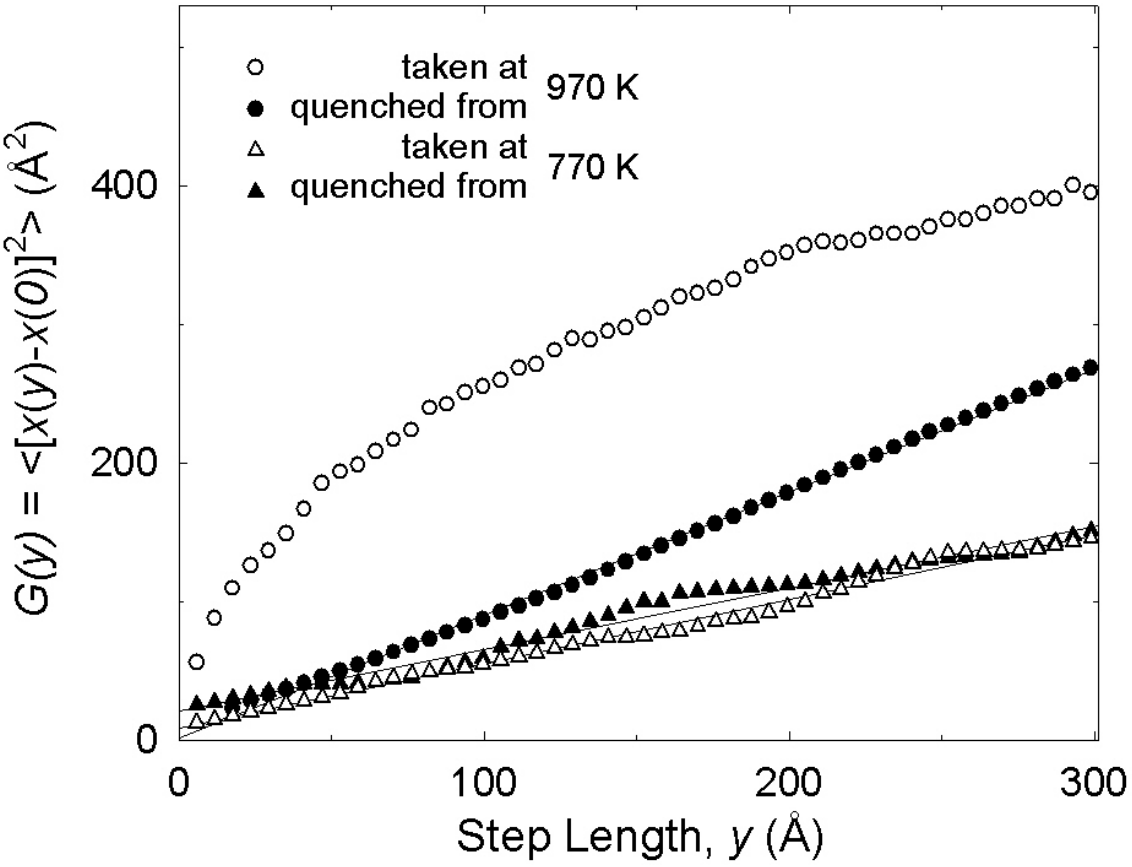

Figure 3.4 The effect of quenching on spatial correlation functions. Open symbols: at temperature, Filled symbols: Quenched. Quenching does not change G(y) significantly below 870 K. Above 870K it removes time information from G(y).

does indeed give a nonlinear spatial correlation function (open circles) at small y and cannot be used to obtain a step diffusivity. Furthermore it shows that the quenched image does give linear growth of *G(y)* (filled circles). Results from a quenching experiment from 770 K, where steps are only barely frizzy, to room temperature are plotted on the same graph. Open triangles represent *G(y)* obtained from steps at temperature and filled triangles represent the same function computed from the quenched surface. Since these curves are nearly identical and the slope of the 970 K quenched curve is significantly larger than the 770 K slope, it can be concluded that quenching from high temperature preserves closely enough the step structure at that temperature. For this surface it was necessary to use quenched surfaces for any temperature above 870 K.

Spatial correlation functions for a wide range of temperatures from 770 K to 1020 K are shown in figure 3.5. There is a clear increase in slope as the temperature is raised as expected since steps become more diffusive at higher temperatures. From the slopes of the lines Fig. 3.5, we find that the reduced step diffusivity , b^2/a_p, changes from 0.45 Å at 770K to 1 Å at 1020 K.

Since steps are known to meander spatially in units of discrete kinks, we can use the temperature dependence of the reduced diffusivity to extract an effective kink formation energy on the $\sqrt{3}\times\sqrt{3}$ steps. For a hexagonal lattice, the temperature dependence is given by[7]

$$\frac{b^2}{a_p} = \frac{3a_p}{2}\exp(\frac{-\varepsilon}{k_B T}) \qquad (3.4)$$

where ε is the effective single kink formation energy. In figure 3.6, the reduced diffusivities are shown in an Arrhenius plot with their common logarithms versus inverse

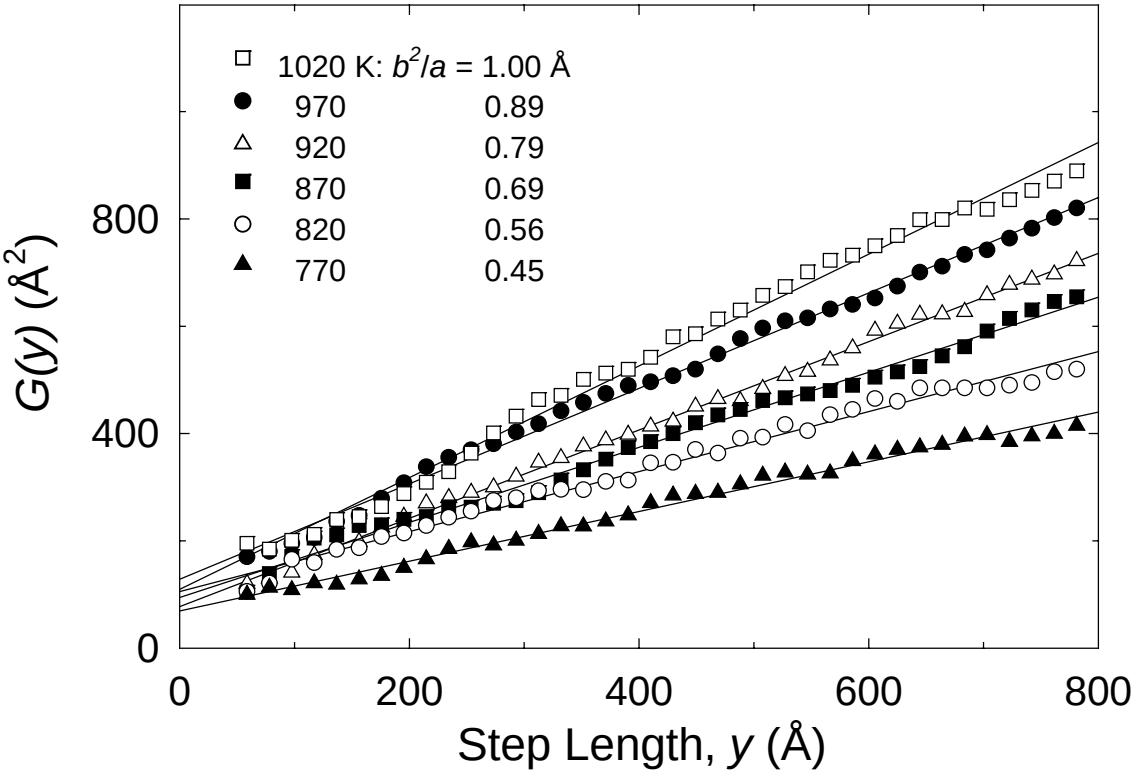

Figure 3.5 Spatial correlation functions for $\sqrt{3}\times\sqrt{3}$ steps between 770 K and 1020 K.

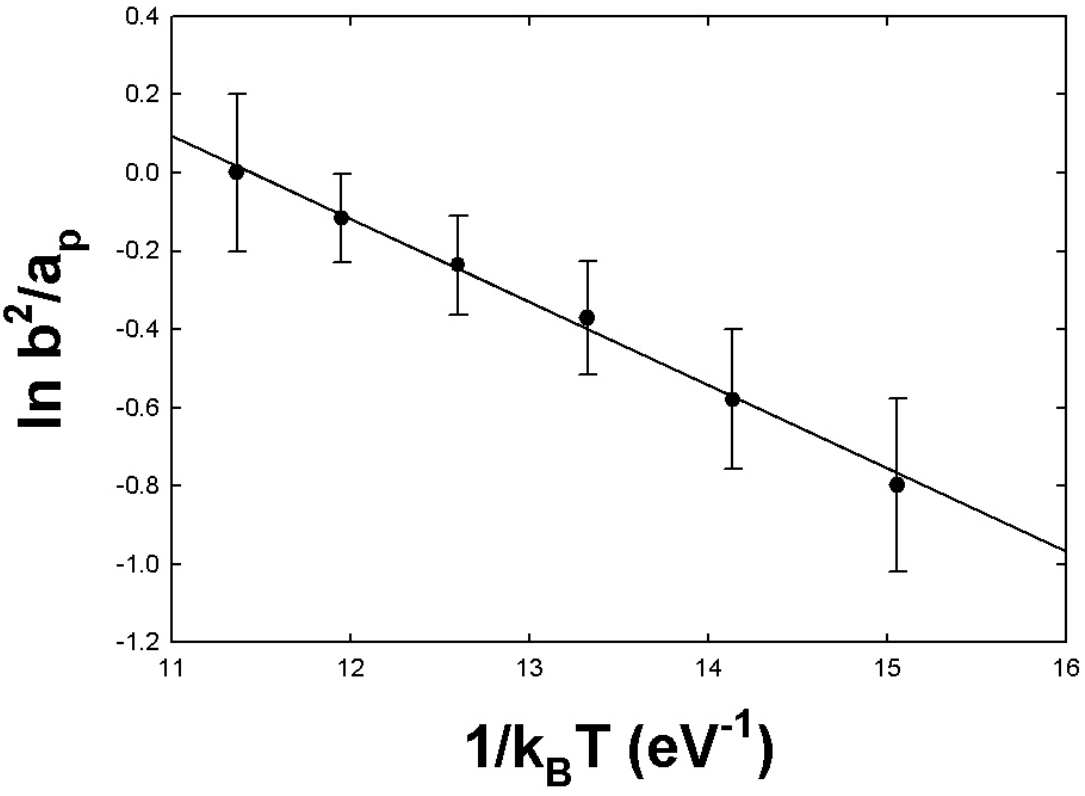

Figure 3.6 Arrhenius plot of step diffusivities for $\sqrt{3}\times\sqrt{3}$ allowing the extraction of an effective kink formation energy. The slope gives a kink formation energy of 0.21 ± 0.01 eV.

temperature. The slope of the line that the points fall on gives the kink energy as 0.21± 0.01 eV. Note that the fact that the diffusivities fall on such a straight line provides more justification for the validity of the quenching procedure.

Next we consider the dynamics of steps on the $\sqrt{3}\times\sqrt{3}$ surface steps. We employ the line scan mode of imaging (see for example figure 3.2) to extract the time dependence of the position of a single point on the step edge. Figure 3.7 shows an example of three such time series of step positions taken at different temperatures on during an experiment on the $\sqrt{3}\times\sqrt{3}$ surface. Obviously, the amplitude of the step fluctuations increases greatly as the temperature is raised. From these time series, we compute the standard temporal correlation function, defined by:

$$G(t) = \left\langle (x(t) - x(t_0))^2 \right\rangle \qquad (3.5)$$

where now the angular brackets signify an average over all t0 in the series. This function typically grows as a power of time:

$$G(t) = c(T)t^{\alpha} \qquad (3.6),$$

with an exponent α characteristic of the mass transport mode governing the fluctuations and a prefactor *c(T)* that depends on temperature through material specific parameters (see chapter 1 and the discussion to follow).

In figure 3.8, we show experimental temporal correlation functions for temperatures ranging from 770 K to 1020 K on a double logarithmic scale. The linearity of the *G(t)* curves on this type of plot indicates that it does grow as a power law with time in the temperature regime studied. From the linear fits shown as solid lines in figure 3.8 the exponent a is 0.47 ± 0.04. The prefactor, c(T), increases from 11.8 $Å^2$/s-a at 770 K to

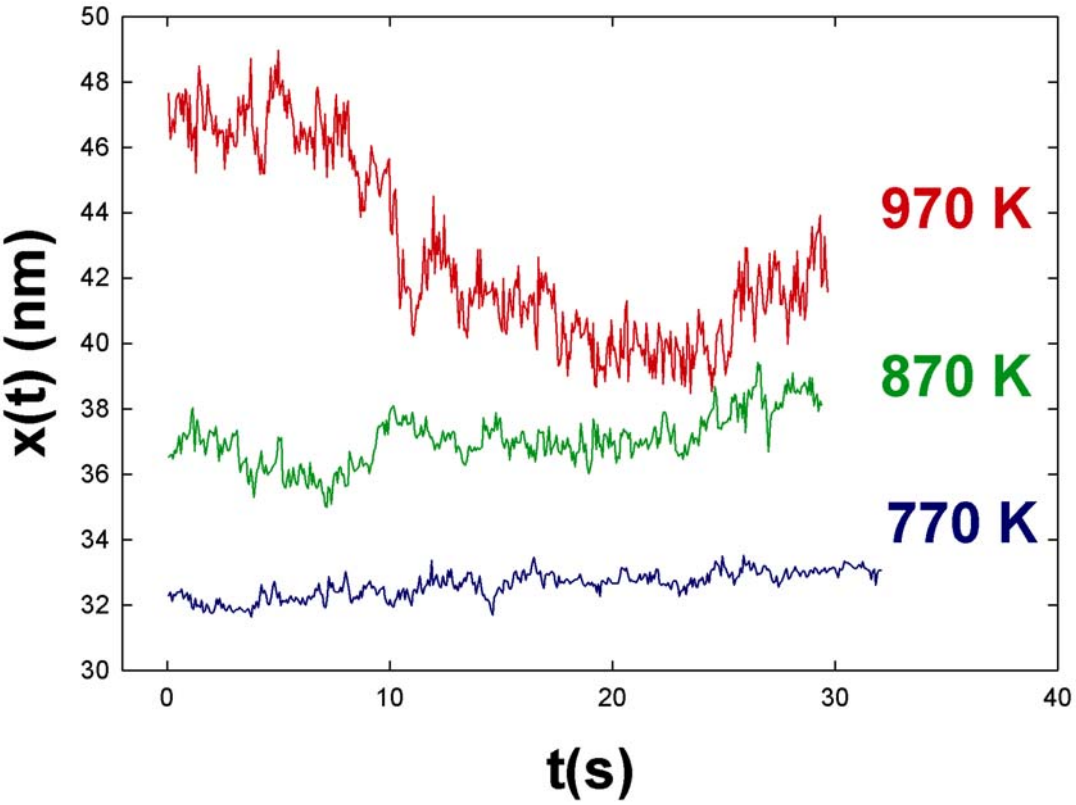

Figure 3.7 Examples of the time evolution of single points on $\sqrt{3}\times\sqrt{3}$ step edges for 3 different temperatures.

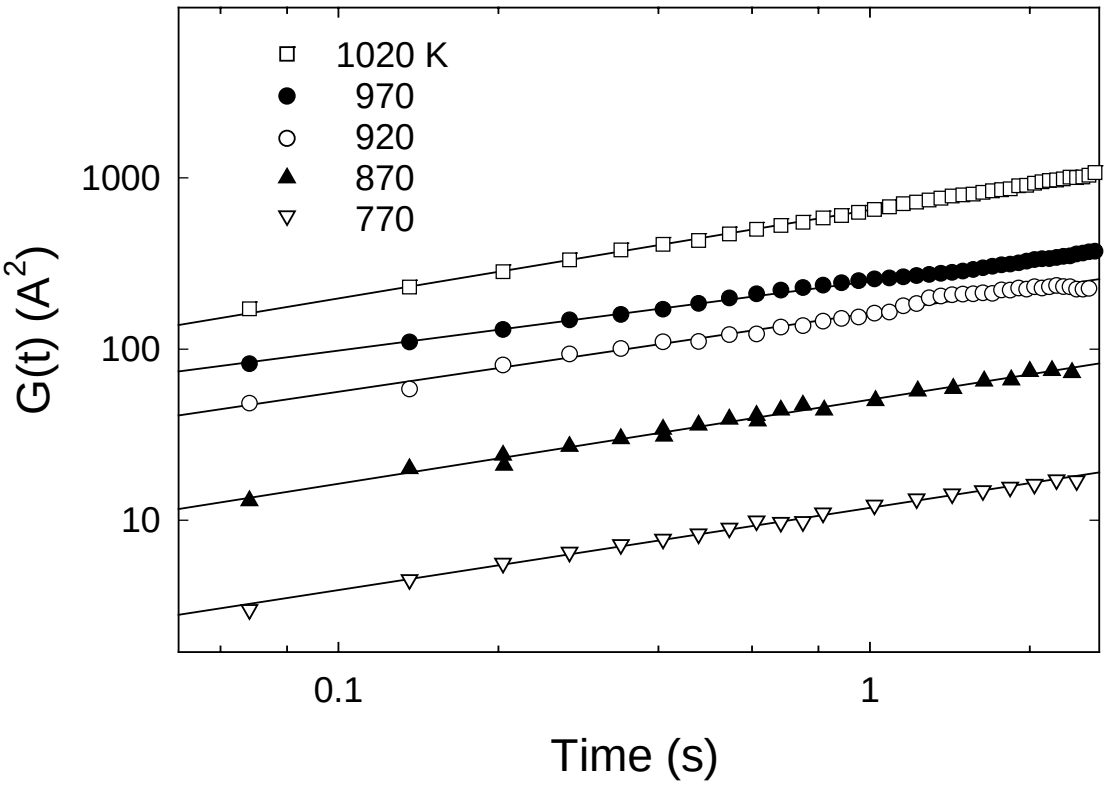

Figure 3.8 Temporal correlation functions on a double log scale for $\sqrt{3}\times\sqrt{3}$ steps.

536 $Å^2$/s at 1020 K. The parameters determined from the fits, as well as the corresponding reduced diffusivities are compiled in table 3.1.

3.4 Discussion and Analysis

The kink formation energy of roughly 0.21 eV obtained from the experimental spatial correlation functions is straightforward to understand. While there are no theoretical predictions for this number for the Si(111)- $\sqrt{3}\times\sqrt{3}$ R30º-Al surface, empirical potential calculations give a formation energy of 0.466 eV for the kink energy on bare Si(111)[54]. These two surfaces are closely related in that the $\sqrt{3}\times\sqrt{3}$ surface is formed by placing Al atoms on the appropriate 4-fold coordinated on-top sites of the Si(111) substrate[52, 53]. Certainly the differences in kink energies between the two can be easily understood as arising from the different energetics and possible step rebonding associated with the presence of Al. Thus, the step thermodynamics, embodied in the thermodynamic diffusivity (or equivalently stiffness) can be said to be reasonably well understood for this surface at a very fundamental level. As a practical matter, the effective kink energy allows the calculation of step diffusivity for any temperature between 770 K and 1020 K and probably extrapolates significantly outside this range.

Understanding the experimental results for dynamics of the step fluctuations is not quite as simple however. The observation that the temporal correlation function grows with approximately the square root of time is most simply understood as the result of attachment/detachment limited step fluctuations (see chapter 1). The exact result, obtained by integrating the linear Langevin equation describing this process is

Table 3.1

T (K)	b^2/a (Å)	c(T) ($Å^2/s^\alpha$)	α	Γ_a (10^4 $Å^3/s$)	τ_a (ms)
1020	1.00	536	.52	23	.28
970	.89	250	.41	5.5	1.2
920	.79	158	.46	2.5	2.6
870	.69	43.6	.47	.22	29
770	.45	11.8	.47	$2.4x10^{-2}$	260

$$G(t) = \sqrt{\frac{4\Gamma_a k_B T t}{\pi \tilde{\beta}}} \qquad (3.7),$$

where Γ_a is the attachment mobility, and $\tilde{\beta}$ is the step stiffness. The AD process can be quite simply thought of as the exchange of mass with a constant chemical potential reservoir that exists on the terraces. Thus, we will often refer to it as 2D evaporation/condensation (2D-EC) to reflect this.

Since in the present experiment we are dealing with a vicinal surface, where steps are spaced on average about 45 nm apart, the simple picture of independently fluctuating steps from which the above equation is obtained is not necessarily valid. On a vicinal surface, there are two purely surface transport processes that can lead to the scaling of *G(t)* with time observed in the present experiment[5, 6, 16, 55]. Figure 3.9 shows schematically the two processes overlaid on a 3D rendering of an STM image. In addition to the attachment/detachment process already mentioned, $G(t) \sim t^{1/2}$ can also result when terrace diffusion is rate-limiting but steps are closely spaced enough that diffusing mass quickly attaches to an adjacent step[5, 6, 16, 55]. This so-called diffusion from step-to-step mechanism (DSS) must be distinguished from AD in order to know how to interpret the magnitude of the prefactor of *G(t)*. The exact result for G(t) for the DSS mechanism is[16]:

$$G(t) = \sqrt{\frac{16 D c k_B T \Omega^2 t}{\pi^3 \tilde{\beta} L}} \qquad (3.8).$$

The most obvious way to differentiate between this equation and Eq. 3.7 is by the presence of *L*, the average step separation in the denominator for the DSS case[55]. We

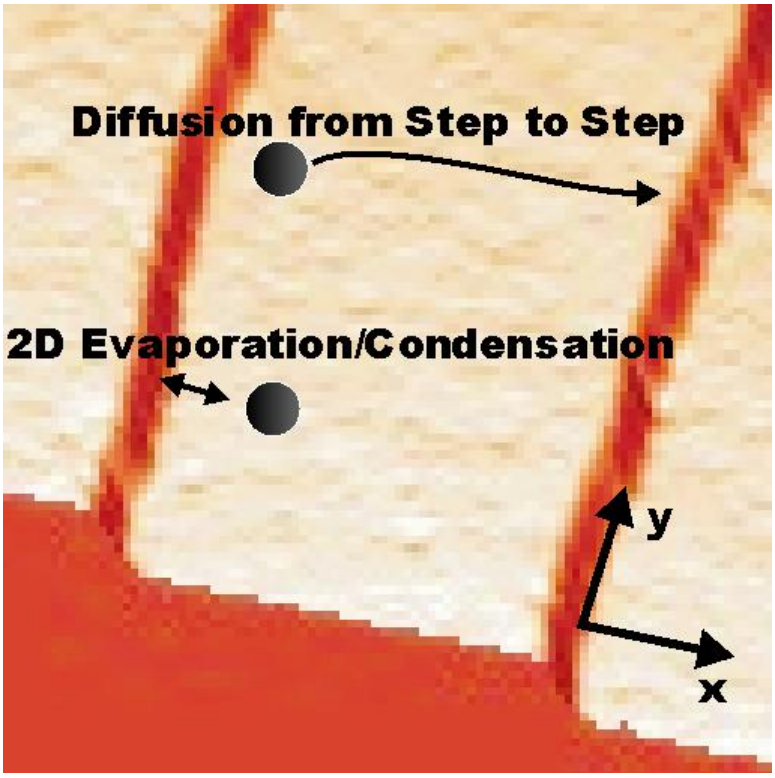

Figure 3.9 Schematic of the two surface transport processes that can lead to the growth of G(t) with the square root of time. Random attachment/detachment and diffusion from step to step.

could imagine searching experimentally for a dependence on average step spacing in the prefactor of the correlation function. For a good vicinal surface like the ones used in the present work however, finding enough variation in L on a single sample to directly test Eq. 3.8 is not likely. The only alternative would then be to perform a series of experiments on many different samples cut from wafers with different miscut angles and hence different step spacings. Such an undertaking would be time consuming and might still not provide enough variation in L to make a clear comparison with Eq. 3.8(see e.g. Bartelt et al.[12]). While the dependence of DSS fluctuations on step separation seems straightforward in principle, and has in fact been applied successfully to several metal surfaces[3], it is not the most practically valuable.

Fortunately, there is another way to distinguish between AD and DSS mechanisms using only the type of line-scan data that would be obtained in the usual determination of $G(t)$. Quite simply, it involves looking for statistical correlations between the fluctuations of near-neighbor steps[16]. If we remember that the evolution of a single point on a step can be treated as a random variable, we can look for correlations between two steps by computing the cross correlation function of their respective x(t)'s. This function is well-known in probability theory and is defined by[16]:

$$C_1(t) = \left\langle x_n(y_0, t + t_0) x_{n+1}(y_0, t_0) \right\rangle \qquad (3.9),$$

where y_0 is the fixed point along the steps t_0 is the initial time, and the average is taken over all t_0 in the time series. Blagojevic and Duxbury (Ref. 9) have addressed theoretically the issue of cross correlations on vicinal surfaces. They obtain exact results for $C_1(t)$ arising from many different transport mechanisms. Most significantly for the

present work is their results for near-neighbor cross correlations resulting from AD and DSS processes[16]:

$$\text{AD}: C_1(t) = 0 \qquad (3.10a)$$

$$\text{DSS}: C_1(t) = \sqrt{\frac{16cDk_BT\Omega^2 t}{9\pi^3 L\tilde{\beta}}} \quad (3.10b).$$

First, the cross correlation functions are computed with each step position referenced to *its own center of mass*. This is simply a convention employed by BD[16] and a different reference could be chosen. Second, the result that the cross correlations vanish for AD limited step fluctuations should be fairly intuitive (the strict *vanishing* is merely a consequence of the choice of reference just mentioned. Other references would simply give an offset from zero). The AD mechanism can only occur if steps are approximately isolated. In fact, BD show that cross correlations vanish for any of the isolated step mechanisms discussed in chapter 1 (AD, step edge dffusion, or terrace dffusion)[16]. Finally (and most importantly), we note the similarity between Eq. 3.10b and Eq. 3.9. Numerically, the cross correlations between adjacent steps due to a DSS transport mechanism are simply 1/6 the magnitude of the temporal correlation function of the individual steps. Equation 3.10 provides a very simple method for determining whether $t^{1/2}$ growth of *G(t)* is due to DSS limited fluctuation kinetics; it tells us the detailed time dependence that is expected for correlated step behavior in such a case.

A subset of the line scan images used in the determination of *G(t)* for the $\sqrt{3}\times\sqrt{3}$ surface steps contained two steps in the field of view (see for example the image in Fig. 3.2). Figure 3.10a shows *G(t)* obtained from several images at 970 K that had two steps visible. In figure 10b we show the cross correlation function for the same subset of

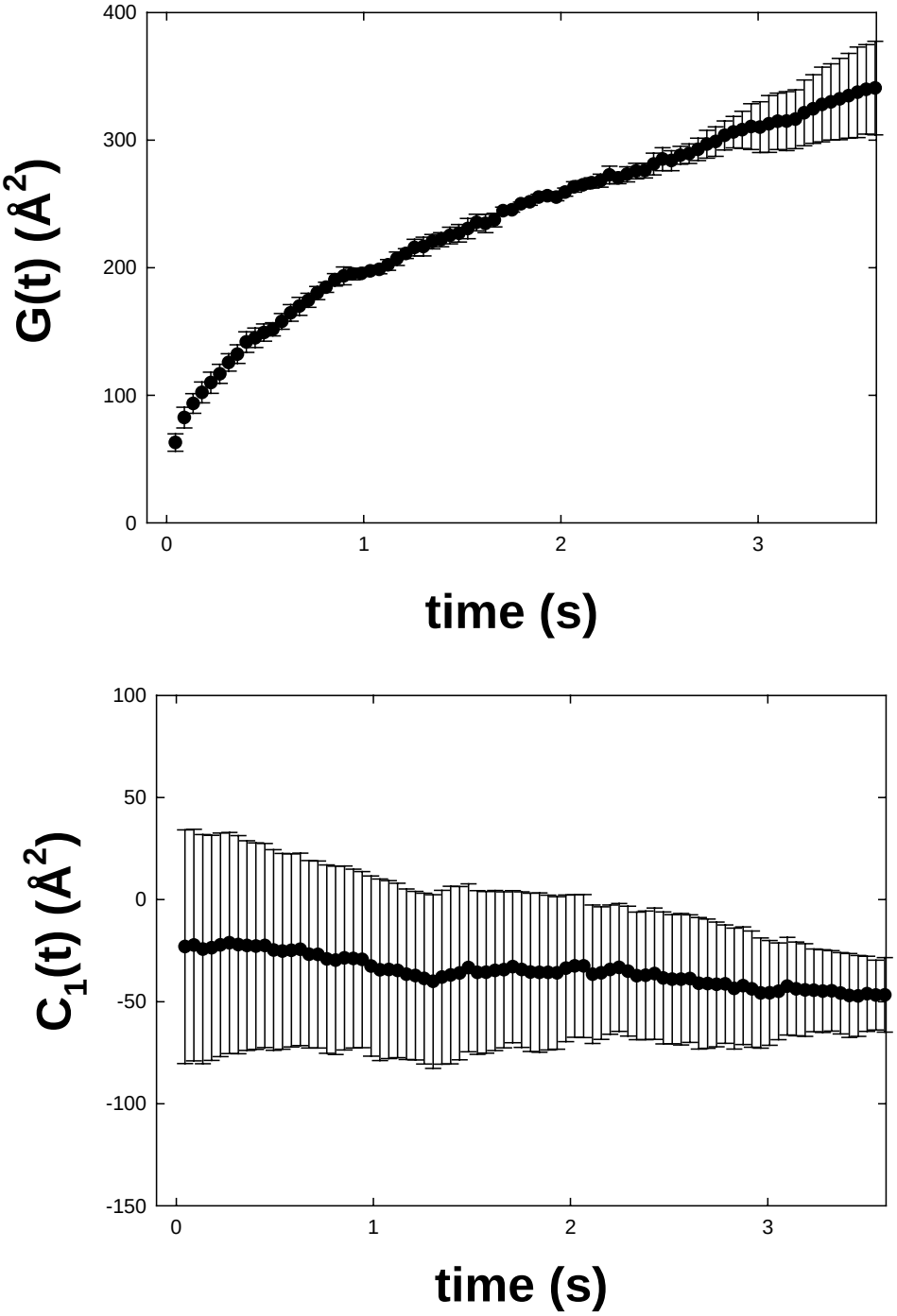

Figure 3.10 a.) Temporal correlation function for 970 K data with 2 steps in the field of view. b.) Cross correlation function between adjacent steps for the same images as in a.)

images. First we note that while *G(t)* grows monotonically with time and has the typical power law form, $C_1(t)$ has no obvious systematic time dependence. The solid lines in each plot represent two parameter power law fits to the data. For *G(t)* the best power lawis $G(t) = (33 \pm 1)t^{(0.41\pm0.03)}$ and for $C_1(t)$ it is $C_1(t) = (-36 \pm 6) \cdot t^{(-0.09\pm0.11)}$. Naturally (being a subset of the full 970 K data set) *G(t)* is in agreement with the parameters in table 3.1. The cross correlation function, as is qualitatively obvious, cannot be said to either grow or decay with time to within the error bars. Thus we have good indication that, despite some systematic offset to $C_1(t)$, it is not consistent with DSS limited step fluctuations.

To make this point even more clear in figure 3.11 we plot $C_1(t)$ (with error bars omitted for clarity) on the same axes as *1/6 G(t)* from Fig. 3.10a. Again, the best fit curves are clearly very different for the two functions. While the error bars for $C_1(t)$ do overlap the *G/6* curve for small times (less than about 1 second) we attribute this to the finite measurement time. When the measurement begins, the steps must be moving either towards or away from one another and so for the smallest time windows in the average (Eq. 3.9) there will always be some offset. This can only be alleviated by following the step fluctuations for very long (theoretically infinite) times.

Based on the above arguments, we can reasonably conclude that the $t^{1/2}$ growth of the temporal correlation function is not due to diffusion from step to step. Given the large step spacing relative to the amplitude of fluctuations, it is not surprising that the steps can be treated as effectively isolated. We attribute the scaling of *G(t)* to AD-limited kinetics but point out that this absolutely does *not* mean that no other transport process

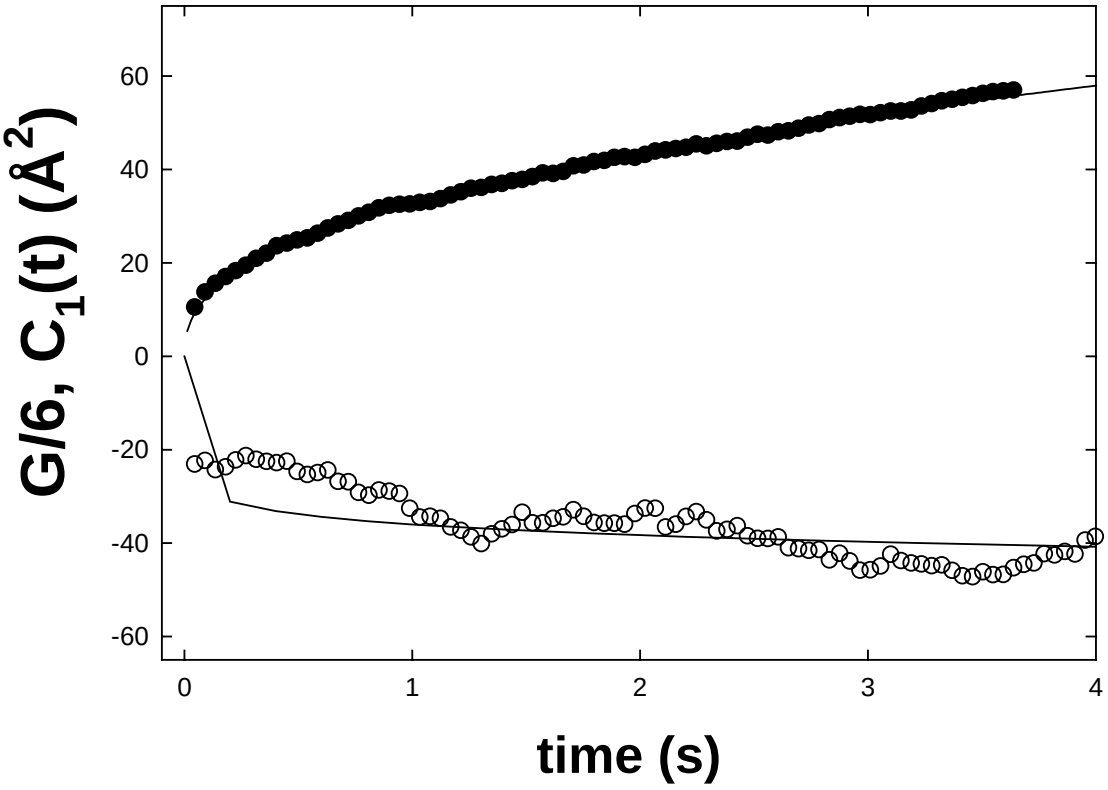

Figure 3.11

occurs on this surface. In fact, it is rather likely that many processes occur in parallel. Only the rate-limiting one (in this case AD) actually contributes to the observed *G(t)* [1, 6].

Armed with a qualitative knowledge of the nature of the rate-limiting mechanism for the $\sqrt{3}\times\sqrt{3}$ steps, we can extract specific kinetic parameters from *G(t)*. Using the experimental prefactors, diffusivities, and Eq. 3.7, the attachment mobility Γ_a can be determined. This parameter (which appears in the Langevin equation in chapter 1) is proportional to a rate constant for attachment and detachment from step edges and is also therefore inversely related to a time constant for this process via $\Gamma_a = a_n^2 a_p / \tau_a$ [1, 12]. The time constants vary from 260 ms at 770 K to 0.23 ms at 1020 K. Mobilities and corresponding time constants are compiled in table 3.2.

The rapid increase of time constant with temperature immediately suggests a simple activated form for this quantity. Figure 3.12 shows the inverse time constant plotted versus inverse temperature on a semi-log scale. The slope of the plot gives an activation energy of 1.9 ± 0.1 eV and the intercept gives an attempt frequency of $10^{12\pm2}$ Hz. At first glance these numbers seem rather reasonable. The attempt frequency is very close to a typical phonon frequency and the activation energy is typical for a chemical bonding situation as expected for Al on Si(111)[52]. Thus, the simplest picture for the attachment/detachment kinetics on this surface is that the rate-limiting step involves the thermal breaking of an Al-Si bond.

Because the surface unit cell is fairly complicated, consisting of 1 Al and 6 Si atoms, the details of the kinetic picture suggested by the Arrhenius above may well be too naïve. In the absence of theoretical or experimental studies into the microscopic energy barriers on the $\sqrt{3}\times\sqrt{3}$ surface, our understanding of the microscopic processes

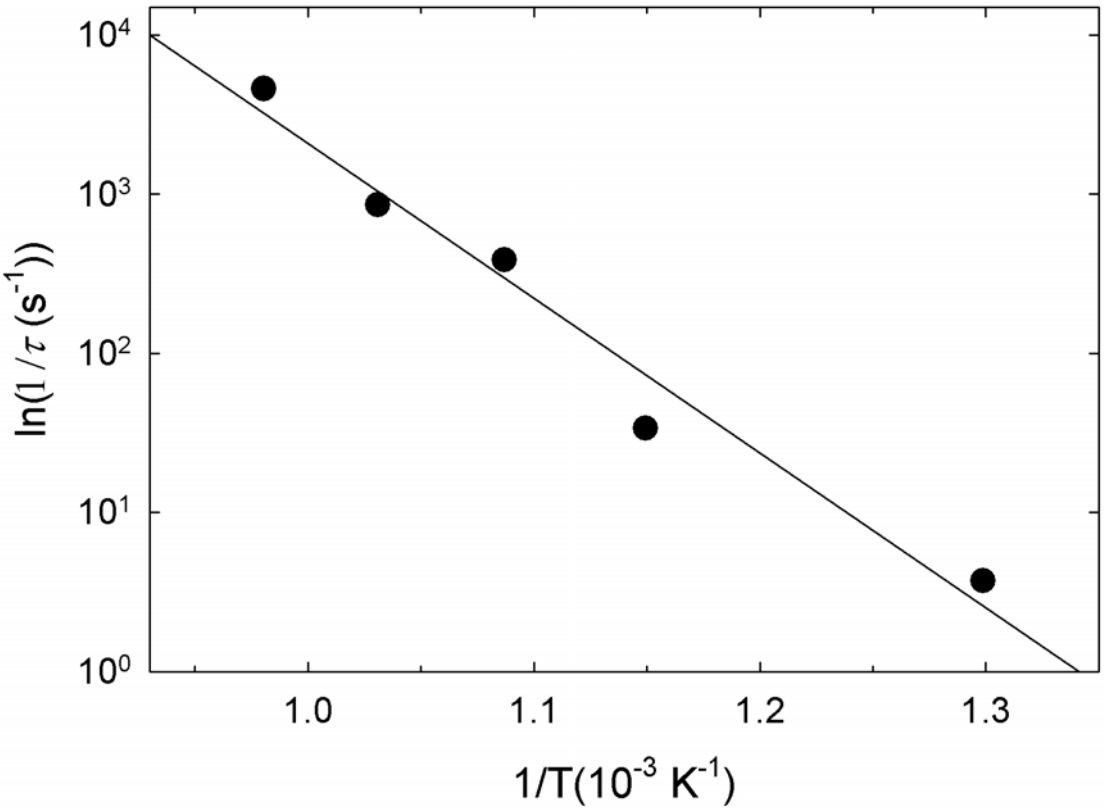

Figure 3.12 Arrhenius plot of AD time constants.

underlying the step fluctuations can only be considered tentative. From a practical perspective however, uncertainty about the atomic-level details does not in any way detract from the practical value of knowing the AD time constants and the effective energy scale that determines them. These parameters can be used to interpolate step dynamics to any temperature necessary. They are often found to determine the rates of relaxation of nonequilibrium surface features[3, 56, 57] as well as the possibility and nature of surface or step instabilities[27, 58]. The understanding of the kinetics of surface steps on uniform Si(111)- $\sqrt{3}\times\sqrt{3}$ R30-Al can in fact be considered essentially complete at the level of the continuum step model.

3.5 Summary and Conclusion

We have shown that step fluctuations on a complicated reconstructed surface containing a many-atom unit cell and two chemical species can be understood within a simple continuum step model. The model incorporates the microscopic complexity into one thermodynamic parameter (the step diffusivity) and one kinetic parameter (the step attachment mobility).

The diffusivity for steps on a uniform Si(111)- $\sqrt{3}\times\sqrt{3}$ R30-Al surface has been determined by STM measurements (both at temperature and after quenching to room temperature) of the equilibrium step configurations between 770 K and 1020 K. From the temperature dependence of the diffusivity we have extracted an effective kink formation energy of 0.21eV.

The rate-limiting mass transport mechanism governing the fluctuation kinetics has been determined from time-dependent STM tracking of step edge positions in the same

temperature range. Using the scaling of the temporal correlation function with the square root of time and the apparently uncorrelated fluctuations of adjacent steps, we conclude that the rate-limiting process is attachment and detachment at step edges. From the magnitude of the temporal correlation function we extract the step attachment mobility. The temperature dependence of this continuum step parameter gives an effective energy scale governing the AD process of 1.9 eV. While the exact microscopic processes from which this energy arises cannot be determined from the present experiment, it is certainly consistent with expectations for a chemisorption system where one or more bonds are made or broken in the attachment or detachment process.

Ultimately, the microscopic understanding of the fluctuation kinetics is not the most relevant level for many practical issues of current interest in nanotechnology. It is mesoscopic parameters like attachment mobilities (or time constants) that are expected to determine the stability and temporal evolution of nanoscale structures[56, 57, 59, 60]. The experiments presented in this chapter illustrate that such a mesoscopic description can be fruitfully applied even to chemically and structurally complicated systems.

Chapter 4

Crossover in step fluctuation kinetics due to coexistence of surface phases

Variable Temperature STM is used to study step fluctuations in real time on an Si(111)-$\sqrt{3} \times \sqrt{3}$ R30-Al surface where a minor amount of a second structural phase, γ-Al/Si(111), has begun to grow. The measured temporal correlation function follows a $t^{0.27\pm0.02}$ power law, in dramatic contrast to the thermal fluctuations of steps on the uniform Al-$\sqrt{3} \times \sqrt{3}$ R30-Si(111) surface. This change is consistent with step fluctuations limited by step edge diffusion as opposed to the previously determined random attachment/detachment on the uniform surface. The depletion of a reservoir of mobile species from the surface as the new phase grows is proposed as the mechanism for the change in the observed rate-limiting relaxation mechanism.

4.1 Introduction

In the previous chapter, it was established that the Langevin formalism for step fluctuations could be applied to the relatively complicated reconstructed surface Si(111)-$\sqrt{3} \times \sqrt{3}$ R30-Al[21]. Despite this success, the rate-limiting attachment/detachment mechanism observed is not likely to be the only mass transport process active on the surface. Indeed, there is every reason to expect that all other surface transport processes are occurring in parallel in the temperature range 770 K to 1020 K but that the others (step-edge diffusion, terrace diffusion, etc) are masked by the relatively slow attachment/detachment. As pointed out in the introductory remarks of the work of Geisen et al. on Pt(111) [61], it is desirable to know as much about as many surface kinetic processes as possible in order to obtain the most quantitative understanding of growth and evolution processes relevant to technology. In the present chapter we describe the exploitation of the rich and complicated Al/Si(111) phase diagram to suppress the dominant AD process studied in chapter 3 and allow other transport processes to become accessible to our VTSTM experiments. In doing so, we will first revisit much of the theoretical background presented in chapter 1 and also provide a brief introduction to the various unified theories of step dynamics that have developed over the past 10 years.

The vast complexity of mass transport on solid surfaces has resulted in phenomenological understanding primarily of simplified limiting cases. Beginning with the seminal work of Burton, Cabrera, and Frank (BCF)[2], who treated crystal growth in the diffusion-limited regime, the use of such limits has fortunately been useful in describing a number of experimental systems[1, 3, 4, 12, 15, 20, 21, 25, 49, 50, 56, 60-66]. In fact, this success is not merely good fortune but essentially the result of the thermally activated

nature of most transport processes that translates even small differences in energy barriers into large differences in rates. Thus it often suffices to consider all processes but the slowest to be infinitely fast.

In the work of BCF, the importance of steps as active sites in mass transport was emphasized[2]. Recent high-resolution observations of the stochastic motion of surface steps have provided access to microscopic transport processes. The thermal fluctuations of step positions can be quantitatively related to the kinetic parameters governing the relaxation back to equilibrium[1, 3, 6, 15, 16, 55]. Analysis of the statistics of step fluctuations has been carried out on a variety of metal and semiconductor surfaces[1, 3] and supports the idea that a single rate-limiting process typically governs relaxation. A coarse-grained Hamiltonian for the rate limiting process can then be used to obtain a Langevin equation for the step position as a function of time (see chapter 1 of this work). Examples include Si(111) steps limited by random exchange of mass with a 2D gas of adatoms on the terraces[12] and Pb(111) steps limited by diffusion parallel to the step edges[63, 65].

An important question, particularly given the practical value of predicting and controlling mass transport, is how the relative rates of step relaxation can change as a function of some external parameter like temperature. Such "crossovers" have been reported by Kammler et al. for Si(001)[50], Giesen for Cu(111)[25] and Ondrejcek et al. for Pt(111)[20, 61]. The treatment of limiting cases as described above obviously cannot deal with these situations and more complete treatments have been developed to allow the consideration of a variety of competing relaxation paths. Almost simultaneously, Khare and Einstein (KE)[6] and Ihle, Misbah, and Pierre-Louis (IMP)[5] published detailed formalisms by which step fluctuations resulting from a realistic variety of transport

processes can be understood. Both treatments essentially formalize an original rough (though physically appealing) description developed by Pimpinelli and co-workers[55]. The formalisms generalize the boundary value problem first solved by BCF, and indicate under what conditions to expect simple limiting behavior as well as how one limiting behavior can be supplanted by another.

In the present chapter we describe the experimental observation of a crossover in rate limiting step relaxation mode on a Si(111) - $\sqrt{3} \times \sqrt{3}$ R30-Al surface caused by the nucleation of minor amounts of a second Al-induced structural phase on Si(111). At temperatures less than 920 K, an incommensurate substitutional phase of Al on Si(111), henceforth called the γ-phase, can nucleate at the $\sqrt{3} \times \sqrt{3}$ step edges[52, 67]. Step fluctuations were observed with variable temperature STM on regions of the steps far from the nucleation sites and compared with previous observations of structurally identical steps on surfaces that did not show any sign of phase separation. The measured statistical properties of the fluctuations were found to be dramatically different even at identical temperatures, and indicate a previously unobserved crossover phenomenon. This crossover can be understood as the result of the reduction of mobile adatom concentration on the terraces as the second phase forms. Support for this conclusion is obtained from previous experimental studies of the kinetics of γ-phase growth[67] as well as the unified theoretical pictures of fluctuation kinetics found in IMP[5].

4.2 Background

When a rate-limiting, atomic-scale mass transport mechanism exists on a surface, it determines the kinetics of step fluctuations[1, 3, 15, 55]. For the purpose of mass transport

studies, it is convenient to treat steps as continuous functions (recall chapter 1) and to describe their time evolution by a Langevin equation of the general form[6],

$$\partial_t x(y,t) = F[x(y,t)] + \eta(y,t) \qquad (4.1).$$

Here x(y,t) describes the step position as a function of time t and position parallel to the average step edge y, with coordinates as shown in the STM image in figure 4.1a. The first term is a functional of the (usually local) step position that accounts for relaxation of the step positions towards equilibrium and is phenomenologically obtained for the presumed rate-limiting process. The second "noise" term models the thermal excitations in the system. Near equilibrium, noise correlations must be chosen to enforce any conservation laws and the fluctuation-dissipation theorem. In most systems observed to date, step fluctuations have been found to be well-modeled by relatively simple forms of Eq. 4.1: F = $\nabla^2 x(y,t)$ with white noise or F = $\nabla^4 x(y,t)$ with volume conserving noise[1]. These two common cases correspond to fluctuations for which the rate-limiting microscopic process is random attachment/detachment at the step edge or diffusion along the step edge, respectively. From Eq. 4.1, analytical predictions can be obtained for the experimentally accessible temporal correlation function,

$$G(t) = \left\langle [x(t+t_0) - x(t_0)]^2 \right\rangle . \qquad (4.2)$$

The average is taken over all initial times t_0 and x(t) is the step position at a fixed y on the step edge. When there is a single, rate-limiting fluctuation mechanism for the step edge, the correlation function usually increases as a simple power law [14,15]

$$G(t) = c(T)t^{\frac{1}{z}} \qquad (4.3),$$

The exponent, z, has a universal value determined only by the generic rate-limiting mechanism, while the temperature dependent prefactor is determined by the detailed thermodynamics and kinetics of the system in question. In fact, the prefactor for most reported situations contains only one thermodynamic and one kinetic parameter, reflecting the existence of well-defined effective energy scales for mass transport on the surface.

In addition to the temporal correlations, the spatial correlations of the step edge position are useful within the continuum step approximation[1, 3]. The spatial correlation function,

$$G(y) = \left\langle [x(y + y_0) - x(y_0)]^2 \right\rangle \qquad (4.4),$$

has the well-known small y limit[1, 3]

$$G(y) = \frac{k_B T}{\tilde{\beta}} y \qquad (4.5).$$

In the above, $\tilde{\beta}$ is the thermodynamic step stiffness that is determined microscopically by the energy cost to form a kink in a straight step[1, 3]. Thus, with the analysis of both spatial and temporal correlation functions, all of the macroscopic quantities governing step fluctuations can be extracted from experiments. Reasonable choice of a microscopic model (almost always the Terrace-Step-Kink model[1, 3, 68]) allows the determination of effective energy scales governing both the step thermodynamics and kinetics.

Complete analysis of step fluctuations on uniform Al-$\sqrt{3} \times \sqrt{3}$ R30-Si(111) surfaces as described in chapter 3[21, 69] shows that the time correlation function follows a power law for temperatures between 770 K and 1020 K with the average z in Eq. 3 of 2.17 ± 0.09. This fact, along with the determination of kinetic and thermodynamic

parameters, is consistent with fluctuation kinetics limited by random attachment/detachment events exchanging mass with the 2-D gas of ad-species on the terraces. Single attachment/detachment events occur with time constants of 260 ms at 770 K and 0.28 ms at 1020 K and almost certainly involve the collective motion of at least one aluminum atom and a number of silicon atoms.

The $\sqrt{3} \times \sqrt{3}$ surface reconstruction is one of several that can be induced on Si(111)-(7x7) by the adsorption of Al[51, 52, 67, 70]. It is relatively easy to form large, homogenous $\sqrt{3} \times \sqrt{3}$ regions, whereas the other reconstructions tend to coexist with one another due to slow kinetics of conversion[52, 67]. The $\sqrt{3} \times \sqrt{3}$ phase is stable between 920 K and 1020 K. At high temperatures it disorders via a first order phase transition[71], while at low temperatures it converts to a mixture of disordered Al clusters on Si(111)-(7x7) and the incommensurate gamma phase. This phase has a bilayer structure with Al (0.68 ML) atoms forming the upper half of the bilayer and Si atoms (1.0 ML) forming the lower half[72]. As a result, nucleation of this phase occurs at step edges rather than in isolated domains on terraces[67]. The unit cell does not have a constant relationship to the underlying Si(111) bulk-terminated surface but rather consists of various odd multiples (on average(9x9)) of the (1x1) cell separated by missing Al rows[52, 73]. The substitutional Al gives a small surface corrugation relative to the other Al-induced phases and STM images thus often appear as disordered arrays of flat triangles as shown in Fig. 4.1.

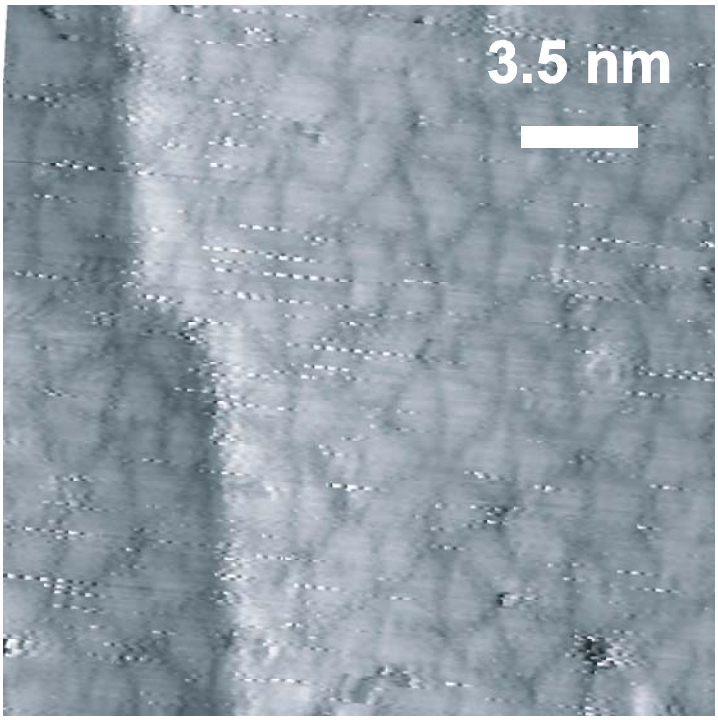

Figure 4.1 Room temperature STM image of γ-Al/Si(111)

4.3 Experimental

Si(111)-(7x7) substrates were prepared in UHV (base pressure ~6 x 10^{-11} torr) by annealing Si(111) samples cut from a wafer (As-doped, 10 mΩ · cm, ~0.5° miscut toward $\left[2\bar{1}\bar{1}\right]$) for 2-12 hours at ~ 1070 K. Repeated flashes to 1520 K with subsequent slow cooling through the (1x1)-(7x7) phase transition resulted in a clean, ordered surface with monatomic steps separated by an average terrace width of 45 nm. Aluminum was deposited in the same UHV chamber onto a substrate held between 970 and 1020 K. Surface ordering was periodically monitored by LEED (Physical Electronics Industries); when a sharp $\sqrt{3}\times\sqrt{3}$R30 pattern was observed, the sample was transferred to a Variable Temperature STM (Omicron). Surface ordering and uniformity was verified by atomically resolved STM at room temperature (Fig. 3.1). If large regions of uniform Al-$\sqrt{3}\times\sqrt{3}$R30-Si(111) were easily located, the sample was then heated in-situ for real time observation of step fluctuations. Measurements of step fluctuations were made with the sample held at temperature, over a range of 770 to 920 K. At each temperature, the microscope was allowed to thermalize for about one hour prior to imaging at the elevated temperature, so that no special thermal drift correction was necessary. To overcome the inherent limitations of STM imaging rate, real-time observations were made by scanning the tip over a single point on the step edge repeatedly for between 23 and 107 seconds. A typical such line-scan image is shown in figure 4.2a for a surface held at 920 K after having been imaged and equilibrated for over 4 hours at temperatures between 720 K and 870 K beforehand. Standard STM snapshots were also obtained at elevated temperatures to monitor the surface and to allow the analysis of spatial step wandering[69] in addition to

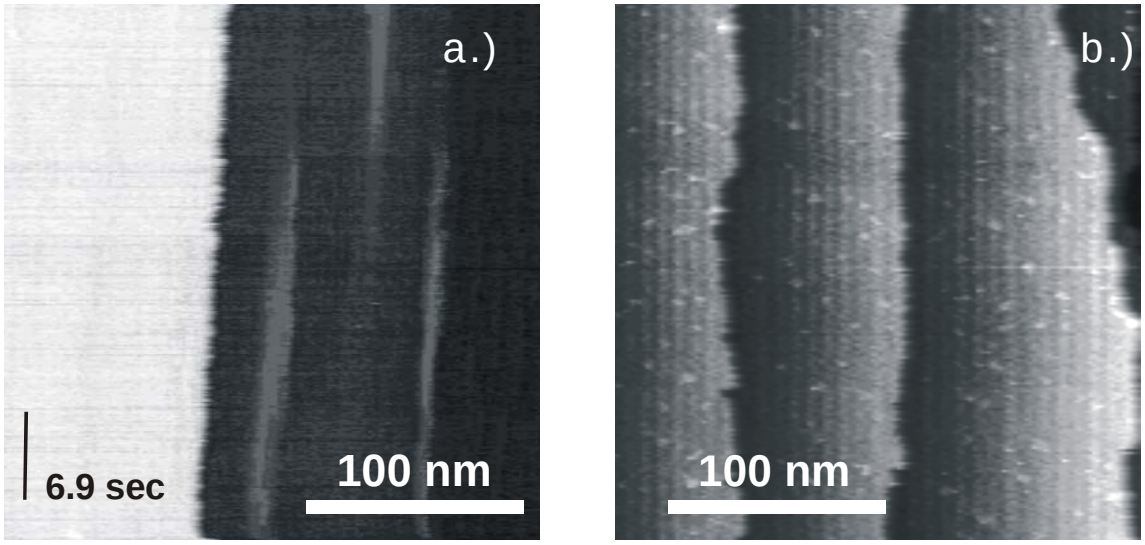

Figure 4.2 a.) Line-scan pseudo image of fluctuating step far from γ-phase domains. b.) Spatial snapshot of a region of the same surface showing large lengths of step free of γ-phase nucleation sites.

the temporal information provided by the line scans. Figure 4.2b shows an example of a spatial image obtained at 820 K on a sample that had been held for 2.5 hours at 720 K. Images were collected using varied scan rates (3000-15000 nm/s) and tunneling parameters (2-3.5 V, 0.05-0.3 nA) to help rule out the influence of the electrochemically etched tungsten STM tip on measurements.

Observations of the uniform gamma phase (Fig. 4.1b) were made in a separate UHV chamber (base pressure ~ $4x10^{-11}$ torr) by depositing approximately 1 ML of aluminum onto a clean Si(111)-(7x7) sample cut from the same wafer described above. The substrate was held at 970 K and the Al flux kept above 0.5ML/min. After a sharp gamma LEED pattern was observed, the sample was quenched to room temperature and transferred to a home-built STM. Imaging was performed at room temperature, again under varied tunneling conditions.

4.4 Results and Observations

A surface that was initially composed of completely uniform $\sqrt{3} \times \sqrt{3}$, as confirmed by room temperature imaging following transfer to the VTSTM, was observed to begin conversion to the incommensurate γ-Al/Si(111) if the sample was allowed to thermally equilibrate at a temperature between 720 K and 920 K over time scales of at least one hour. Figure 4.3a illustrates the features of such a phase-separated surface. The arrow in the figure points to a region near the step edge where the apparent height in the STM image decreases by less than a monatomic Si(111) step height as illustrated in the line profile of Fig. 4.3b. Despite the fact that the unit cell is not resolved in this region, the apparent height decrease clearly indicates the presence of the gamma phase, since the

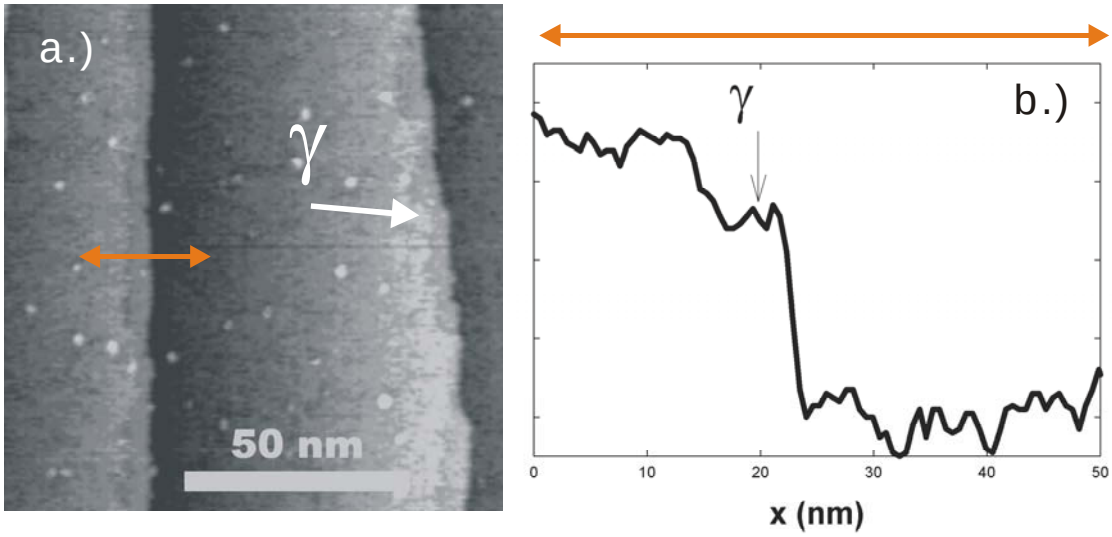

Figure 4.3 a.) STM image showing step edges decorated by γ-Al/Si and clusters on terraces that have formed after 105 minutes at 720 K b.) Line profile from the STM image corresponding to the orange arrow showing the apparent height decrease at the step edge.

other known phases would exhibit larger corrugation and an apparent height *increase* relative to the $\sqrt{3} \times \sqrt{3}$. In addition, the small bright spots visible on the terraces in Fig. 4.3 are well known defects associated with the growth of the γ-Al/Si(111) bilayer[67, 73]. The bright spots grow in size over time once the phase separation begins as shown in Fig. 4.4. Here the evolution of the surface morphology is shown at particularly advanced stages of the conversion. After holding the sample at 720 K for ~ 4 hours the image of Fig. 4.4a was obtained with the sample temperature increased to 820 K. Fig. 4.4b shows a different but presumably still representative area of the same surface 2 hours later at 920 K. The large amplitude spatial wandering of the steps that increases with time and in proportion to the size of clusters was observed with LEEM by Michely et al.[67] during the growth of the γ phase under different conditions. In this large-scale view, the most obvious sign of phase separation appears as this "etching" of the step edges. The generic features of clusters and decorated or etched steps were reproduced over the course of two months in many separate Al depositions on several different pieces of the same wafer when initially imaging at temperatures below 920 K. In contrast, surfaces that were initially thermally equilibrated *above* 920 K and then cooled for imaging to lower temperatures did not develop the jagged step morphology and large clusters associated with the growth of the gamma phase in the time scale on which the surface was observed.

As shown in the line-scan image of figure 4.2a, even after the formation of the small clusters on the terraces that are characteristic of the onset of the gamma phase, most regions of the step edge still show temporal wandering qualitatively like that reported in chapter three[21] for the pure $\sqrt{3} \times \sqrt{3}$ phase. On such surfaces, large lengths of the step edge are free from the nucleation sites of the gamma phase, and spatial snapshots as in

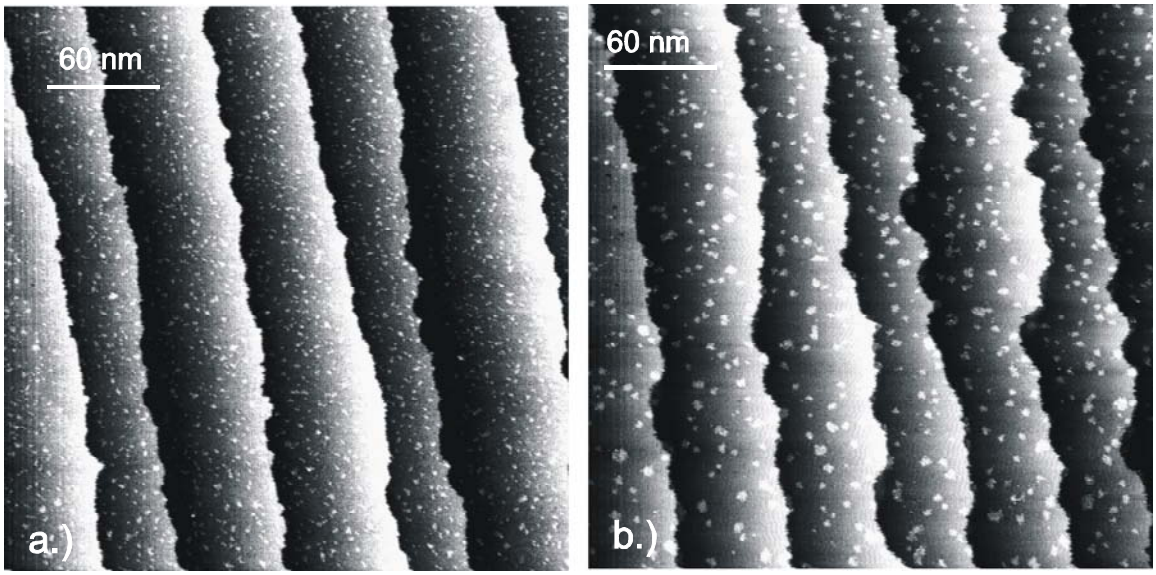

Figure 4.4 a.) STM at 820 K after 4 hours annealing at 720 K and about 30 minutes at 820 K. b.) STM of a different region of the same sample after 2 hours at 920 K.

figure 4.2b show little evidence of phase coexistence. The fluctuations described in the present work are thus attributed to portions of the step edges that retain the $\sqrt{3} \times \sqrt{3}$ structure and are at least a few tens of nanometers distant from any γ-phase domain.

Quantitative measurements of the temporal correlation functions were performed both for surfaces prepared by initial equilibration above 920K (previously reported in Ref. 3 and described in chapter 3) and for surfaces prepared with initial equilibration below 920K. Figure 4.5 shows the temporal correlation functions extracted from time-dependent STM images taken for surfaces initially equilibrated below 920K. Each curve is the result of averaging correlation functions for 4-7 line-scan images similar to figure 4.2a. Data are fit to a power law of the form shown in equation 3 except at long times (not plotted) where there were insufficient statistics to give a smooth curve. The average dynamic exponent from the power-law fits to the curves in Fig. 4.5 was found to be z = 3.7 ± 0.3, nearly a factor of 2 larger than for the uniform phase[21].

4.5 Discussion

The observed scaling of the temporal correlation function with approximately the ¼ power of time, as presented above, is normally associated with rate-limiting diffusion along the step edge[1, 3] and modeled with the linear Langevin equation,

$$\partial_t x(y,t) = -\frac{\tilde{\beta}\Gamma_h}{k_B T}\nabla^4 x(y,t) + \eta_c(y,t) \qquad (4.6).$$

Γ_h is the hopping mobility along the step edge[4], $\tilde{\beta}$ is the step diffusivity, and the noise has correlations that conserve average step position. The hopping mobility is a kinetic parameter that is inversely related to an effective hopping time constant τ_h through

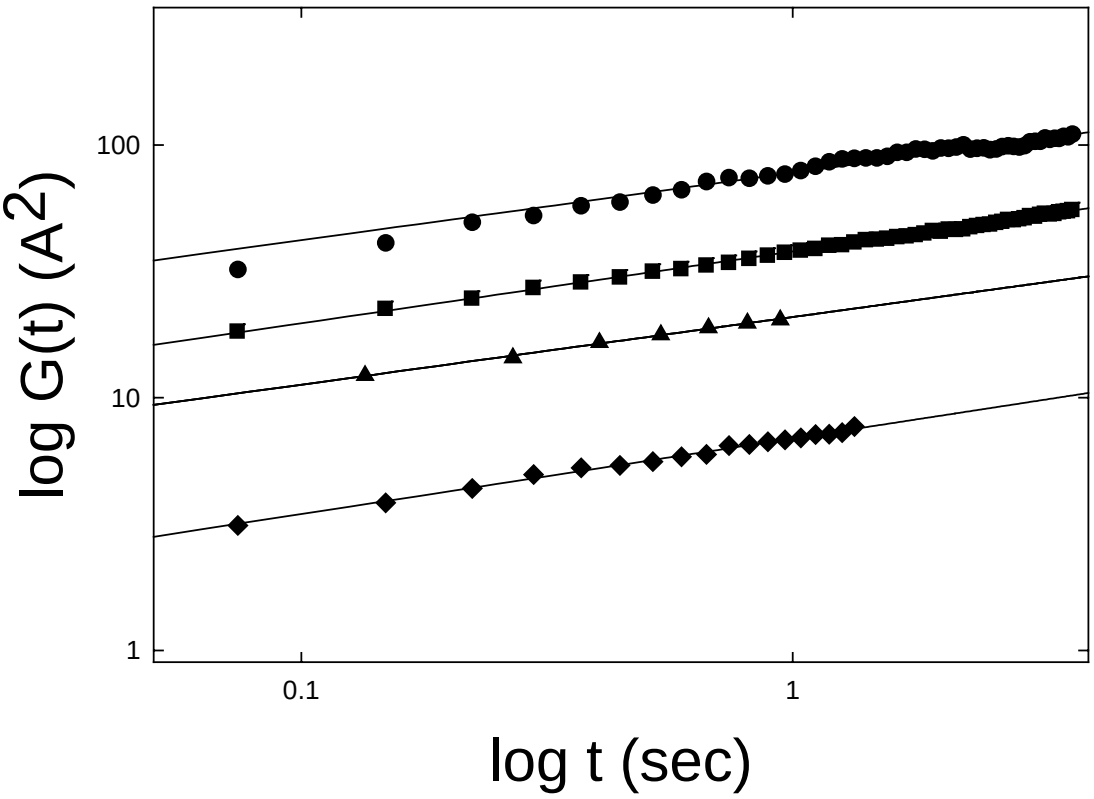

Figure 4.5 Temporal correlation function for different temperatures: circles 970 K, squares 920 K, triangles 820 K, diamonds 770 K.

$\Gamma_h = \frac{a_p^2 a_n^3}{\tau_h}$, where a_p and a_n are parallel and normal projections of the surface unit cell along the step, respectively[4].

Given the generic transport modes limiting the kinetics, the underlying energies and time constants governing step motion can be extracted from fits to the time correlation function. In particular, the exact form of the correlation function resulting from equation 7 is[1, 3, 4, 23]

$$G(t) = 0.78\left[\left(\frac{b^2}{a_p}\right)^3 \Gamma_h\right]^{1/4} t^{1/4} \qquad (4.7).$$

From fits to the experimental data, the prefactor can be used to extract the mobility and corresponding energy scale governing the fluctuation kinetics if an independent determination of the step diffusivity can be made. If care is taken to avoid convolving temporal and spatial information, this quantity can be measured from the spatial correlation function of the (stationary) step edge using Eq. 4.5 as already shown in chapter 3. In the phase-separated case however, as noted above, gamma-phase nucleation sites locally immobilize the step edge. These features would result in a contribution to the roughness that is not due to the thermal meandering of the step and therefore would overestimate the diffusivity. Since the time-correlation measurements were only made far from the nucleation sites where the step structure remains pure $\sqrt{3} \times \sqrt{3}$, it is reasonable to use the diffusivities previously measured for this phase for evaluating the prefactor of Eq. 4.7[69]. These values are listed in the second column of Table 4.1.

The temperature-dependent prefactors for the time correlation function, c(T), extracted by a fit to the data of Fig. 4.5, are listed in the third column of Table 4.1. The

Table 4.1 Kinetic parameters from temporal correlation functions in figure 4.5.

T (K)	b^2/a (Å)	c(T) ($Å^2/s^{1/z}$)	Γ_h ($Å^5/s$)	τ_h (ms)
970	.79	63.1	8.7×10^7	$2.4x10^{-1}$
920	.69	37.9	1.7×10^7	$1.2x10^{-1}$
870	.56	20.9	2.9×10^6	$7.3x10^{-1}$
770	.45	6.9	6.7×10^4	32

mobility and time constant extracted from these values are listed in the 4th and 5th columns. The time constants for hopping along the step edge vary from 2.4×10^{-1} ms at 920 K to 32 ms at 770K, indicating a rate-limiting step almost an order of magnitude faster than for the attachment/detachment process measured for the homogenous $\sqrt{3} \times \sqrt{3}$ phase. An Arrhenius plot of the measured prefactors on the phase-separated surface (column 3 in Table 4.1) is shown in figure 4.6. From equation 4.7, the slope of the linear fit to these points is equal to ¼ ($E_h + 3\varepsilon_k$), where ε_k is the effective kink energy of ~ 0.2 eV [17] and E_h is an effective step edge hopping activation energy. The slope of -0.66 eV in Fig. 4.6 gives an effective activation energy for diffusion along the step edge of 2.0 ± 0.1 eV [40]. This value is comparable to the corresponding attachment/detachment energy scale of 1.9 eV measured for the uniform $\sqrt{3} \times \sqrt{3}$ phase. Based on this comparison one can speculate that attachment/detachment transition states may be triggered by the breaking of similar chemical bonds as transition states involved in step-edge diffusion.

The obvious question that then arises is: What causes the apparent crossover from evaporation/condensation (EC) limited kinetics on a uniform surface to step edge diffusion (SED) limited kinetics on $\sqrt{3} \times \sqrt{3}$ domains of a surface where gamma has nucleated? Given the current understanding of the kinetics of formation of the γ phase[67, 72] as involving the consumption of 1ML of Si to form the lower part of a (1x1) bilayer and the substitution of 0.68 ML of Al to form the upper part, the global changes occurring during phase separation can be assessed. Obviously forming the lower half of

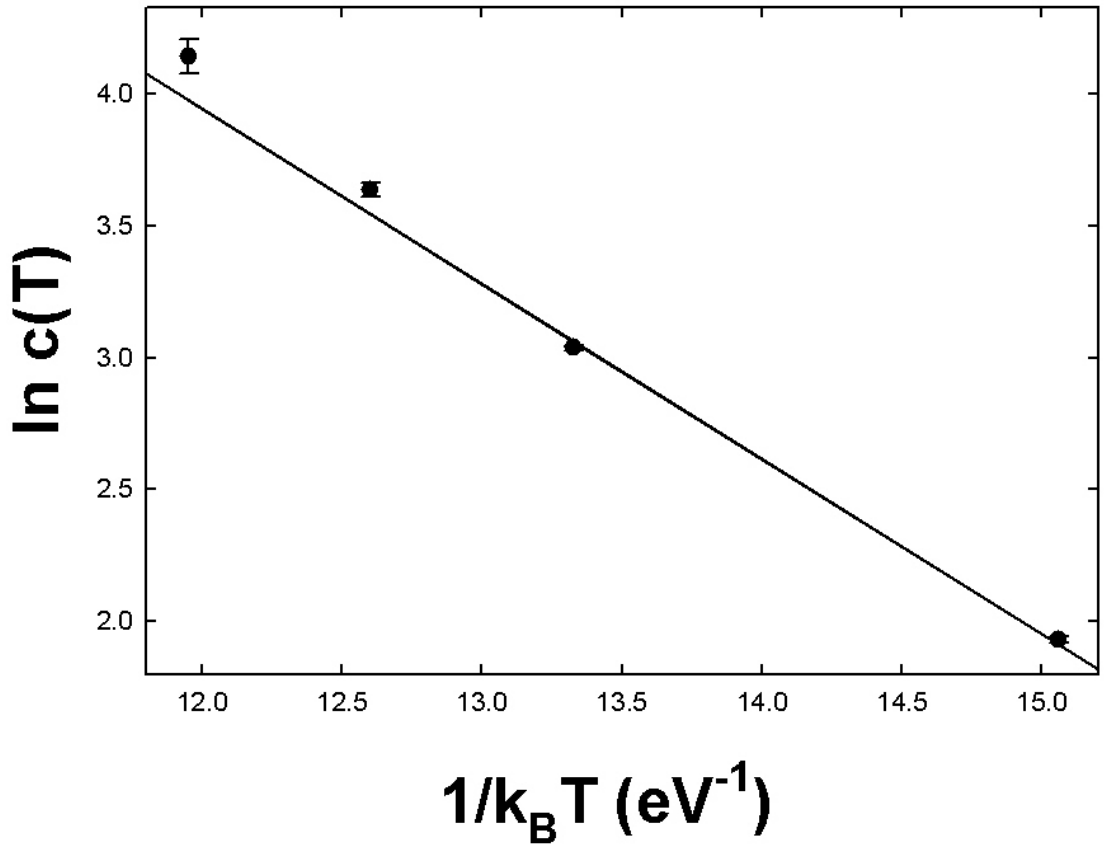

Figure 4.6 Arrhenius plot of prefactors of the temporal correlation function.

a bilayer is most likely at a step edge[72]. Locally however, the concentration of Al in the $\sqrt{3} \times \sqrt{3}$ overlayer at the step edge cannot provide sufficient material to complete the γ-bilayer and mobile Al on the terraces must therefore diffuse to the step edge and make up the difference. Thus, the major change brought about by the growth of the γ phase must be the consumption of mobile species containing Al. This explains the "etching" of step edges observed both in our experiments and in Ref. 33 as simply the natural response of the step edge to a nonequilibrium defect concentration on the terraces. The step is gradually "evaporates" to restore the concentration to its equilibrium value for the remaining $\sqrt{3} \times \sqrt{3}$ terraces.

The changes in the rate-limiting transport processes can be explained as arising from these proposed gamma-phase-induced changes in the concentrations of such freely diffusing species. Below we will show that this picture, in addition to being qualitatively consistent with what is known about the growth of the gamma phase, is also semi-quantitatively consistent with the theoretical formalism developed by Ihle, Misbah, and Pierre-Louis[5].

We assume that the measured values of z in Eq. 3 for both the pure and phase-separated surfaces correspond to the pure limiting cases described in the discussion. This amounts to considering surface diffusion to be infinitely fast and then addressing how a crossover can occur between rate-limiting EC and SED. Unfortunately diffusion coefficients on Si(111) are not known. Since $t^{1/3}$ scaling is never indicated in our *G(t)* measurements, we believe that the assumption that terrace diffusion is significantly faster than the other processes is acceptable. Furthermore, we have roughly checked, using

plausible diffusion barriers, that including finite diffusion in the treatment below does not qualitatively change the conclusions.

To proceed we simplify the integral expression for *G(t)* derived in Ref. 5 using the assumption of infinite diffusion coefficient and our independent determination of isolated step behavior (see chapter 3). The resulting expression shows how a crossover between the AD (or 2D-EC) and SED mechanisms can occur as the relative edge hopping and attachment mobilities change. It is

$$G(t) = \frac{k_B T}{\pi \tilde{\beta}} \int_0^\infty \frac{1 - \exp\left\{ -t\left(\frac{\tilde{\beta}\Gamma_a}{k_B T} k^2 + \frac{\tilde{\beta}\Gamma_h}{k_B T} k^4 \right) \right\}}{k^2} dk \qquad (4.9).$$

Recall that the attachment mobility, Γ_a, is a macroscopic parameter that is related to a microscopic "rate constant", k, through $\Gamma_a = 2c\kappa\Omega^2$, where c is the ad-species concentration[27]. The edge-hopping mobility has no dependence on the concentration on the terraces, so the effect of the proposed reduction of concentration should, in this approximation, be a proportional reduction of the attachment mobility of the steps. The first step in the numerical evaluation of Eq. 4.9 is to decide what wave numbers k to integrate over. The nature of the line-scan STM imaging means that our experiments do not sample every possible wavelength fluctuation. Instead, only those wavelengths that have substantial time to relax within the imaging time contribute to the measured *G(t)*. This finite imaging time sets the minimum k in Eq. 4.9 while the necessity of maintaining the continuum limit sets the maximum k (about 0.5 $Å^{-1}$). Knowing the step mobilities for the two processes under consideration allows us to roughly estimate what these limits should be. The relaxation time for a fluctuation mode of wave number *k* by an AD process is[15]

$$\tau_k = \frac{b^2 \tau_a}{\Omega^{3/2} a_p k^2} \qquad (4.10),$$

where τ_a is the AD time constant, Ω is the surface unit cell volume (0.191 nm^2) and b^2 is the diffusivity.

We set τ_k to the observation time of a line-scan image and solve for k to obtain an estimate of its minimum as about 0.005 $Å^{-1}$ at 770 K using our measured diffusivities and mobilities and a typical observation time of about 30 s. This corresponds to a maximum sampled wavelength of about 1000 Å. Obviously, at higher temperatures with correspondingly higher mobilities, longer wavelengths will have time to relax in the same time. This dependence will be relatively weak, however, due to the square root taken in solving for *k*, so we will roughly take the temperature effect to be about a factor of 5. An equation for τ_k in the case of edge diffusion can also be written and used in the same way. At least to a factor of 2-5, the range of *k*'s sampled is not different than what is obtained from the AD form.

Thus, we proceed with the numerical integration as follows: using the mobilities measured for the uniform $\sqrt{3} \times \sqrt{3}$ phase and the phase coexsiting with γ, we integrate from 0.005 $Å^{-1}$ to 0.5 $Å^{-1}$ at 770 K and from 0.001 $Å^{-1}$ to 0.5 $Å^{-1}$ at 970 K. Then the AD mobility is reduced below the measured value from chapter 3 to mimic the effect of a reduction in terrace concentration, and the effect on G(t) is monitored for the same range of k. Figure 4.7 shows the results of such a numerical integration for the extreme temperatures of this study. For Γ_a equal to our measured mobilities on the homogeneous surface, the temporal correlation function scales as approximately the square root of time. As Γ_a is reduced, corresponding to the physical process of a reduction in concentration,

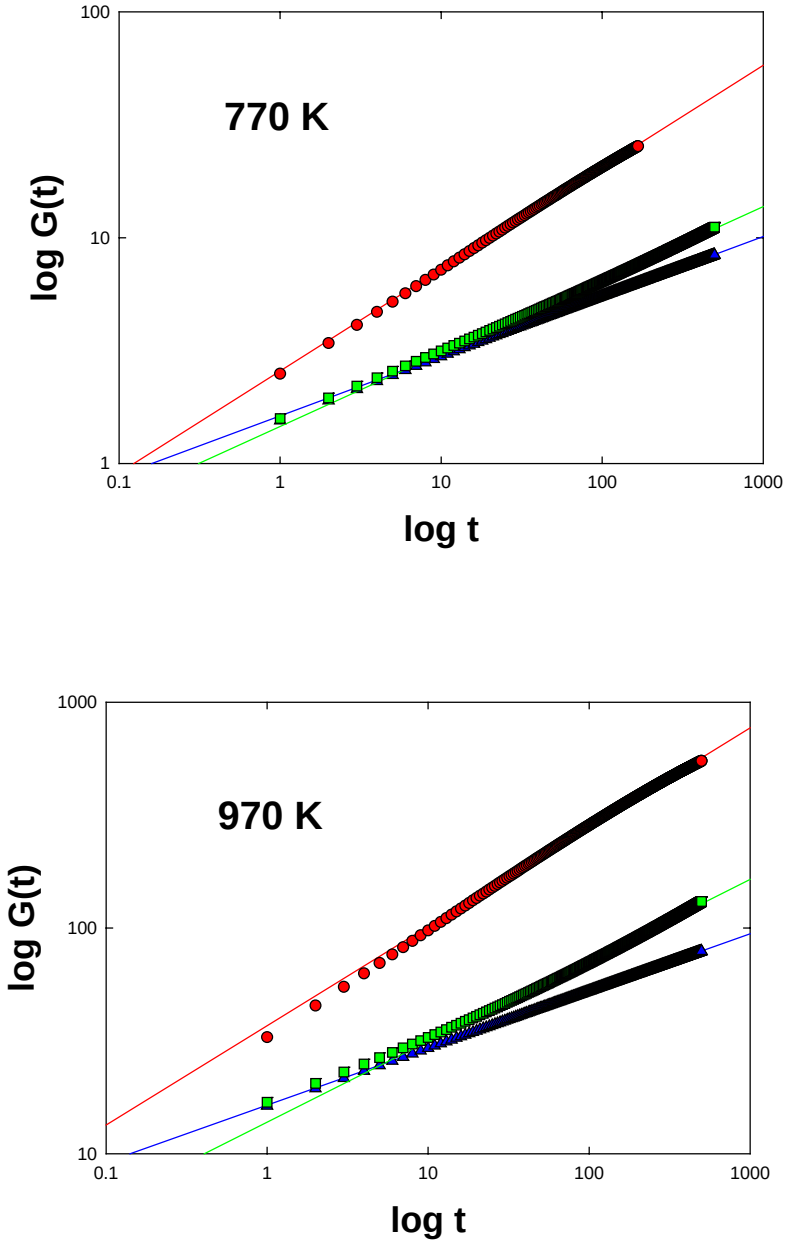

Figure 4.7 Numerical integration of Eq. 4. for the two extreme temperatures of the present experiment. Circles: AD mobility equal to that reported in chapter 3, slope = 0.45 at 770 K and 0.44 at 970 K. Squares (0.32 at 770 K, 0.36 at 970 K) and triangles (0.26 at 770 K, 0.25 at 970 K) : successive reductions in mobility made to model decrease in ad-species concentration.

the scaling of *G(t)* becomes a smaller fraction of time. It passes through values near 1/3 for minor reductions (up to about a factor of 10), illustrating a crossover regime since we have excluded the possibility of isolated step terrace diffusion by assuming an infinite diffusion coefficient. In addition, there is noteable curvature on the double log scales of Fig. 4.7, indicating that in this regime the curves are not true power laws. For large enough reductions in Γ_a, *G(t)* scales with roughly the fourth root of time, consistent with our observations on surfaces with growing gamma domains and with rate-limiting edge diffusion. For 770 K this behavior results after a reduction by a factor of 1000, while for 970 K only a factor of 100 reduction is required. Whether these numerical observations bear any relation to the true reduction in concentration in the experiment is not clear. Naturally for truly quantitative results, finite diffusion coefficients must be considered. Thus, the numerical result are presented only as qualitative confirmation that a reduction in mobile terrace concentration can result in the experimentally measured change in scaling of *G(t)*.

The hypothesis of the depletion of surface concentration as the cause of the observed crossover in step relaxation mechanism is thus consistent with the detailed theoretical model of surface mass transport in Ref. 11. The approximation of infinitely fast terrace diffusion is certainly artificial but, based on the fact that z=3 behavior is two standard deviations from either of our measured exponents, we feel that the conclusions above are acceptable. Nevertheless, it is important to understand the influence of a finite diffusion constant on step fluctuations[17, 21]. This can only be done with independent measurements of the terrace diffusion kinetics on Si(111) - $\sqrt{3} \times \sqrt{3}$ R30º-Al or detailed theoretical calculations of the energetic parameters underlying it.

4.6 Summary and Conclusions

A crossover in measured scaling of the temporal correlation function scaling occurs for a Si(111)- $\sqrt{3} \times \sqrt{3}$ R30º-Al surface when even minor amounts of a second surface phase, γ-Al/Si(111), coexists with it. The change in scaling from $t^{1/2}$ to $t^{1/4}$ indicates a change in rate-limiting transport mechanism from attachment/detachment to step edge diffusion. This can be understood by noting that the formation of the γ phase requires the consumption of Al that can most easily be obtained from the mobile reservoir that is involved in the AD processs. With the depletion of this reservoir, the AD process is suppressed and only SED contributes to the measured correlation functions. Qualitatively, the depletion of the reservoir is also seen in the long-time behavior of step morphology. As the γ phase grows over time scales, much longer than those required to make fluctuations measurements, the steps appear to "etch" as they release mass to restore the equilibrium adspecies concentration on the terraces. In fact, we expect that if fluctuation measurements were made on such an etched step, the AD mechanism might well be observed instead of SED if the concentration were sufficiently recovered.

We were able to obtain qualitative theoretical support, using the theoretical formalism developed by Ihle et al.[5] for the hypothesis that a reduction in terrace concentration is responsible for the change in scaling of *G(t)*. By numerical integration of a simplified expression for G(t), we can reproduce the observed crossover via reductions in concentration by a factor of 100-1000. This suggests that the adspecies reservoir is severely depleted by the coexistence but truly quantitative results require a more complete knowledge of the terrace diffusion process on this surface.

This previously unobserved example of a crossover in fluctuation kinetics provides an important illustration of the true complexity of mass transport at surfaces. In particular, it shows how step fluctuation measurements can only access the rate-limiting transport mechanism even while other mechanisms are also active. From a more speculative point of view, it shows a remarkable sensitivity of surface transport to even minor structural inhomogeneities. Such sensitivity may be important in the burgeoning field of nanotechnology where it could be exploited for purposes of enhanced control or carefully eliminated for purposes of avoiding unwanted changes in transport behavior.

Chapter 5

Fluctuation kinetics of spiral steps on Pb(111) Microfacets

The kinetics of the edge diffusion process on spiral steps generated by a screw dislocation intersecting the (111) plane of a supported Pb crystallite have been studied using variable temperature STM. The temporal correlation function for a single point measurement on these spirals grows as roughly $t^{1/4}$ in the temperature range of 300 K to 390 K. The magnitude of this function allows an estimation of the time constant for edge diffusion and its temperature dependence allows extraction of its effective energy scale of 710 meV. In addition, by studying the fluctuations of rotating spiral steps on crystallites that have been quenched from high temperature, nonequilibrium effects on step fluctuations are addressed. It is observed that the step edge kinetically roughens as it loses mass and therefore the scaling of the step width over relatively long times grows with a power law that is not consistent with the growth of the temporal correlation function. This is attributed qualitatively to the fact that the dynamics of a moving step cannot be conserved and the possibility of describing the motion with more detailed growth models is addressed.

5.1 Introduction

In the previous two chapters, experimental studies of step fluctuations on complicated reconstructed surfaces were described. In the present chapter we return to the investigation of simple, elemental metal surface steps for several purposes. There is always the practical value of determining as many transport parameters as possible for a surface. To that end, we will describe a temperature-dependent study of step fluctuations due to edge diffusion on Pb(111) steps. This will allow the determination of continuum step parameters and effective energy scales. In addition, we will describe a situation in which we are able to study fluctuations on a slowly moving step, thereby experimentally accessing the nonequilibrium physics of a 1D interface.

Step dynamics on Pb(111) single crystals at room temperature were first studied using STM in the mid-1990's by two groups. Speller et al.[63] and Kuipers et al.[65] both observed that the temporal correlation function for step fluctuations grows as approximately $t^{1/4}$, indicative of rate-limiting edge diffusion[1, 3]. Since these experiments were restricted to a single temperature, a detailed quantitative study of the kinetics of edge diffusion was not possible. The first order of business of the present chapter will be to provide this missing information.

The edge diffusion process is rather important in understanding nanometer-scale surface morphology. While it does not play a very significant role in large-scale surface processes, its effect on island morphology and step meandering can be quite dramatic. The mere presence of edge diffusion can determine whether islands will have fractal or compact shapes[74], whether a step can have a meandering instability during growth[75], or even whether a single island can "pinch-off" during its evolution into two separate

islands[76]. Clearly, in order to predict and control two-dimensional morphologies, a quantitative understanding of edge diffusion processes is essential.

After describing the somewhat unusual experimental system employed in the study of Pb(111) steps, we will present temperature dependent results for the temporal correlation function and briefly mention results for the temporal autocorrelation function, as well as the temporal correlation function for *moving* Pb(111) steps. The temporal correlation function results will lead to a discussion of the edge diffusion mobility and its associated effective energy scale. The related autocorrelation function will illustrate the interplay between observation time and the maximum sampled wavelength in an STM experiment as mentioned already in chapter 4. Finally, the nonequilibrium observations on moving spirals will be discussed from the perspective of the theory of 1D interfaces.

5.2 Experiment

Rather than using (111)-oriented Pb single crystals as in previous work[63, 65], we studied spiral steps originating from screw dislocations on (111) microfacets of small supported Pb crystallites. Such crystallites have long been employed as a valuable model system in the study of the statistical physics of solid surfaces[60, 77-79]. In particular, they have provided a remarkable experimental testing ground for the long-established theory of equilibrium crystal shapes[77, 78].

We prepare the supported Pb crystallites on a Ru(0001) substrate by depositing 20-30 nm of Pb at room temperature in UHV (base pressure ~ 10^{-10} torr). The substrate is first cleaned by 5-7 cycles of dosing 300 L of molecular oxygen at 520 K followed by flashing to ~ 1000 K. Figure 5.1a shows an STM image of the resulting substrate

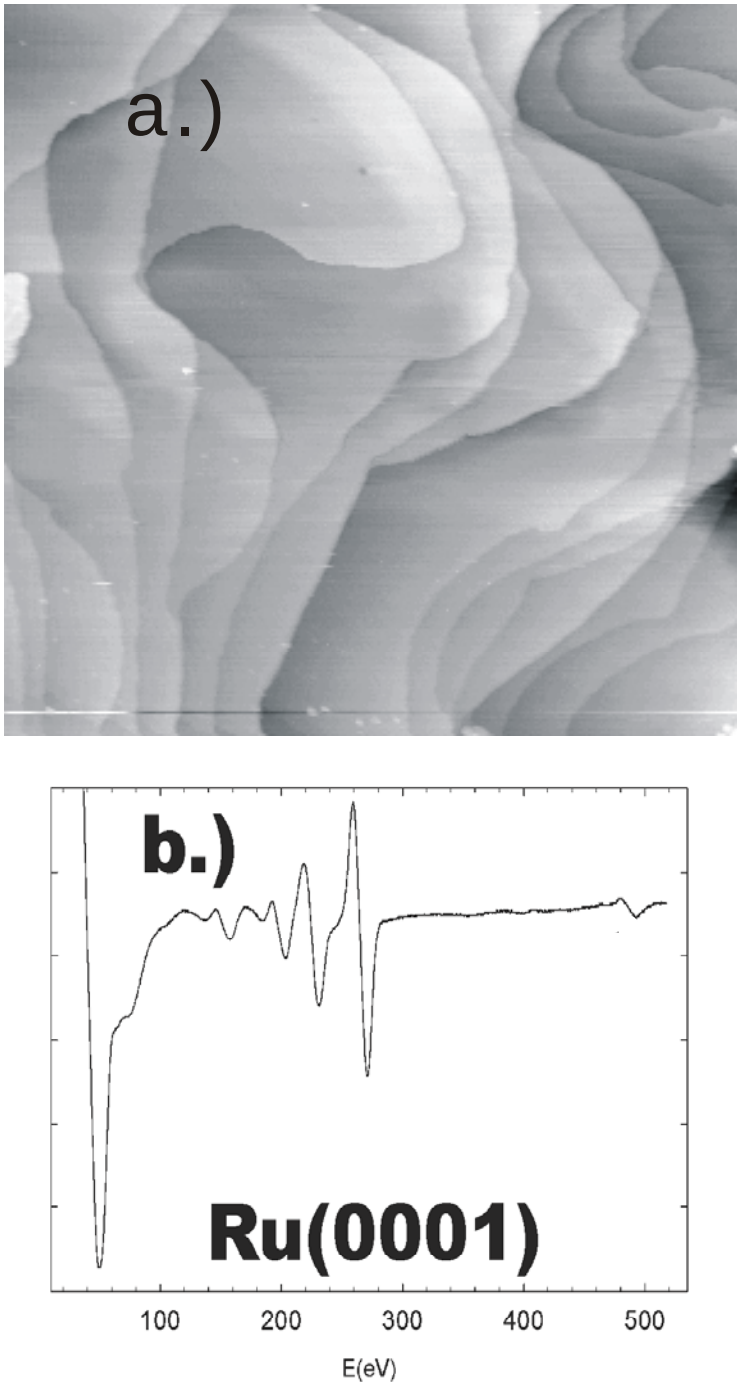

Figure 5.1 a.) 300 nm STM image of Ru(0001). b.) Representative Auger spectrum.

morphology and 5.1b shows a representative Auger pattern showing residual surface oxygen as the only minor contaminant. After depositing the continuous Pb film at room temperature, the entire sample is heated to the melting point of Pb (600 K) and held there until it is visually observed to have melted. Because of the low vapor pressure of molten Pb, it stays on the surface in the form of liquid droplets. These droplets are frozen by cooling the sample to below the melting point of Pb and then quenched to a temperature (300 K-420 K) where surface transport processes can be conveniently observed with STM.

The resulting frozen Pb crystallites are nearly all topped with perfect (111) facets as shown in figure 5.2a, and very often have other facets visible on their sides[60]. A small percentage of the crystallites (5-30 % depending somewhat on cooling rate and annealing time just below the melting point of Pb) have one or more screw dislocations intersecting the (111) facet as shown in Fig.5.2b. Since such a dislocation results from a distortion of the crystal lattice parallel to the dislocation line, when it intersects a surface, a step emerges[2]. The steps spiral around the core of the dislocation until they meet the area vicinal to the (111) plane and are constrained by step repulsions. Like most steps on metal surfaces, these spiral steps exhibit frizziness associated with fast atomic motions at their edges even at room temperature. We performed standard fluctuation measurements using line-scan imaging as described in detail in previous chapters. A typical pseudo-image showing the time evolution of a single point on a spiral step edge at 320 K is shown in figure 5.3. We note that, because of the well-documented severity of tip-sample interactions on Pb(111), we always used fairly mild tunneling conditions of typically 30 pA and 300 mV (corresponding to a gap resistance of 10 GΩ). We also

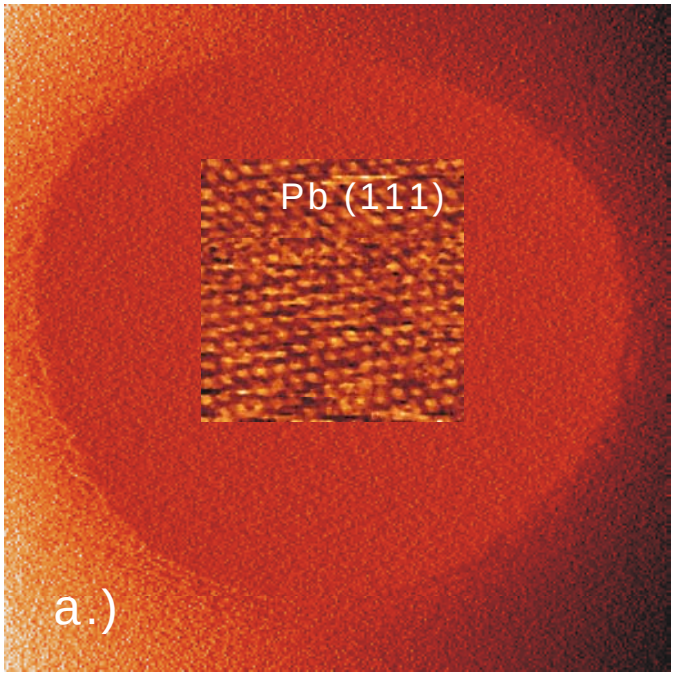

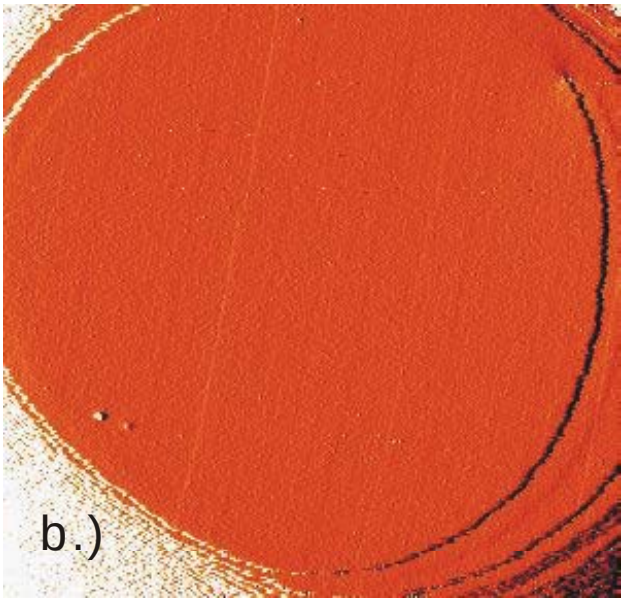

Figure 5.2 a.) Perfect (111) microfacet (350nm x 350 nm) with an example of an atomically resolved STM image in the inset. b.) STM image (475 nm x 475 nm) at 320 K of a (111) facet with a single screw dislocation. Both images differentiated for clarity.

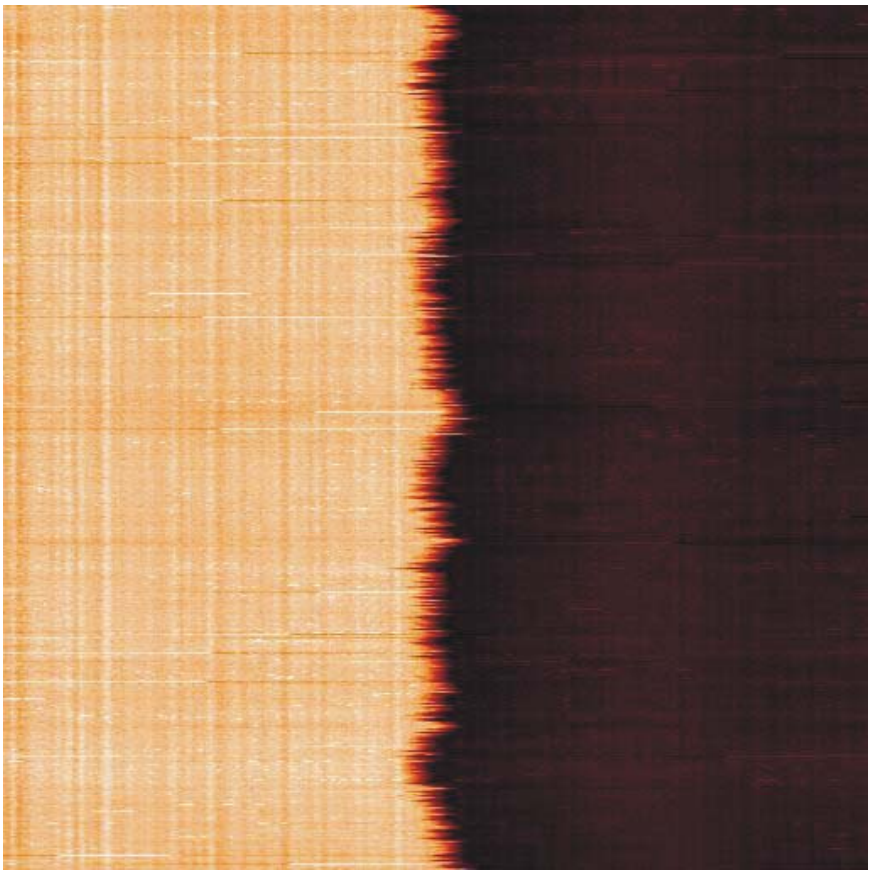

Figure 5.3 STM pseudo image of a fluctuating spiral step on a Pb(111) microfacet at 320 K. Total imaging time is 24 s and the lateral scan range is 67.2 nm.

changed the tunneling current by an order of magnitude and found that it had no noticeable effect on our results. Furthermore, we checked that the results presented below were independent of scan rate (with the exception of the autocorrelation function) and scan direction.

Typically, we observed fluctuations many hours after quenching of the crystallites so that overall motion of the steps due to thermal reshaping had stopped. Sometimes, however, we made fluctuation measurements soon enough after the quench that the spiral steps were still slowly rotating around the dislocation core in response to the abrupt temperature change (see chapter 8 for more details about this rotation). In this situation, we could make line scan images during the slowest part of the spiral rotation in an effort to understand non-stationary effects on the step fluctuations.

5.3 Results

In figure 5.4 the averaged temporal correlation functions from the line-scan measurements on Pb(111) spiral steps are plotted on a double log scale. Each curve is the result of averaging *G(t)* from at least 6 and up to 26 separate line scan sequences of varying duration. The solid lines are linear fits to the data, the slopes yield the experimental exponent of the correlation function. The thick dashed line is the theoretical prediction of $t^{1/4}$ scaling for pure step edge diffusion. Clearly all the data are in good agreement with this prediction. Figure 5.4 shows one temperature sweep (made over the course of several days and surveying many crystallites). We took data at each temperature 3-5 times (i.e. we made several of these sweeps in temperature) and used the

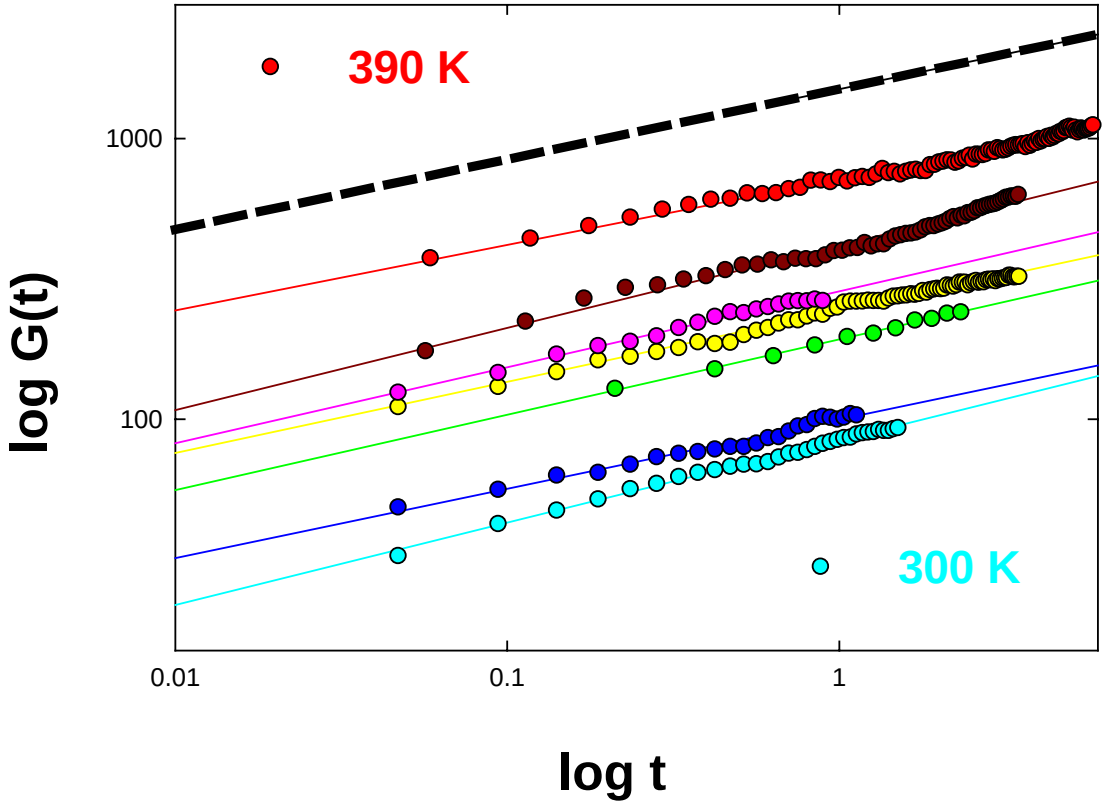

Figure 5.4 Temporal correlation functions for different temperatures (top to bottom): 300 K (light blue), 320 K (blue), 330 K (green), 335 K (yellow), 350 K (pink), 370 K (dark red), 390 K (red). Dashed line is the SED prediction of $t^{1/4}$ scaling.

scatter at a given temperature as a measure of the experimental uncertainty in the determination of *G(t)*.

As a brief aside, we present in figure 5.5 the result of computing the temporal autocorrelation function for some of the fluctuation data taken at 320 K. The autocorrelation function is defined by:

$$C(t) = \langle x(t + t_0)x(t_0) \rangle \qquad (5.1),$$

where the average is, as usual taken over all initial times. For linear Langevin equations, such as the one describing SED, the analytic form of *C(t)* is known exactly. We plot only the early time points of *C(t)*, which should decay as a power law, for line scan data sets of different durations in figure 5.5 since the later time data display large statistical fluctuations. The solid lines are fits to a three-parameter power law. Note that the curves, though taken at the same temperature *and on the same spiral step*, are offset from one another by nearly a factor of two.

Finally we present the results for the fluctuations of a slowly rotating spiral. We computed the temporal correlation function as usual for a spiral at 390 K during a very slow part of its rotation. A full rotation of the spiral took just over 20 minutes and a set of 6 line scan images took roughly 7 minutes to complete. This corresponded to only about one quarter turn of the spiral. Figure 5.6a shows *G(t)* for this set of six images on a double log scale. In this figure, each set of data points comes from only one line scan image and is therefore not as smooth as the averaged curves in figure 5.4. Despite this, there remains good agreement with the SED prediction of $t^{1/4}$ scaling (represented by the heavy dashed line in the plot). Remarkably however, there is a clear and rather large increase in the magnitude of *G(t)* as the spiral rotates. In addition to G(t), we also simply

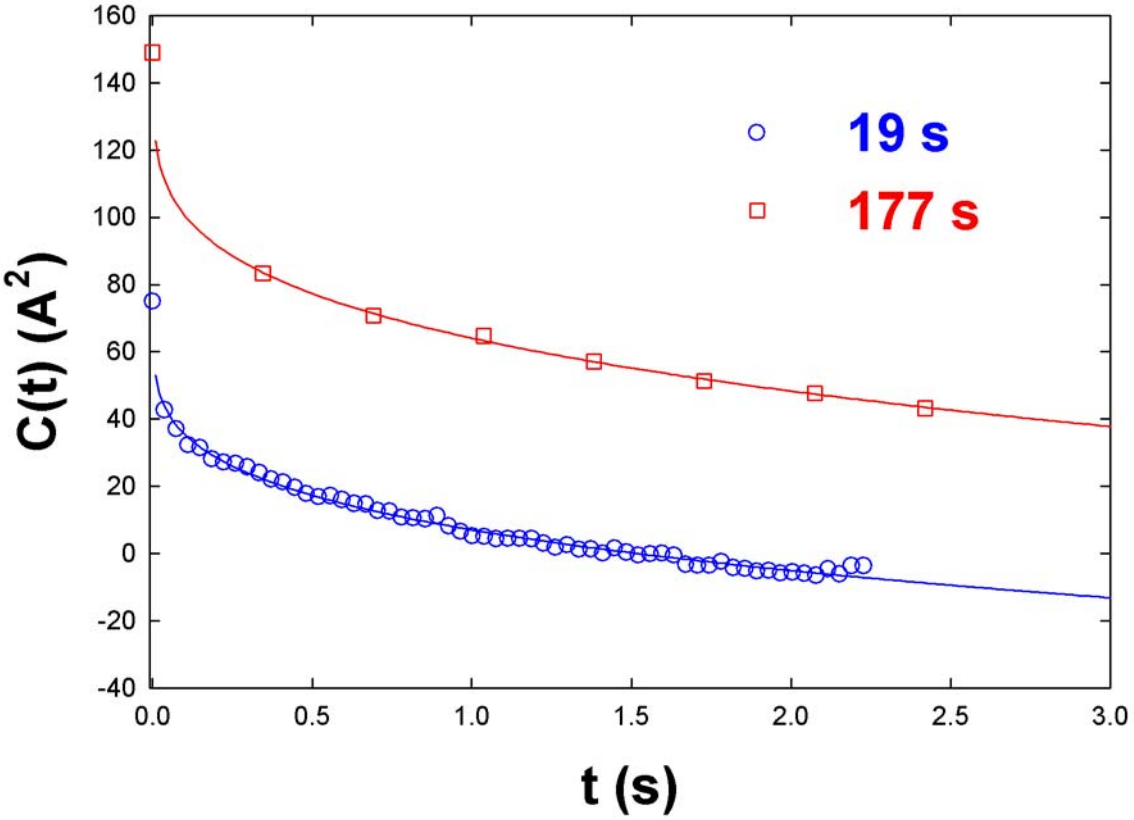

Figure 5.5 Autocorrelation function for the same spiral step at 320 K taken using different total imaging times.

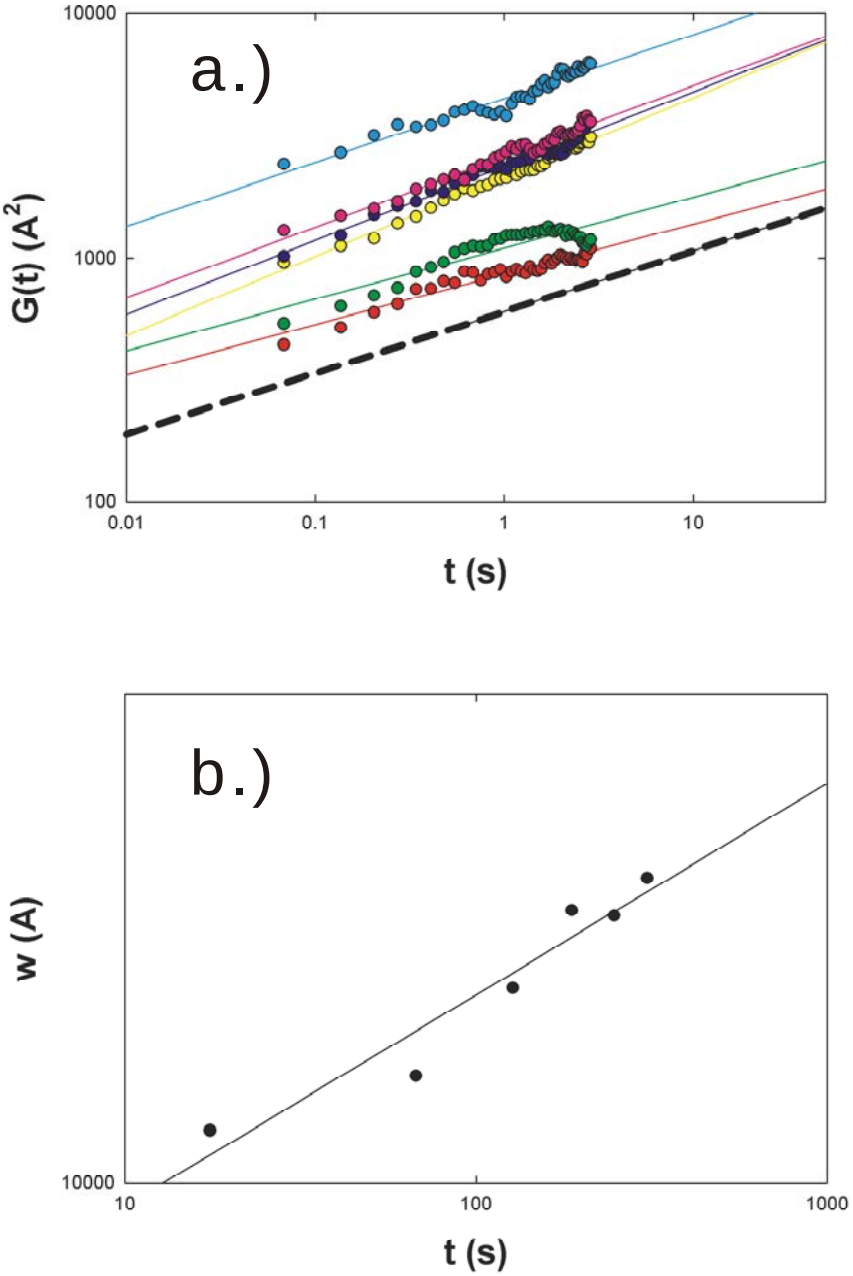

Figure 5.6 a.) Temporal correlation functions measured during spiral rotation. b.) Time-averaged step widths from the same set of images.

computed the standard deviation of the step position in each of the six time-images in the sequence. We plot this quantity as a function of time on a double log scale in figure 5.6b. It fits to a power law with an exponent of 0.30±0.05.

5.4 Discussion

5.4.1 Near equilibrium step kinetics

The temporal correlation function results for spiral steps suggest the same edge-diffusion limited fluctuations as observed for steps on Pb(111) single crystals at room temperature[63, 65]. This is no great surprise; the spiral steps have a rather gentle curvature that is certainly not significantly more than the typical curvature of a step on the single crystals studied in the past. Between 300 K and 390 K, the rate-limiting mechanism is clearly SED for steps on Pb(111). At temperatures above 390 K our measurements indicate a possible crossover from SED to AD limited kinetics but nothing further will be said about this possibility here.

We focus our attention on the lower temperature SED kinetics in an attempt to quantitatively characterize the edge diffusion process. Figure 5.7 shows the edge hopping time constant obtained from the measured prefactors of the temporal correlation function. These are extracted as described in chapter 4. The time constants, compiled in Table 5.1, vary from about 0.8 μs at 300 K to about 0.7 ns at 390 K and have very large error bars due to the fourth root in the expression for *G(t)* (this results in the error in τ_h being a factor of four larger than the error in c(T) itself). Figure 5.7a shows the time constants plotted versus temperature and figure 5.7b shows them plotted in an Arrhenius

Table 5.1 Summary of prefactors of the temporal correlation function and the SED time constants derived from them. Use is made of a kink energy of 0.05 eV[7] and the formula for step stiffness on a triangular lattice derived by Akutsu and Akutsu[80].

T (K)	c ($Å^2/s^{1/z}$)	Δc ($Å^2/s^{1/z}$)	τ_h (μs)	$\Delta\tau_h$ (μs)
300	83	10	.8	.4
320	121	6	.4	.2
330	193	20	6×10^{-2}	2×10^{-2}
340	294	64	1×10^{-2}	1×10^{-2}
350	249	73	3×10^{-2}	3×10^{-2}
370	362	71	8×10^{-3}	6×10^{-3}
390	769	147	7×10^{-4}	6×10^{-4}

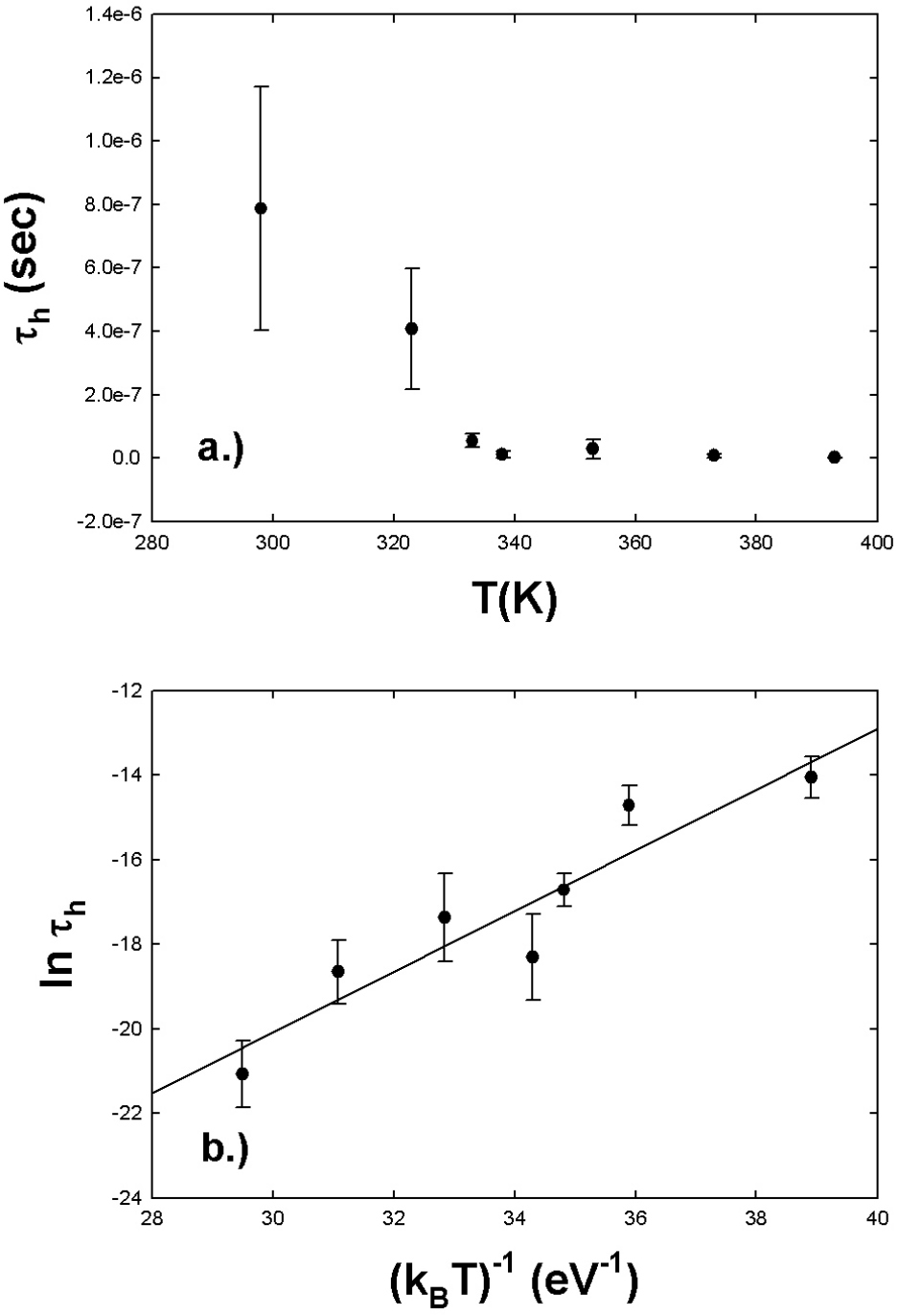

Figure 5.7 a.) Edge hopping time constant versus temperature for Pb spiral steps. b.) Time constants plotted in an Arrhenius plot.

plot. The slope of the Arrhenius plot gives an effective activation energy for the SED process of 0.71±0.08 eV and the intercept gives an effective attempt frequency of $10^{18\pm3}$ Hz.

The activation energy is not unreasonable, especially when it is recalled that it is an *effective* scale that may well be comprised of several separate hopping processes. For comparison, the same energy scale on Pt(111) is 1.50±0.16 eV[61]. Given that Pb melts at a much lower temperature than Pt, the trend in effective SED barriers is as expected. Interestingly, the ratio of the barriers is nearly the ratio of the Debye temperatures for the two metals[81]. This is not a generally applicable rule of thumb, however, since the SED energy on Cu(111) is actually smaller (0.3 eV)[3] than that on Pb(111) even though its Debye temperature is higher. Once again, this simply reminds us that we are working with a continuum step model, and indeed making mesoscale as opposed to atomic-scale observations. Thus, the energy extracted from G(t) most likely corresponds to some form of collective motion.

The complexity underlying the SED kinetics embodied in Fig. 5.7 is further emphasized by the magnitude of the apparent attempt frequency for the process. Even taking into account the enormous uncertainty (a factor of 1000) in this parameter, it is significantly higher than the typical phonon frequency of 10^{12} Hz that would be naively expected for thermal activation. The simplest explanation for this observation comes from an appeal to the complete expression for the rate processes from transition state theory. In this theory, the *entropy* of the transition state (i.e. the configuration of atoms at the saddle point of the potential energy curve for a given process) contributes to the rate of the process as follows[82]:

$$\frac{1}{\tau} = \frac{k_B T}{h} \exp\left(\frac{\Delta S^*}{k_B}\right) \exp\left(\frac{-\Delta E^*}{k_B T}\right) \qquad (4.2).$$

In this expression, the asterisks represent differences between the transition state and the initial state and h is Planck's constant. ΔS^* is thus the entropy difference between the starting configuration and the transition state, and can account for deviations from the canonical $k_B T/h$ attempt frequency. For many simple *atomic* hopping events on a surface, the effect of entropy is thought to be negligible,[82] and attempt frequencies are in the Terahertz range. However, recent studies of more complicated processes involved in so-called "long jumps" on surfaces suggest that entropy can play an important role in surface mass transport[83] and lead to attempt frequencies of up to 10^{18} Hz.

In fact, this seems to be the case for the mesoscale edge diffusion processes often studied by STM techniques. For SED kinetics on both Cu(111)[84] and Pt(111)[61], apparent attempt frequencies are large enough to suggest entropy factors of 10-100 in Eq. 4.2. Using the current experimental data, there is no good way to speculate on the details of the transition states that are involved in edge diffusion processes. Certainly, it is conceivable that such states could have significantly more vibrational degrees of freedom than an atom incorporated in a perfect step edge. However additional work, both experimental and theoretical, is necessary to unravel this complicated issue. Once again we point out, however, that lack of detailed microscopic information does not lessen the value of the continuum step picture we have developed. The attempt frequencies and activation energies can simply be taken as *mesoscale* parameters that allow the computation of time constants for edge diffusion in the temperature range from 300 K to 390 K.

After having discussed our measurements of the kinetics of edge diffusion on Pb(111), it is appropriate to compare with the results obtained in the past at room temperature[63, 65]. While we certainly obtain agreement with previously reported work on the qualitative nature of the rate-limiting transport process involved in Pb(111) fluctuations, there is remarkable disagreement between the kinetic parameters extracted from the different studies. From the measurements at 300 K presented here the prefactor of G(t) is 80±10 $Å^4$/s. By inspection of the *G(t)* curve presented by Speller and co-workers[63], we find a prefactor of about 18 $Å^4$/s from the value of the curve at t = 1 s. Similarly, from the plots in Kuipers et al.[65], we obtain a prefactor of 650 $Å^4$/s. Of course, our measurements are performed on steps emanating from screw dislocations on very small facets, and one could speculate that comparing to the prior work is not even sensible. As stated earlier however, there seems to be little reason to think that the spiral steps are substantially different than steps on a good single crystal. The facets have large diameters (200-1000 nm) and thus allow the curvature of the spiral to be comparable to the curvature typically seen on steps on metal single crystals. In addition, the dislocation core can be merely thought of as a kind of pinning site, and these features are also present on single-crystal surfaces. We were not able to detect a significant difference in correlation functions measured at different positions on the spiral relative to the dislocation core, so it seems that is effect on the fluctuations should not be very significant.

It is difficult to speculate about the reason for the disagreement on room temperature prefactors between the three sets of measurements. In the work of Speller et al.[63], we note that the figure showing fluctuating steps seems to show a relatively small

step spacing (about 50 Å) and that this may limit the amplitude fluctuations that can be seen and make the measured prefactor smaller than our measurements on relatively isolated spirals. This would also explain the tendency toward saturation in their *G(t)* plots for times greater than about 1.5 seconds. Such saturation was never clearly observed in our data, but was also observed by Kuipers et al.[65]. This group made extremely high-speed STM measurements and observe a leveling off of *G(t)* after only 0.1 s. The prefactor suggested by their plots is enormous, and may be the result of sampling only extremely short wavelength fluctuations. These fluctuations would quickly saturate in amplitude, but why they would result in such a high prefactor is not clear. The only other plausible explanation is that the apparently high SED mobility is the result of the well-documented tip-sample interactions on Pb(111)[85]. In other words, it is possible that the observed edge diffusion is actually tip-assisted in Ref. 85.

Finally, we discuss the unexpected result that autocorrelation functions extracted from observations of fluctuations of the same spiral differ in magnitude by a factor of about two when the total observation times differ by a similar magnitude. The exact form for the early time correlation function can be expressed as:

$$C(t) = C(0)\left[1 - \Gamma\left(\frac{3}{4}\right)\left(\frac{t}{\tau_c}\right)^{\frac{1}{4}}\right] \qquad (5.4)$$

where τ_c is called the correlation time and is proportional to the effective length of the step to the fourth power. This is important because, as we saw in the last chapter, the effective length of a very long surface step is set by the longest wavelength mode that has time to decay in the observation time of the pseudo-image. Thus, the apparent correlation time will be significantly longer for the 177 s data set than the 19 s data set. This leads to

the discrepancy in the *C(t)* curves presented in the results section, and the quantitative agreement between the expected offset and the measured one is good. Luckily, *G(t)* does not suffer from this effect as will be discussed more completely in chapter 7.

5.4.2 Fluctuations of a rotating spiral

It is of course possible to naively extract time constants for edge diffusion from the temporal correlation functions shown in figure 5.6. For the first two images, the time constants are consistent with the static 390 K data to within the error bars. As the spiral continues to rotate, however, the apparent time constant decreases to significantly smaller values than expected for a static spiral at the same temperature. Smaller average spiral radii correspond to later images in the sequence. Is the increase in time constant simply a curvature effect? This is not likely to be the case since, in the process of sampling many static spiral steps, we often made fluctuation measurements on steps with comparable curvatures. Instead we propose that the behavior observed on the rotating spiral steps is the result of the interplay between the conservative SED process (see chapter 1) and the nonconservative process driving the rotation. In essence, on long time scales, the step is undergoing what is known in growth models as *kinetic roughening* as mass evaporates from its edge. On shorter time scales, the dynamics of the step looks approximately conserved, i.e. the temporal correlation function grows as $t^{1/4}$, but there is a progressively larger contribution of the nonequilibrium roughening effect to the *magnitude* of the temporal correlation function.

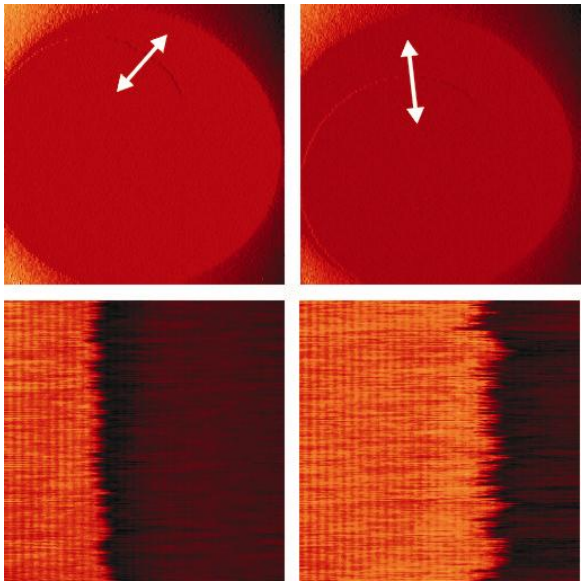

Figure 5.8 Left: Approximate spiral shape (1000 nm x 1000 nm) corresponding to the line scan in the lower pseudo-image (35 s x 150 nm). The spiral configuration 7 minutes later, showing roughening of the step (same image and pseudo image scales). In the short time (~30 s) required for a line scan image, step edge position appears to be approximately conserved, but over the several minutes it takes to obtain the sequence of images nonconserved step dynamics becomes visible in the growth of the mean-squared step width. This roughening effect can be seen by inspection of the line scan images. White arrows in the upper images show approximate positions on the spiral where line-scans were made.

Here we show the first and last images in the sequence of 6 images already mentioned alongside spatial images taken later. The spatial images roughly correspond to the configurations of the spiral when the corresponding line-scan images were obtained. In any event, the line scan image taken on the more highly curved spiral displays remarkably larger amplitude fluctuations than the earlier image, demonstrating that the step is roughening.

Given that the apparent growth exponent calculated from *w(t)* is nearly 1/3, there are several alternative growth models for nonconserved step dynamics in this case. Such a growth exponent actually characterizes the famous KPZ equation in 1D[86]. Unfortunately, this model is not very realistic since it does not include conservative edge diffusion-like terms. The observed growth exponent is also consistent with an even more complicated nonlinear growth model suggested by Lai and Das Sarma[87]. The Langevin equation for this model reads:

$$\partial_t x(t) = -\nu\nabla^4 x(y;t) + \lambda\nabla^2\left|\nabla x(y,t)\right|^2 + \eta(y,t) \qquad (5.5),$$

where η is a white noise in space and time. It has been widely used as one of the simplest models of nonlinear kinetic roughening[14]. While the width data presented above is certainly consistent with this model, it may be naïve to simply accept it in the absence of other scaling exponents or physical arguments as for the terms present. As it stands, we merely suggest the Lai-Das Sarma model as a possibility and suggest that slowly moving steps may provide a useful experimental system for the study of nonlinear interface dynamics.

In fact the scaling of the width over long times may simply be an indication of a crossover in fluctuation mechanism as a function of time for the very specific situation

where the step is emitting mass. In any case, it is clear that the behavior is the result of the interplay between conserved and nonconserved dynamics and should be understandable within some suitable continuum model.

5.5 Summary and Conclusions

We have shown that the previously observed[63, 65] step edge diffusion mechanism that governs fluctuations of Pb(111) steps at room temperature is also the rate-limiting mechanism at temperatures up to at least 390 K. Furthermore, we have quantified the edge diffusion kinetics and found that the time constant for the process varies from about 0.8 ms at room temperature to 0.7 ns at 390 K. An Arrhenius plot of the time constants yields an effective energy scale for the process of 0.71 eV with a very large attempt frequency which we attribute to entropy effects in the potentially microscopically complicated transport of mass along the step edge.

We also studied fluctuations of a slowly moving spiral step. Scaling of the temporal correlation function indicates that edge diffusion remains important for short time intervals but the step is observed to roughen kinetically over longer intervals. This increases the apparent magnitude of $G(t)$ and also seems to mask the conserved dynamics associated with edge diffusion. We find a growth exponent for the roughening process of about 0.3, consistent with both the KPZ and Lai-Das Sarma models of 1D interface dynamics. Unfortunately, there is no independent support for either of these models and we cannot rule out the possibility that the growth exponent observed is a only manifestation of some crossover effect due to the loss of conserved dynamics.

The detailed study of the simple system described in this chapter clearly demonstrates that understanding mesoscale mass transport remains an important problem. Even a process as simple as edge diffusion on Pb(111) seems to be riddled with microscopic uncertainty. Nevertheless, working within a continuum step model we find that it is possible to develop a practical and quantitative understanding of this process. As shown by Giesen on Cu(111)[28], this type of quantitative understanding is directly transferable to predicting the evolution of morphology and is therefore the most appropriate level of description for nanometer-scale mass transport.

Chapter 6

Fluctuations of Pb/Si $\sqrt{3}\times\sqrt{3}$ -(1x1) Domain Boundaries

The fluctuating boundaries between coexisting Si(111)- $\sqrt{3}\times\sqrt{3}$ R30°-Pb and Si(111)-(1x1)-Pb phases are studied using VTSTM. At temperatures below the (1x1) desorption regime, $t^{1/3}$ scaling of the temporal correlation function indicates rate-limiting surface diffusion. In the (1x1) desorption regime there is a change in scaling of the temporal correlation function to $t^{1/2}$. Based on observations of local surface disordering due to the desorption process, the change in functional form is attributed to the coupling of the boundaries to nearby defects rather than a true change in rate-limiting surface transport process. We estimate the effective surface diffusion barrier associated with these transport processes and address its relation to prior studies of mass transport in this system.

6.1 Introduction

The success of the continuum step model suggests that other linear defects on surfaces may be treated using a similar formalism. One example of a common linear surface defect is a domain boundary between two coexisting surface phases. Mass transport at such a boundary will clearly govern the kinetics of surface phase transitions[88]. In addition, understanding the physics of domain boundaries is likely to be relevant for unraveling relations between nanoscale structure and elastic or electrical transport properties at surfaces. For example, nanometer-scale statistical mechanics of dislocation networks in thin films has recently been an important subject of research[89].

In this chapter, we describe the application of the Langevin formalism used in the previous chapters to the fluctuations of domain boundaries between two phases of Pb on Si(111). Pb on Si(111) is a much-studied prototype of a nonreactive metal-semiconductor interface. It displays a host of interesting properties from Schottky barriers[90] to quantum size effects[91, 92]. Its phase-formation diagram is fairly complicated[93]. There are many different surface reconstructions that can form at different combinations of Pb coverage and depostion (or annealing) temperature. We will concentrate on the coexistence between a high-density Si(111)-(1x1)-Pb phase and the typical Si(111)- $\sqrt{3}\times\sqrt{3}$ R30 –Pb phase that occurs for nominal Pb coverages around 1 ML and temperatures between 520 K and 770 K. An STM image of a typical surface showing phase coexistence is presented in figure 6.1. More sample preparation details will be described in the following section. For now we note that the boundaries between these phases have been a topic of interest for many years[94-100]. The mobility of the

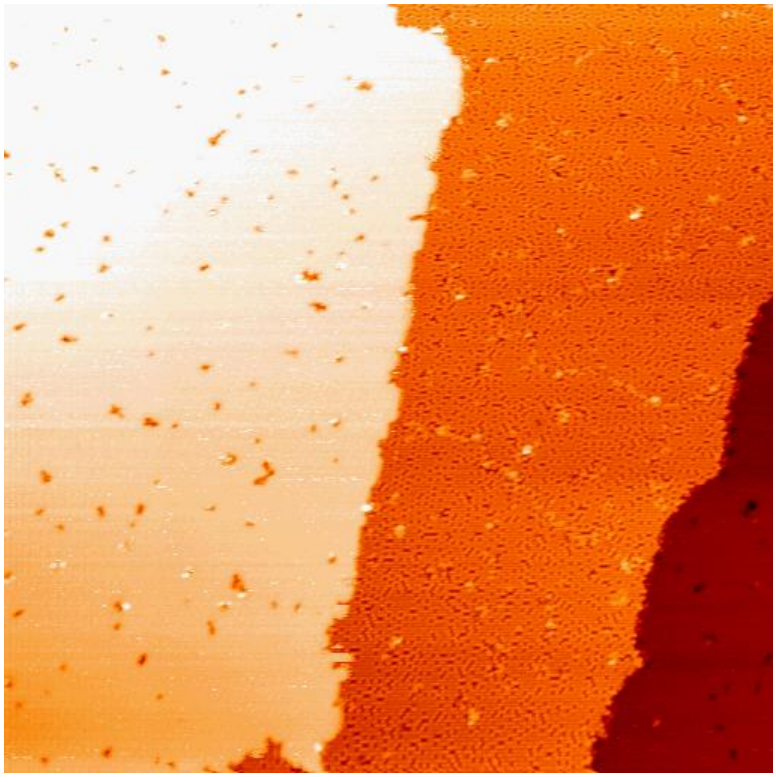

Figure 6.1 100 nm image taken at room temperature of a domain boundary. The bright area on the left is the (1x1) phase and the darker area with point defects is the $\sqrt{3}\times\sqrt{3}$ phase.

boundaries is notable even at room temperature. Recent studies[100] have attempted to understand the motion of the boundaries from a continuum interface perspective somewhat different from the Langevin formalism we will pursue in what follows. The most important mass transport studies have however been performed using traditional desorption studies[94, 96, 98]. From these studies a simple picture of the desorption of the high-density (1x1) phase has emerged. Thermal desorption kinetics have been found to be zeroth order[94, 96, 98], indicating that the rate of desorption is independent of the amount of the phase on the surface[101]. This implies that the rate-limiting step in the process is something other than the simple exchange of Pb atoms between the (1x1) phase on the surface and the vapor phase. It was proposed by Saitoh et al. that there was rapid exchange of Pb atoms between the (1x1) phase and a two-dimensional adatom gas on the lower density $\sqrt{3}\times\sqrt{3}$ phase[98]. This could lead to the observed kinetic order and similar situations have been found to govern desorption in systems involving $\sqrt{3}\times\sqrt{3}$ phases on other metal-Si(111) sytems[102]. We will see in what follows that such a picture of mass transport on the Pb/Si(111) surface has useful and testable consequences for the local fluctuations of domain boundaries.

Before discussing the results however, the experimental system will be described in some detail. The results will then be presented and discussed with particular attention paid to the relationship to the earlier desorption studies. In addition, the discussion will address important issues in temperature-dependent crossover effects for interface fluctuations and the exciting question of how to relate mesoscopic continuum step parameters to microscopic details of atomic transport.

6.2 Experiment

The Si(111)-(7x7) substrates were prepared by the same procedure described in chapters 3 and 4 and appendix A. They were cut from n-type wafers misoriented about 0.4º toward the $[2\bar{1}\bar{1}]$ direction and mounted in a commercial sample holder (Omicron) where they could be heated by direct current. After the standard cleaning of the sample and flashing to about 1500 K to produce the (7x7) reconstruction, the sample temperature was calibrated with an infrared pyrometer. We correlated sample heating current, which is controlled in the Omicron VTSTM, with pyrometer readings and judged them to be accurate to about 20 K in the range 520 K to 870 K.

Pb was deposited onto a room temperature Si(111)-(7x7) substrate from a heated alumina tube evaporator with a water-cooled copper shield. The flux was calibrated with a quart crystal microbalance (Inficon) and we usually deposited 1-1.4 ML of Pb. In this chapter all ML are referred to the number of atoms in a Si(111) plane: $7.8\text{x}10^{14}$ cm^{-2}. This means that Pb-(1x1) is a superstructure of Pb that has the bulk-terminated Si surface lattice constant. Next, the Pb-deposited Si sample was annealed at 600 K –700 K for 2-6 minutes until a $\sqrt{3}\times\sqrt{3}$ pattern was observed by LEED in addition to the (1x1) pattern by moving the electron beam laterally across the sample: There was always one end of the sample that was clamped more strongly to the sample holder and therefore not as effectively heated. This end maintained the simple (1x1) LEED pattern while the hotter end developed a $\sqrt{3}\times\sqrt{3}$ pattern.

After checking LEED, the sample was then transferred to the VTSTM stage (Omicron) where it was imaged to ascertain useful domain structure and overall cleanliness and order at room temperature. If the surface seemed unsuitable for domain

boundary fluctuation studies (for example if the (1x1) phase covered too much of the surface making the $\sqrt{3}\times\sqrt{3}$ domains too small) then the sample was further annealed at 600-700 K until room temperature STM showed a useful domain structure. Basically, this means a structure where the domain boundaries between (1x1) and $\sqrt{3}\times\sqrt{3}$ were long enough that it was possible to perform line-scan imaging without the tip drifting off of the boundary.

The (1x1) phase begins to desorb rapidly at about 600 K according to our observations of the total surface area covered by this phase over time using VTSTM. There have been reports that slower desorption occurs at temperatures as low as 480 K[100] but we did not find any evidence for this. Most thermal desorption experiments have been performed between 650 K and 750 K[94, 96, 98, 103]. We made line-scan type STM measurements of the domain boundaries (which in fact look like surface steps in STM images since the (1x1) phase sits higher than the $\sqrt{3}\times\sqrt{3}$ phase) in two temperature regimes. First, we studied the fluctuations of the boundaries above 600 K where the (1x1) phase is desorbing (as observed by the slow reduction in percentage of covered area). Then we made the same kind of measurements below 600 K where desorption was not observed. The two temperatures at which we made measurements in this study were measured to be 570 K and 620 K by infrared pyrometry. Thus, working just barely in the desorption regime, our fluctuation measurements were made on a time scale very much shorter than the time required for noticeable desorption of the (1x1) phase. A set of line scan images was obtained in several minutes while a decrease in (1x1) coverage was not noticeable for 30 minutes to 1 hour. Figure 6.2a shows a line-scan image taken at 570 K while figure 6.2b shows a line-scan from 620 K.

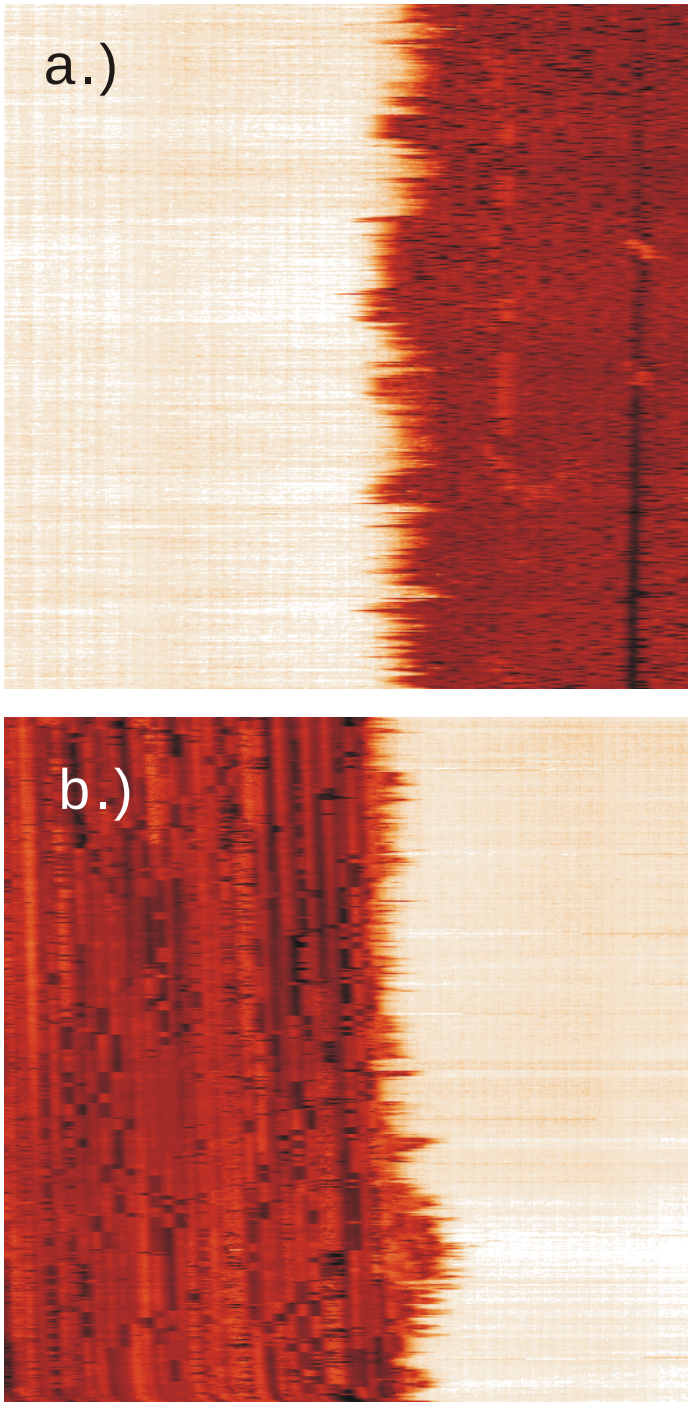

Figure 6.2 a.) 23 sec line scan taken at 570 K. Lateral range is 28 nm, 0.04 nA tunnel current. b.) 29 sec line scan at 620 K. Lateral range 28.3 nm, 0.15 nA tunnel current.

Clearly, the boundary is fluctuating significantly at both temperatures. In the next section we will present the detailed fluctuation statistics at the different temperatures.

6.3 Results

The most useful characterization of a fluctuating interface in the Langevin formalism is the real-space temporal correlation function *G(t)*, which measures the growth of the local interface width as a function of time. Briefly, we recall its definition in terms of an average over all possible initial times in a line-scan STM image:

$$G(t) = \left\langle \left[x(t + t_0) - x(t_0) \right]^2 \right\rangle \qquad (6.1)$$

In figure 6.3, we plot experimental temporal correlation functions for domain boundary fluctuations both above and below 600 K. On the double logarithmic scale of the figure, both curves show straight line behavior indicating power law growth in time of *G(t)*. The first three points of each curve are omitted from the plots and fits in figure 6.3. They were observed to grow approximately linearly in time as expected for the independent diffusion of kinks in the domain boundary. In other words, at short times, the continuum step approximation seems to have broken down for the small lateral-scale pseudo images shown in figure 6.2. Beyond these points, power law growth was clear.

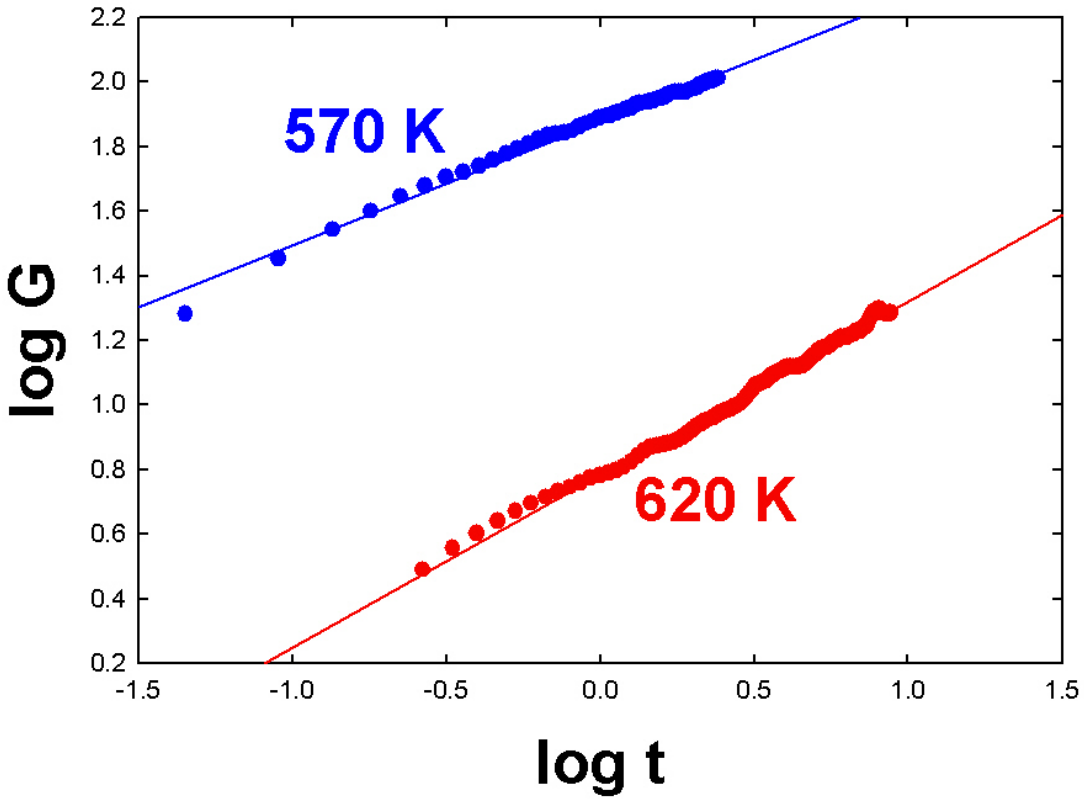

Figure 6.3 Temporal correlation functions for different temperatures on a double log scale. Solid lines are least-squares linear fits to the data whose slope gives the scaling exponents. The 570 K curve is the result of averaging correlation functions from 13 line-scan images and the 620 K curve is the result of averaging from 7 images. The exponent for 570 K is 0.38±0.04 and for 620 K it is 0.59±0.05.

We point out two distinguishing features of the correlation functions in figure 6.4. First, the slope of the solid fit line below the desorption temperature is smaller than the slope above the desorption temperature indicating growth with a different power law. Below the desorption temperature, G(t) grows with a power of time equal to 0.38±0.04. The higher temperature curve grows with a power law exponent equal to 0.59±0.05. Perhaps more remarkably, the magnitude of the temporal correlation function *decreases* as the temperature is *increased* above the desorption temperature. At 620 K the prefactor from the intercept of the solid fit lines is 7.0±0.2 $Å^2/s^{0.59}$ while at 570 K it is 76±1 $Å^2/s^{0.38}$. This result is fairly counterintuitive, since we have seen in previous chapter that the prefactor of *G(t)* depends on linear kinetic parameters that are typically thermally activated. Both fit parameters clearly indicate fundamental differences in mass transport in the high versus the low temperature regime.

6.4 Discussion

From chapter 1, we recall that power law growth of the temporal correlation function is expected for three limiting cases of surface mass transport for isolated steps. In the case of steps that correspond to the domain boundaries under consideration in the present chapter, we find clear experimental evidence of power law growth in both the low and high temperature regimes. The generic form of the correlation function for these limiting cases is:

$$G(t) = c(T)t^{\alpha} \qquad (6.2).$$

The value of the exponent α was shown in chapter 1 to be ½ for attachment/detachment limited kinetics, ¼ for periphery diffusion limited kinetics, and $^1/_3$ for terrace diffusion (i.e. just usual surface diffusion) limited kinetics. From the last section we see that the

simplest interpretation of the experimental correlation function scaling at low temperatures with $t^{1/3}$ is that the boundary fluctuations are limited by surface diffusion. As described in chapter 3, the scaling of *G(t)* with the ½ power of time is much more difficult to interpret. Naively, we might consider a crossover to AD-limited kinetics at 620 K. This type of crossover is however not physically reasonable given the surface diffusion limited kinetics at lower temperature. For such a situation, AD processes must already be faster than surface diffusion and increasing the temperature should only make them faster. In figure 6.4, we show an STM image that suggests an alternative. At 620 K, desorption apparently results in the local disordering of the $\sqrt{3}\times\sqrt{3}$ phase at random locations around the surface[104]. Such a disordered region would act as a "sink" for diffusing Pb atoms in the sense described recently by Flynn[17]. If a Pb atom meets one of these sinks before it returns to the step edge, then it will be immobilized and the effect on G(t) will be the same as that described in the Diffusion Step to Step case[5, 6, 16, 55] of chapter 3: it will scale as $t^{1/2}$. In figure 6.4, we see that there are disordered regions of the surface within several nanometers of the (1x1)/$\sqrt{3}\times\sqrt{3}$ domain boundaries at 620 K.

Despite an apparent crossover in fluctuation mechanism, surface diffusion on the $\sqrt{3}\times\sqrt{3}$ phase is rate-limiting in both temperature regimes. In the desorption regime however, the environment of diffusing species changes enough to change the scaling of *G(t)*. In effect, the phase boundaries are no longer isolated but rather diffusively coupled to surface defects nearby. Zero-order desorption kinetics typically implies the existence of a 2D gas on the surface with which the interface or step can exchange mass[1]. This is certainly consistent with our fluctuation experiments. At low temperatures, rapid exchange between the phase boundary and the terrace occurs that keeps the interface in

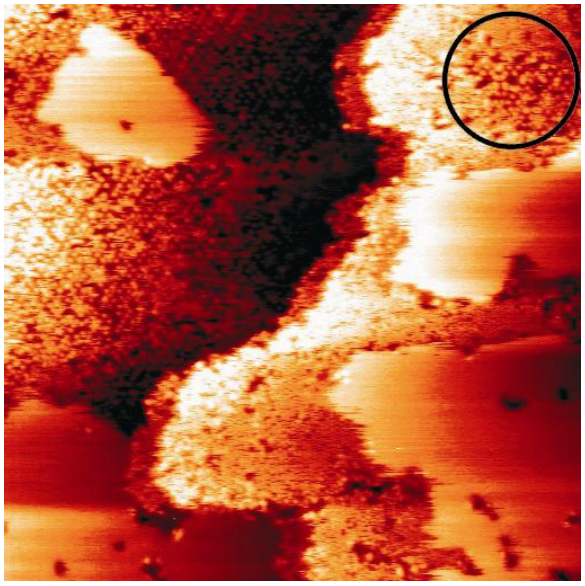

Figure 6.4 STM topograph (50 nm x 50 nm) taken at 620 K with a disordered region labeled. The brightest areas are (1x1) domains and are mostly separated from the disordered regions by $\sqrt{3} \times \sqrt{3}$ regions.

equilibrium with the 2D vapor phase. The rate-limiting transport process is the diffusion of Pb in this phase. When desorption occurs, the same picture holds with the only modification being the presence of regions near the step that can trap diffusing atoms before they return.

Using the prefactor of *G(t)* at 620 K we can attempt to understand the kinetics of surface diffusion in this system. The correlation function for DSS is:

$$G(t) = \sqrt{\frac{16cD\Omega^2 k_B T}{\pi^3 L\tilde{\beta}}} \qquad (6.3)$$

The surface diffusion coefficient *D* and adatom concentration *c* refer to the $\sqrt{3}\times\sqrt{3}$ phase and the interfacial stiffness refers to the boundaries. We have not independently measured the stiffness of the domain boundaries. Most likely it is not very large, otherwise the boundaries would not fluctuate so strongly at such moderate temperatures. For purposes of comparison with desorption results, we will focus on estimating from our data the sum of the effective diffusion barrier, adatom formation energy, and the kink formation energy. We use an Arrhenius form for the quantity *cD* given by[4]:

$$cD = \nu \exp\left(\frac{-(E_{diff} + E_{form})}{k_B T}\right) \qquad (6.4),$$

where ν is an attempt frequency (typically ~ $k_B T/h$), E_{diff} is the surface diffusion barrier, and E_{form} is the adatom formation energy. The step stiffness is given in terms of the kink energy ε by:

$$\frac{\tilde{\beta}}{k_B T} = \frac{2}{3a}\exp\left(\frac{\varepsilon}{k_B T}\right) \qquad (6.5).$$

Combining the prefactor, determined from fits in the last section, with these results allows us to compute the sum $E_{diff}+E_{form}+\varepsilon = 1.6 \pm 0.1$eV.

The activation energy for thermal desorption was determined by Saitoh et al.[98] to be 2.31±0.06 eV. The value determined here is in better agreement with the results of Nakamura et al.[97] for the *potential barrier to desorption* due to ion-irradiation. They determined this quantity to be 1.8±0.1 eV. Of course, our determination of the effective activation energy from data taken at only one temperature cannot be expected to be as accurate as results made over a broad temperature range. It would be preferable to make the same measurements over a range of temperatures and extract the energy from an Arrhenius plot. Unfortunately, at much higher temperatures than used in this experiment, desorption is so fast that making fluctuation measurements by STM would not be possible. In addition, at much lower temperatures, the accuracy of the sample temperature is expected to be poor and the step fluctuations so slow that statistics will not be good. Thus, the moderate agreement (30-40%) between our energy and that determined by Saitoh et al.[98] is perhaps as good as can be expected.

At 570 K, where surface diffusion is the rate-limiting process, we can make a quantitative estimate in the same way as above. In this $t^{1/3}$ case, the prefactor of G(t) is:

$$c(T) = 0.86\left(2cD\left(\frac{k_B T\Omega}{\tilde{\beta}} \right)^2 \right)^{\frac{1}{3}}, \qquad (6.6)$$

where Ω is the atomic volume of the surface unit cell, c is the adatom concentration, and D is the surface diffusion coefficient. The product, cD, will be assumed to have the same form as in Eq. 6.4. Again, we can't separate the kink energy, so from the experimental prefactor we can extract the sum $E_d+E_f+2\varepsilon$ = 1.3±0.1 eV. This number is not in very good agreement with the comparable sum of energies determined from the 620 K experiment. Given the rough nature of the data analysis in both cases however, we

consider the result acceptably consistent. In particular, the choice of the attempt frequency of k_BT/h is almost certainly too simplistic in both temperature regimes. Hibino and Ogino have observed that an exchange process on the $\sqrt{3}\times\sqrt{3}$ surface of Pb/Si has an attempt frequency that is significantly dependent on local Pb coverage. Such an effect could very easily be operative on the surfaces described here and more extensive observations spanning several temperatures and Pb coverages are necessary to understand the kinetics of surface diffusion in more detail. Interestingly, the activation energy to Pb/Si exchange was found by Hibino and Ogino to be 1.2 eV, consistent with the effective surface diffusion barrier that we determined at 570 K. We can thus speculate that the microscopic process involved in the interface fluctuation is surface diffusion by an exchange process.

Before concluding, we note that the observation of a surface diffusion mechanism for step (or interface) fluctuations is remarkably rare. For many years, it was not seen at all. Recently it has been reported for apoferritin steps[105], Cu(111) steps in acid solution[106], and, at long last, at very high temperatures on clean Pd(111), Pt(111), and Mo(110)[20]. Our observations represent the first determination of this mechanism for a metal-semiconductor interface in UHV. More importantly, the rough kinetic analysis that we have performed is an experimental extraction of the surface diffusion kinetics on the Si(111)- $\sqrt{3}\times\sqrt{3}$ R30-Pb surface. Such kinetics could be checked by first principles calculations[93].

6.5 Summary and Conclusions

By analyzing the temporal fluctuations of domain boundaries between Si(111)-(1x1)-Pb and Si(111)- $\sqrt{3}\times\sqrt{3}$ R30-Pb we have observed a change in scaling of the temporal correlation function from $t^{1/3}$ at temperatures below the onset of desorption to $t^{1/2}$ at temperatures above the onset. We attribute this change to a change in the immediate environment of the boundaries rather than a change in rate-limiting transport process. In both temperature regimes, the rate-limiting process is simply surface diffusion but in the desorption regime the boundaries are no longer isolated but exchange mass with nearby defective surface regions formed as a result of the desorption process. In contrast, at low temperatures, the only place to capture diffusing mass is the boundary itself. From both temperatures in this study, we estimated the effective diffusion barrier and found it to be between 1.2 and 1.7 eV. The assumptions used in extracting this estimate were undoubtedly over-simplified and increasing the precision of the barrier will require further experiments.

The most important conclusion of this work is the qualitative agreement between our local fluctuation measurements with STM and more traditional desorption measurements. Both result in a picture of rapid exchange of mass with a dilute 2D gas existing on the $\sqrt{3}\times\sqrt{3}$ phase as an essential intermediate step in desorption. This agreement is very important in demonstrating the general value of continuum step parameters, not just for understanding interface fluctuations, but also for a basic understanding of surface mass transport. In addition, the estimation of effective energy scales governing the processes described in this chapter should provide added insight into the microscopic origin of the continuum step parameters particularly if support from first-principles calculations can be obtained.

Chapter 7

Persistence and Survival Probabilities for Fluctuating Steps: Nontrivial Scaling and Experimental Subtleties

Two different, nontrivial first-passage statistics are determined from experimental step fluctuation data on a wide variety of surfaces. Si(111)- $\sqrt{3} \times \sqrt{3}$R30º-Al and Si(111)-(1x1)-Pb domain boundaries, with fluctuations that have the same scaling of temporal correlations, have persistence exponents of nearly ¾ in agreement with numerical predictions. The phase-separated Al/Si surface and Pb(111) spiral steps have persistence exponents of about $^7/_8$ in agreement with predictions for the edge-diffusion Langevin equation and corresponding S.O.S. models. All systems studied display roughly exponentially decaying survival probabilities indicating the Gaussian nature of the underlying stochastic processes. Surprisingly, neither persistence nor survival seems to have a measurable dependence on material-specific parameters. Instead, the absolute magnitudes of these quantities are determined by the time resolution of the experiment and the total measurement time in the case of survival.

Some material published in:

1.) Dougherty et al., Phys. Rev. Lett. 89 (2002) 136102.

2.) Dougherty et al., Surf. Sci. 527 (2003) L213.

3.) M. Constantin et al., Phys. Rev. Lett 91 (2003) 086103.

4.) Dasgupta et al., Phys. Rev. E 69 (2004) 022101.

7.1 Introduction

In previous chapters we have employed spatial and temporal correlation functions and average widths to characterize step fluctuations. These quantities are essentially the standard quantitative tools of statistical physics and have remarkable power. Their primary use is to allow the extraction, within the context of the appropriate models, of thermodynamic and linear kinetic parameters governing surface morphology and transport. Of course, despite the overwhelming importance of such information, there are statistical questions about step fluctuations (or any stochastic process) that it cannot address. Ultimately, correlation functions are determined by a small number of moments of the full probability distribution for the random process. It is not hard to imagine that more detailed information could be valuable.

One instance where a small number of moments are not sufficiently descriptive is that of first-passage problems (see chapter 1). For example, what is the probability that a random walker reaches a point *x for the first time* at time *t*? The problem, though exactly solvable for simple random walks, requires a knowledge of *all* moments of the distribution function[30, 107]. When we consider complicated, spatially extended stochastic systems like surface steps, exact theoretical results are nearly non-existent[31].

For steps on surfaces, theoretical interest has focused on two types of first-passage statistics: persistence and survival probabilities[32, 108, 109]. The persistence probability is the probability that an interface has *not returned* to its initial configuration up to a time t. In other words, the interface fluctuation has *persisted.* Formally we can write persistence for an interface as[32]

$$P(t_0,t) = prob\{x(y,s) \neq x(y,t_0) \forall t_0 < s < t_0 + t\} \qquad (7.1).$$

Here *x(y,t)* is the continuous random variable describing the interface (or step) height (or x position) at time t. This expression is useful in developing a method for computing persistence probability from experimental data that will be described in the following section. Numerical studies of interface fluctuations (and many other stochastic processes[31]) have shown asymptotic power law decay of the persistence probability. Letting t_0 become very large in Eq. 7.1 we get:

$$P(t_0 \to \infty, t) = p(t) \sim t^{-\theta} \qquad (7.2)$$

where θ is a new dynamic critical exponent called the persistence exponent[31, 32]. The scaling in equation 7.2 has been observed in several experimental systems[108, 110-114] and a significant number of numerical studies[31, 32, 115-118]. There is some imbalance between the number of experimental tests of the usefulness of the persistence idea and the number of theoretical studies. In the present work, we take advantage of the experimental ability to monitor the stochastic motion of surface steps to help remedy this imbalance.

The persistence exponent is an independent characterization of the dynamic universality class of a stochastic process as mentioned in chapter 1. Furthermore, the notion of θ can be generalized to obtain an infinite family of exponents associated with interface fluctuations. The existence of such a family suggests a remarkable depth to the notion of universality for stochastic models. The generalization is obtained by defining the "sign" of the interface height as $S(t)=sgn[x(y,t+t_0)-x(y,t_0)]$. If we then average this value over a time interval and define the probability of persistent large deviations[116] as $P(t,s) = prob\{S_{av}(t') \geq s, \forall t' \leq t\}$, the parameter *s* defines a continuous set of exponents $\theta(s)$ so that $P(t,s) \sim t^{-\theta(s)}$. Such a family was first obtained theoretically by Dornic and Godreche for the Ising model with Glauber dynamics[116].

The survival probability is a slight modification of the persistence probability in that it asks for the probability of not crossing a specified reference level up to time t. We can write this idea formally as

$$S(t) = prob\{x(y,s) \neq x_0 \forall s < t\} \qquad (7.3),$$

where x_0 is a fixed reference level (most often the average interface position). The fundamental difference between survival and persistence is that survival is computed with respect to an *absolute* reference whereas persistence is computed with respect to a the initial point relative to a specific time interval (note dependence on t_0 in Eq. 7.1). This ultimately results in a faster decay of survival than persistence. In fact, the survival decays exponentially in time instead of as a power law:

$$S(t) \sim \exp\left(-\frac{t}{\tau_s}\right) \qquad (7.4).$$

Here τ_s is the survival time constant that characterizes the rate of its decay.

First-passage type questions have clear practical potential for addressing issues of stability and reliability of nanofabricated objects that may show significant structural fluctuations. For example, we might attempt to judge whether Al or Cu were the more reliable material with which to make connections in some future nanocircuit where first-passage might mean the utter failure of the circuit due to shorting. In this case it is necessary to know how the persistence and survival probabilities depend on material-specific parameters like step stiffness, mobility, or surface diffusion coefficient. One of the major goals of this work is to understand this very practical materials science side of first-passage. Ultimately, we will conclude that experimental subtleties of sampling

create serious problems for quantifying the material-dependence of persistence and survival and that great care is required in interpreting such measurements.

In the following sections the method for computing persistence and survival probabilities from STM data will be described in detail. We will then present experimental persistence and survival measurements from all of the experimental systems mentioned so far in this thesis as well as a demonstration of the infinite family of exponents for the case of uniform Si(111)-$\sqrt{3}\times\sqrt{3}$ R30-Al. Next we will show that the dependence of the magnitude of these quantities on material parameters like step mobility is completely masked by the discrete-time sampling of the step fluctuation process. Finally, the implication of these results for the future value of persistence and survival measurements is addressed.

7.2 Experiment and Data Analysis

Line-scan STM data obtained on the experimental systems described in detail in chapter 2 through chapter 6 of this work was used to compute persistence and survival probabilities. Thus, no further experimental details will be provided and we will proceed directly to a description of how to compute these statistics from STM pseudo-images. Naturally, the step position as a function of time was digitally extracted from the images (see chapter 2) so that we begin our analysis with a time series of step positions denoted by *x(t)*.

In the initial theoretical study of Krug and co-workers of persistence for interfaces, probabilities were easy to compute by counting the fraction of “persistent” sites (non-returning sites) on the lattice set up for the SOS simulation or the numerical

integration[32]. For a time series, where we are only monitoring one site on the step edge, this is not possible. Instead, the probability must be computed as the fraction of time intervals of size t for which the step position has not returned to the initial value in the interval under consideration. For survival, the data analysis is the same except that rather than looking for returns to the interval's initial position we look for crossings of the average step position *computed from the entire image*. Figure 7.1 shows schematically the distinction between the two quantities. In this figure we give examples of persisting and surviving time intervals. If there are, for example, 400 different-size time intervals in an $x(t)$ data set, then the fraction of persisting intervals of size δt gives us $p(\delta t)$. Of course, for small intervals, there are many overlapping ways to partition $x(t)$ into small intervals. We compute $p(\delta t)$ for the average over all time intervals of size δt, allowing them to overlap. This is standard procedure for computing step statistics and its validity as a way of obtaining smoother curves has been checked many times. It has the effect of making the statistical uncertainty in the experimental curves for large time intervals significantly worse than for the small time intervals. For most data sets it is clear visually when the calculated averages are limited by insufficient statistics, and we always omit such long time data points from inclusion in any fits.

The way that persistence and survival are computed automatically introduces a normalization to the data. If we are looking through a time series where the time between successive points in the series is Δt, then a *return* is never possible in this interval because in the smallest interval no changes can be observed. Thus, the persistence probability for intervals of the smallest size in the series is necessarily unity. In the next

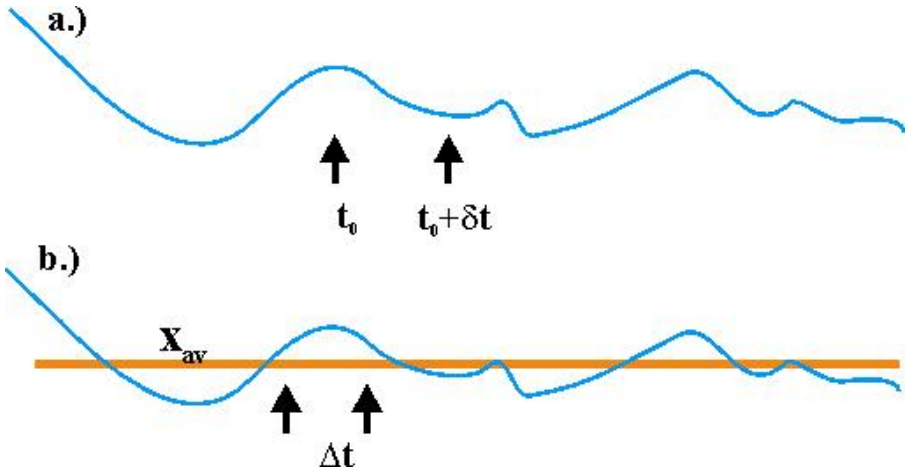

Figure 7.1 a.) Schematic time series of step positions showing a persistent interval δt b.) Schematic time series showing a surviving interval (with respect to average position) Δt.

two sections, we will see that this normalization has important consequences for the kind of information that can be obtained from these statistical quantities.

It should also be pointed out that Krug et al. defined persistence probabilities for returns from both the positive and negative directions[32]. The two are only expected to be different in nonequlibrium situations and for the study of near-equilibrium step fluctuations the distinction will not be important.

7.3 Results and observations

In this section, first-passage statistics for all the systems described in chapters 3-6 will be presented. To emphasize the apparent universality of, for example, the persistence exponent, the results will be grouped according to the growth exponent determined from temporal correlations functions described in earilier chapters. First, $\beta = 1/4$ step fluctuations, as observed in uniform Si(111)- $\sqrt{3}\times\sqrt{3}$ R30-Al (AD kinetics) and in high temperature Si(111)-(1x1)-Pb domain boundaries (diffusion to nearby defects) will be shown.

Figure 7.2 shows persistence probabilities for step fluctuations on two different surfaces that show $t^{1/2}$ scaling of $G(t)$. In Fig. 7.2a, experimental persistence probabilities for uniform Al-$\sqrt{3}\times\sqrt{3}$ at several temperatures are shown with arbitrary offsets for clarity. The average persistence exponent determined from these curves is 0.77 ± 0.03[108]. Figure 7.2b shows the persistence probability for domain boundary fluctuations of Pb/Si-(1x1)/ $\sqrt{3}\times\sqrt{3}$ interfaces at 620 K. The exponent from this curve is $\theta=0.73\pm0.04$. Clearly two different systems that fluctuate via the same rate-limiting mechanism have exponents that agree with one another.

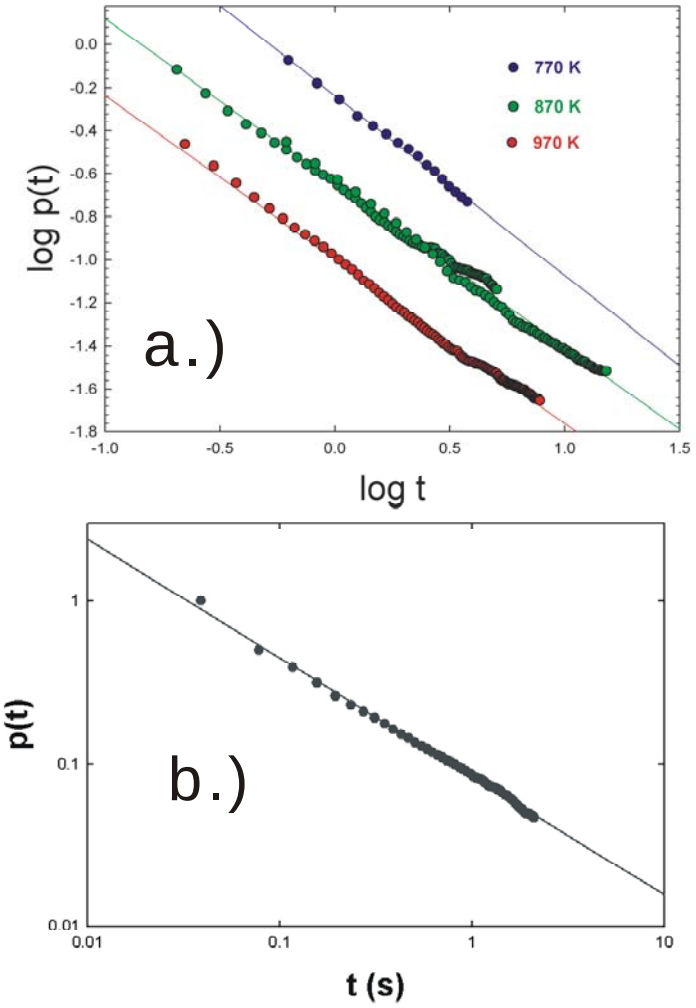

Figure 7.2 a.) Persistence at 770 (blue, top), 870 (green, middle), and 970 K (red, bottom) for Al/Si-$\sqrt{3}\times\sqrt{3}$ b.) Persistence at 620 K for Pb/Si-(1x1).

Next, we present persistence exponents for steps with SED-limited fluctuation kinetics. In this class are steps on a Al/Si - $\sqrt{3}\times\sqrt{3}$ surface coexisting with γ-Al/Si and clean Pb(111) spiral steps. Figure 7.3 shows persistence probabilities at different temperatures for the Al/Si (Fig 7.3a) and Pb(111) (Fig 7.3b) surface steps corresponding to the data presented in chapters 4 and 5, respectively. The exponents have no systematic temperature dependence, and the average for Al/Si is 0.86±0.04 while for Pb(111) spirals it is 0.88±0.04 Again, there is agreement between persistence exponents for fluctuations limited by the same mechanism. It should be kept in mind that the absolute magnitude of the persistence probabilities in both figures 7.2 and 7.3 is set arbitrarily for clear presentation of the separate curves. The issue of the absolute magnitudes will be addressed in detail in the discussion section of this chapter after we present the observation of the dependence of this quantity on sampling interval.

Before moving on to this important issue, however, we show in figure 7.4 survival probabilities obtained from experimental fluctuation data. Figure 7.4a shows the initial observation that the survival probability for uniform $\sqrt{3}\times\sqrt{3}$ steps does not decay as a power law. It can be reasonably well fit by an exponential decay, but it is not clear that this is proper over the entire data set either. The same behavior is seen for Pb(111) spiral steps in figure 7.4b. The characteristic feature of survival probability seems to be exponential decay, and using this quantity, there is no clear way to distinguish between an AD and an SED fluctuation mechanism.

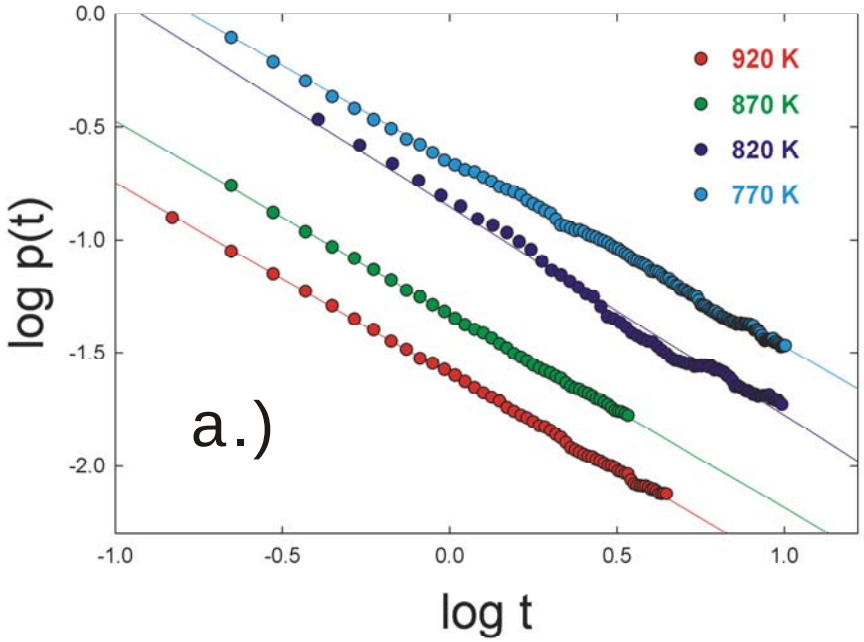

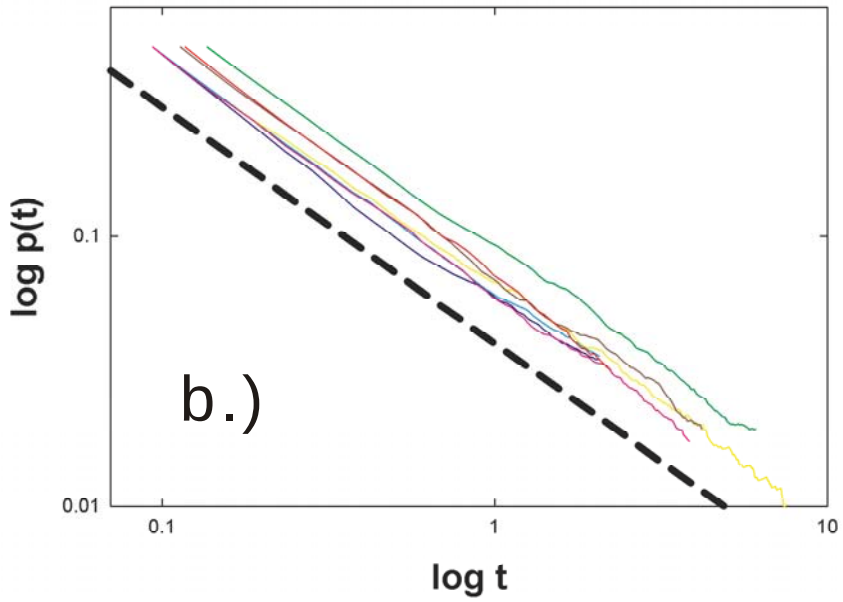

Figure 7.3 Persistence probabilities for SED-limited kinetics. a.) Multiple phase Al/Si steps b.) Pb(111) spiral steps from 300 K to 390 K. Dashed line is the theoretical prediction for the slope. All offsets are arbitrary in both a.) and b.).

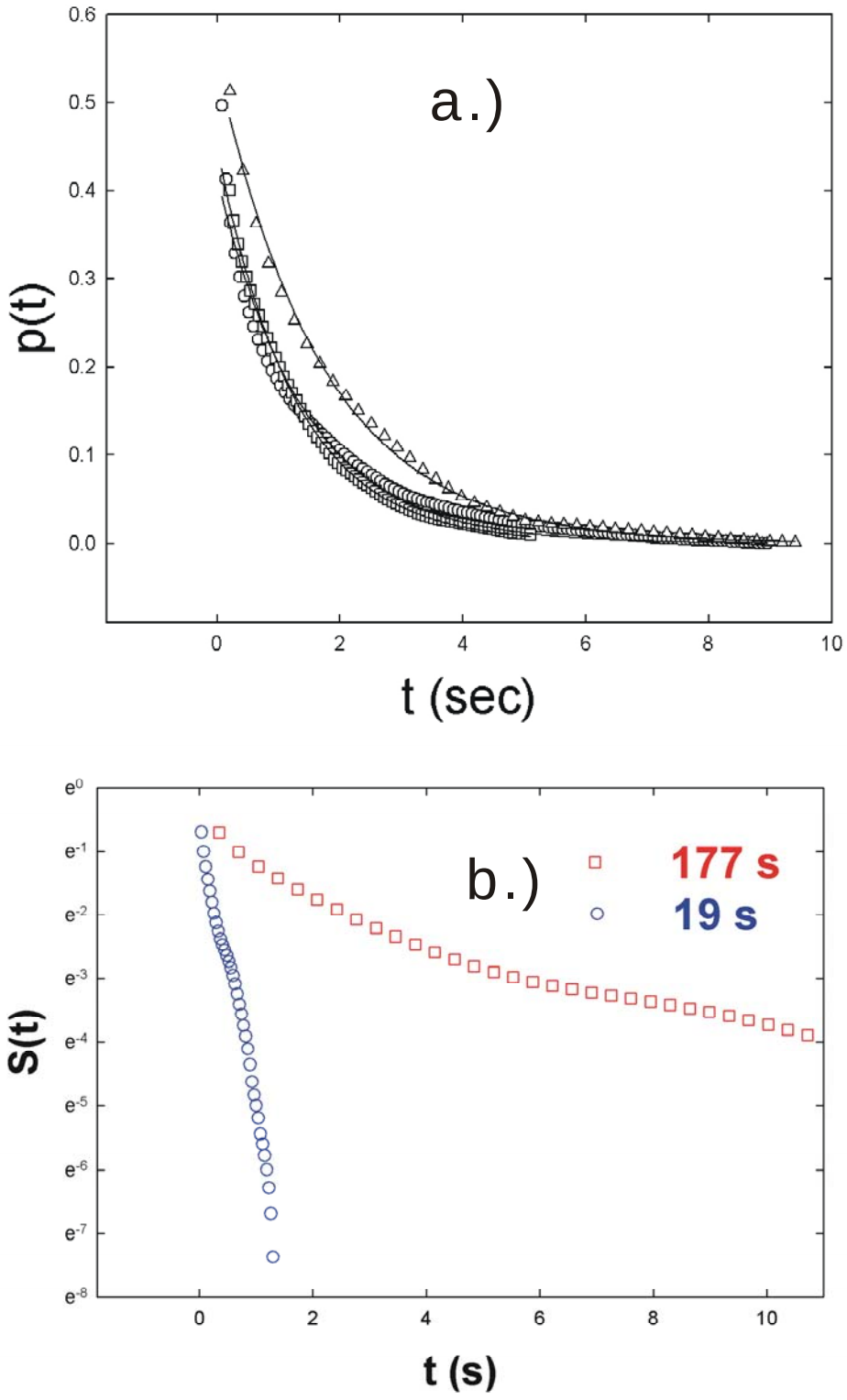

Figure 7.4 a.) Survival for uniform $\sqrt{3}\times\sqrt{3}$ steps with exponential fits as solid lines. b.) Survival for Pb(111) spiral steps on a semilog scale to show expoenential decay.

Really, this lack of distinguishing features in survival isn't much of an impediment since the persistence exponent already seems to be unique for a given universality class. In addition, we plot in figure 7.5 a set of experimental curves indicating the existence of a universal continuous family of exponents for uniform Si(111) $\sqrt{3}\times\sqrt{3}$ R30-Al step fluctuations. This family can also be seen for SED-limited fluctuation kinetics, but these results will not be presented here.

Universality is an important and deep issue in the statistical physics of complicated spatially extended systems. From a practical, material-science point of view, the nonuniversal properties of such systems are equally interesting. For example, how does persistence behavior depend on whether we are considering Si(111)-(1x1)-Pb/ $\sqrt{3}\times\sqrt{3}$ domain boundaries or Si(111)- $\sqrt{3}\times\sqrt{3}$ R30-Al steps? We first attempted to address nonuniversal persistence properties by looking for the temperature dependence of the persistence probability for uniform Al/Si $\sqrt{3}\times\sqrt{3}$ steps. Recall that increasing the sample temperature from 770 K to 970 K results in an increase in AD step mobility from 240 $Å^3$/s to 55000 $Å^3$/s. In other words, step motion is faster by more than two orders of magnitude. Nevertheless, computing persistence probabilities as described in the previous section resulted in no difference in absolute magnitudes between 770 and 970 K. In fact, the only way to obtain p(t) curves that differed in their magnitude was to compare data taken with different sampling times. The situation is illustrated for the uniform Al/Si(111)- $\sqrt{3}\times\sqrt{3}$ steps is shown in figure 7.6. In figure 7.6a, we plot experimental curves obtained for different temperatures and different sampling intervals. It can be seen that the only differences in the curves come from the minimum time step

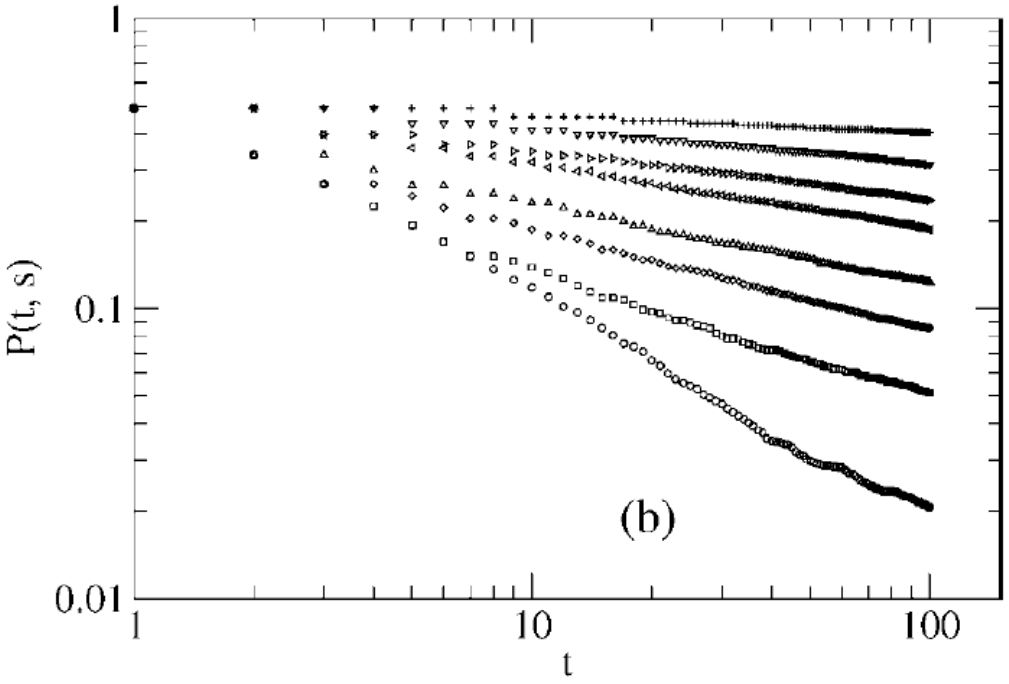

Figure 7.5 Family of persistent large deviations for uniform $\sqrt{3} \times \sqrt{3}$ with s= 1.0, 0.75, 0.5, 0.25, 0, -0.25, -0.5, -0.75, -1.0 from bottom to top on a double log scale.

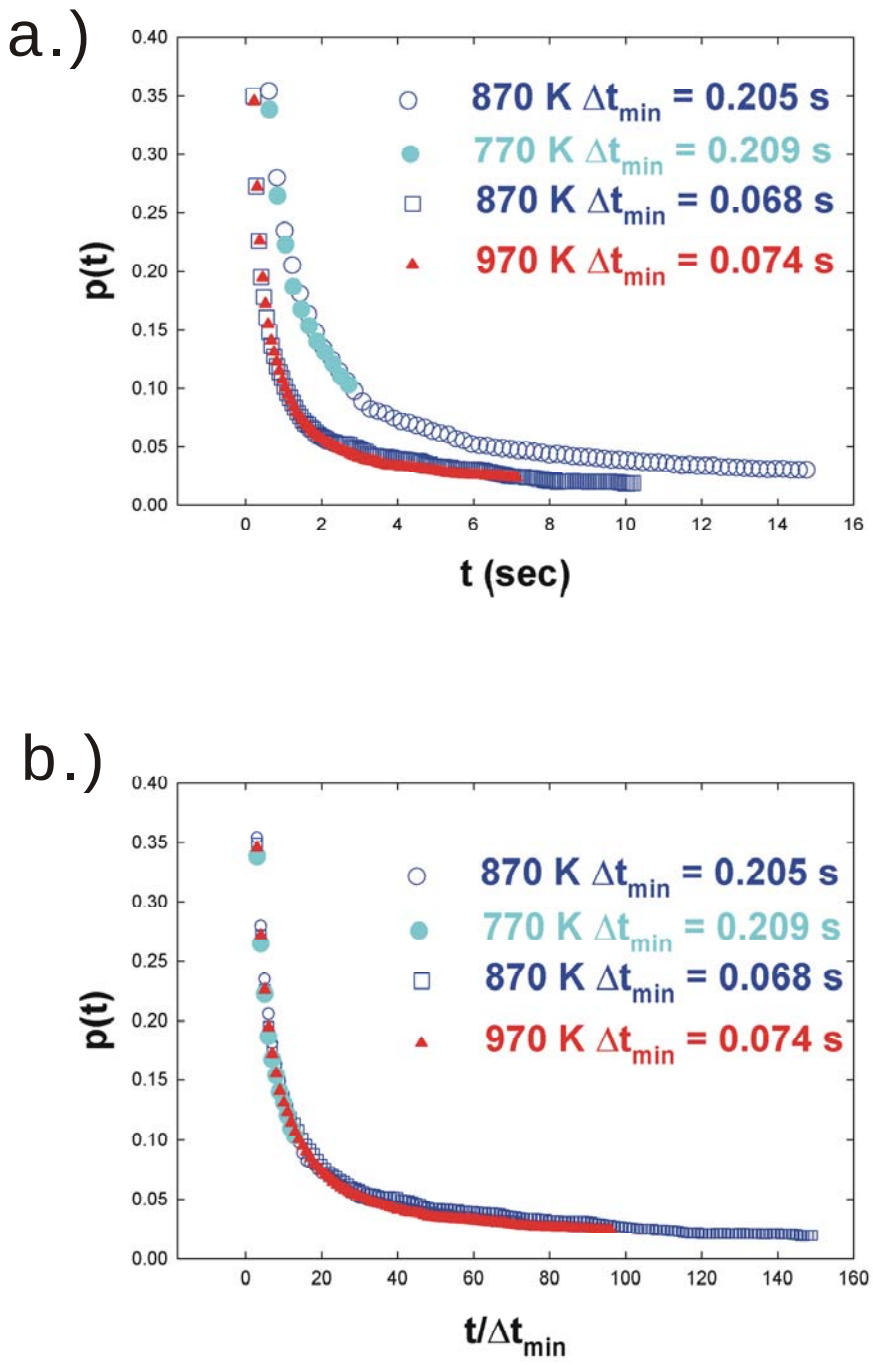

Figure 7.6 Persistence for Al/Si at different temperatures and sampling times. b.) Collapse of curves in a.) when plotted versus scaled time.

differences. Curves obtained at different temperatures with the same sampling interval are indistinguishable despite the known drastic differences in underlying kinetics at the different temperatures. This is clearly demonstrated in figure 7.6b where we have plotted the data from 7.6a versus time scaled by sampling interval Δt. All the data collapses to the same power law decay when plotted in this way. The same is true for the survival probability. Figure 7.7 shows survival probabilities for Pb(111) spiral steps obtained with sampling times that differ by almost a factor of 10. They give completely different survival curves when plotted in real time (Fig. 7.7a) but collapse when plotted versus scaled time (Fig. 7.7b).

7.4 Discussion and Analysis

The most important observation of the last section is that experimental persistence exponents seem to be universal for fluctuations described by linear Langevin equations. Krug et al. argued that for such models, the persistence exponent is related to the growth exponent from chapter 1 via

$$\theta = 1 - \beta \qquad (7.5).$$

This relationship, though quite simple, cannot be obtained as merely a trivial consequence of dimensional analysis. The argument presented by Krug and co-workers[32] relies on mathematical results for first passage times of fractional Brownian motion. Fractional Brownian motion[119] is so-called because it described diffusion where the law for mean-square displacement is some fractional power of time rather than the simple linear dependence on time of the mean-square displacement of a random walker. Of course this is just the situation for the growth of the mean-square width of an interface

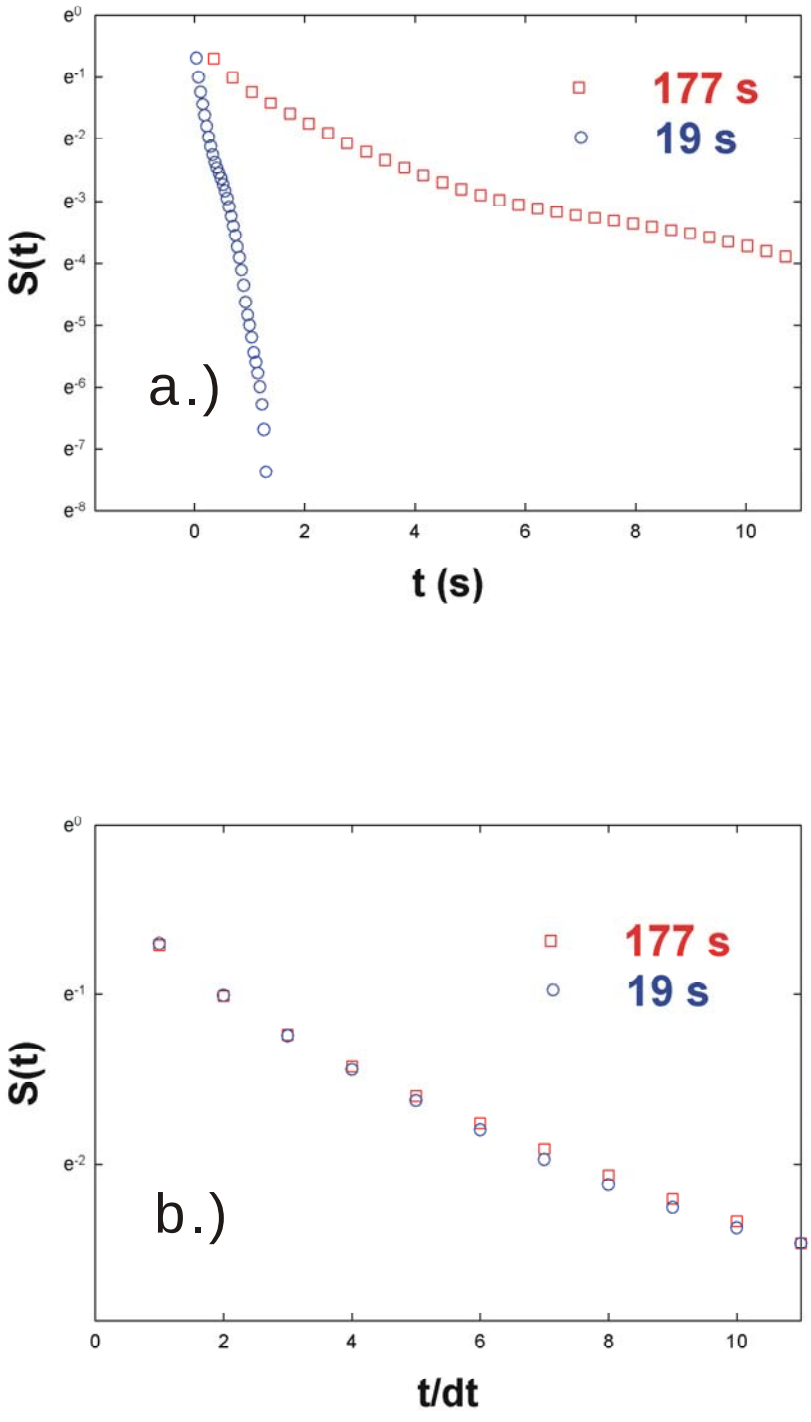

Figure 7.7 a.) Survival for Pb(111) spiral step at 320 K for different sampling intervals. b.) Data collapse when plotted versus scaled time.

with growth exponent β. Using the equivalence between these two physical situations and the known return times[120] for fractional Brownian motion, Krug et al. argue that Eq. 7.5 is exact. Our experimental observations support this contention. The experimentally extracted persistence exponents for the Edwards-Wilkinson equation that model AD-limited fluctuation kinetics are in agreement with prediction of Krug et al[32] that θ = ¾. This is justified numerically and by the proposed scaling relation, $\theta = 1 - \beta$. Figure 7.8 shows results of a simple numerical integration (see appendix C) of the Edwards-Wilkinson equation that we performed using the same Euler discretization procedure described by Krug and company[32]. Rather than using the entire lattice to compute *p(t)*, as these authors did originally, we mimicked our STM line scan data by only monitoring the central point of our discrete lattice and computing *p(t)* as described in section 7.2. Of course we obtain a persistence exponent in very good agreement with the prediction $\theta = 1 - \beta$. In addition, we note that this relation is valid for the Pb/Si domain boundaries even though they are *not* AD limited in the desorption regime. This is strong support for the validity of the derivation in Ref. 32, since it starts only with the scaling of *G(t)* and not with a specific Langevin equation.

Our measured exponents for SED-limited fluctuations with $\beta = 1/8$ are also in agreement with the expression in Eq. 7.5, giving $\theta = 7/8$. This particularly satisfying given that the crossover in rate-limiting mechanism described in chapter 4 appears in the persistence exponent as well as the temporal correlation function. Of course, *G(t)* simply scales with the growth exponent so if Eq. 7.5 is valid, the change in θ for the phase coexistence situation is absolutely essential.

Thus, the persistence exponent seems to be universal, at least in the same sense as the growth exponent. To emphasize this point, we show in figure 7.9 the agreement between experimental and numerical studies of the continuous family of persistence exponents obtained using the notion of persistent large deviations described in the introduction[116, 121]. The set of curves in figure 7.9a closely resembles the experimental set in figure 7.7. The main plot is the result of a numerical integration similar to the one performed to get the curve in figure 7.8. The inset is the result of a discrete SOS-type lattice model that is in the same universality class[121]. The agreement between theory and experiment is shown quantitatively in figure 7.9b, where the actual continuous function $\theta(s)$ that generalizes the persistence exponent θ is plotted (note that the ordinary persistence exponent as defined by Krug et al.[32] is simply $\theta(s=1)$). To within the uncertainty, the experimental function agrees well with the results of the numerical studies. This result is suggested as a very strong indication of the depth and potential utility of first-passage statistics as characterizations of dynamic universality classes.

The survival probability, as stated in the previous section, does not seem to have any clear dependence on the underlying model universality class. In fact, it has been shown that a stochastic process with an exponentially decaying autocorrelation function (see chapter 5) should always have an exponentially decaying survival probability[122]. Since equilibrium step fluctuations satisfy these requirements at long times, regardless of whether they are limited by AD or SED, it is clear that at least approximate model-independence of the decay of survival is expected as is the approximate form of the measured survival probabilities.

While the issues discussed above clearly demonstrate the fundamental value of

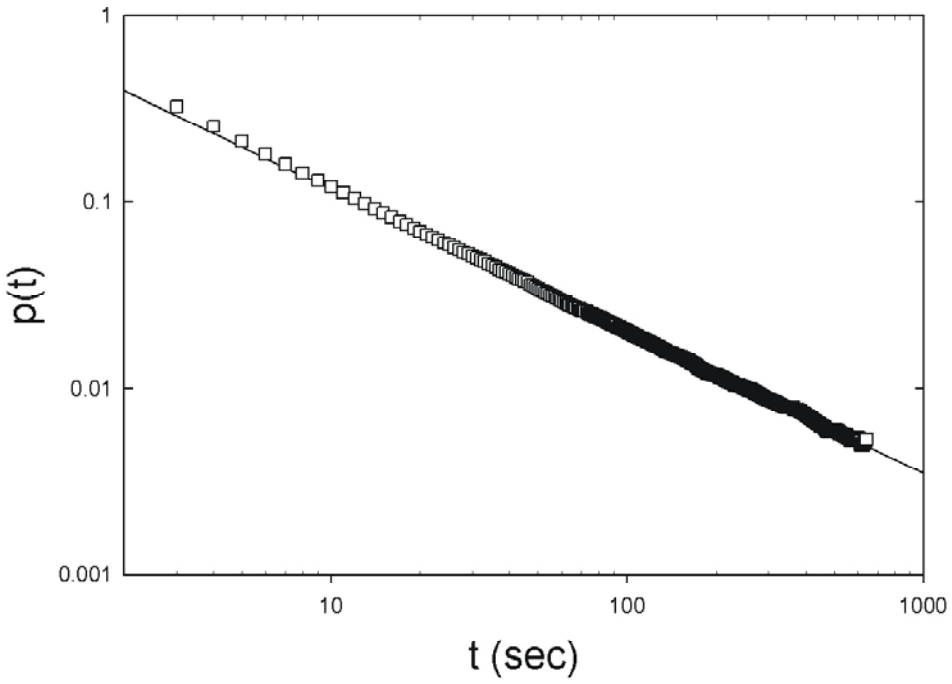

Figure 7.8 Persistence probability from numerical integration of EW equation with sampling of only one point of the lattice to mimic STM pseudo-imaging. The slope on the double log scale gives an exponent of $\theta = 0.76$.

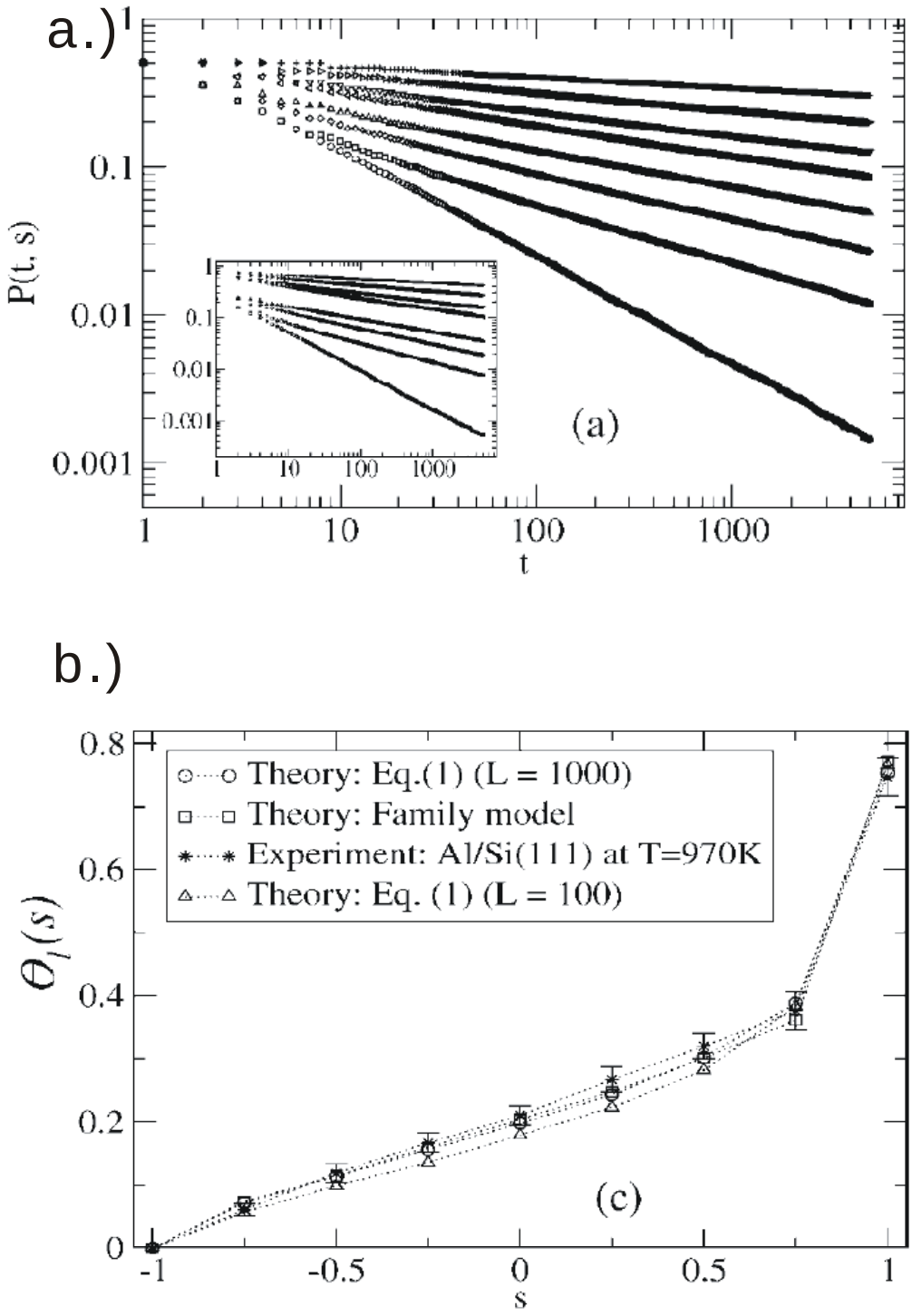

Figure 7.9 a.) Numerical infinite family of persistent large deviations for the EW model. b.) Comparison of numerical values of $\theta(s)$ with experimental value from Fig. 7.5

persistence and survival for describing the universal properties of stochastic dynamics of extended systems, first-passage statistics seem to speak to intuitively practical questions. As mentioned several times, they are natural candidates for quantifying stability and reliability of fluctuating structures. For such quantitative uses to be realized however, it is essential to extend the current understanding of the *non-universal* properties of persistence and survival. How do they depend on variables like material or temperature?

In the previous section, the perplexing temperature independence of persistence and survival probabilities was described. Ultimately this effect must be traced to the fact that the experiments in this work (and actually any real experiment or numerical study) can only sample the fluctuating step *at discrete times*. In the experimental section of this chapter, it was noted that an automatic normalization of the persistence probability is built into the fact that it is not possible to observe a return or a zero-crossing that happens more quickly than the step position is sampled. This sets $p(t)=1$ for the smallest time step. What happens when the time step is changed? For example, if we sample 512 lines in 177 seconds the smallest time step is 0.346 seconds and p(0.346s)=1. From this point, the persistence probability decays with the exponent characteristic of the underlying Langevin equation. If we did another experiment where 512 lines were sampled in 19 seconds then the decay would start from p(0.037s)=1. Remarkably, it has been shown theoretically that *discrete-time sampling does not alter the persistence exponent*[123]. We have verified this unintentionally with our step fluctuation data. Discrete-time sampling does have a serious effect on the absolute value of the persistence probability. This was recognized by Ehrhardt et al[124]. but not studied in any detail. Clearly if $p(t)$ starts from a different point for different sampling times but decays with the same exponent, it has to

have a different prefactor in the power law. Almost trivially, the empirical form of the persistence probability is:

$$p(t) = \left(\frac{\delta t}{t} \right)^{\theta} \qquad (7.6)$$

where δt is the sampling interval. Recalling the practical motivation for wondering about the absolute magnitudes, we see that any non-universal information that might be expected to enter into the persistence probability is totally obscured by the discrete-time sampling artifact. If one expects to obtain quantitative information about a *first*-passage statistic for a stochastic process, it is obviously unacceptable to under-sample the process in time. Missing events like level crossings or returns means that the magnitude of the probability computed from an under-sampled process is meaningless. For fast step fluctuations it is probably necessary to use a faster technique than STM to obtain meaningful non-universal first-passage properties. It may turn out that any technique other than atom-scale observation (with FIM or possibly atom-tracking STM) will suffer from this problem. For such observations, the continuum step model would break down and one would be dealing with the random walk of atoms on a surface. First passage questions are still very relevant for such studies but it is not clear that the results could be extrapolated to the nanoscale features of interest in this work.

Survival probability was observed in the last section to suffer from a similar scaling with sampling interval. The dependence in this case is significantly more complicated than in the case of persistence. Dasgupta and co-workers[109] have shown numerically that survival should have a fairly complicated two-variable scaling form:

$$S(t, L, \delta t) = f\left(\frac{t}{L^z}, \frac{\delta t}{L^z} \right) \qquad (7.7)$$

where L is the system size and z is the dynamic exponent introduced in chapter 1. As was described in chapters 4 and 5, the system size for step fluctuations is given by the maximum wavelength mode that can decay in the measurement time (this is material dependent but doesn't help understand the material dependence of *survival*). Thus, survival is not just a function of sampling time but also *total measurement time*. Despite making the numerical understanding of survival more complicated, the practical effect of Eq. 7.7 is to leave us in the same situation as in the case of persistence. While we can qualitatively understand the decay of the survival probability, using it as a quantitative characterization that depends on specific kinetic details is not feasible using the kind of experiments presented here.

7.5 Summary and Conclusions

In this chapter, the experimental measurement of persistence, survival, and persistent large deviations has been described for a wide variety of surface steps. The persistence exponents θ were all found to be in agreement with the theoretical prediction that $\theta = 1-\beta$ whrere β is the growth exponent characterizing the Langevin equation for the underlying rate-limiting step dynamics. Thus, it provides a new universal exponent characterizing dynamic universality classes that is non-trivially related to the other universal exponents. Going even further, the notion of persistent large deviations that generalizes the persistence exponent from a single number to a continuous function was investigated for AD-limited fluctuations on the uniform Si(111)- $\sqrt{3}\times\sqrt{3}$ R30 –Al surface. The infinite family of exponents was found to be characteristic of the underlying Langevin equation and was checked by comparing the experimental family with two different numerical

implementations of the underlying dynamics. The survival probability was found to decay approximately exponentially with time in all cases, regardless of underlying dynamics, as expected from the long-time behavior of the autocorrelation function for near-equilibrium step-fluctuations.

Despite these obvious successes, the attempt to understand dependence of persistence and survival on things like temperature or material-specific transport coefficients was limited by an experimental artifact. The necessity of sampling the step position at discrete times essentially lead to a set normalization of the absolute magnitudes of both quantities that obscured any physically meaningful dependence that they might have on details of mass transport kinetics. As an aside, the observation that the persistence exponents can still be recovered despite discrete-time artifacts verifies a recent theoretical prediction. Nevertheless, the kind of experiments described in this work cannot be useful for understanding the more pressing issue of how to use first-passage statistics as a practical characterization of the stability of nanostructures.

Thus, the notions of persistence and survival appear to be of primarily fundamental interest for step fluctuations. They point out the deep significance of the idea of dynamic universality classes for the fluctuations of spatially extended systems. Furthermore, they provide necessary experimental test systems for a significant recent body of theoretical work in statistical physics. Ultimately, there are fairly severe limitations to the practical value of experimental first-passage statistics obtained via discrete-time sampling of a continuous stochastic process. Such limitations may be disappointing, but the fact that they exist is an important experimental fact to bear in mind.

Chapter 8

Detachment-limited Mass Transport on Pb(111) Microfacets

Observations of a variety of real-time mass transport processes on (111) facets of Pb microcrystals supported on Ru(0001) can be interpreted in terms of attachment-limited kinetics. Experiments spanning length scales from tens of nanometers to a micrometer yield consistent transport parameters when approached from this perspective. We describe the deterministic decay of small adatom islands, the 3D reshaping of very perfect crystallites, and the 3D reshaping of crystallites with single screw dislocations. Standard transport equations are used to extract the product of the attachment rate constant and adatom concentration. The activation energy governing this kinetic parameter is found to be 680 meV and the prefactor 10^{11} Hz.

8.1 Introduction and Background

In chapter 5, the edge diffusion process on spiral steps on Pb(111) facets was studied using the statistics of step fluctuations. While diffusion of mass along the periphery of a step can be quite important for nanostructure evolution and shape relaxation, it is by nature a conservative process, and therefore not relevant in some situations. For example, an unstable structure on a surface cannot decay by edge diffusion but only alter its shape. In the present chapter we will describe nonconservative mass transport processes on the same (111) facets discussed in chapter 5. Since step fluctuations on Pb(111) are limited by periphery diffusion in a broad temperature range, the study of other transport processes requires observing different phenomena. The decay and/or relaxation of out-of-equilibrium features on Pb(111) microfacets will provide experimental access to nonconservative surface mass transport processes like attachment/detachment and surface diffusion.

Dealing with deterministic evolution on solid surfaces often comes down to solving the diffusion equation with appropriate boundary conditions[1, 3, 56, 125-129]. As an example that will be relevant to the experimental results presented later in this chapter, we will describe the boundary value problem that arises in the decay of an isolated adatom island by surface transport (i.e. in the absence of 3D evaporation). Figure 8.1 shows the geometry of the problem. There is a concentration profile on the surface due to the presence of the island. Gradients in concentration (or equivalently chemical potential) on the surface drive mass transport, and the curved step bounding the island creates an excess in concentration near the step[128]. This excess near a curved step is the well-known

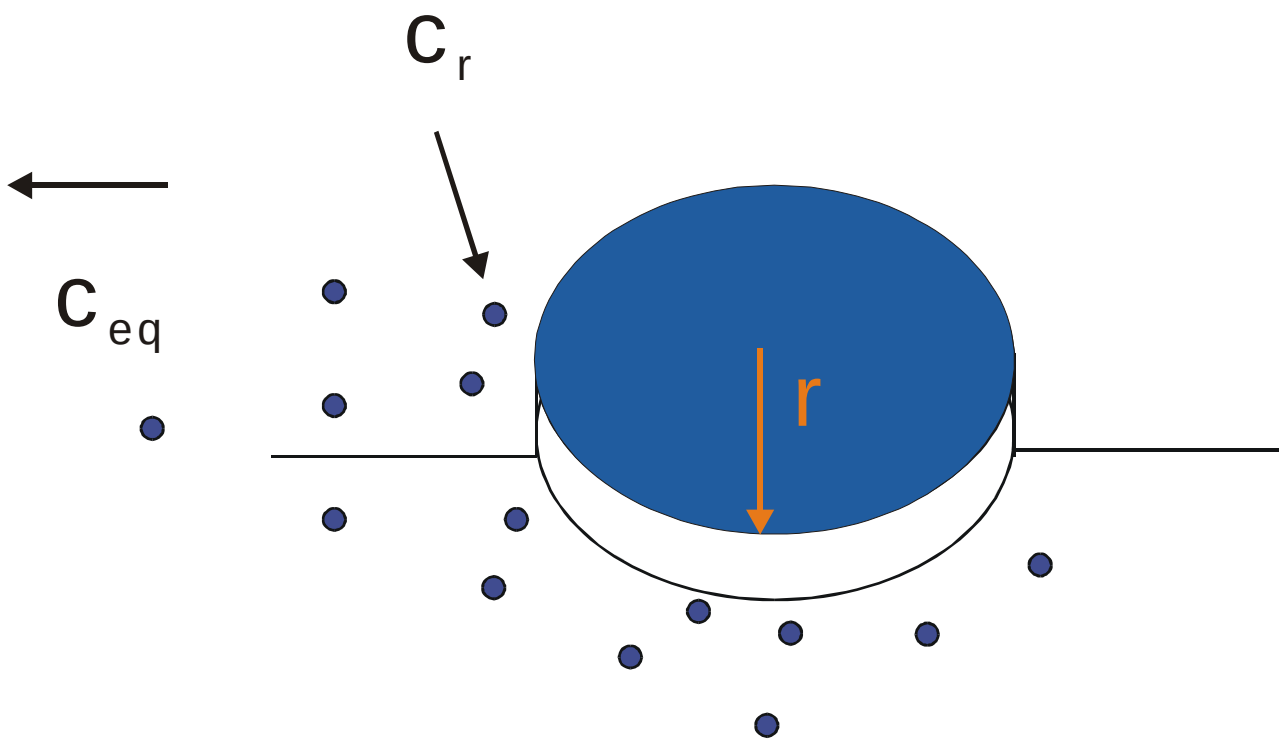

Figure 8.1 Schematic of a nearly circular island of radius r on a flat surface. The concentration of adatoms near the curved island edge is higher than the equilibrium concentration far from it.

Gibbs-Thomson effect[1, 127, 128] and can be intuitively understood by imagining step curvature to result in a slightly reduced coordination of edge atoms and therefore a slightly enhanced tendency for them to leave the step. Naturally, atoms will tend to move from the higher concentration areas near the island edge to the lower concentrations far away from the island, and this mass flow leads to the shrinking and eventual disappearance of the island.

To begin with, we write the concentration near the curved step due to the Gibbs-Thomson (GT) effect as[128]:

$$c_r = c_{eq} \exp\left(\frac{\tilde{\beta}\Omega}{k_B T r} \right) \qquad (8.1)$$

Here c_{eq} is the equilibrium adatom concentration near a perfectly straight step, $\tilde{\beta}$ is the step stiffness, Ω is the surface unit cell area, and r is the radius of curvature of the step. From equation 8.1, the fundamental thermodynamic nature of the GT effect is visible; the continuum step parameter appearing in it is the step stiffness. The specific dynamics of the flow of mass away from the step will be seen to be determined by linear kinetic parameters, but the enhanced concentration (or chemical potential) is only energetic.

The dynamics can be influenced by two processes (ignoring evaporation into the vapor or dissolution into the bulk): detachment of mass from the step edge and diffusion of mass on the flat surface. Mass current for each of these processes can be written. The detachment current is the simplest since it is only proportional to the difference in concentration between the region near the step and the flat surface far from the step. It can be expressed as[128]:

$$I = 2\pi r \kappa \left(c(r) - c_{eq} \right) \qquad (8.2),$$

where κ is the attachment/detachment rate constant that was briefly mentioned in chapter 1. It is related to the more familiar AD mobility via[27] $\kappa = 2c_{eq}\Omega^2\Gamma_a$. The diffusion current is more difficult to express in that it requires the solution of the radial diffusion equation. To proceed, we assume a stationary concentration profile and solve the stationary diffusion equation with boundary conditions on $c(r)$ set by the geometry in Fig. 8.1. Luckily the solution to this problem is well-known and the diffusion current is[128]:

$$I = \frac{2\pi D}{\ln(R/r)}\big(c(r) - c(R)\big) \qquad (8.3),$$

where D is the diffusion coefficient and R is a radius far from the curved step edge.

With these results, and assuming that the concentration at R is approximately equal to c_{eq} and that the exponential in the GT expression (Eq. 8.1) can be approximated by only the linear term in its expansion[128] , the net detachment current is given by McLean et al.[128] as

$$I = \frac{2\pi c_{eq}\tilde{\beta}\Omega}{rk_BT\left(\frac{1}{D}\ln(R/r) + \frac{1}{\kappa r}\right)} \qquad (8.4).$$

Naturally, a mass current is not something readily measured directly. To obtain an experimentally useful prediction, we would rather understand the time dependence of island size. This can be expressed as the time derivative of the island area:

$$\frac{dA}{dt} = -I\Omega \qquad (8.5)$$

As usual it is useful to consider the two extreme limits of mass transport that can lead to a decaying island. For example, if diffusion is very much faster than detachment then the first term in the denominator of Eq. 8.4 can be neglected and we end up with a

constant rate of areal decay. The area of the island as a function of time in this limit is then given by integration of Eq. 8.5

$$A(t) = \frac{2\pi\Omega^2 \tilde{\beta}\kappa c_{eq}}{k_B T}(t_0 - t) \qquad (8.6).$$

In the opposite case, when detachment is much faster than surface diffusion, we neglect the second term in the denominator and obtain an area that decays according to

$$A(t) = \left(\frac{3\Omega^2 \tilde{\beta} D c_{eq}}{k_B T \ln(R/r)} \right)^{2/3} (t_0 - t)^{2/3}. \qquad (8.7)$$

Thus, by measuring with STM which of these equations is satisfied, we can determine the rate-limiting step in the decay of an island on a surface. In addition, by determining the prefactors from experiment, the kinetic parameters associated with the rate-limiting step can be determined. This has been done in a wide variety of experimental systems[3, 49, 130, 131]. For example, detachment-limited kinetics has been observed on TiN(111)[132] and Si(001)[49] while diffusion-limited kinetics has been found for Si(111)[131]. Of course, all of these experiments refer to very specific temperature ranges, and crossover effects should be as common as in the study of rate-limiting processes for step fluctuations. In addition, it has often been found to be the case[3] that the rates of diffusion and detachment are close enough that neither limit is acceptable. Giesen[3] has, for example, reported a situation that is best modeled by a numerical integration of the full boundary value problem without taking any limits. Of course, this makes interpretation of the resulting kinetic information less straightforward but nevertheless informative.

The above results were obtained for an isolated adatom island on an infinite, flat surface. In many experiments, the environment of an island is not so simple. Of

particular interest is the case of multiple layer islands, or "wedding cakes"[3, 56, 60]. Here the decay of the upper-most layer is strongly influenced by the presence of the lower layers. One of the most important modifications necessitated by nearby lower layers is the inclusion of step interactions. The best way to do this is to re-write the GT relation in a more general way by using a general step chemical potential:

$$c_r = c_{eq} \exp\left(\frac{\mu_s}{k_B T}\right) \qquad (8.8).$$

The step chemical potential, μ_s, has been introduced in this expression. This idea is of very fundamental importance to the treatment of deterministic mass transport within the continuum step model. As usual, this model treats steps as the fundamental discrete objects on surfaces and then describes mass flow as the result of chemical potential gradients between steps or between steps and terraces.

In Eq. 8.1, the traditional GT form, the chemical potential is determined only by the step radius, we can also include a term in the chemical potential for step interactions[1, 60, 133]:

$$\mu_s = \frac{\Omega\tilde{\beta}}{r} + \frac{2\Omega g h^3}{(\rho - r)^3} \qquad (8.9).$$

In this expression, the second term characterizes inverse square step interactions that are generally repulsive and can be elastic in addition to the ever-present entropic repulsion. The parameter g is the step interaction coefficient[1], h is the step height, and r is the second layer radius. The form of g in various cases can be found in Jeong and Williams[1] or in Giesen[3]. It depends on temperature and step stiffness for purely entropic repulsions, but has a more complicated dependence when there are true energetic step interactions. Ultimately, step interactions are absolutely essential to understanding the evolution of

multi-layer structures[1, 3, 56, 60, 125, 126, 129, 133]. In particular, the question of how close a small object can come to its thermodynamic equilibrium shape is intimately related to the effect of the interactions on mass flow. There is a regime of evolution, however, where step interactions can be neglected. If the radius of the top-most layer of a wedding cake structure is small enough then the evolution is only governed by the usual GT-type curvature effects. In the present chapter we will mostly be dealing with such situations. Possible modifications due to step interactions will be discussed where appropriate.

The seminal modern work on surface mass transport was the theory of Burton, Cabrera, and Frank[2] for diffusion-limited crystal growth. One of the important points made in that work was that the screw dislocations were essential to crystal growth under weak supersaturation. Thus, the study of mass transport associated with such dislocations is of fundamental importance. We will describe below a treatment of dislocation motion in the detachment-limited regime on a supported Pb crystallite that requires only the GT relation for curvature-driven mass transport.

Before doing so, however, we will describe the important experimental procedures and present a re-analysis of some older kinetic data obtained on the 3D reshaping of supported Pb microcrystals. This analysis will guide our interpretation of newer experiments on small, isolated islands that exist on the (111) top facets of these crystallites as well the analysis of the motion of spiral steps emerging from a screw dislocation. We will discuss the self-consistent picture of the detachment process on Pb(111) that emerges from the analysis of these three different experiments.

8.2 Experiment

The preparation of supported Pb microcrystals is well-developed and they have been successfully employed as model systems for understanding the equilibrium shapes of (approximately) isolated crystals[60, 78, 133-135]. An example the top region of such a 3D crystallite is shown in figure 8.2. The inset shows an atomically resolved image obtained on the flat top facet of a different crystallite, showing the (111) orientation. This orientation can also be inferred from the 3-fold symmetry of the top facet that becomes visible around room temperature (even when it is visible, the anisotropy this introduces into the step stiffness is small enough to be neglected at the level of approximation of the models we will use in this chapter[7, 79]). The crystallites are prepared in UHV (base pressure ~ 10-10 torr) by depositing 10-35 nm of Pb from a heated Alumina tube onto a clean Ru(0001) substrate. The substrate is mounted in a commercial sample holder (Omicron) with an integrated Pyrolitic Boron Nitride heating element that can produce sample temperatures of around 1000 K. The substrate is cleaned by 5 to 7 cycles of heating to 520 K in a 2×10^{-6} torr O_2 environment for 5 minutes and then flashing to 1000 K after removing O_2 from the chamber. This procedure is less than ideal in that the maximum flashing temperature is insufficient to remove all O from the Ru surface (about 1500 K is required to do so). This can be seen in Auger (see spectra in chapter 5) as well as in a weak (2x2) O superlattice in LEED[136]. The residual surface oxygen has interesting but somewhat irreproducible consequences[136] and will not be discussed further.

After depositing the continuous Pb film onto the room temperature Ru substrate, the sample was heated to about 600 K (the melting point of Pb). After a few minutes, the film was observed to visibly melt. Since the vapor pressure of Pb is so low, the molten

metal stays on the surface (still in UHV) in the form of small droplets. When the droplets are cooled to just below the melting point of Pb they freeze into the small crystallites used in this experiment. By annealing just below the melting point for several minutes, it is possible to achieve nearly perfectly equilibrated high-temperature crystal shapes. Unfortunately, it is not possible to image with the STM at these temperatures on Pb. Instead, the crystallites must be cooled to between 300 K and ~ 420 K. Thurmer et al.[60, 133] were able observe the reshaping kinetics after quenching the crystallites to this temperature regime using time-resolved VTSTM. They found that, after the quench, the top facet grew in size by a layer-peeling mechanism that could be understood by continuum step modeling. By STM, this process appeared as the successive shrinking and disappearance of top (111) layers which went on for many hours (6-18) after the initial quench.

The procedure for locating (111) facets of the supported crystallites is somewhat uncommon. Typically, there are 2-4 cyrystallites of roughly 1 μm diameter in a 25 μm^2 area. Thus, using ordinary STM imaging to hunt for top facets is quite inefficient, especially since the surface has enormous height variations of up to 0.5 μm for a single crystallite. Thus, to find a top facet, we first scanned a large area with very low resolution (300 lines x 120 lines say) with tunnel parameters of about 0.1 nA and 0.3-0.5 V. During this "coarse-scan" a very fast tip response was set (using a loop gain setting on the STM controls of say 50 %) to allow the imaging of large height variations. When a feature appeared in the coarse scan that appeared likely to be a good crystallite (it was not always obvious since the way the image was made resulted in significant distortion of the surface topography) the tip was immediately zoomed in to the center of the feature

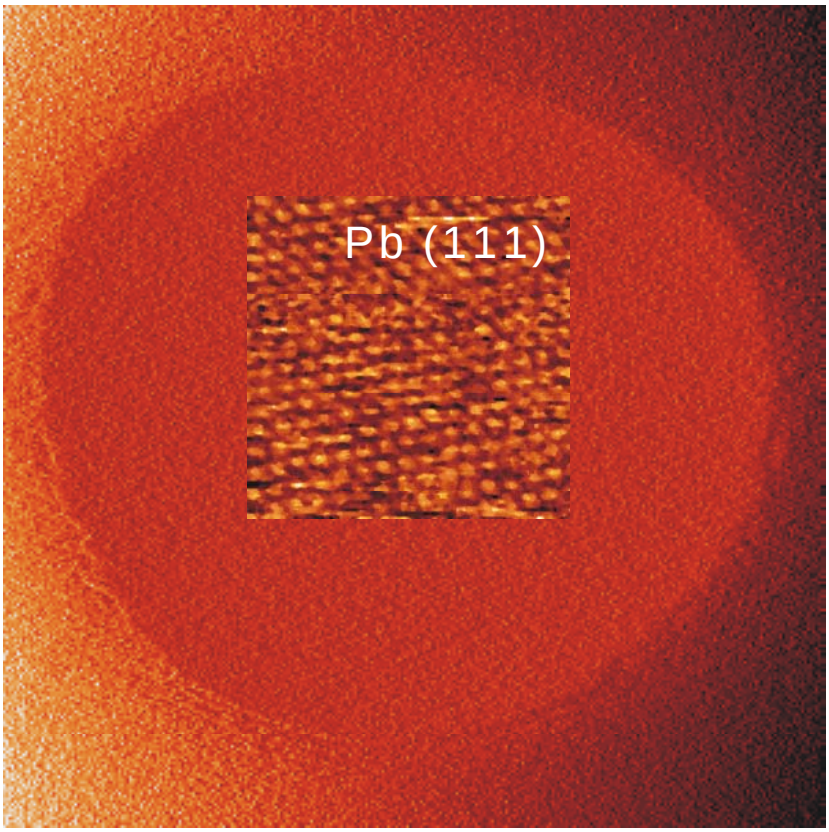

Figure 8.2 STM image (differentiated) of the top (111) facet of a Pb crystallite at 350 K (350 nm x 350 nm). The inset shows an atomically resolved image taken on a similar facet at 320 K (8 nm x 8 nm).

, the tunnel current reduced to ~ 0.03 nA, and the loop gain reduced to 3-12 %. The scan center was then adjusted to put the top facet and some of the upper layers in the field of view. Scan speeds could then be adjusted to properly track any kinetic behavior occuring on the top facet.

Standard electrochemically etched tungsten tips were used to image the crystallites. The interaction between Pb surfaces and these tips is known to be severe[85]. For this reason, we always used low tunnel currents to image the top facets. Nevertheless, especially near the curved crystallite areas vicinal to the (111) facets, there were sometimes short-circuits between the tip and the crystallite. Most often, such jumps to contact did not damage the crystallite, but if too much time was spent imaging the highly curved areas, permanent damage sometimes occurred.

8.3 Results and Observations

On many of the (111) facets, small layered structures were found immediately after zooming in from the coarse scan. An example of such a metastable wedding cake structure is shown in figure 8.3 at 350 K. The structure quickly decayed and left behind a flat (111) facet. These metastable structures presumably formed as the result of Pb, which coats the STM tip after several experiments, falling from the tip to the facet. Such processes are known to occur on Pb(111)[85]. The size and frequency of metastable structures formed in this way was not very predictable and probably depends on the microstructure of the specific STM tip being used. Of particular interest from the point of view of determining mass transport parameters were the single layer islands that were sometimes found. Figure 8.4 shows a sequence of an adatom island decaying at 330 K

with linear areal decay (curves in Fig. 8.5) discussed further in the next section. Vacancy islands were also sometimes found on the facets, particularly at lower temperatures, probably due to STM tips actually picking up mass from the surface[85]. A triple-layer deep vacancy "wedding cake" is shown in Figure 8.6. The decay of each layer could be analyzed in the same way as for adatom islands but for simplicity we will ignore the filling in of vacancies here.

In chapter 5 we described the measurement of nonequilibrium step fluctuations on a slowly rotating spiral step on a (111) facet. The deterministic view of a such a rotation must be amenable to the same treatment as the deterministic decay of wedding cakes and the 3D crytal shape change observed by Thurmer et al.[60] We performed essentially the same experiment as in Ref. 14, but on crystallites with a single screw dislocation. Instead of the layer decay mode[60], the crystal is geometrically constrained to reshape by rotation of the spiral step around the static screw dislocation core. Figure 8.8 shows a sequence of one rotation of a spiral step over the course of about 21 minutes. The shape and angular momentum of the spiral *are not constant* during the rotation. Instead, as the spiral rotates into a higher curvature shape forced by the edges of the top facet, the rotation speeds up.

In this section we have presented observations of mass transport on top facets that span nearly a micrometer in size for the spiral decays to less than 100 nm for the isolated layer decays. When combined in the next section with a re-analysis of the data of Thurmer et al.,[60] these observations will result in a compelling picture of curvature-driven transport on Pb(111).

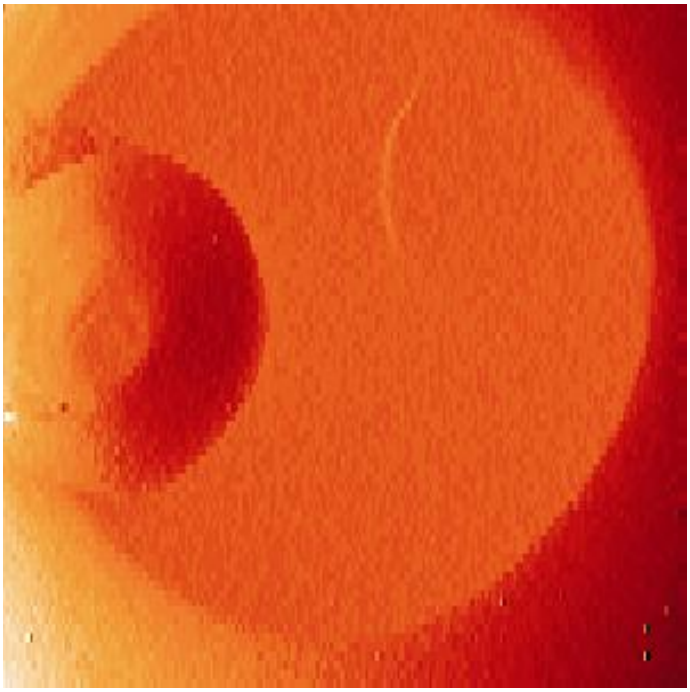

Figure 8.3 Wedding Cake at 350 K (500 nm x 500 nm).

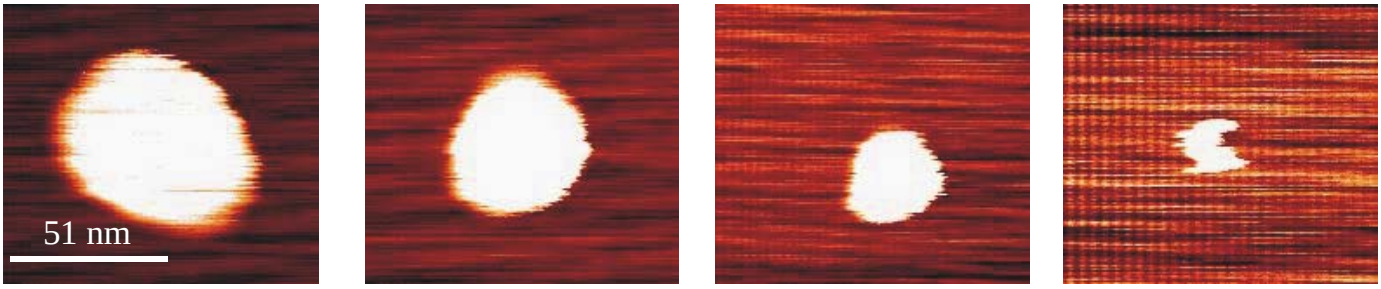

Figure 8.4 Sequence showing the end of an adatom island decay at 330 K.

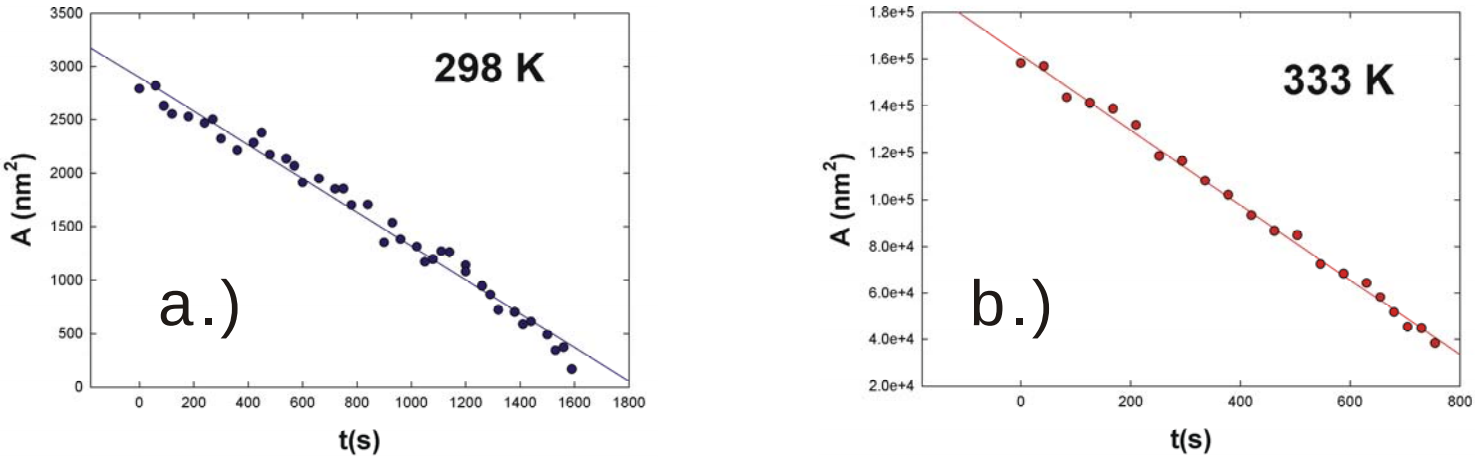

Figure 8.5 Decay of adatom island areas at a.) 298 K and b.) 333 K. Solid lines are linear fits to the data.

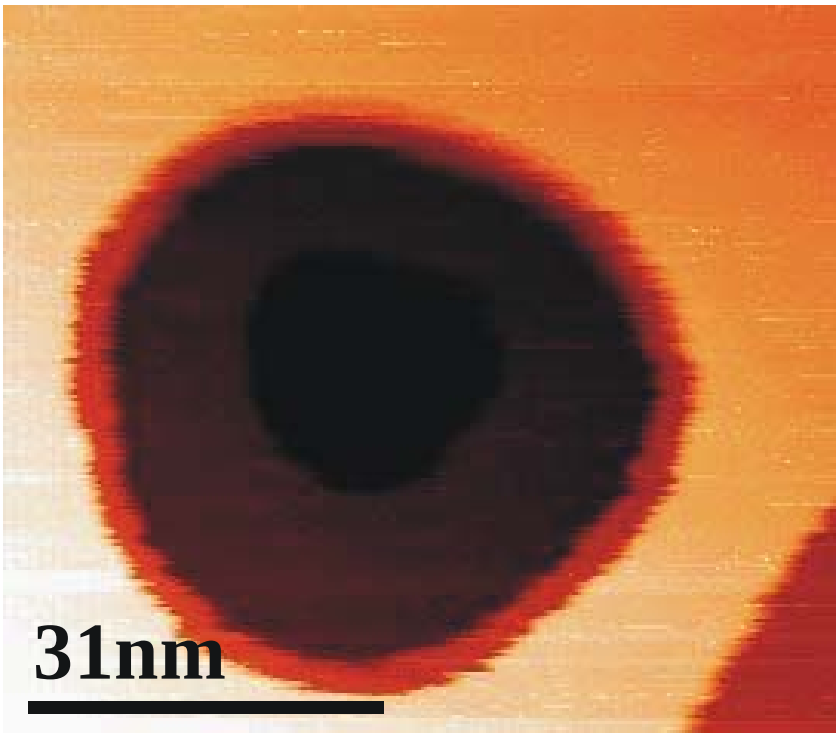

Figure 8.6 Triple layer pit on a Pb(111) facet at 300 K.

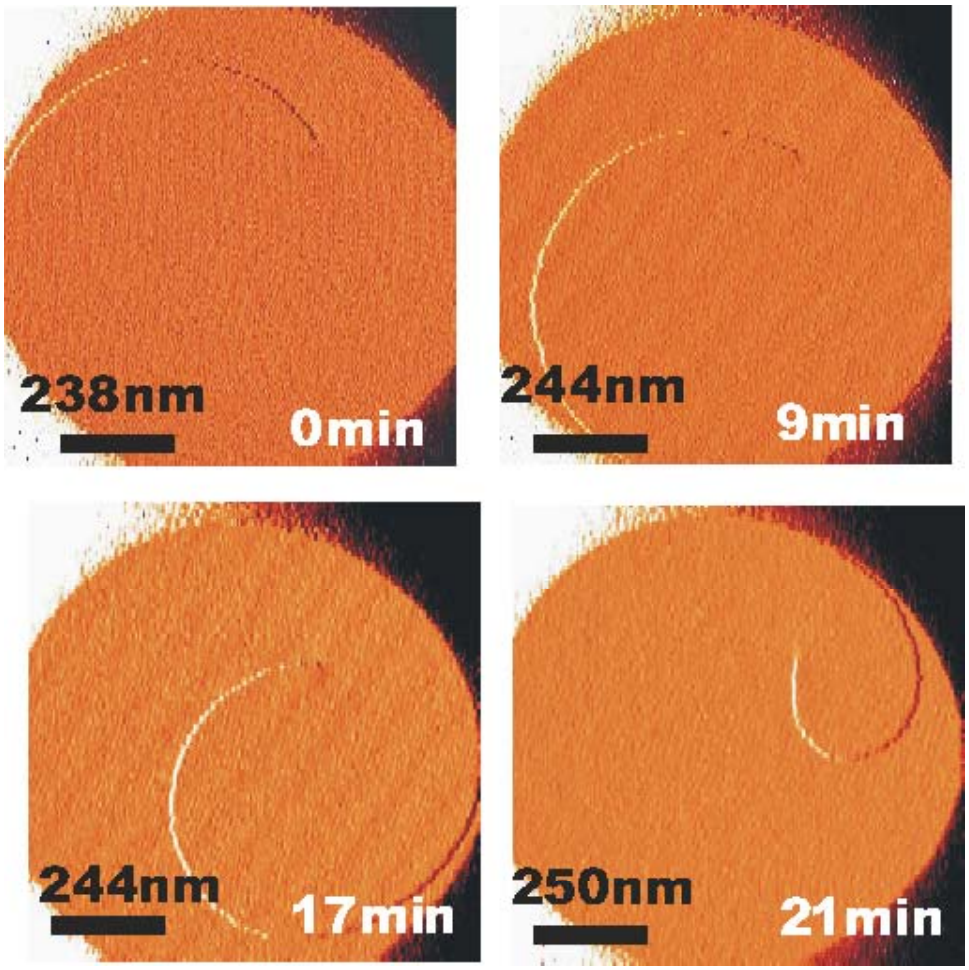

Figure 8.7 One rotation of a spiral decay at 390 K. Total time is about 21 minutes.

8.4 Analysis and Discussion

The layer-peeling data of Thurmer et al.[60] was analyzed in the GT-driven regime by assuming a diffusion limit. The analysis was not entirely successful and a piecewise fit to the data was actually necessary. Recently, Degawa and Williams[137] have succeeded in analyzing the same data without assuming either a diffusion limit *or* a detachment limit. They solve Eq. 8.5, substituting the full form of 8.4 and obtain the best ratio for D/κ using the stiffness known from theory and experiment. Figure 8.8 shows an example of the new fit (solid line) to the data (points). Clearly the fit is very good over the whole range of data at 353 K. It gives a ratio of $D/\kappa = 16\ nm$. A similar fit to data at 368 K gives a ratio $D/\kappa = 14\ nm$. In both cases, the diffusion coefficient is at least a factor of ten bigger than the detachment rate. Thus, the notion that the transport can be treated as detachment-limited on Pb(111) is at least approximately valid. The fitting procedure used by Degawa and Williams allows the independent determination of $c_{eq}D$ in addition to the ratios already presented[137]. For 353 K $c_{eq}D=15000$ s^{-1} and for 368 K $c_{eq}D=40000$ s^{-1}. Using these value with the ratios of D/κ allows the extraction of the detachment kinetic parameter combination $c_{eq}\kappa$. This is equal to 940 $nm^{-1}s^{-1}$ at 353 K and 2900 $nm^{-1}s^{-1}$ at 368 K. We emphasize that these parameters are *not* obtained by assuming any limits but are the results of fitting the data to the solution of the full differential equation in the GT-regime as in Eq. 8.5.

Given the apparently linear decay of adatom islands as shown in the previous section, we use the slopes of the solid fits in figure 8.5 to extract the combination $c_{eq}\kappa$ at two lower temperatures. For 300 K we find $c_{eq}\kappa=20\ nm^{-1}s^{-1}$ and for 330 K we find

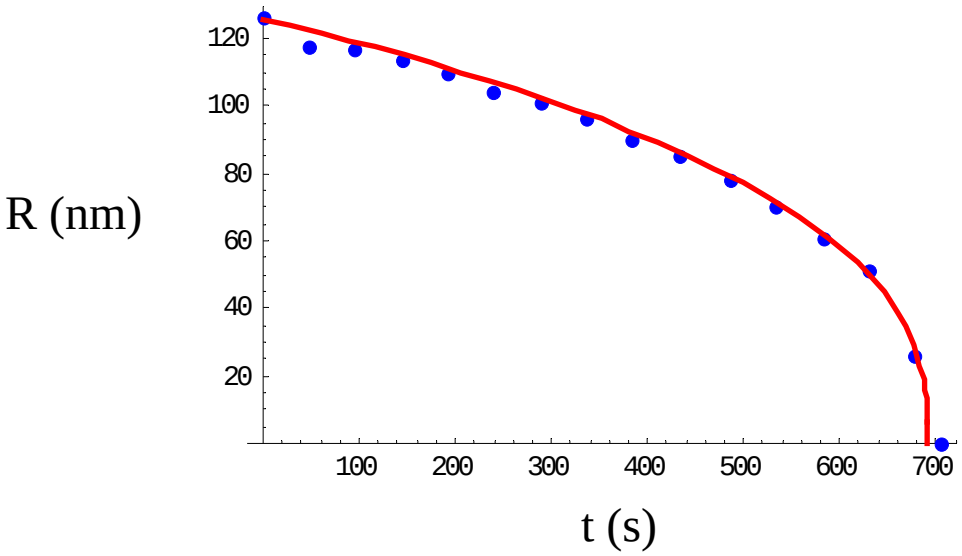

Figure 8.8 Fit of data from Thurmer et al. to the full solution of the differential equation for the area (or radius in this case).

$c_{eq}\kappa$=550 $nm^{-1}s^{-1}$. Already, the large increase of detachment rate with temperature is evident and suggests activated mass transport. The numbers obtained from the slopes in figure 8.5 assume detachment-limited kinetics and are therefore not as reliable in principle as those obtained by Degawa and Williams. However, given the fact that diffusion coefficient is found by their complete solution to be bigger by at least a factor of 10 than the detachment rate constant[137], it is worth pursuing the detachment limit. In addition, the adatom islands are very much smaller than the layers involved in the peeling processes fit by Degawa and Williams. It is well-known that smaller objects are more likely to fall in a detachment-limited regime[128].

The motion of spiral steps presumably occurs via the same mass transport processes that drive the other types of evolution on the (111) facets. In fact, we can model the process as curvature driven just like an island decay. The most important feature of the modeling is to constrain the geometry of the spiral in a way that mimics the constraints in the experiment. This implicitly puts in some effect of step repulsions at the facet boundary and fixes the core of the dislocation. Then the step velocity can be written in terms of radius of the spiral as:

$$v_s(r) = \frac{\tilde{\beta}\kappa c_{eq}\Omega^2}{k_B T}\left(\frac{1}{r} - \frac{1}{r_c}\right) \qquad (8.10).$$

The parameter r_c is the radius of an island that gives a concentration equal to that on the equilibrium flat terrace and all other quantities are as defined above. Using the geometry shown in figure 8.9, it is possible to solve the following PDE for the time evolution of the shape of the spiral step:

$$\frac{\partial r}{\partial t} = \frac{\tilde{\beta}\kappa c_{eq}\Omega^2}{k_B T}\frac{(r^2 + (r')^2)^{1/2}}{r}\left[\frac{r^2 + 2r'^2 - rr''}{(r^2 + (r')^2)^{3/2}} - \frac{1}{R}\right] \qquad (8.11).$$

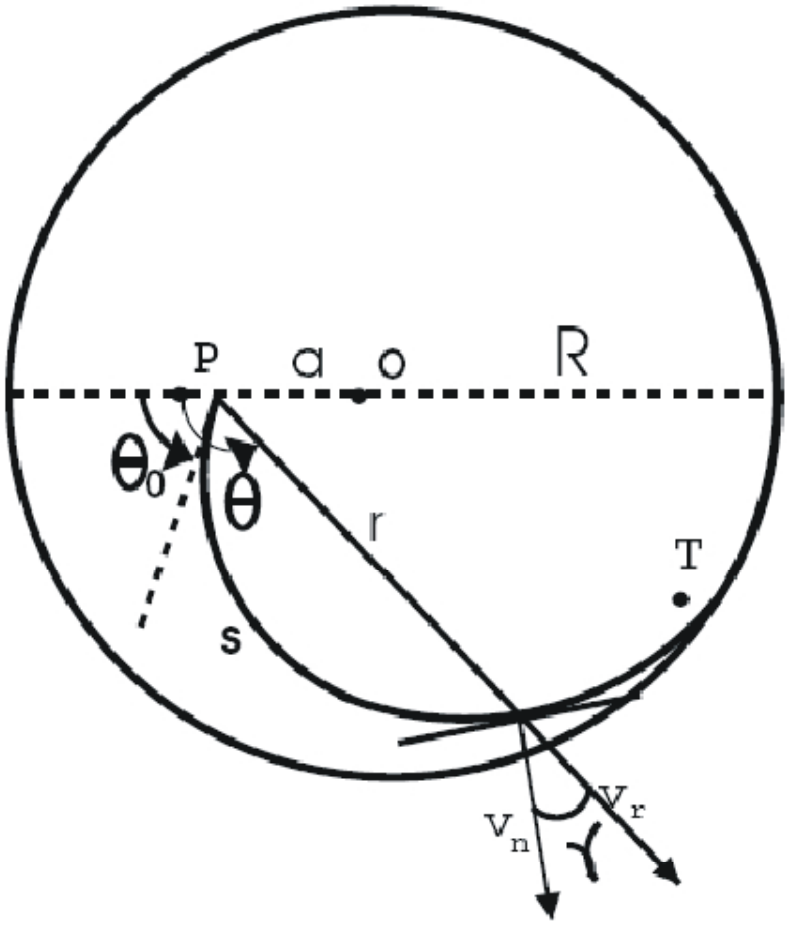

Figure 8.9 Geometry of numerical integration for spiral decay of a crystallite. Polar coordinates are used and the core is fixed at point *P* a distance *a* from the origin. The spiral joins the circular boundary continuously at a point *T* after which time it follows the boundary perfectly.

In this relation, primes denote differentiation with respect to the θ coordinate in the polar coordinate system of figure 8.9. The boundary conditions are just that the core remains fixed at a distance *a* from the origin (the center of the facet) and that the spiral joins continuously with the circular boundary. Figure 8.10 shows the results of a numerical integration of this equation corresponding to the experimental images in figure 8.7. The qualitatitive agreement between the shapes is good, as is the speeding up of the spiral as its curvature increases. Note that in both equations 8.9 and 8.10, the parameter $c_{eq}\kappa$ appears as a coefficient. Thus, by scaling the integration time and crystallite size up to the real time and size we can simply extract the kinetic parameter from the numerical study. For the spiral decay at 390 K shown in figure 8.10 and discussed in chapter 5, the value obtained is $c_{eq}\kappa = 4900\ nm^{-1}s^{-1}$. As in the case of the island decays, this number is the result of assuming detachment-limited kinetics.

We are now, however, in a position to judge the validity of the detachment-limit approximation. Shown in figure 8.11 are all five data points for the 3 different experiments described above on an Arrhenius plot. The error bars are around 20 % and derived from the scatter in the decay rates of islands (or pits) at the same temperature on the same facet. The data points fit to a single line on an Arrhenius plot remarkably well. The parameters from the fit line (solid) give an activation energy of 610 ± 30 meV and a prefactor of $10^{12\pm1}$ Hz. The energy determined is the sum of the adatom formation energy and the barrier to detachment from the step edge, and the prefactor is remarkably consistent with a typical phonon frequency.

Perhaps the most important point about this result is that two of the five points in the plot are obtained from the full solution of the surface transport problem in the absence

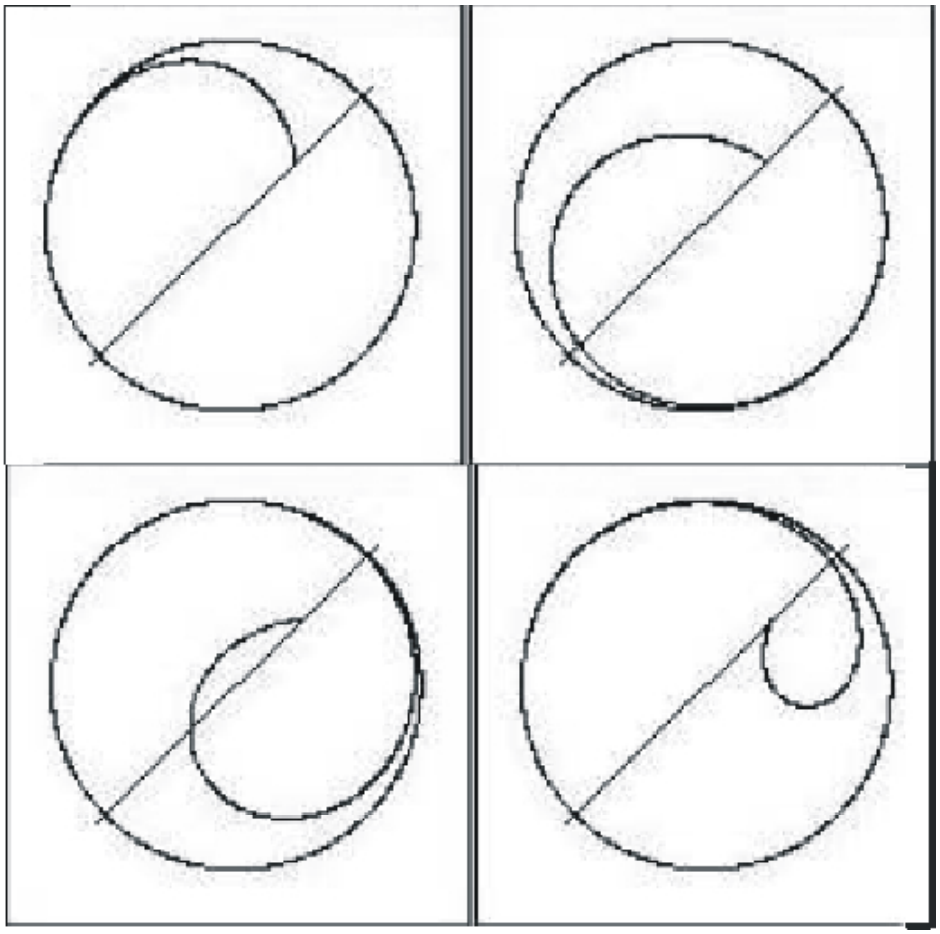

Figure 8.10 Result of numerical integration of Eq.8.11 for configurations of a spiral decay corresponding to the experimental configurations shown in Fig. 8.7.

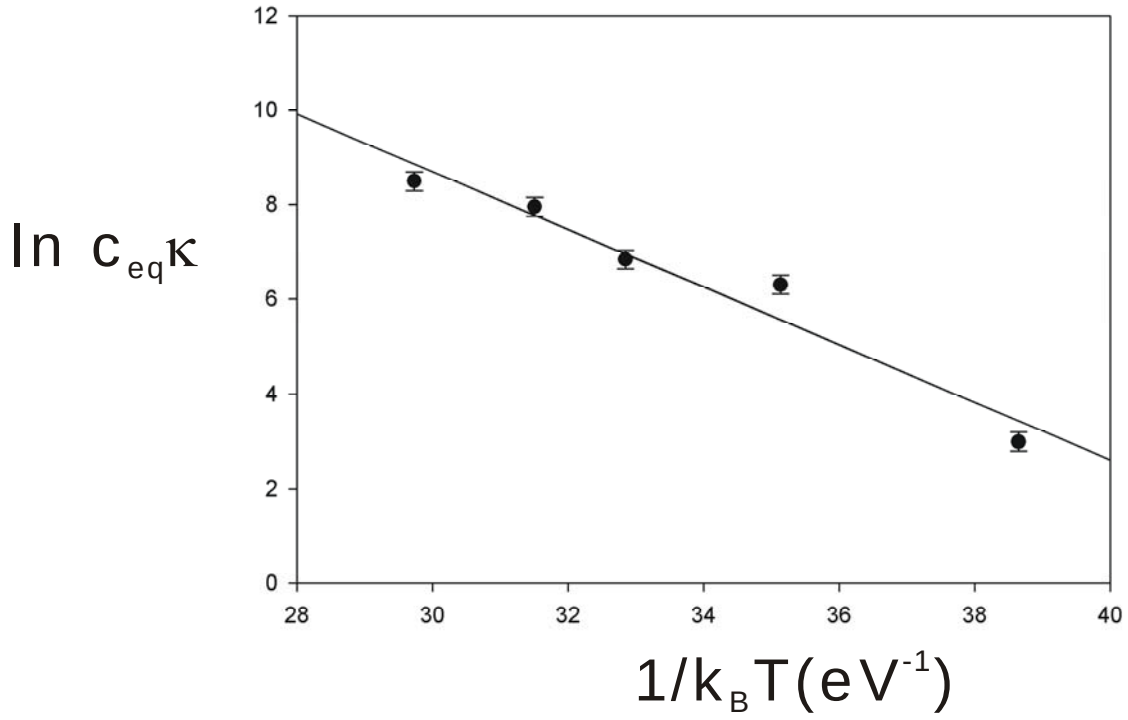

Figure 8.11 Arrhenius plot of all of the kinetic data described in this chapter.

of any limiting assumptions. The other points deviate from the fit line more than these two but only slightly. Thus, it is clear that assuming detachment limited kinetics only results in a small error. In other words, the occurrence of surface diffusion on this surface is a relatively minor effect relative to the slower detachment process. Therefore, the activation energy for detachment determined from these experiments can be considered a fairly accurate result.

8.5 Summary and Conclusions

We have analyzed the kinetics of layer decay for adatom and islands tens of nanometers ion diameter on Pb(111) microfacets assuming a detachment limit. This limit is justified by the approximately linear decay of the island areas with time and the comparison with an exact analysis of earlier work on 3D reshaping of these crystallites. The exact analysis shows that detachment rates are at least a factor of ten slower than surface diffusion rates. From the island decays we extract the product of detachment rate constant and adatom concentration, which is proportional to the step mobility as defined in chapter 1 and used in chapter 3.

In addition to these small-scale decays we observed the 3D reshaping or supported crystallites with a single screw dislocation. This process was modeled by assuming simple geometric constraints, motion driven by the Gibbs-Thomson effect, and a detachment limit. Numerical solution of the resulting partial differential equation gave spiral decay motion consistent with the qualitative motion observed experimentally. It also allowed the extraction of the same product of parameters as in the island decay experiments.

When all of the products $c_{eq}\kappa$ are compiled from the island decays, the spiral reshaping, and the layer reshaping, an internally consistent activated detachment process emerges. The activation energy for detachment and adatom formation is 610 meV and the prefactor is consistent with a phonon frequency. That this consistent picture arises when data from such different length scales are considered suggests that the detachment limit is a good approximation for deterministic mass transport on Pb(111) between 300 K and 390 K. In addition, the data analyzed using the assumption of this limit are consistent with data analyzed without any assumptions about the limiting process.

When there are nonequilibrium features on a Pb(111) surface, we can thus conclude that they will decay by an approximately detachment-limited transport process. As seen in chapter 5, equilibrium step fluctuations seem to be limited by periphery (or step-edge) diffusion. When steps are curved enough, the Gibbs-Thomson effect creates a high concentration of adatoms near the step that allows the detachment process to occur. Under equilibrium conditions where clear PD-limited step fluctuations are observed, the idea is then that detachment may still occur but is balanced by attachment and is not rate-limiting for the fluctuations.

Chapter 9

Electrical transport at solid surfaces

The importance of understanding electrical transport at surfaces and in thin layers is addressed. DC transport properties of disordered systems are introduced with particular attention to issues of the often dramatic changes in transport properties such systems undergo as a function of density. In this context, the onset of conduction in very thin metal films is described using standard percolation theory and exceptions to this type of behavior are also noted. Low-frequency fluctuations in the electrical resistance of such systems are used to gain a more detailed understanding of underlying transport processes than is possible using simple DC measurements alone. The basic measurement techniques for both resistance and resistance fluctuations are described.

9.1 Introduction

9.1.1 Motivation

Previous chapters of this work have focused on the transport of mass at solid surfaces. This work has demonstrated how one can obtain mass transport information, how nanoscale transport observations relate to atomic-scale details, and finally what one can do with such transport information. Naturally, there are other kinds of transport processes at surfaces that rival and perhaps surpass in importance the transport of mass. The simple example of the Field Effect Transistor (FET) provides undeniable proof of this. FET's in their various incarnations are not only of supreme current practical importance, but variations on them are also the most promising candidates for the future development of electronics. In these devices, conduction occurs in an extremely narrow conducting channel where the current is controlled by the application of a gate voltage between the channel and an electrode isolated from it by a dielectric. The conduction in such a channel is essentially a surface problem since charge carriers are confined to a narrow region where their scattering will be dominated by interface effects at the channel/gate junction. For example, the current noise in a Si MOSFET is determined by the charge traps at the channel/SiO_2 interface[138-140]. Thus, charge transport near surfaces (or interfaces) is of imminent practical concern.

An early review of surface conduction described three basic ways that charge can be transported at a surface[141]. Of particular interest to fundamental surface science is the role of metallic *surface states* in the conduction processes at surfaces[141]. While surface states are known to exist without question from spectroscopic measurements, no measurements have yet been made that can unambiguously access their effect on

electrical transport[141, 142]. These states form truly 2D bands (electron wave functions die off exponentially into the bulk or the vacuum) and conduction parallel to the surface should be possible through these bands. The presence of surface states can create a charge separation in the near-surface region that leads to another type of surface conduction. In the presence of charge separation, carriers can be confined to the surface by the resulting dipole field and conduction through the space-charge layer can result. The contribution of space charge layers to surface conductivity is well-studied and understood[141, 142] and will not be addressed further in this work. Finally, and most significantly for what will follow, conduction at the surface can occur through very thin layers of another material grown on the surface. This can mean simply the growth of a very thin film that confines carriers inside its quasi-two-dimensional region but it can also mean the formation of a more conductive surface reconstruction induced by adsorption[142]. In fact, the distinction between a thin ad-layer and an ultra-thin *film* may blur considerably as will be described partially below and in more detail in the next chapter. Such situations provide fertile model systems for developing a basic understanding of surface conduction and our purpose in what follows is to establish the basic machinery with which to understand surface conduction through atomically thin films or adsorbed layers. Essential to this machinery will be dealing with the effects of disorder on electrical conduction.

In the present chapter, the basic picture of DC electrical transport in bulk materials will be reviewed first. The effects of disorder on conduction will then be described. We will recall the basic theoretical models of the onset of conduction in disordered systems and some experimental results pertaining to this topic, particularly for thin films grown

on insulating substrates. Low-frequency fluctuations in the resistance of condensed matter systems will then be introduced as an important tool for understanding electrical transport at the nanoscale and in particular for disordered systems near the onset of conduction.

9.1.2 DC Transport

The standard phenomenological treatment of DC transport can be found in any solid-state physics text[143]. The simplest approach (which can be justified by more complete treatments if necessary) is to write the equation of motion for electrons with a friction term describing their scattering:

$$m\frac{d\vec{v}}{dt} = e\vec{E} - \frac{m}{\tau}\vec{v} \qquad (9.1).$$

Here m is the (effective) mass of the carriers, E is the applied electric field and τ is the momentum relaxation time describing the "friction" due to scattering. Solving this equation for a steady-state velocity (going to the frequency domain and ultimately letting the frequency approach zero) gives the current density in a perfect metal under an applied electric field. If the charge density is n, then the current density must be $\vec{j} = ne\vec{v}$ so that we can write Ohm's law using the steady-state solution to Eq. 9.1 as:

$$\vec{j} = \frac{e^2 n\tau}{m}\vec{E} \qquad (9.2).$$

The proportionality factor between j and E is the so-called Drude conductivity :

$$\sigma = \frac{e^2 n\tau}{m} \qquad (9.3).$$

The quantity τ, the relaxation time, is the essential phenomenological parameter of this simple picture. It is proportional to the inverse friction coefficient for the scattering processes and cannot be understood in detail without more complete microscopic theories of conduction.

The above classical equations describe what is known as *diffusive transport*. The equations of motion are obtained simply from the steady balance between accelerating electric fields and opposing friction forces due to the collisions of charge carriers (presumably with phonons, but other scatterers can be treated in this framework). From the relaxation time and the typical carrier velocity one can estimate the mean-free path between scattering events. We can write that $\lambda = v_F \tau$ where λ is the mean-free path and v_F is the Fermi-velocity (only carriers near the Fermi-level of a metal are active in transport[143]).

There are many ways in which the Drude model can fail and most can be traced back to issues with the carrier mean-free path. For example, *ballistic transport* can result when the mean-free path is larger than the sample and carriers can travel across it without scattering[144]. More important to the discussion that follows is the situation where strong disorder in a solid system makes the entire concept of a carrier mean-free path ill-defined. Disorder can reduce the free path of carriers to the point where it becomes smaller than the interatomic spacing, *a*, of the solid. Carriers are then essentially localized, and the notion of them moving as a classical gas between collisions is no longer valid. This leads to the idea of Ioffe and Regel[145] that the interatomic spacing is the minimum sensible mean-free path for a carrier and that anything below this value indicates an insulating sample. In the two dimensions relevant to surface conductivity, this brings up the

interesting possibility of a universal minimum conductance for a metal[146]. The Fermi wave vector for a 2D system is $k_F = \sqrt{2\pi n}$, and when this is substituted into the Drude conductivity we get

$$\sigma = \left(\frac{e^2}{2\pi\hbar} \right) \lambda k_F \qquad (9.4)$$

where λ is the mean-free path and the quantity in parenthesis is a universal constant. Since $k_F \sim 1/a$, the minimum metallic conductivity occurs when $l \sim a$ or $k_F\lambda \sim 1$. This gives:

$$\sigma_{\min} = \left(\frac{e^2}{2\pi\hbar} \right) \qquad (9.5).$$

Numerically, this means that the maximum resistance of a *metal* is 25.8 kΩ in 2D. This interesting result has been called into question by a more sophisticated theoretical treatment which suggests that a true metal does not exist in 2D. Nevertheless, it is clear that conduction in highly disordered systems is quite distinct from the ordinary Drude picture. In 3D, violations of the Ioffe-Regel criterion are common and include high-T_c superconductors and doped fullerenes.

9.2 Percolation Theory

The standard phenomenological description of disordered systems uses the ideas of *percolation theory*[147-150]. This theory describes the structure and properties of systems with at least somewhat random geometries. For strongly disordered systems, this is often enough to capture the essential physics. Percolation theory has been applied to such

diverse topics as flow in porous media, magnetic semiconductors, as well as electrical transport in disordered systems.

Imagine a square lattice, where sites are occupied with probability p (and thus vacant with probability (1-p)). For small p, very few lattice sites will be occupied and the lattice will look like figure 9.1.a, where white represents occupied sites and black represents vacant ones. The system consists of randomly distributed, isolated clusters of varying sizes. If p is increased enough, there is a critical value p_c where there suddenly exists a cluster large enough to span the entire lattice (see Fig 9.1b). Above this p_c, more and more lattice sites become connected to the spanning cluster and the lattice becomes more completely filled with occupied sites as shown in figure 9.1c. Alternatively, one could imagine connecting bonds between sites with probability p, so-called *bond percolation*. This variant changes only exact critical p but none of the more generic scaling results to be described below. If the occupied sites (or connected bonds) represent a high conductivity species and the unoccupied site represent an insulating species, the lattice system could describe localized conduction in the sense of the previous section. In fact the use of such *random resistor networks* has been a popular theoretical technique.

The percolation model as described is very simple, but the question remains as to how we can really exploit it. What makes percolation so powerful is that it displays a continuous phase transition as a function of occupation probability p that is directly analogous to thermal phase transitions well-known from equilibrium statistical mechanics. Percolation describes a *geometric* phase transition, but quantities can be defined that have universal scaling near p_c just like, for example, the Ising model of

ferromagnetism. It has even been demonstrated that there is a one-to-one correspondence between random percolation and the 1-state Potts model[151]. Let *P(p)* be the probability of belonging to the spanning cluster as a function of *p*. Below p_c, the spanning cluster does not exist so *P(p) = 0*. At p_c, the *P(p)* becomes finite and rapidly grows via a universal power law: $P(p) \sim (p-p_c)^{\beta}$. Thus, the quantity *P(p)* is the *order parameter* for percolation analogous to the average magnetization in the Ising model[147, 150]. Any other quantity of interest in thermal phase transitions has an analogy in percolation theory. The exponents are universal in the sense of ordinary critical phenomena (they depend only on spatial dimension: in 2D $\beta = 5/36$[152]) but the critical probabilities depend on details like whether percolation occurs on a discrete lattice and what the symmetry of the lattice is.

Yet still, what does this tell us about electrical transport? Equilibrium critical phenomena describe static properties, so we can't expect to reason by analogy to understand charge transport in this model of a disordered conductor. At first we might like to guess that the conductance across the lattice is simply proportional to *P(p)* but this turns out to be incorrect[153]. The entire spanning cluster does not participate in conduction since there are numerous dead ends. Luckily, the conductance of the lattice seems to obey a universal scaling law at the percolation threshold, but with a unique *non-thermal* exponent t:

$$G(p) = (p - p_c)^t \qquad (9.6).$$

In two dimensions, numerical studies show that $t \sim 1.32$[147, 150, 153, 154]. This is significantly greater than the order parameter exponent β, reflecting the fact that, once the spanning cluster forms, its conductivity grows much more rapidly than the number of

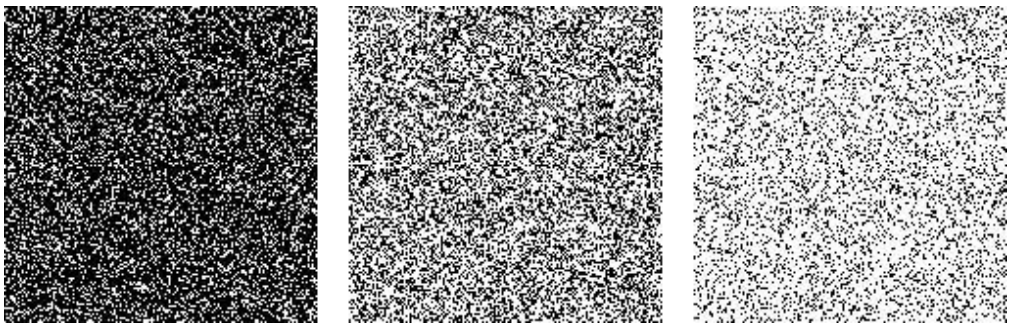

Figure 9.1 Examples of random percolation generated on a square lattice. Form left to right the occupation probability is 0.2, 0.593, and 0.8. The lattice in the center is an example of a lattice at the theoretical critical point for the square lattice.

sites belonging to it (since many sites are just dead ends).

Experimental evidence for the critical scaling shown in Eq. 9.6 is quite remarkable in its diversity. Song and co-workers[155] measured an exponent in agreement with theoretical predictions for chrome masks on glass substrates that had been etched away randomly using electron beam lithography techniques. In addition, they measured a critical probability of 0.5, very close to the prediction for a square lattice of $p_c=0.593$. Alternatively, Octavio and co-workers measured the exponent for Ag films grown at 77 K on a glass substrate by vapor deposition in high vacuum[156]. Even more surprisingly, the theoretical conductance exponent was also found by Lobb and Forrester[157] by milling holes randomly into a sheet of steel. Thus, the claim that the conductance exponent is "universal" is well-supported given the remarkable differences in underlying details of the experiments mentioned.

The value of understanding the origin of apparently universal scaling is unquestionable. Particularly in the case of electrical transport, however, more extensive microscopic details are necessary in practice. Percolation is a phenomenological model, and part of its value is that it is independent of many microscopic details. It has nevertheless been used in the past to calculate very detailed properties of disordered conductors[147, 148]. Specifically conduction processes by which carriers thermally hop from one localized state to another are well-modeled within a percolation framework. The basic idea (described in several standard reviews [147, 148]) is to use a master equation for the rates of carrier transfer between sites of a percolation (i.e. random resistor) network and use this equation to calculate observable transport properties.

There are two important regimes of hopping conduction appropriate to transport at a surface with strong disorder. The first is simply activated hopping in which a carrier is transferred to its nearest neighboring localized site by surmounting an energy barrier E. In this case the sample resistance is given by:

$$R = R_0 \exp\left(\frac{2r}{a}\right)\exp\left(\frac{E}{k_B T}\right) \qquad (9.7).$$

The first factor essentially gives the tunneling rate between localized states separated by a distance r. *Near-neighbor hopping* is generally expected at relative high temperatures when the second factor in Eq. 9.7 is nearly unity [141, 147, 148]. A second type of hopping conduction is possible when the energy barrier to hop to a near neighbor site is high enough that hopping to farther neighbor sites (with smaller barriers) is actually more likely. This has been termed *variable range hopping* and is a common process at very low temperatures. The form of the resistance of a system due to VRH is distinct from ordinary hopping and the resistance for a *d*-dimensional sample is[141, 147, 148, 158]:

$$R = R_0 \exp\left(\frac{T_0}{T}\right)^{\frac{1}{d+1}} \qquad (9.8).$$

The temperature dependence of resistance, as given in equations 9.7 and 9.8, is typically considered the most important characterization of the electrical transport properties of a system. In the next section, we will describe yet another characterization, the resistance fluctuation spectrum, that can provide even more subtle details about the conduction processes. The next chapter will then apply the critical percolation exponents, temperature dependence of resistance, and resistance fluctuation spectra to a transport problem of considerable interest in surface science.

9.3 Resistance Fluctuations in Disordered Conductors

A remarkable number of condensed matter systems show voltage fluctuations that scale roughly inversely with frequency under DC bias[138-140, 153]. The intriguing possibility of a universal mechanism for such so-called *1/f* noise seems to be a red herring[140], but the study of low-frequency noise in specific situations has been found to be very useful as a tool for unraveling details of conduction in solids[139]. For many bulk or thin film metals, the low-frequency fluctuations have been correlated successfully with the slow motion of defects[139, 140]. These fluctuations, while often measured as current or voltage noise, are generally attributed physically to fluctuations in the *resistance* of the system in question. Thus, they provide a valuable and material-specific transport tool[139]. Empirically, Hooge developed the following formula[159]:

$$S_V = \frac{\alpha V^2}{Nf} \qquad (9.9),$$

where S_v is the Fourier transform of the voltage autocorrelation (power-spectral density), N is the number of carriers, V is the DC bias voltage, f is the frequency, and α is a phenomenological noise magnitude that may depend on material and temperature[138-140, 153]. Despite the fact that 1/f noise did not turn out to be as deeply significant as was suggested initially by its ubiquity, it continues to be a valuable topic of research.

Rather than focusing on the form of the resistance fluctuation spectra for disordered systems, however, we will pay closer attention to the *magnitude* of low-frequency noise in disordered systems and how it scales near a percolation threshold. The model will simply be to imagine the random resistors that make up a percolation network all fluctuating essentially independently[153]. The exact spectral form of the fluctuations turns out not to be particularly important in what will follow but, as noted

already, it is typically a *1/f* – type spectrum[153, 160, 161]. The random network then has a fluctuation in total resistance given by (for applied current I)[153]

$$\delta R(t) = \sum_m (i_m^2 / I^2)\delta r_m(t) \qquad (9.10)$$

with i_m equal to the current through the mth link of the network and δr_m the fluctuation in the individual resistor making up the mth link. The quantity of experimental interest is the spectral density of the resistance fluctuations for the individual resistors, which is twice the Fourier transform of the resistance autocorrelation function:

$$s(f) = 2\int \langle \delta r(t)\delta r(0)\rangle \exp(i\omega t)dt\,. \qquad (9.11)$$

In fact this could be re-written in terms of voltage or current autocorrelation functions but resistance is in reality the relevant physical quantity. The scaled noise can be written for the percolation network as follows (letting applied current I = 1)[153]

$$\frac{S_R}{R^2} = s(f)\frac{\sum_m i_m^4}{(\sum_m i_m^2)^2} \qquad (9.12)$$

where s(f) is the spectral density. Not surprisingly, the scaled resistance noise displays critical behavior near the percolation transition. It has a new critical exponent, κ, which is found from[153, 160, 161]:

$$\frac{S_R}{R^2} \sim (p - p_c)^{-\kappa}\,. \qquad (9.13)$$

Interestingly, this new exponent is not nearly as insensitive to underlying details of the percolating system as the conductance exponent. For example, on a discrete lattice of resistors, κ takes a value of 1.339[160]. Alternatively, if a lattice is not involved and we imagine filling a continuous region with conducting disks (the inverted random void

model), then near the point when the disks form a percolating path, κ takes a value of 1.15[161]. Even more surprisingly, if we approach the threshold from above by removing conducting material from a continuous conducting region, the so-called random-void model, then $\kappa \sim 4.2$[161]. It is essential to stress that in all three cases *the conductance exponent is the same*. The noise is therefore a more sensitive characterization of the details of disordered transport than the conductance alone. As seen in Eq. 9.11, the scaled noise depends on the fourth moment of the current distribution in the network whereas the total resistance of the network depends only on the second moment[153].

Many experiments have been performed to measure the critical behavior of noise[153, 155, 156, 162, 163] and its extraordinary sensitivity to underlying details of the systems under study is evident. While observations of scaling exponents consistent with the inverted random void model are common[155, 156], systems are often found that seem to have large exponents not necessarily consistent with the random void model[162, 163]. In particular, Garfunkel and Weissman sandblasted gold film and found large noise exponents that scattered significantly[163]. While this situation is somewhat unsatisfactory, it highlights the potential utility of noise measurements; presumably modified models can be found that capture enough of the essential physics of those experiments to understand the observed noise scaling.

In the following chapter, we will apply the ideas developed here to a new experimental system that has been of interest to surface science in recent decades. It is hoped that the level of detail offered by combining measurements of the several types of transport properties described will be sufficient to understand almost any kind of transport in disordered systems. In fact, there are levels of sophistication beyond what

has been described above that can be employed if needed. For example, the variable-range hopping conduction formula has often been found to be modified when conduction occurs on a fractal backbone[147]. In any case, the basic ideas of this chapter will still be relevant after suitable modification.

Chapter 10

Resistance Noise and Nanoscale Morphology in Percolating Films of Ag on Si(111)

The transport properties of Ag films grown at temperatures less than 150K on a Si(111)-(7x7) substrate have been correlated with simultaneous observations of film structure using low-temperature STM. The previously observed percolation-type conduction onset between 0.7 ML and 1.1 ML was verified and resistance-noise measurements have been made to check the details of the percolation model. The noise critical exponent suggests that the best model for the conduction onset is an off-lattice Inverted Random Void model and that the conducting paths are simply overlapping islands of disordered Ag. Despite the critical increase of film conductance, the conducting paths remain strongly disordered and transport is via hopping between localized states.

10.1 Introduction

The growth of Ag on Si(111)-(7x7) at low temperatures provides a nice demonstration of how to control film morphology with growth kinetics. At high temperatures, Ag tends to grow in a Volmer-Weber mode and therefore form large 3D islands. By lowering the temperature, and thus the Ag mobility, the tendency to form islands can be suppressed and growth is closer to layer-by-layer. At sufficiently low temperatures, less than about 150 K, growth is nearly perfectly two-dimensional[142, 164-169]. Of course, this altered growth mode at low temperatures has consequences for film properties. Most dramatically, the film conductivity was observed to increase abruptly when only submonolayer quantities of Ag had been deposited[166]. The conductance increase in fact displayed critical scaling consistent with a two-dimensional percolation process.

As mentioned in the previous chapter, percolation is a kind of continuous *geometric* phase transition and therefore the morphology of the film in its critical region should be of great interest. This was immediately recognized by Heun et al.[166] who suggested in-situ low-temperature STM as a valuable future experiment. Indeed, several years after the initial electrical transport measurements, Meyer and Rieder[169] were able to perform the in-situ STM measurements on Ag films grown at about 80 K. Their measurements showed a fairly granular film morphology at 0.85 ML of Ag, which they judged to be in the critical regime of Heun et al[166]. Naturally, after these two experiments, there remained open questions as to the details of the remarkable conduction onset in this system. Most glaringly, the granular appearance of the 0.85 ML films in the STM study[169] suggested that some sort of tunneling process might be

involved in the conduction across the film[169]. Furthermore, the amazingly small film thickness at which percolation was observed made plausible the notion that the percolation might not necessarily be through the deposited silver at all but rather mediated by the (7x7) substrate[142, 166, 169, 170]. Here we see a situation, hinted at in the last chapter, where the line between conduction through an ultra-thin layer and surface conduction changes due to adsorption becomes rather blurred.

In the present chapter we describe new experiments on Ag films grown on Si(111)-(7x7) at temperatures between 50 K and 130 K that attempt to clarify some of the open questions concerning the apparent percolation transition. We will describe simultaneous in-situ measurements of film conductance and film morphology that allow an unambiguous observation of the film in the critical regime. We also measure the low-frequency resistance noise of films in the critical regime in an effort to understand the possible role of the substrate in the percolation process. Finally, we measure the temperature dependence of film resistance to gain more microscopic insight into the transport processes.

10.2 Experiment

Experiments described in this chapter were performed in two separate UHV chambers. Measurements of resistance and resistance noise of percolating Ag films were made in a stainless steel UHV chamber with base pressure better than 10^{-10} torr (~$7x10^{-11}$ torr). In this chamber, the samples were mounted with tantalum spring clips on a sapphire plate that was glued with indium to a homemade OFHC cooling fin as shown in

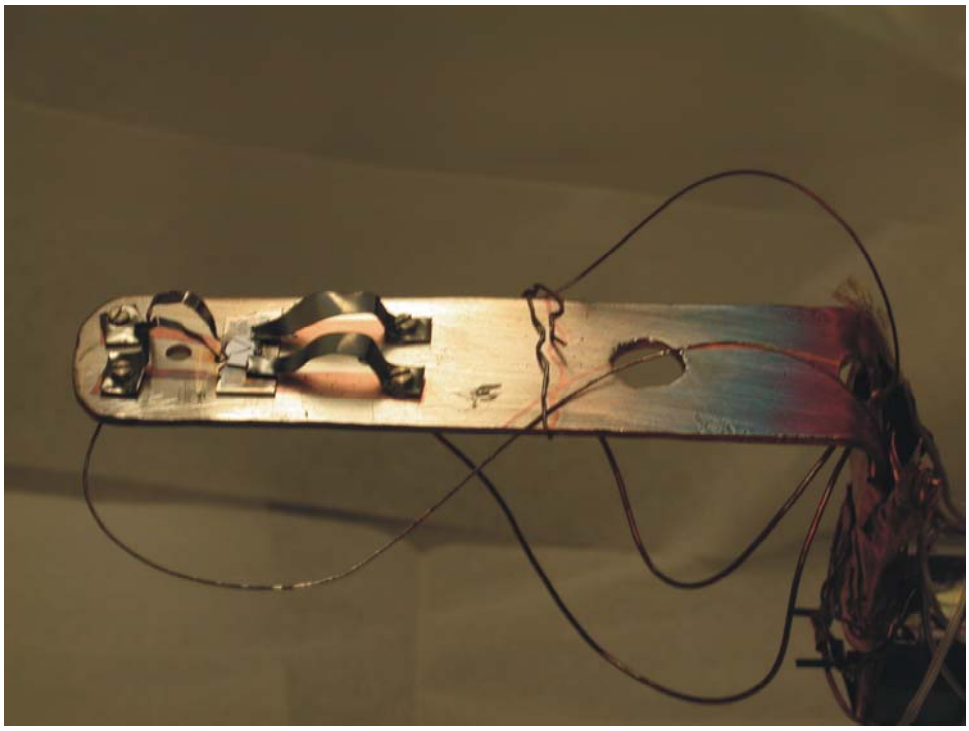

Figure 10.1 OFHC sample mount showing tantalum clips holding the sample to a sapphire insulator. The angled bracket is bolted to a liquid nitrogen reservoir.

figure 10.1. The fin was bolted to the bottom of a liquid nitrogen reservoir that itself was mounted on a differentially pumped rotary stage (continuously pumped by a mini-ion pump). The base sample temperature was calibrated several times by placing a K-type thermocouple in strong contact with a dummy Si sample and was found to be about 100 K. Silver metal was evaporated from an Al_2O_3 tube that was heated by a Tungsten coil wrapped tightly around its entire length. The Ag evaporator was shielded with a tantalum foil disk, but some radiative heating of the sample during film growth was unavoidable. This was not significant enough to change the 2D growth mode of the film and therefore could not have been more than 30-50 K. Silver flux was calibrated with a Quartz Crystal Micobalance (Inficon) that could be moved to the sample position. Sample cleanliness and order was sometimes checked by AES and LEED respectively.

Simultaneous in-situ measurements of film resistance and film morphology were performed in a separate vacuum system. This system was purchased from JEOL and consists of two independently ion-pumped steel chambers: one for sample preparation and one for STM/AFM observation with the JEOL 4500 SPM system. The microscope chamber has a bath cryostat capable of cooling the sample to 100 K with liquid nitrogen or 50 K with liquid helium. Ag was evaporated with the sample on the cold stage from resistively-heated tungsten wire basket. The Ag flux was calibrated periodically by deposition onto a room temperature Si(111)-(7x7) substrate and counting the apparent number of Ag atoms using published results for the number of Ag atoms expected in clusters[164]. In all of the measurements reported in this chapter 1ML is defined as the number of Ag atoms in a perfect Ag(111) plane : 1.5×10^{15} cm^{-2}. The observation chamber also has a scanning electron microscope (JEOL) that can be used to position an

SPM tip over an area of interest on the sample that might be too small to reliably access using optical techniques. The base pressure in the observation chamber is about $5x10^{-10}$ torr and about $1x10^{-10}$ torr in the sample preparation chamber. An SEM image of a typical sample mounted in the commercial JEOL sample holder and installed in the cold SPM stage is shown in figure 10.2. Also in the field of view is a Pt-coated AFM cantilever. The results presented in this chapter were mostly obtained using STM for the observation of film morphology, but some AFM observations were also made. The lighter regions are Molybdenum electrical contacts and the darker region below the cantilever is bare Si(111)-(7x7).

The reliable measurement of electrical transport properties of submonolayer films presents substantial difficulties[142, 166, 167]. We performed measurements more or less in accord with the techniques used in the original transport measurement of Heun et al.[166, 167] The Si(111) substrates used were very low-doped (B-doped, nominally 1000 Ω cm) to minimize conduction through the substrate bulk. We pre-deposited 70 – 100 nm thick molybdenum contact pads (using electron beam evaporation) on small pieces of the (111) wafers and then sonicated them for several minutes each in acetone, ethanol, and deionized water. Samples were mounted either in the commercial sample holder required for use with the JEOL system or on the homemade cooling fin used in the dedicated transport chamber. After installing the sample in vacuum and recovering the expected base pressure, the samples were outgassed for several hours at temperatures between 500 and 1000 K. They were then flashed (following the procedure in Appendix A) to 1500 K in the transport chamber or about 1300 K in the JEOL preparation chamber. The

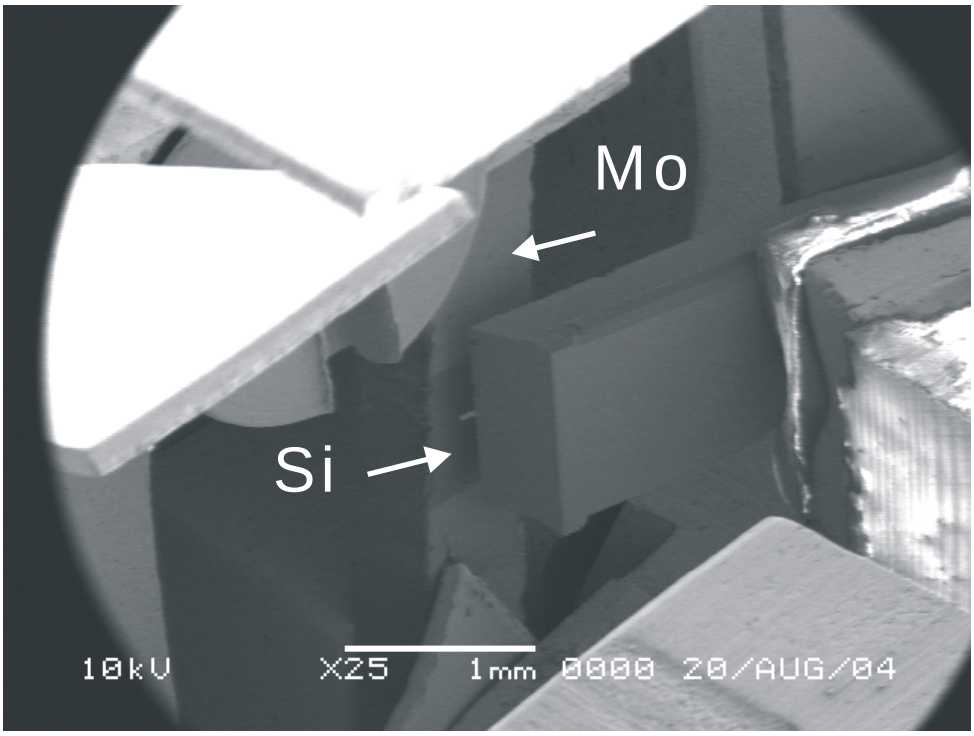

Figure 10.2 SEM image of a Si(111) sample with Mo contacts mounted in a JEOL sample holder and installed in the STM/AFM stage. A Pt coated AFM cantilever is also visible over the sample.

maximum pressure during flashing was always kept around $1x10^{-9}$ torr. Samples were cooled (primarily with liquid nitrogen) and Ag growth started within 20-45 minutes.

Resistance measurements reported in this work were all made with a 2-contact technique using a Keithley Model 2000 DVM (input impedance >10 GΩ). A constant current was driven through the pre-deposited molybdenum contacts and the resulting voltage drop across these same contacts measured (100 averages were made for each resistance measurement). A schematic of the measurement set-up is shown in figure 10.3a. The film resistance was calculated from the total measured resistance by modeling the system as the parallel combination of the substrate resistance (measured upon initial cool-down) and the film resistance. Because of the simple two-contact measurement, there was always a contribution to this value from the contact resistance. We have assumed this contribution is simply a constant offset to the measurements and that it will not impede the observation of critical behavior near the onset of conduction. As will be described below, this assumption is justified *a posteriori* by the agreement between our measurements and the previous four-contact measurements of Heun et al[166].

Resistance noise measurements were made using the same contact geometry on very highly resistive substrates. Any significant conduction through the bulk Si(111) wafer added enough noise to the measurement to mask any Ag coverage-induced changes in noise magnitude. Only rarely did we obtain substrates that were resistive enough to perform sensible noise measurements. In the two-contact set-up, we applied a constant DC bias across the sample using a battery (1.5 V – 21 V) and amplified the resulting current using an SRS570 low-noise current pre-amplifier. The current was first high-pass

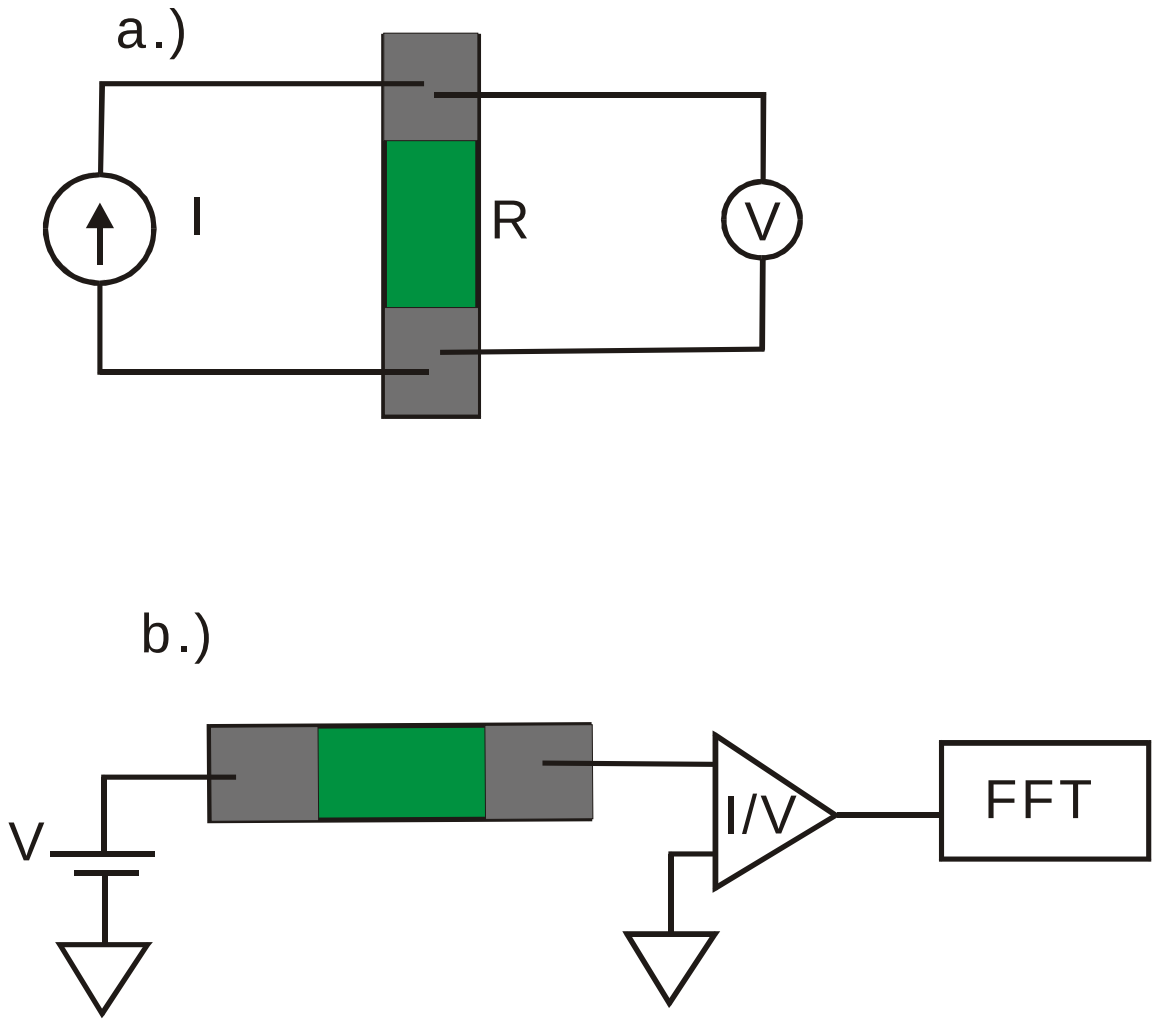

Figure 10.3 a.) Schematic of how the Keithley 2000 DVM measures sample resistance with 2-contacts. b.) Schematic of current noise measurement set-up where the sample is biased with a battery and the amplified current sent to an FFT analyzer.

filtered (with the amplifier's internal filters) with a 12 dB roll off at about 0.1 Hz. After amplification, the (voltage) signal was passed to an SRS760 Fast Fourier Transform analyzer where 1000 averages of the power spectral density were made usually with a frequency span from DC to 20-390 Hz.

Figure 10.3b shows a schematic of the current noise measurement.

Film morphology was observed using the JEOL 4500 SPM primarily in constant-current STM mode. Electrochemically etched tungsten tips were baked for 7 hours in the JEOL preparation chamber and then immediately used for imaging. We employed a wide range of tunneling parameters to obtain stable results but did not notice any clear dependence of film morphology on these parameters (e.g. no clear voltage dependent features were observed).

10.3 Results

Figure 10.4 shows an example of film conductance versus reduced coverage during low-temperature film growth in the dedicated transport chamber described in the previous section. The solid line is a linear fit to the data on a double-log scale and shows that even relatively simple two-contact measurements can uncover the critical behavior of the film conductance. Over the course of more than a year, measurements like the one shown in Fig. 10.4 were made on many different pieces of different Si wafers with different nominal Mo contact thicknesses. In the overwhelming majority of growth runs, the conductance critical exponent t obtained from fitting the data were in the range 0.8 to 1.5. In fact, on average we obtained very good agreement with the percolation prediction

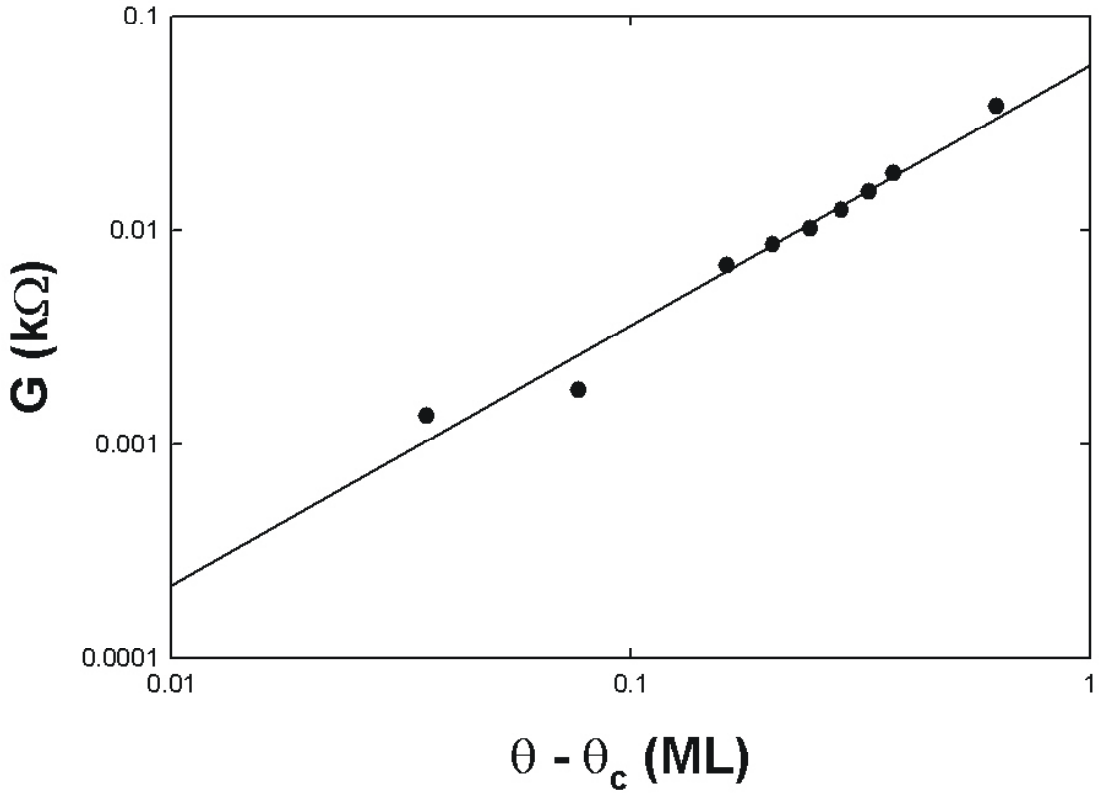

Figure 10.4 Film conductance at 130 K shown versus reduced coverage on a log-log scale. The solid line is a linear fit whose slope gives a conductance exponent of 1.2±0.1. The critical coverage in this case was 0.6 ML.

of t ~1.32. Thus, our rather extensive set of measurements of film conductance confirm and reproduce the percolation behavior first observed by Heun et al.[166] The critical coverage used in figure 10.4 was judged by plotting film conductance versus coverage on a linear scale and extrapolating the apparent conductance onset back to zero conductance. The coverage at which the extrapolation intercepted $G=0$ was taken as the critical coverage. Again, our results for the critical coverage confirmed the initial measurements and fell in the range of 0.6 to 1.1 ML. In the results that follow, we point out that it is possible in many cases to find a better fit to the data by letting the critical coverage be a free parameter. Often this resulted in critical coverage lower than the coverage for which a change in sample conductance was observed. Thus, we judge those fit results to be physically invalid and follow Heun et al. in fixing θ_c as the coverage for which a film conduction onset could be *measured*.

In the JEOL chamber we could monitor typical film morphologies for identically prepared samples at low temperature. Figure 10.5 shows a sequence of STM images taken at 100 K for various Ag coverages. At less than 0.5 ML, we see the film dominated by isolated Ag islands (~ 1.5 Å in height) on top of a low-density (~0.25 ML) wetting layer. As the Ag coverage is increased, the number and size of these islands also increases while the distance between them decreases. When the coverage reaches about 1ML, there seem to be more or less connected pathways of Ag islands across the images, and presumably the films are percolated.

The primary goal of this experiment, however, is to make a *direct* correlation between the conduction onset evident in the curve in Fig. 10.4 and the morphology of the Ag film. In the top panel of figure 10.6 we show another example of a film conductance

versus reduced coverage plot (this time on a linear scale). This curve was obtained in-situ in the JEOL cold stage in the observation chamber. The solid line is a power-law fit to the data and again shows good agreement with the 2D-percolation model. The lower panel of figure 10.6 shows a sequence of STM images obtained at various steps *during the same growth run*. In other words, while obtaining the conductance curve, growth was periodically interrupted to monitor the film structure. The lower panel shows essentially the same morphological features as figure 10.5 for coverages of 0.4, 0.85, 0.95, and 1.0 ML. Most importantly, within 0.15 ML (at 0.85 ML for this particular film) of the conduction onset, we observe Ag islands seemingly just barely creating a continuous pathway across the field of view of the STM.

In the dedicated transport chamber we made noise measurements on several of the films for which the substrate resistance was high enough at low temperature (greater in fact than 100 MΩ). Figure 10.7 shows an example of power spectral densities of current noise expressed in terms of reduced resistance noise. These spectra scale approximately inversely with frequency like many other solid-state systems[138-140, 153]. More importantly, the magnitude of the noise decreases as the film becomes more continuous. To characterize the dependence of noise magnitude on Ag coverage, we multiply the quantity S_R/R^2 by the power of frequency determined by least squares fits to the spectra (solid lines in figure 10.7 with slopes between 0.9 and 1.2). The result of computing this quantity should be a constant that characterizes the noise magnitude. We show the average value of this quantity from 1 Hz to 24 Hz (frequency span picked to make sure none of the interference at 60 Hz and their harmonics contribute anomalously to the

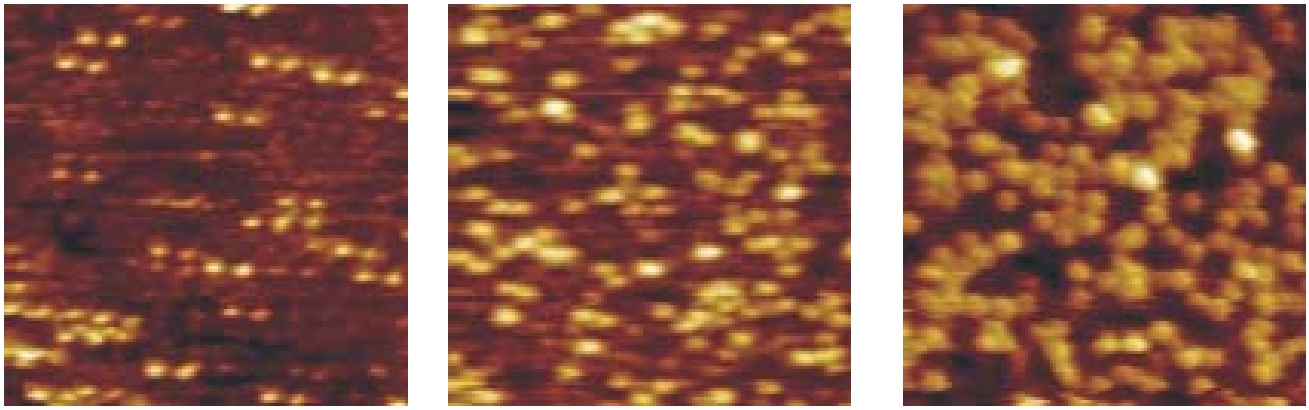

Figure 10.5 From left to right, 0.4. 0.8, and 1.0 ML of Ag deposited on Si(111)-(7x7) at 100K.

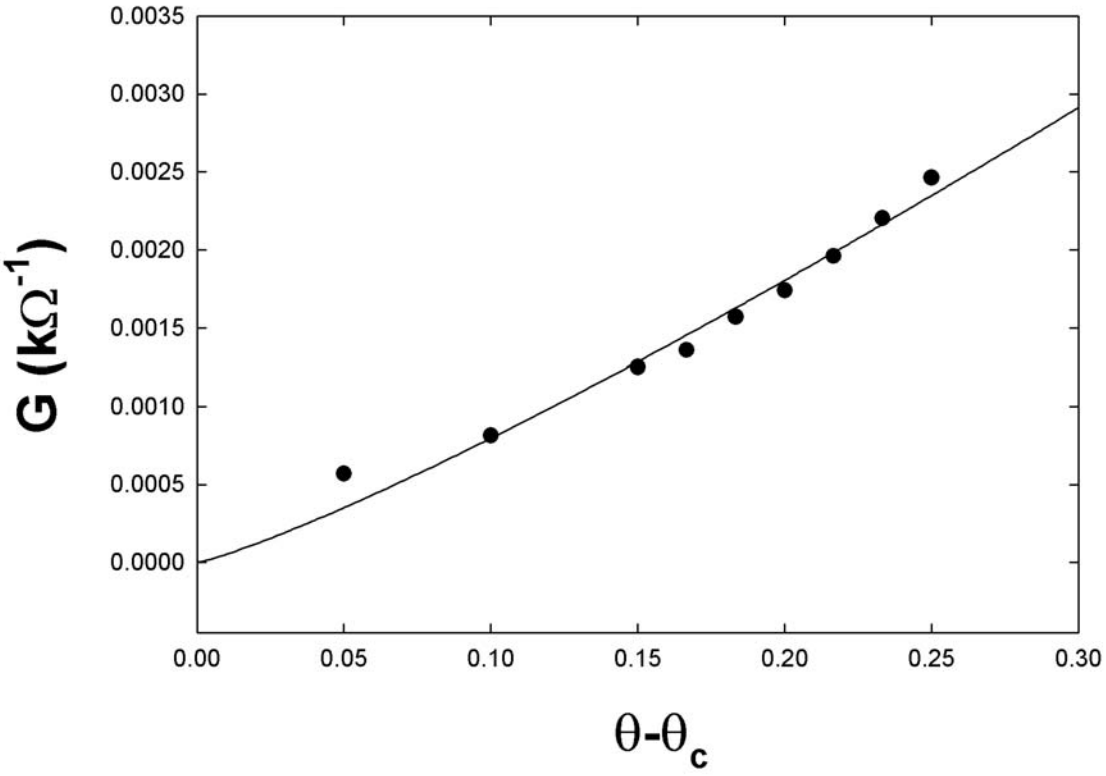

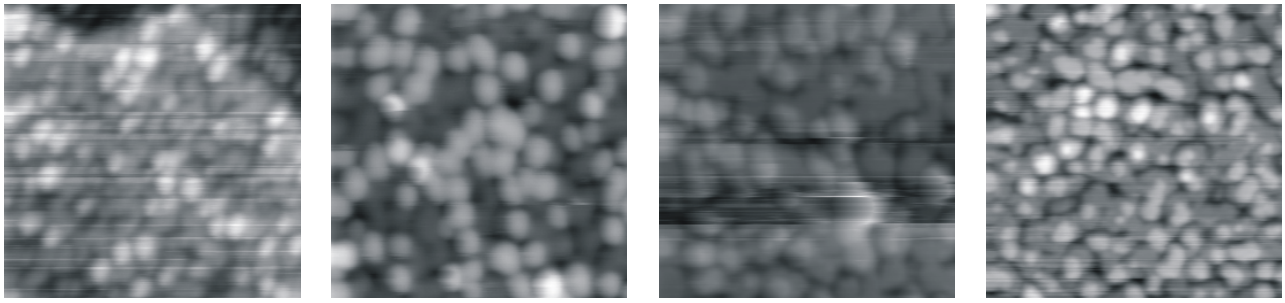

Figure 10.6 Top : Conductance versus reduced coverage with solid line showing the power law fit to the data. The critical coverage is 0.7 ML. Bottom: STM images taken during growth at 100 K for the experiment in the top plot. From left to right: 0.4, 0.85, 0.95, 1.0 ML. All images $(50\ nm)^2$.

magnitude). Figure 10.8a shows the averaged noise magnitude and its probable error[171] versus Ag coverage for three separate growth runs on two different (but identically prepared) Si(111) substrates. Figure 10.8b shows the result of plotting the same data points versus reduced coverage. The data collapse is far from perfect but the tendency to collapse is nevertheless clear, strongly suggesting critical behavior of the noise associated with percolation. In fact, if we fit all the data in figure 10.8b to a straight line, we obtain a noise critical exponent of 1.06±0.09. So, despite being more difficult to observe than the conductance critical behavior, the resistance noise of the Ag films also seems to display critical scaling with coverage.

Finally, figure 10.9 shows two measurements of the temperature dependence of resistance of approximately 1 ML Ag films. The plot in 10.9a was obtained in the transport chamber where only liquid nitrogen cooling was possible. In both cases measurements were made as cryogen boiled off and temperature was monitored by a sensor near the sample (K-type thermocouple for Nitrogen cooling and Si diode for He cooling). The semi-log axes show that for low enough temperatures the conduction is activated. Above about 155 K, there is an abrupt and irreversible change due to annealing of the film. The solid curve is a linear fit to the data for temperatures below 155 K, and gives an activation energy of 48.3 meV and a resistance prefactor of 11.1 kΩ. The plot in 10.9b was obtained in the JEOL observation chamber using liquid Helium cooling to obtain a wider range of temperatures. Again, a semi-log plot shows simple activated conduction with an energy of 13.7 meV and a resistance prefactor of 11.8 kΩ. Fits were also possible to alternative models of the form

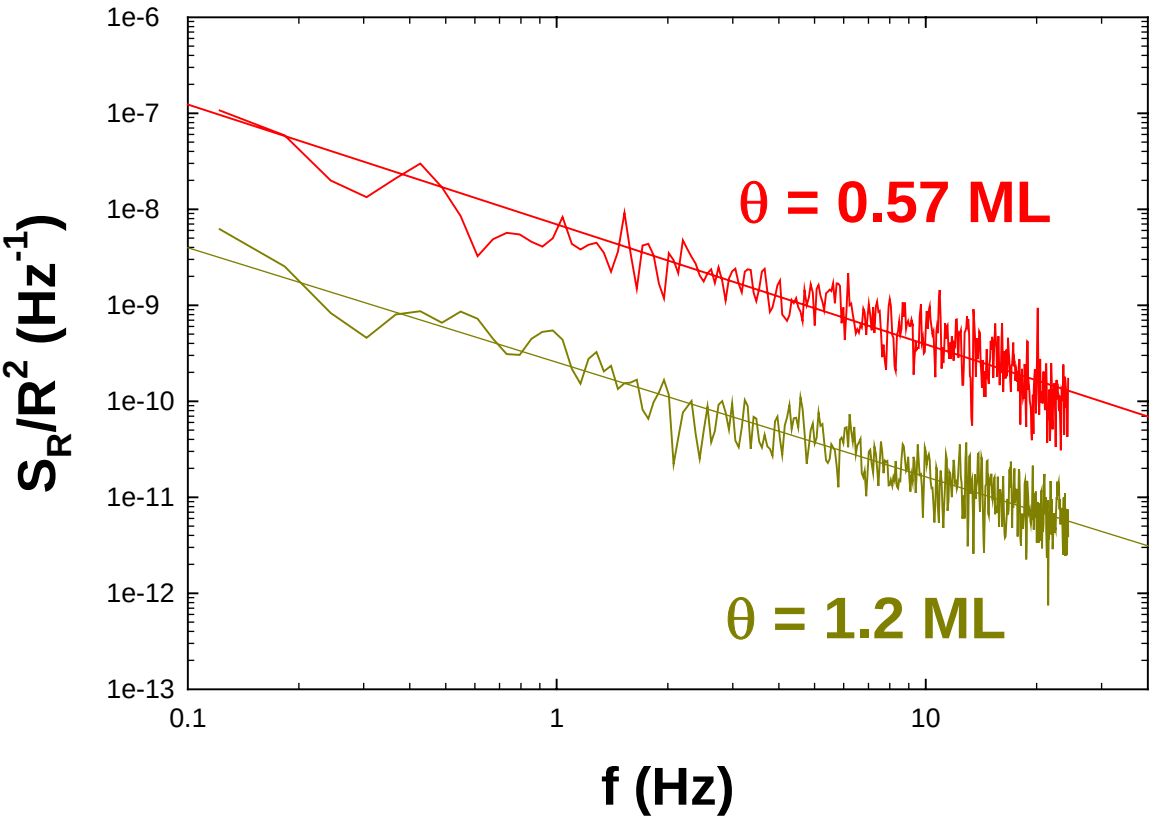

Figure 10.7 Typical noise spectra during Ag growth at 130 K. The critical coverage for this film was 0.6 ML.

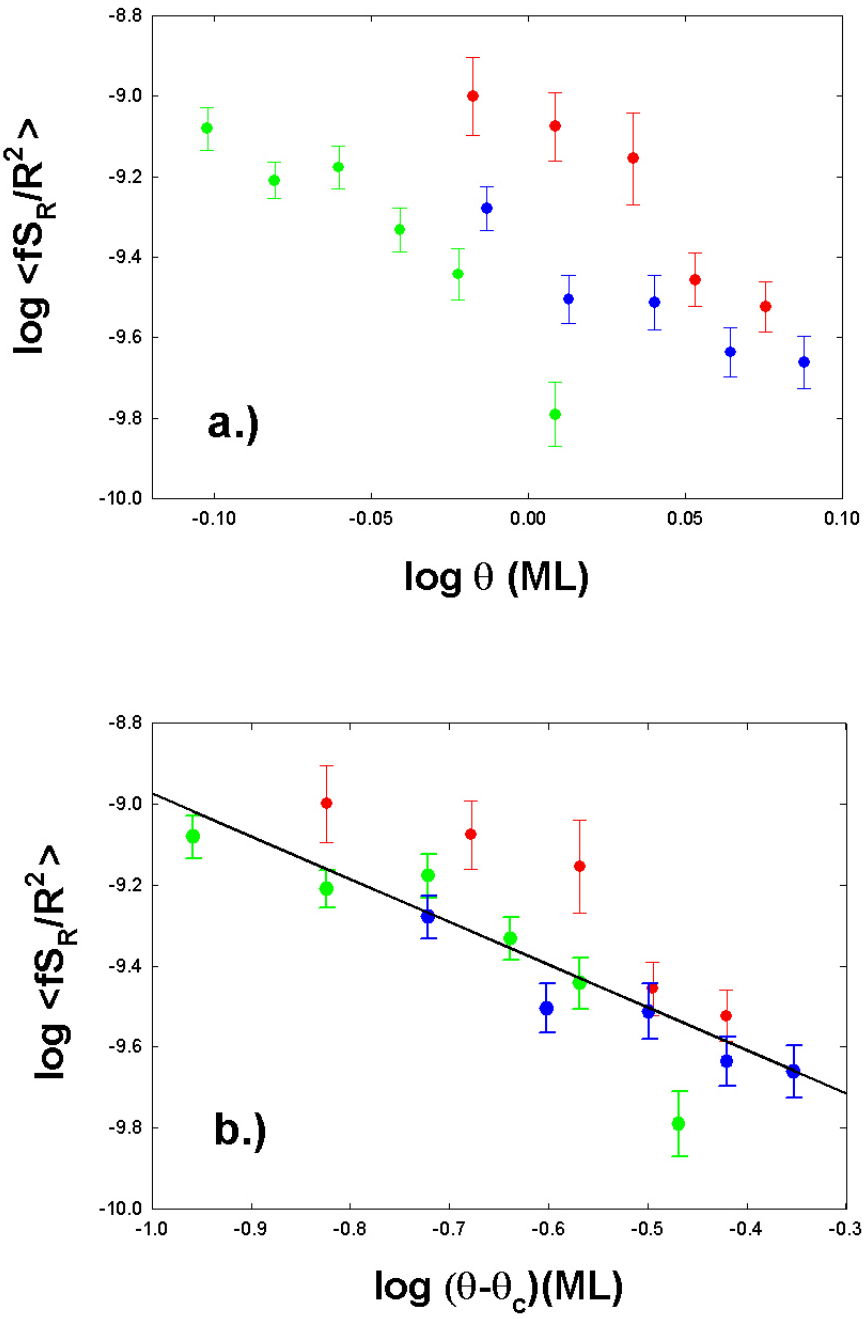

Figure 10.8 a.) Averaged noise magnitude versus coverage for three separate films. b.) The same data plotted versus reduced coverage showing at least a tendency towards collapse. The solid line is a linear fit whose slope gives the noise scaling exponent.

$$R(T) = R_0 \exp\left(\frac{T_0}{T}\right)^{\alpha} \qquad (10.1)$$

where α could vary from ¼ to ½ . This could describe variable range hopping conduction or hopping on a fractal network as described in the previous chapter. All of these fits tended to be worse than the fit to a simple Arrhenius activated form. In addition, the relatively high temperatures of this experiment make VRH conduction rather unlikely and the alternative hopping models will therefore not be discussed further.

10.4 Discussion and Conclusion

Combining the transport and STM results presented in the previous section allows a rather complete qualitative picture of the onset of conduction in ultra-thin films of Ag on Si(111)-(7x7). The confirmation of Heun and co-worker's 2D percolation critical exponents for this system is very satisfying but naturally does not address any of the lingering questions that were mentioned in the introduction. To make progress toward this end, the noise critical exponent is extremely valuable. Initial arguments concerning the critical behavior in the Ag/Si system assumed that percolation occurred on the underlying honeycomb lattice provided by the Si(111)-(7x7) substrate. Our noise measurements suggest that this assumption is not correct and that the substrate symmetry has nothing to do with the conduction onset. The noise critical exponent for any *lattice percolation* model is expected to be 1.339[160]. Our measurement of this exponent gives a value of 1.06±0.09 in clear disagreement with the lattice result. In fact, the measured exponent is only consistent with the *continuum percolation* of inverted random voids

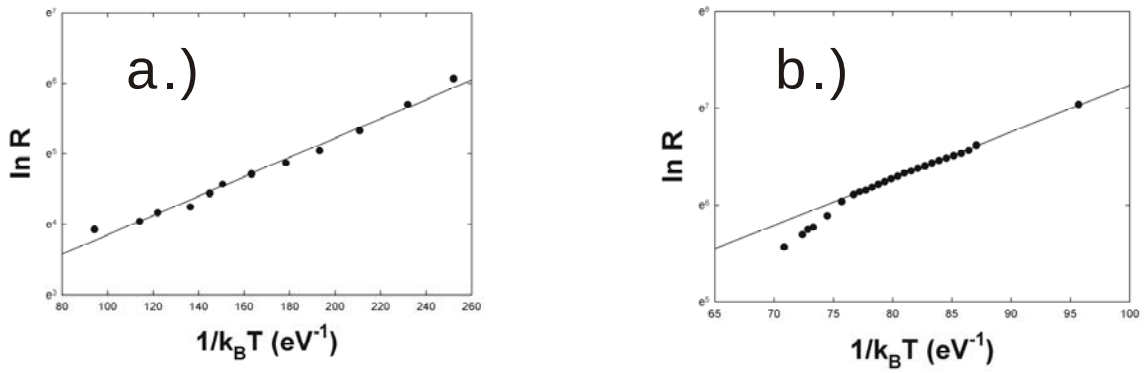

Figure 10.9 a.) Natural log of resistance versus inverse temperature measured with liquid Helium cooling in the JEOL system. b.) The same plot for data taken on a different sample with liquid Nitrogen cooling in the dedicated transport chamber.

(IRV)[161]. As discussed in chapter 9, this model essentially imagines dropping conducting disks onto random positions in an insulating region until they form a connected pathway across it. In retrospect, this seems a rather plausible model for the onset of conduction in a growing thin film and has in fact been observed for Ag films grown on glass substrates[156].

When one considers the in-situ STM observations, the IRV model of percolation becomes even more attractive. Figures 10.5 and 10.6 show that very close to the percolation threshold there exists a tenuous path of Ag islands that are touching or almost touching. Remarkably, if one simply binarizes images near the threshold and computes the box-counting dimension of the apparently connected pathway, the result is very nearly that expected for the infinite cluster in 2D percolation. Figure 10.10 shows a percolated image at about 1 ML on the left and the result of the binarization procedure on the right. The black parts of the binary image correspond to Ag islands. We imagine covering the black part with boxes of size L and seeing how many of these boxes are required. The number of boxes is related to the size of the box by

$$N(L) = L^{-D_B} \qquad (10.2)$$

where L is the box size, N is the number of boxes required to cover the Ag cluster, and D_B is the box-counting dimension. The exact result for the dimension of a 2D percolation cluster is 91/48 (~1.896)[150]. Figure 10.11 shows N(L) versus L on a double log scale for several images such as in figure 10.10 and yields an average D_B=1.85±0.03. In addition to being in good agreement with the measured box-counting dimension, the value extracted from images ranging in size from 30 nm to 300 nm is nearly identical. This

scale invariance was *not* observed when the same binarization procedure was applied to images taken below the percolation threshold.

Thus, the morphological observations show that percolation seems to occur due to connecting paths of Ag metal. These paths seem to have the fractal geometry expected for 2D percolation. Furthermore, the picture of randomly connected disks is strongly supported by the measurement of a noise critical exponent in agreement with the inverted random void model of continuum percolation[161]. The activated temperature dependence of the resistance is certainly consistent with conduction in strongly disordered systems at not very low temperatures. In particular, our measurements suggest a tunneling mechanism often found in the study of granular materials where a small charging energy determines the temperature dependence of resistance of the film[172]. More extensive temperature-dependent experiments are needed to further elucidate these details.

In conclusion, we propose an answer to the most pressing qualitative question concerning the conduction onset in the Ag/Si(111) system: does percolation occur simply through the growing Ag film or does it involve some more complicated interplay between the film and substrate? Based on the observation of *continuum* noise critical exponents as well as the direct correlation of morphological features with conduction onset using in-situ STM, we believe that *the role of the substrate in the percolation behavior in this system is minimal*. Very close to the threshold coverage it is not possible to rule out some sort of substrate-mediated tunneling completely given the fact that there may be small gaps between the Ag islands. However, these gaps are probably also small enough for ordinary vacuum tunneling to occur and therefore the simplest interpretation of the noise measurements is that the substrate simply provides a flat, fairly reproducible region in

which IRV-type continuum percolation can occur.

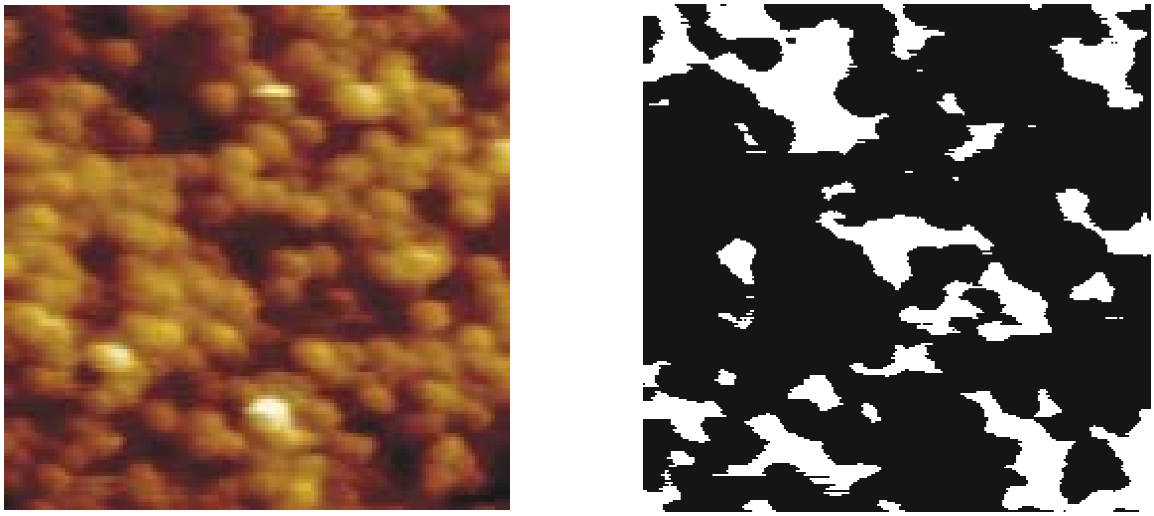

Figure 10.10 Left: 50 nm STM image at 100 K of 1ML Ag on Si(111)-(7x7). Right : result of binarization procedure.

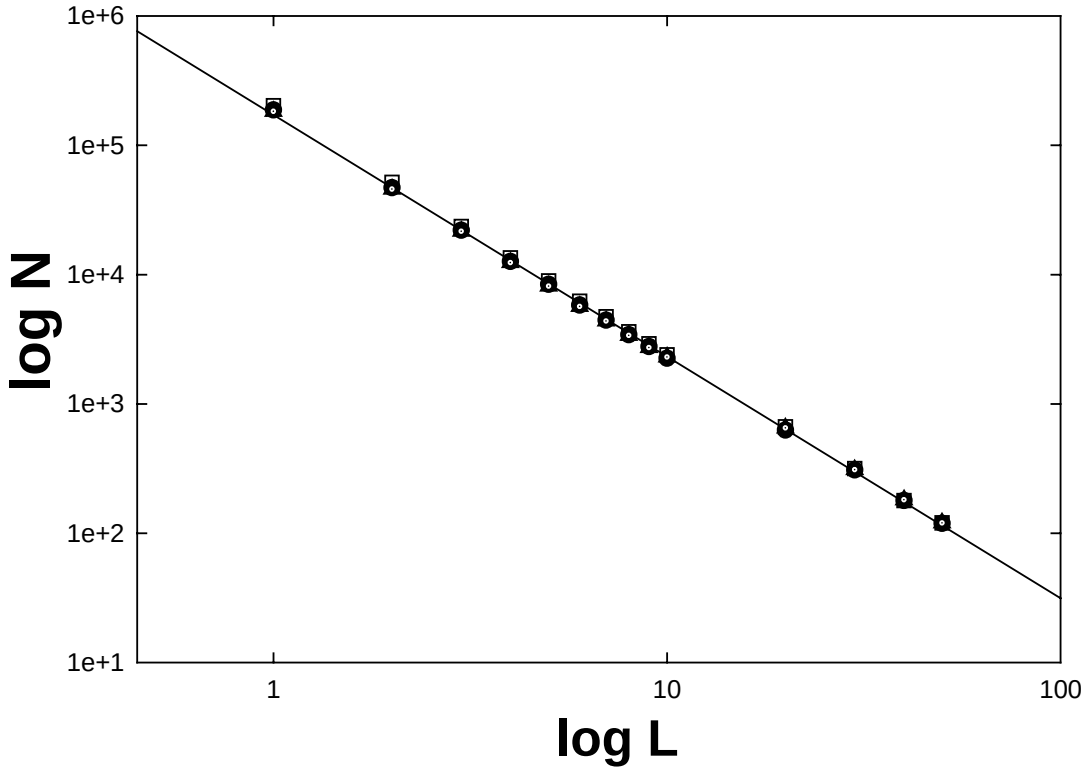

Figure 10.11 Double log plot of number of boxes versus box dimension for extracting fractal dimension of a percolation cluster of an ~ 1 ML film. Different symbols correspond to different images but overlap each other well.

Appendix A

Preparing Si(111)-(7x7) from low-doped wafers

The following is simply a recipe book for cleaning low-doped Si wafer pieces by direct current heating. We'll forgo detailed discussions of physics since it is either totally obvious or totally mysterious. Here "low-doped" will mean wafers with nominal resistivities greater than or equal to about 1 Ωcm. The reason such samples warrant an appendix is that if you aren't careful you can blow them up when you first try to drive current through them. This is a huge waste of time and samples. Depending on the UHV chamber where such a disaster occurs, it can cost 24 hrs to a week.

A Si sample at room temperature always has to be "broken down" to heat by direct current. For highly doped (i.e. low resistivity) samples it's not a big deal. The procedure is to set a small (20-50 mA) current limit on the power supply, and then turn up the voltage until the current limit is reached. Depending on the power supply the current limit will be overshot to a greater or lesser degree, but for low resistance samples this small surge almost never causes any damage. You then set a high (say 10-12 V) voltage limit and control the current output to heat the sample.

For low-doped samples the voltage required to break the samples down can be very high. This means that current surges during breakdown can locally melt or even totally shatter a sample. In chapters 9 and 10 of this thesis, we used Si wafers with nominal room temperature resistivities greater than 1000 Ωcm. Breakdown voltages were sometimes as high as 400 V. Even for resistivities of 1 Ωcm though, it would be very wise to follow the procedure that follows.

What you basically have to do is keep a current limiting resistor in series with the sample during breakdown. After breakdown, you short this resistor and let all the current go through the sample. Our current limiting resistor in Williams' lab has been an old soldering iron for the past 5 years. This procedure was taught to me by Igor Lyubinestky (now at PNNL). It feels awkward (and a little dangerous) at first, but has been pretty reliable.

Connect one sample lead to the power supply and the other sample lead to a prong of the (2-prong) soldering iron. Then connect the second soldering iron prong to the second power supply lead. Use alligator clips that have nice rubber grips to attach leads to the prongs. Turn the voltage of the power supply up until the sample breaks down. You'll see this as a sudden drop in voltage output of the power supply. The sample is now "metallic". At this point you (carefully!) grab one of the alligator clips on a prong by its rubber insulation and short it to the other prong. Now all of the current is flowing through the sample. You then just start turning the current up to get the temperatures you need for cleaning (see below). If your sample is less than 50 Ωcm you can get away with this using only one power supply. I like the HP6030A's, of which there are at least 2 in the Williams' group now.

For higher resistivity samples, the HP's will not always supply enough voltage to break the sample down. In this case, I modified the procedure a little (mainly for the purpose of doing the experiments described in chapter 10). Now you start the whole thing using a LEED supply (Bertran Model 210-01R) which can output 1000 V and 250 mA. A kilovolt should be more than enough to break down any Si sample. You do the same thing with the soldering iron that was described above but after you short the leads

you can only turn the current up to 250 mA. This is not sufficient to do any of the cleaning steps for Si(111). What you have to do is just let your (broken-down) sample sit at the maximum current for 5-15 minutes and then *very quickly* change all the leads over to a higher current output supply (preferably the HP6030A). You should put the soldering iron back in series with the sample when you do this. The idea is to warm the sample up with the LEED supply and then re-break it *while it is still hot* with the HP supply. It is important to stress that you have to move quickly for this to work. It might feel reckless at first, but it is necessary. Otherwise the sample will cool down and you'll be back where you started: not enough voltage for breakdown. Once the iron is back in series and the power supply leads are changed over, crank the voltage as fast as you can until you see the drop that indicates breakdown. Then short the prongs as usual and proceed with sample cleaning.

The procedure we usually use in Williams' lab goes like this: 15 minutes to an hour at 600 ºC, basically until the pressure gets in the mid 10-10 torr. During this step the maximum pressure may rise even into the 10-8 torr range. The next step is to spend several hours between 700 and 750 ºC. You can even leave a sample like this overnight if you want to. Both steps are just for general outgassing and leave the sample with its native oxide and not in the (7x7) reconstruction.

Removing the native oxide requires flashes of up to 1250 ºC to be most effective. At the same time, it is important in many experiments to keep the chamber pressure low (say not greater than 2 x 10-9 torr). We do this by making repeated flashes to high temperature and then rapidly quenching the sample to some low temperature (but not so low as to require another breakdown procedure). These fast flashes are what make the

HP6030A the preferred supply for cleaning Si. Once you get used to the dial, it is very easy to rapidly run the current up to where you need it and then rapidly run it back down. Basically, you should do 5-10 seconds at the flash temperature enough times to give a total time of a little over 1 minute. In the JEOL system (see chapter 10), our maximum temperature was about 1100 ºC and this procedure gave very nice surfaces. It shoud be even better in systems where the heating set-up allows you to attain the ideal flash temperature of 1250 ºC.

After about 1 minute cumulative flash time, you do one final flash (definitely only about 5 seconds) and *slowly cool* from about 900 ºC to 750 ºC to ensure that all of the surface transforms from (1x1) (the equilibrium phase above 830 ºC) to (7x7). There are many opinions in the literature about how slowly this should be done. Experience in our group indicates that about 1 minute to go through this temperature range will give you a good (7x7) surface everywhere. You can even get away with half of that time.

Appendix B

Analysis of STM Line-Scan Images

Once you have obtained a line-scan image (by disabling the slow scan direction and letting the tip scan over the same point on a step for a given time) it is necessary to digitally extract the step position. Of course, you could attempt to do this with a ruler, but it is very painful. We did it a couple of times to check that our digital processing was working OK. We use the step-position-extracting procedure that was used nearly a decade ago at the University of Maryland. The only reference I know for it is in an appendix of W.W. Pai's Ph.D thesis. Larry Pai was a student of J.E. Reutt-Robey in the early 1990's and studied step fluctuations on Ag(110) using line-scanning.

First the pseudo-image has to be flattened. In the Omicron Scala software, simply open the image and click on the background processing menu. In this menu, start by subtracting the slope from the whole image and then choose a roughly square area that is on top of a terrace and subtract this plane from the image. You will be left with an image that looks like a regular flat staircase in line profile.

The next steps are done in home-written programs using the IDL language. They are slightly modified from W.W. Pai's appendix. The idea is to pick a function that has a staircase-like shape and fit the pseudo-image line profiles to this function. Some fit parameter can then be taken as the step position. We use the function, $y=A_0 tanh((x-A_1)/A_2)+A_3$, which has a staircase shape and enough free parameters to fit nearly any line profile, almost regardless of noise. The parameter A_1 is the center of the staircase and thus represents the step position. In IDL, this function is defined as a true *function* in the

sense of IDL programming at the very beginning of the program. Below is the little fitting loop that goes through the image and pulls out the step position from every line.

```
For j=0, (LY-1) Do Begin
For m=0, (LX-1) Do Begin
  Y[m]= CroppedImg[m,j]
EndFor
Line=CurveFit(X,Y,weights,A,sigma,Function_Name='gfunct',tol=1.e5)
   steppos[j]=A[1]
EndFor
```

CroppedImg *[x,y]* is the array read in from the pseudo-image and ***A*** is the vector of fitting parameters. Here we note that this procedure is designed to analyze one step at a time so that you have to crop the image before you start the fitting. This brings up the only unreliable part of the whole procedure: for some reason cropping the image in certain ways results in unstable fitting. It is often necessary to play with the exact amount you crop to get the fit to be stable. Sometimes even changes of less than a percent in the amount of cropping can make all the difference (it can be frustrating). Several other group members have developed other techniques for finding step positions. I like the fitting procedure: it is traditional and relatively impervious to large z- noise on the terraces. Obviously, simple thresholding runs into problems if you have big ripples on the terraces.

Next we'll just reproduce the loops for computing statistical quantities of interest from the extracted step positions.

1.)Temporal Correlation Function, *G(t)*:

```
 Openw, 10,'c:\My Documents\Analysis\' +rawfilename+'.corrfcn.txt'
 For j=0,(LY-1) Do Begin
      For i=j+1,(LY-1) Do Begin
        ns[i-j]=ns[i-j]+1
        G[i-j] =G[i-j]+(steppos[i]-steppos[j])^2
      EndFor
    EndFor
 For i=1, (LY-1) Do Begin
      G[i]=G[i]/ns[i]
      printf, 10, i, G[i]
 EndFor
Close, 10
```

In this code, ns[j] is a list containing the number of time segements from the x(t) function of size j. Since we average overlapping segments from the time series it is necessary to normalize by the total number of segments of a given duration.

2.) Persistence probability, *p(t)*:

```
For k=1,(LY-2) Do Begin
 For j=(k+1),(LY-1) Do Begin
   nseg[j-k]=nseg[j-k]+1
      i=k
      Repeat Begin
        p[j-k]=1
        If StepPos[i] Gt StepPos[k] Then p[j-k]=0  ;Current:p-
```

```
      i=i+1
    EndRep Until ((p[j-k]Eq 0)Or(i Eq j))
    pt[j-k]=pt[j-k]+p[j-k]
  EndFor
 EndFor
Openw, 11,'c:\My Documents\Analysis\' +rawfilename+'.persmin.txt'
For k= 1,(LY-1) Do Begin
 pt[k]=pt[k]/nseg[k]
 printf, 11, k, pt[k]
EndFor
Close, 11
```

The above loop computes returns to the initial configuration from the below. The returns from the other side (which should have the same functional form for steady state, linear models) can be computed using the same loops but with GT replaced by LT in the If-Then statement inside the Repeat…Until loop. Again, we define a vector nseg to normalize the quantity of interest by the number of time segments that go into its average.

3.) Autocorrelation , $C(t)$, and Cross Correlation, $C_1(t)$

```
    For j=0,(LY-1) Do Begin
     NMAX=lY-1-J
     CT=0.0
      For i=1,(NMAX) Do Begin
       ct =CT+((steppos[i+j])*(steppos[i]))
```

```
    EndFor
    AC[j]=ct/NMAX
  EndFor
```

This algorithm is a little different than the above simply in its implementation. It was given to me by M. Constantin and I just translated it to IDL. The only important thing to remember is that in computing autocorrelations you have to first normalize the $x(t)$data to have zero mean. Just compute the average step position and subtract it off before you compute $C(t)$. The same goes for the cross correlation function. Use the above algorithm with *both* of the near-neighbor step positions referred to their own, individual averages, but just substitute the product $x_1(i+j)x_2(j)$ in center loop above to get $C_1(t)$.

Appendix C
Numerical Integration of Langevin Models

In this appendix, we will briefly describe the simple numerical solution of the stochastic differential equations used to model the AD and SED limited step fluctuations described in several chapters of this thesis. The procedure is a very simple Euler discretization of the differential operators appearing in the Langevin equations for these processes. The only really nontrivial point will be the description of how to implement a conservative noise appropriate for modeling edge diffusion.

To start, we'll just list the discretizations of $\nabla^2 x(y,t)$ and $\nabla^4 x(y,t)$. These are the same that were used by Krug et al. in Ref. 32. (Letting *dx=1* as in that work):

$$\nabla^2 x(i,t) = x(i-1,t) - 2x(i,t) + x(i+1,t). \qquad \text{(C.1)}$$

$$\nabla^4 x(i,t) = x(i-2,t) - 4x(i-1,t) + 6x(i,t) - 4x(i-1,t) + x(i-2,t). \qquad \text{(C.2)}$$

The discretization of time derivatives appearing in the Langevin models is even simpler:

$$\partial_t x(i,t) = 1/dt(x(i,t) - x(i,t-1)). \qquad \text{(C.3)}$$

The final component of the numerical integration is to add in the stochastic noise term. For the AD process, modeled by the Edwards-Wilkinson equation, this is simply done by adding a random number term using any standard random number generator. The distribution from which the number is pulled can be either uniform of Gaussian. In the work described in this thesis a normally distributed random number was usually used. It was implemented with the IDL function *RandomN(seed)*.

To model edge-diffusion, the noise has to be conservative of average step position and so a simple random number can't just be added. Instead, we make a *vector* of

random numbers and then add the *first derivative* of this vector to the deterministic part of the discrete Langevin equation. This ensures conservation since the noise is written as the gradient of a stochastic *current*. This procedure was taken from an older numerical study of spinodal decomposition by T.M. Rogers and co-workers (see Phys. Rev. B 37 (1988) 9638.) and has been used by myself and M. Constantin working in S. Das Sarma's group.

Below is a section of code showing the iteration that integrates the SED Langevin equation. It is most likely possible to significantly improve on the efficiency of this code, but it runs and is not prohibitively time-consuming.

```
For n=1, (time-1) Do Begin
  For m=0,lx-1 Do Begin
    eta[m]=sqrt(D)*Randomn(Seed)
  EndFor
  For i=0, (LX-1) Do Begin
  etad=Sqrt(Dd)*Randomn(sdd)
  t=n*dt
  If i EQ 0 Then Begin
    h[i,n]=h[i,n-1]-dt*Kap*(h[LX-2,n-1]-4*h[LX-1,n-1]+6*h[i,n-1]-4*h[i+1,n-1]+h[i+2,n-
1])+Sqrt(2*D*dt/dx)*(eta[i+1]-eta[i])
  EndIf Else Begin
    If i Eq(LX-1) Then Begin
      h[i,n]=h[i,n-1]-dt*Kap*(h[i-2,n-1]-4*h[i-1,n-1]+6*h[i,n-1]-4*h[0,n-1]+h[1,n-
1])+Sqrt(2*D*dt/dx)*(eta[0]-eta[i])
```

```
    EndIf Else Begin
    If i Eq 1 Then Begin
      h[i,n]=h[i,n-1]-dt*Kap*(h[LX-1,n-1]-4*h[i-1,n-1]+6*h[i,n-1]-4*h[i+1,n-1]+h[i+2,n-
1])+Sqrt(2*D*dt/dx)*(eta[i+1]-eta[i])
    EndIf Else Begin
    If i Eq (Lx-2) Then Begin
      h[i,n]=h[i,n-1]-dt*Kap*(h[i-2,n-1]-4*h[i-1,n-1]+6*h[i,n-1]-4*h[i+1,n-1]+h[0,n-
1])+Sqrt(2*D*dt/dx)*(eta[i+1]-eta[i])
    Endif Else Begin
      h[i,n]=h[i,n-1]-dt*Kap*(h[i-2,n-1]-4*h[i-1,n-1]+6*h[i,n-1]-4*h[i+1,n-1]+h[i+2,n-
1])+Sqrt(2*D*dt/dx)*(eta[i+1]-eta[i])
    EndElse
    EndElse
    EndElse
    EndElse

  ht[i]=h[i,n]
  hb[i]=h[i,1]
  EndFor
EndFor
```

Here *eta[k]* is the noise vector, and the long broken lines move the step configuration forward in time using the discretizations already described. There are many lines here to explicitly implement the periodic boundary conditions within two sites of the end of the 1D interface.

References

[1] H. C. Jeong and E. D. Williams, Surface Science Reports **34**, 171 (1999).

[2] W. K. Burton, N. Cabrera, and F. C. Frank, Philos. Trans. R. Soc. London Ser. A **243**, 299 (1951).

[3] M. Giesen, Progress in Surface Science **68**, 1 (2001).

[4] N. C. Bartelt, J. L. Goldberg, T. L. Einstein, et al., Surf. Sci. **273**, 252 (1992).

[5] T. Ihle, C. Misbah, and O. Pierre-Louis, Phys. Rev. B **58**, 2289 (1998).

[6] S. V. Khare and T. L. Einstein, Phys. Rev. B **57**, 4782 (1998).

[7] P. J. Feibelman, Phys. Rev. B **62**, 17020 (2000).

[8] R. K. Pathria, *Statistical Mechanics* (Butterworth-Heinemann, Oxford, 1999).

[9] A. Einstein, Ann. Phys. **17**, 549 (1905).

[10] M. v. Smoluchowski, Ann. Phys. **21**, 756 (1906).

[11] P. Langevin, Comptes Rend. Acad. Sci. Paris **146**, 530 (1908).

[12] N. C. Bartelt, J. L. Goldberg, T. L. Einstein, et al., Phys. Rev. B **48**, 15453 (1993).

[13] S. Majaniemi, T. Ala-Nissila, and J. Krug, Phys. Rev. B **53**, 8071 (1996).

[14] A.-L. Barabasi and H. E. Stanley, *Fractal Concepts in Surface Growth* (Cambridge University Press, Cambridge, 1995).

[15] N. C. Bartelt, T. L. Einstein, and E. D. Williams, Surf. Sci. **312**, 411 (1994).

[16] B. Blagojevic´ and P. M. Duxbury, Phys. Rev. E **60**, 1279 (1999).

[17] C. P. Flynn, Phys. Rev. B **66**, 155405 (2002).

[18] R. Kubo, Rep. Prog. Phys. **29**, 255 (1966).

[19] R. E. Wilde and S. Singh, *Statistical Mechanics: Fundamentals and Modern Applications* (John Wiley and Sons, Inc., New York, 1998).

[20] M. Ondrejcek, W. Sweich, and C. P. Flynn, Surf. Sci. **566-568**, 160 (2004).

[21] I. Lyubinetsky, D. B. Dougherty, T. L. Einstein, et al., Phys. Rev. B **66**, 085327 (2002).

[22] P. C. Hohenberg and B. I. Halperin, Rev. Mod. Phys. **49**, 435 (1977).

[23] J. Kallunki and J. Krug, Surf. Sci. **523**, L53 (2003).

[24] A. M. Cadilhe, C. R. Stoldt, C. J. Jenks, et al., Phys. Rev. B **61**, 4910 (2000).

[25] M. Giesen, Surf. Sci. **442**, 543 (1999).

[26] Y.-N. Yang, E. S. Fu, and E. D. Williams, Surf. Sci. **356**, 101 (1996).

[27] D.-J. Liu and J. D. Weeks, Phys. Rev. B **57**, 14891 (1998).

[28] M. Giesen and G. Schulze Icking-Konert, Surf. Sci. **412-413**, 645 (1998).

[29] S. F. Edwards and D. R. Wilkinson, Proc. R. Soc. London A **381**, 17 (1982).

[30] S. Redner, *A Guide to First-Passage Processes* (Cambridge University Press, Cambridge, 2001).

[31] S. N. Majumdar, Curr. Sci. **77**, 370 (1999).

[32] J. Krug, H. Kallabis, S. N. Majumdar, et al., Phys. Rev. E **56**, 2702 (1997).

[33] M. G. Lagally, J. Vac. Sci. Technol. A **21**, S54 (2003).

[34] G. Binnig, H. Rohrer, C. Gerber, et al., Phys. Rev. Lett. **49**, 57 (1982).

[35] G. Binnig, H. Rohrer, C. Gerber, et al., Phys. Rev. Lett. **50**, 120 (1983).

[36] K. Takayanagi, Y. Tanishiro, M. Takahashi, et al., J. Vac. Sci. Technol. A **3**, 1502 (1985).

[37] R. M. Feenstra, J. A. Stroscio, J. Tersoff, et al., Phys. Rev. Lett. **58**, 1192 (1987).

[38] R. J. Hamers, R. Tromp, and J. E. Demuth, Phys. Rev. Lett. **56**, 1972 (1986).

[39] Y. Kuk and P. J. Silverman, Rev. Sci. Instrum. **60**, 165 (1989).

[40] J. Tersoff and D. R. Hamann, Phys. Rev. B **31**, 805 (1985).

[41] J. Tersoff and D. R. Hamann, Phys. Rev. Lett. **50**, 25 (1983).

[42] J. Bardeen, Phys. Rev. Lett. **6**, 57 (1961).

[43] R. J. Hamers, in *Scanning Tunneling Microscopy I*, edited by R. Wiesendanger and H.-J. Guntherodt (Springer-Verlag, Berlin, 1992).

[44] C. J. Chen, *Introduction to scanning tunneling microscopy* (Oxford University Press, New York, 1993).

[45] G. Binnig and D. P. E. Smith, Rev. Sci. Instrum. **57**, 1688 (1986).

[46] D. Jeon and R. F. Willis, J. Vac. Sci. Technol. A **9**, 2418 (1991).

[47] A. J. Melmed, J. Vac. Sci. Technol. B **9**, 601 (1991).

[48] L. Kuipers, Ph.D Thesis (University of Amsterdam, 1994).

[49] N. C. Bartelt and R. Tromp, Phys. Rev. B **54**, 11731 (1996).

[50] M. Kammler, M. Horn von Högen, N. Voss, et al., Phys. Rev. B **65**, 075312 (2002).

[51] J. J. Lander and J. Morrison, Surf. Sci. **2**, 553 (1964).

[52] R. J. Hamers, Phys. Rev. B **40**, 1657 (1989).

[53] J. E. Northrup, Phys. Rev. Lett. **53**, 683 (1984).

[54] S. Kodiyalam, K. E. Khor, N. C. Bartelt, et al., Phys. Rev. B **51**, 5200 (1995).

[55] A. Pimpinelli, J. Villain, D. E. Wolf, et al., Surf. Sci. **295**, 143 (1993).

[56] A. Ichimiya, K. Hayashi, E. D. Williams, et al., Phys. Rev. Lett. **84**, 3662 (2000).

[57] E. S. Fu, M. D. Johnson, D.-J. Liu, et al., Phys. Rev. Lett. **77**, 1091 (1996).

[58] M. Degawa, K. Thürmer, I. Morishima, et al., Surf. Sci. **487**, 171 (2001).

[59] S. Tanaka, N. C. Bartelt, C. C. Umbach, et al., Phys. Rev. Lett. **78**, 3342 (1997).

[60] K. Thurmer, J. E. Reutt-Robey, E. D. Williams, et al., Phys. Rev. Lett. **87**, 186102 (2001).

[61] M. Giesen, G. Schulze Icking-Konert, D. Stapel, et al., Surf. Sci. **366**, 229 (1996).

[62] K. Yagi-Watanabe, D. Suzuki, and H. Fukutani, Surf. Sci. **518**, 155 (2002).

[63] S. Speller, W. Heiland, A. Biedermann, et al., Surf. Sci. **331-333**, 1056 (1995).

[64] L. Masson, L. Barbier, J. Cousty, et al., Surf. Sci. **317**, L1115 (1994).

[65] L. Kuipers, M. S. Hoogeman, J. W. M. Frenken, et al., Phys. Rev. B **52**, 11387 (1995).

[66] E. H. Conrad, A. Menzel, S. Kiriukhin, et al., Phys. Rev. Lett. **81**, 3175 (1998).

[67] T. Michely, M. C. Reuter, and R. M. Tromp, Phys. Rev. B **53**, 4105 (1996).

[68] E. D. Williams and N. C. Bartelt, in *Handbook of Surface Science*, edited by W. N. Unertl (Elsevier, North Holland, 1996), Vol. 1, p. 51.

[69] I. Lyubinetsky, D. B. Dougherty, H. L. Richards, et al., Surf. Sci. **492**, L671 (2001).

[70] E. A. Kramstova, A. V. Zotov, A. A. Saranin, et al., Appl. Surf. Sci. **82-83**, 576 (1994).

[71] R. Q. Hwang, E. D. Williams, and R. L. Park, Surf. Sci. **193**, L53 (1988).

[72] M. Yoshimura, K. Takaoka, T. Yao, et al., J. Vac. Sci. Technol. B **12**, 2434 (1994).

[73] A. A. Saranin, V. G. Kotlyar, A. V. Zotov, et al., Surf. Sci.**??** (2002).

[74] R. Q. Hwang, J. Schroder, C. Gunther, et al., Phys. Rev. Lett. **67**, 3270 (1991).

[75] O. Pierre-Louis, M. R. D'Orsogna, and T. L. Einstein, Phys. Rev. Lett. **82**, 3661 (1999).

[76] W. W. Pai, J. F. Wendelken, C. R. Stoldt, et al., Phys. Rev. Lett. **86**, 3088 (2001).

[77] J. C. Heyraud and J.- J. Metois, Surf. Sci. **128**, 334 (1983).

[78] S. Surnev, P. Coenen, B. Voigtländer, et al., Phys. Rev. B **56**, 13 (1997).

[79] M. Nowicki, C. Bombis, A. Emundts, et al., Phys. Rev. B **67**, 075405 (2003).

[80] N. Akutsu and Y. Akutsu, J. Phys. Condens. Matter **11**, 6635 (1999).

[81] M. P. Marder, *Condensed Matter Physics* (John Wiley and Sons, Inc., New York, 2000).

[82] G. L. Kellogg, Surf. Sci. Rep. **21**, 1 (1994).

[83] G. Antczak and G. Ehrlich, Phys. Rev. Lett. **92**, 166105 (2004).

[84] M. Giesen and G. Schulze Icking-Konert, Surf. Sci. **412-413**, 645 (1998).

[85] L. Kuipers, M. S. Hoogeman, and J. W. M. Frenken, Surf. Sci. **340**, 231 (1995).

[86] M. Kardar, G. Parisi, and Y.-C. Zhang, Phys. Rev. Lett. **56**, 889 (1986).

[87] Z.-W. Lai and S. Das Sarma, Phys. Rev. Lett. **66**, 2348 (1991).

[88] J. B. Hannon, F.-J. Meyer zu Heringdorf, J. Tersoff, et al., Phys. Rev. Lett. **86**, 4871 (2001).

[89] A. K. Schmid, N. C. Bartelt, J. C. Hamilton, et al., Phys. Rev. Lett. **78**, 3507 (1997).

[90] H. H. Weitering, A. R. H. F. Ettema, and T. Hibma, Phys. Rev. B **45**, 9126 (1992).

[91] M. Hupalo, V. Yeh, L. Berbil-Bautista, et al., Phys. Rev. B **64**, 155307 (2001).

[92] M. Hupalo, S. Kremmer, V. Yeh, et al., Surf. Sci. **493**, 526 (2001).

[93] T.-L. Chan, C. Z. Wang, M. Hupalo, et al., Phys. Rev. B **68**, 045410 (2003).

[94] E. Ganz, I.-S. Hwang, F. Xiong, et al., Surf. Sci. **257**, 259 (1991).

[95] O. Custance, I. Brihuega, J.-Y. Veuillen, et al., Surf. Sci. **482-485**, 878 (2001).

[96] G. Le Lay, J. Peretti, M. Hanbucken, et al., Surf. Sci. **204**, 57 (1988).

[97] D. Nakamura, J. Yuhara, and K. Morita, Surf. Sci. **425**, 174 (1999).

[98] M. Saitoh, K. Oura, K. Asano, et al., Surf. Sci. **154**, 394 (1985).

[99] D. Tang, H. E. Elsayed-Ali, J. F. Wendelken, et al., Phys. Rev. B **52**, 1481 (1995).

[100] J. Slezak, P. Mutombo, and V. Chab, Surf. Sci. **454-456**, 584 (2000).

[101] K. Oura, V. G. Lifshits, A. A. Saranin, et al., *Surface Science: An Introduction* (Springer-Verlag, Berlin, 2003).

[102] S. Hasegawa, H. Daimon, and S. Ino, Surf. Sci. **186**, 138 (1987).

[103] E. Ganz, F. Xiong, I.-S. Hwang, et al., Phys. Rev. B **43**, 7316 (1991).

[104] H. Hibino and T. Ogino, Surf. Sci. **328**, L547 (1995).

[105] S.-T. Yau, B. R. Thomas, and P. G. Vekilov, Phys. Rev. Lett. **85**, 353 (2000).

[106] M. Giesen and S. Baier, J. Phys. Condens. Matter **13**, 5009 (2001).

[107] W. Feller, *An Introduction to Probability Theory and its Applications Vol. 1*,(John Wiley and Sons, Inc., New York, 1950).

[108] D. B. Dougherty, I. Lyubinetsky, E. D. Williams, et al., Phys. Rev. Lett. **89**, 136102 (2002).

[109] C. Dasgupta, M. Constantin, S. Das Sarma, et al., Phys. Rev. E **69**, 022101 (2004).

[110] M. Marcos-Martin, D. Beysens, J. P. Bouchaud, et al., Physica A **214**, 396 (1995).

[111] G. P. Wong, R. W. Mair, R. L. Walsworth, et al., Phys. Rev. Lett. **86**, 4156 (2001).

[112] B. Yurke, A. N. Pargellis, S. N. Majumdar, et al., Phys. Rev. E **56**, 40 (1997).

[113] W. Y. Tam, R. Zeitak, K. Y. Szeto, et al., Phys. Rev. Lett. **78**, 1588 (1997).

[114] D. B. Dougherty, O. Bondarchuk, M. Degawa, et al., Surf. Sci. **527**, L213 (2003).

[115] B. Derrida, V. Hakim, and V. Pasquier, Phys. Rev. Lett. **75**, 751 (1995).

[116] I. Dornic and C. Godreche, J. Phys. A **31**, 5413 (1998).

[117] H. Kallabis and J. Krug, Europhys. Lett. **45**, 20 (1999).

[118] M. Constantin, C. Dasgupta, P. Punyindu Chatraphorn, et al., Phys. Rev. E **69**, 061608 (2004).

[119] B. B. Mandelbrot and J. W. van Ness, SIAM Rev. **10**, 422 (1968).

[120] S. M. Berman, Ann. Math. Stat. **41**, 1260 (1970).

[121] M. Constantin, S. Das Sarma, C. Dasgupta, et al., Phys. Rev. Lett. **91**, 086103 (2003).

[122] G. F. Newell and M. Roseblatt, Ann. Math. Stat. **33**, 1306 (1962).

[123] S. N. Majumdar, A. J. Bray, and G. C. M. A. Ehrhardt, Phys. Rev. E **64**, 015101R (2001).

[124] G. C. M. A. Ehrhardt et. al., Phys. Rev. E **65**, 041102 (2002).

[125] M. Uwaha and K. Watanabe, J. Phys. Soc. Jpn. **160**, 497 (2000).

[126] M. Uwaha, J. Phys. Soc. Jpn. **57**, 1681 (1988).

[127] A. Pimpinelli and J. Villain, *Physics of Crystal Growth* (Cambridge University Press, Cambridge, 1998).

[128] J. G. McLean, B. Krishnamachari, D. R. Peale, et al., Phys. Rev. B **55**, 1811 (1997).

[129] N. Israeli and D. Kandel, Phys. Rev. Lett. **80**, 3300 (1998).

[130] S. Kodambaka, V. Petrova, S. V. Khare, et al., Phys. Rev. Lett. **89**, 176102 (2002).

[131] H. Hibino, C.-W. Hu, T. Ogino, et al., Phys. Rev. B **63**, 254402 (2001).

[132] S. Kodambaka, V. Petrova, S. V. Khare, et al., Phys. Rev. Lett. **89**, 176102 (2002).

[133] K. Thürmer, J. E. Reutt-Robey, and E. D. Williams, Surf. Sci. **537**, 123 (2003).

[134] C. Rottman, M. Wortis, J. C. Heyraud, et al., Phys. Rev. Lett. **52**, 1009 (1984).

[135] M. Wortis, in *Chemistry and Physics of Solid Surfaces VII*, edited by R. Vaneslow and R. F. Howe (Spriger-Verlag, Berlin, 1988).

[136] D. B. Dougherty, K. Thürmer, M. Degawa, et al., Surf. Sci. **554**, 233 (2004).

[137] M. Degawa and E. D. Williams, unpublished results (2004).

[138] P. Dutta and P. M. Horn, Rev. Mod. Phys. **51**, 497 (1981).

[139] A. K. Raychaudhuri, Curr. Op. in Sol. St. and Mat.Sci. **6**, 67 (2002).

[140] M. B. Weissman, Rev. Mod. Phys. **60**, 537 (1988).

[141] M. Henzler, in *Surface Physics of Materials*, edited by J. M. Blakely (Academic Press, New York, 1975), Vol. 2.

[142] S. Hasegawa, Prog. Surf. Sci. **60**, 89 (1999).

[143] N. W. Ashcroft and N. D. Mermin, *Solid State Physics* (Saunders College Publishing, Fort Worth, 1976).

[144] S. Datta, *Electronic transport in mesoscopic systems* (Cambridge University Press, Cambridge, 1995).

[145] A. F. Ioffe and A. R. Regel, Prog. Semicond. **4**, 237 (1960).

[146] P. A. Lee and T. V. Ramakrishnan, Rev. Mod. Phys. **57**, 287 (1985).

[147] M. Sahimi, *Applications of Percolation Theory* (Taylor and Francis, Bristol, PA, 1994).

[148] B. I. Shklovskii and A. L. Efros, *Electronic Properties of Doped Semiconductors* (Springer-Verlag, Berlin, 1984).

[149] H. E. Stanley, Rev. Mod. Phys. **71**, 358 (1999).

[150] D. Stauffer and A. Aharony, *Introduction to Percolation Theory* (Taylor and Francis, London, 1992).

[151] P. W. Kasteleyn and C. M. Fortuin, J. Phys. Soc. Jpn. Suppl. **26**, 11 (1969).

[152] B. Nienhuis, Phys. Rev. Lett. **49**, 1062 (1982).

[153] S. Kogan, *Electronic Noise and Fluctuations in Solids* (Cambridge University Press, New York, 1996).

[154] M. Murat, S. Marianer, and D. J. Bergman, J. Phys. A **19**, L275 (1986).

[155] Y. Song, S.-I. Lee, and J. R. Gaines, Phys. Rev. B **46**, 14 (1992).

[156] M. Octavio, G. Guitierez, and J. Aponte, Phys. Rev. B **36**, 2461 (1987).

[157] C. J. Lobb and M. G. Forrester, Phys. Rev. B **35**, 1899 (1987).

[158] N. F. Mott, J. Non-Cryst. Solids **8-10**, 1 (1968).

[159] F. N. Hooge and A. Hoppenbrouwers, Physica **42**, 331 (1969).

[160] R. Rammal, C. Tannous, P. Breton, et al., Phys. Rev. Lett. **54**, 1718 (1985).

[161] A.-M. S. Tremblay, S. Feng, and P. Breton, Phys. Rev. B **33**, 2077 (1986).

[162] R. H. Koch, R. B. Laibowitz, E. I. Alessandrini, et al., Phys. Rev. B **32**, 6932 (1985).

[163] G. A. Garfunkel and M. B. Weissman, Phys. Rev. Lett. **55**, 296 (1985).

[164] S. Tosch and H. Neddermeyer, Phys. Rev. Lett. **61**, 349 (1988).

[165] F. Moresco, M. Rocca, T. Hildebrandt, et al., Surf. Sci. **463**, 22 (2000).

[166] S. Heun, J. Bange, R. Schad, et al., J. Phys. Condens. Matter **5**, 2913 (1993).

[167] R. Schad, S. Heun, T. Heidenblut, et al., Appl. Phys. A **55**, 231 (1992).

[168] R. Schad, S. Heun, T. Heidenblut, et al., Phys. Rev. B **45**, 11430 (1992).

[169] G. Meyer and K.-H. Rieder, Appl. Phys. Lett. **64**, 3560 (1994).

[170] K. R. Kimberlin and M. C. Tringides, J.Vac. Sci. Tecnol. A **13**, 462 (1994).

[171] P. R. Bevington, *Data Reduction and Error Analysis for the Physical Sciences* (McGraw-Hill Book company, New York, 1969).

[172] B. Abeles, P. Sheng, M. D. Coutts, et al., Adv. in Physics, 407 (1975).